Universidade de Aveiro Departamento de Química
2013

CELINE ISABELLE LOPES JUSTINO

DESENVOLVIMENTO DE UM NANOSENSOR PARA DETEÇÃO DE RISCO DE DOENÇAS CARDIOVASCULARES

NANOSENSOR FOR ASSESSING THE RISK OF A CARDIOVASCULAR DISEASE

Universidade de Aveiro Departamento de Química
2013

CELINE ISABELLE LOPES JUSTINO

DESENVOLVIMENTO DE UM NANOSENSOR PARA DETEÇÃO DE RISCO DE DOENÇAS CARDIOVASCULARES

NANOSENSOR FOR ASSESSING THE RISK OF A CARDIOVASCULAR DISEASE

Tese apresentada à Universidade de Aveiro para cumprimento dos requisitos necessários à obtenção do grau de Doutor em Química, realizada sob a orientação científica do Doutor Armando da Costa Duarte, Professor Catedrático no Departamento de Química da Universidade de Aveiro e da Doutora Teresa Alexandra Peixoto da Rocha Santos, Professora Associada no ISEIT/Viseu do Instituto Piaget.

Apoio financeiro da FCT e do FSE no âmbito do QREN – POPH – Tipologia 4.1 – Formação Avançada.

Dedico este trabalho à minha família, especialmente aos meus pais e irmão.

o júri

presidente

Prof. Doutor João Manuel Nunes Torrão
Professor Catedrático da Universidade de Aveiro

Prof. Doutora Maria Isabel Almeida Ferra
Professora Catedrática da Universidade da Beira Interior

Prof. Doutor Armando da Costa Duarte
Professor Catedrático da Universidade de Aveiro

Prof. Doutora Teresa Alexandra Peixoto da Rocha Santos
Professora Associada do ISEIT/Viseu – Instituto Piaget

Prof. Doutora Susana Isabel Pinheiro Cardoso de Freitas
Professora Auxiliar Convidada do Instituto Superior Técnico e Investigadora Sénior do INESC-MN

Doutora Regina Maria Brandão de Oliveira Duarte
Equiparada a Investigadora Auxiliar do CESAM – Centro de Estudos do Ambiente e do Mar da Universidade de Aveiro

agradecimentos

Aos meus orientadores, Professor Doutor Armando Duarte e Doutora Teresa Rocha Santos, pela inteira disponibilidade e ajuda ao longo do trabalho de doutoramento, assim como pela troca de experiências científica e pessoal. A par da exigência, permitiram-me crescer e adquirir mais confiança, sendo os dois uma referência pessoal pelo empenho, dedicação e interesse pelo mundo científico.

A todos os membros do INESC-MN (Lisboa) pelo simpático acolhimento e ajudas prestadas por todos, nomeadamente ao Doutor Paulo Freitas e Doutora Susana Freitas pela oportunidade em aceder às instalações do INESC-MN, proporcionando todos os recursos disponíveis de forma a realizar o trabalho de microfabricação dos transístores de efeito de campo (FET), ao Pedro Novo (pela iniciação em AutoCAD), ao Fernando Silva (pela ajuda na fotolitografia), à Virgínia Soares (pela ajuda na máquina de corte), à Joana Loureiro e Cláudia Costa (pelo ensino da técnica de deposição de silicone nos FET), ao José Pedro Amaral (pelo ensino da integração dos FET em placas de circuito impresso), ao José Bernardo (pela ajuda no *wirebonding*), à Diana Leitão (pela ajuda na aquisição de imagens de microscopia eletrónica) e à Natércia Correia pelo acolhimento.
À Doutora Helena Nogueira e à técnica Maria Celeste Azevedo (Departamento de Química da Universidade de Aveiro) pela ajuda na aquisição de espetros de Raman.
À Doutora Florinda Costa e ao Pedro Costa (Departamento de Física da Universidade de Aveiro) pela aquisição de imagens de microscopia eletrónica.
Ao Doutor Iqbal Ahmad (Investigador Auxiliar no CESAM e Departamento de Química da Universidade de Aveiro) pela disponibilidade e ajuda no leitor de microplacas.
Ao Instituto Piaget de Viseu pela disponibilização dos laboratórios para o desenvolvimento de muitas das etapas deste trabalho de doutoramento, e à professora Suzana Lucas pela iniciação em SPSS.
Aos membros do projeto CARDIOSENSOR (FCOMP-01-0124-FEDER-010902, PTDC/SAU-BEB/099042/2008) principalmente pela ajuda na elaboração de inquéritos e recolha de amostras biológicas (sangue e saliva de pacientes do Hospital de São João do Porto).

À Fundação para a Ciência e a Tecnologia (FCT, Portugal) pela Bolsa de Doutoramento concedida (SFRH/BD/60429/2009) no âmbito do Quadro de Referência Estratégico Nacional-Programa Operacional Potencial Humano (QREN-POPH) comparticipado pelo Fundo Social Europeu e por fundos nacionais do Ministério da Educação e da Ciência (MEC).

Por último, e com a maior das considerações, aos membros da minha família pelos momentos de alegria, apoio e carinho, com um profundo e especial obrigado às pessoas mais importantes da minha vida: à minha mãe Maria Emília, ao meu pai Manuel, ao meu irmão Victor e ao meu namorado Jorge. Não esqueço os dois membros da minha família que infelizmente já não se encontram entre nós, e que com certeza foram e serão sempre um forte pilar nos momentos mais difíceis; também para vós, tio e avó, o meu pensamento e saudade.

palavras-chave

biossensor, doenças cardiovasculares, imunorreação, nanotubos de carbono de parede simples, proteína C-reativa, técnica de ELISA, transístores de efeito de campo.

resumo

A incidência de doenças cardiovasculares (CVD) tem vindo a aumentar de acordo com as estatísticas europeias e globais. Assim, o desenvolvimento de novos dispositivos analíticos, tais como os biossensores para avaliar o risco de CVD pode constituir uma ferramenta valiosa para a melhoria dos cuidados de saúde. Nos últimos anos, a nanotecnologia tem proporcionado a criação de novos materiais com excelentes propriedades eletrónicas que têm uma contribuição importante no mecanismo de transdução dos biossensores. Assim, nesta tese, foram desenvolvidos biossensores com uma configuração de transístores de efeito de campo com nanotubos de carbono de parede simples (NTFET) para deteção da proteína C-reactiva (CRP) em amostras biológicas, isto é, soro e saliva de um grupo de pacientes controlo e de outro com pacientes que sofrem de doenças que afetam os níveis de CRP (grupo de risco de CVD). A CRP é uma proteína de fase aguda que é conhecida como o melhor marcador validado para a deteção de risco de CVD, os nanotubos de parede simples (SWCNT) foram aplicados como parte do componente de transdução e a imunorreação, ou seja, a interação entre a CRP e o seu anticorpo específico, foi utilizada como mecanismo de reconhecimento molecular para a deteção da CRP. Após a microfabricação dos transístores de efeito de campo (FET), a seleção das variáveis mais importantes para a dispersão dos SWCNT, a montagem dos NTFET, e a aplicação dos NTFET a soluções padrão de CRP, verificou-se que os dispositivos respondem com precisão à CRP, tanto nas amostras de soro como nas de saliva, uma vez que os NTFET e a metodologia de referência (ELISA) determinaram níveis semelhantes de CRP. Por outro lado, uma forte correlação foi encontrada entre os níveis de CRP em soro e saliva determinados com os NTFET, o que significa que a saliva pode ser utilizada, com base numa amostragem não-invasiva, como alternativa ao soro. Estes dispositivos conseguem ainda discriminar os pacientes do grupo de controlo e os do grupo de risco tendo por base os níveis de CRP na saliva, permitindo assim a determinação de um nível de corte para a CRP na saliva de 1900 ng L^{-1}, que corresponde ao nível de corte estabelecido para a CRP no soro de 3 mg L^{-1}, havendo assim a possibilidade de estabelecer uma nova gama de valores para os níveis de CRP na saliva. Tendo em conta os resultados obtidos a partir do perfil lipoproteico e dos hábitos de vida, concluiu-se que os pacientes do grupo de controlo e os do grupo de risco de CVD podem ser separados com base nos fatores de risco já estabelecidos na literatura e que contribuem para o desenvolvimento de CVD, tais como os triglicerídeos, a CRP do soro, o colesterol total, o colesterol LDL, o índice de massa corporal, a pontuação de Framingham, a hipertensão, a dislipidemia, e a *diabetes mellitus*. Assim, este trabalho relata o desenvolvimento de dispositivos de baixo custo, rápidos, descartáveis, e sem a presença de marcadores para a deteção da CRP, com base numa amostragem não-invasiva, para avaliação de risco de CVD podendo constituir um avanço nos cuidados de saúde.

keywords

biosensor, cardiovascular diseases, C-reactive protein, ELISA technique, field effect transistors, immunoreaction, single-walled carbon nanotubes.

abstract

The incidence of cardiovascular diseases (CVD) has been increasing according to the European and global statistics. Thus, the development of new analytical devices, such as biosensors for assessing the risk of CVD could become a valuable approach for the improvement of healthcare service. In latest years, the nanotechnology has provided new materials with improved electronic properties which have an important contribution in the transduction mechanism of biosensors. Thus, in this thesis, biosensors based on field effect transistors with single-walled carbon nanotubes (NTFET) were developed for the detection of C-reactive protein (CRP) in clinical samples, that is, blood serum and saliva from a group of control patients and a group of CVD risk patients. CRP is an acute-phase protein, which is commonly known as the best validated biomarker for the assessment of CVD, the single-walled carbon nanotubes (SWCNT) were applied as transduction components, and the immunoreaction (interaction between the CRP antigen and the antibodies specific to CRP) was used as the mechanism of molecular recognition for the label-free detection of CRP. After the microfabrication of field effect transistors (FET), the screening of the most important variables for the dispersion of SWCNT, the assemblage of NTFET, and their application on standard solutions of CRP, it was found that NTFET respond accurately to CRP both in saliva and in serum samples, since similar CRP levels were found with the NTFET and the traditional methodology (ELISA technique). On the other hand, a strong correlation between salivary and serum CRP was found with NTFET, which means that saliva could be used, based on non-invasive sampling, as an alternative fluid to blood serum. It was also shown that NTFET could discriminate control patients from CVD risk patients, allowing the determination of a cut-off value for salivary CRP of 1900 ng L^{-1}, which corresponds to the well established cut-off of 3 mg L^{-1} for CRP in serum, constituting an important finding for the possible establishment of a new range of CRP levels based on saliva. According to the data provided from the volunteer patients regarding their lipoprotein profile and lifestyle factors, it was concluded that the control and the CVD risk patients could be separated taking into account the various risk factors established in literature as strong contributors for developing a CVD, such as triglycerides, serum CRP, total cholesterol, LDL cholesterol, body mass index, Framingham risk score, hypertension, dyslipidemia, and *diabetes mellitus*. Thus, this work could provide an additional contribution to the understanding of the association of biomarkers levels in serum and saliva samples, and above all, cost-effective, rapid, label-free, and disposable NTFET were developed, based on a non-invasive sampling, for the assessment of CVD risk, thus constituting a potential point-of-care technology.

mots-clés

biocapteur, immunoreaction, maladies cardiovasculaires, nanotubes de carbone monofeuillet, protéine C-réactive, technique d'ELISA, transistors à effet de champ.

résumé

L'incidence des maladies cardiovasculaires (CVD) a augmentée selon les dernières statistiques européennes et mondiales. Ainsi, le développement de nouveaux appareils d'analyse, tels que les biocapteurs pour évaluer le risque de CVD pourrait être une approche intéressante pour l'amélioration des services de santé. Dans les dernières années, la nanotechnologie a fourni de nouveaux matériaux avec d'excellentes propriétés électroniques qui ont une contribution importante pour le mécanisme de transduction des biocapteurs. Ainsi, dans cette thèse, les biocapteurs basés sur des transistors à effet de champ avec des nanotubes de carbone monofeuillet (NTFET) ont été développés pour la détection de la protéine C-réactive (CRP) dans des échantillons de sérum et de salive d'un group de patients de contrôle et un autre groupe de patients avec un risque élevé de développer une CVD. La CRP est une protéine de phase aiguë qui est connu comme le meilleur biomarqueur validé pour la détection de CVD, les nanotubes de carbone monofeuillet (SWCNT) on été appliqués comme parti de l'élément de transduction, et la réaction immunologique (interaction entre l'antigène CRP et ses anticorps spécifiques) a été utilisée comme le mécanisme de reconnaissance moléculaire pour la détection de la CRP. Après la microfabrication des transistors à effet de champ (FET), la sélection des variables les plus importantes pour la dispersion des SWCNT, l'assemblage des NTFET, et leur application sur des solutions de CRP, il a été constaté que les dispositifs de NTFET on répondu précisément à la CRP tant dans les échantillons de sérum comme dans ceux de salive, une fois que les NTFET et la méthodologie traditionnelle (technique d'ELISA) ont déterminés des taux similaires de CRP. D'autre part, une forte corrélation entre la CRP de la salive et du sérum a été trouvée avec les NTFET, ce que signifie que la salive, qui demande un échantillonnage non-invasif, pourrait être utilisée comme une alternative au sérum. Il a été également démontré que les NTFET on la possibilité de discriminer les patients de contrôle des patients de risque de CVD, permettant la détermination d'un taux limite pour la CRP salivaire de 1900 ng L^{-1}, qui correspond au taux limite de 3 mg L^{-1}, celui-ci bien établi pour la CRP dans le sang, ce qui constitue un résultat important pour l'éventuelle création d'une nouvelle gamme de taux de CRP basée sur la salive. Selon les données fournies par les patients volontaires concernant leur profil de lipoprotéines et des facteurs de style de vie, les patients de contrôle et de risque de CVD ont étés séparé pris en compte les différents facteurs de risque établis dans la littérature comme contribuant fortement pour le développement de CVD, tels que les triglycérides, la CRP, le cholestérol total et LDL, l'indice de masse corporelle, le score de Framingham, l'hypertension, la dyslipidémie, et les diabètes. Ainsi, cette thèse rapporte le développement de dispositifs peu couteux, rapide, jetable et sans la présence de marqueurs pour la détection de la CRP, basées sur un échantillonnage non-invasif, pour l'évaluation du risque de CVD, pouvant être une percée dans les soins de santé.

ANOVA	Analysis of variance
Anti-CRP	Specific antibody for C-reactive protein
BMI	Body mass index
BSA	Bovine serum albumin
CATPCA	Categorical principal components analysis
CH	Cerebral haemorrhage
CHD	Coronary heart disease
CNT	Carbon nanotubes
CoMoCAT	Cobalt-molybdenum catalysis
CRP	C-reactive protein
CV	Coefficient of variation
CVD	Cardiovascular diseases
DC	Direct-current
DF	Degrees of freedom
DMF	Dimethylformamide
DOC	Sodium deoxycholate
DOS	Density of states
ELISA	Enzyme-linked immunosorbent assay
FET	Field effect transistors
HDL	High-density lipoprotein
HiPCO	High-pressure carbon monoxide
LDL	Low-density lipoprotein
LOD	Limit of detection
m-CNT	Metallic carbon nanotubes
MEMS	Micro-electro-mechanical-systems
MOSFET	Metal-oxide semiconductor field effect transistors
m-SWCNT	Metallic single-walled carbon nanotubes
MS	Mean square
MW	Molecular weight
MWCNT	Multi-walled carbon nanotubes
NIR	Near infrared
NTFET	Field effect transistors with carbon nanotubes
OD	Optical density
PBS	Phosphate buffered saline
PCB	Printing circuit board

PECVD	Plasma-enhanced chemical vapour deposition
PEG	Poly(ethyleneglycol)
PEI	Polyethyleneimine
POC	Point-of-care
PVD	Physical vapour deposition
QCM	Quartz crystal microbalance
RBM	Radial breathing mode
RCF	Relative centrifugal force
RF	Radio-frequency
ROC	Receiver operator characteristic
RPM	Rotations *per* minute
s-CNT	Semiconducting carbon nanotubes
s-SWCNT	Semiconducting single-walled carbon nanotubes
SA	Sodium alginate
SC	Sodium cholate
SD	Standard deviation
SDS	Sodium dodecyl sulphate
SEM	Scanning electron microscopy
SPSS	Statistical Package for Social Sciences
SS	Sum of squares
SWCNT	Single-walled carbon nanotubes
TFT	Thin-film transistors
UV	Ultraviolet
UV-Vis	Ultraviolet-Visible

Chapter 2

Chapter 3

Chapter 4

Chapter 5

Chapter 2

Chapter 5

Chapter 1

Objectives and Thesis Outline

1.1. Objectives

The main objective of this thesis is the development of biosensors based on the field effect transistors (FET) configuration with a network of single-walled carbon nanotubes (SWCNT) for the assemblage of NTFET in order to detect C-reactive protein (CRP) in clinical samples, that is, blood serum and saliva, for the improvement of healthcare regarding the assessment of risk of cardiovascular diseases.

SWCNT networks are applied as the transduction components, and the immunoreaction (interaction between CRP antigen and CRP specific antibody) is used as the mechanism of molecular recognition with label-free detection of CRP, which is an acute-phase protein, also being currently the best validated biomarker for the assessment of cardiovascular diseases.

The scope of this thesis covers a wide range of scientific areas from the design of FET to their microfabrication and the exposure of NTFET to clinical samples. Therefore, the general objective can be divided into the following specific objectives:

- design and microfabrication of various types of FET;
- deposition of SWCNT on FET for the assemblage of NTFET, and the study of geometry parameters of NTFET;
- comparison of the effectiveness on SWCNT dispersion in two types of dispersants: an organic solvent and a surfactant;
- application of an experimental design, based on a full factorial design, to determine the most important variables to obtain uniform SWCNT dispersion;
- characterization of NTFET regarding their analytical performance, based on measurements of current with applied voltage;
- application of NTFET to CRP standard solutions, and the study of the best analytical calibration model for further use in the determination of CRP concentration in clinical samples;
- application of NTFET to clinical samples, that is, blood serum and saliva, by invasive sampling and non-invasive sampling, respectively, and validation of NTFET by comparison of results with a traditional methodology based on enzyme-linked immunosorbent assay (ELISA);
- establishment of the correlation of CRP with other factors of risk associated with the development of cardiovascular diseases (CVD), such as cholesterol (total, HDL, and LDL), triglycerides, Framingham risk score, and body mass index, as well as with stress,

hypertension, dyslipidemia, diabetes *mellitus*, family history of CVD, physical activity, and consumption of tobacco, alcohol, and coffee.

1.2. Thesis outline

The work presented in this thesis was disclosed in 5 posters at national and international meetings, 2 papers in conference proceedings, and 6 papers published and 1 paper submitted in peer-reviewed international journals in the Science Citation Index (SCI®, Thomson ISI). This thesis contains 6 chapters organized as follows:

- Chapter 1 provides the general and specific objectives of this thesis, as well as its organization in various chapters with reference to their contents;

- Chapter 2 gives an introduction on various topics: characterization of carbon nanotubes (CNT) regarding their structure, properties, synthesis processes and applications, incorporation of nanomaterials, mainly CNT, on biosensing devices, molecular recognition of analytes through biosensors with dispersion of CNT, and functionalization methods of CNT. Furthermore, the theoretical principles of immunoreaction and operational principles of NTFET, as well as the characterization of CRP are also reported due to their importance on this PhD work.

Chapter 2 is partially based on the following published papers:

→ Justino C.I.L., Rocha-Santos T.A.P., Duarte A.C., 2013. Advances in point-of-care technologies with biosensors based on carbon nanotubes. *Trends in Analytical Chemistry* 45, 24-36. (*IF: 6.351; Rank: 2/75; Q1, Area: Analytical Chemistry*);

→ Justino C.I.L., Rocha-Santos T.A.P., Cardoso S., Duarte A.C., 2013. Strategies for enhancing the analytical performance of nanomaterial-based sensors. *Trends in Analytical Chemistry* 47, 27-36. (*IF: 6.351; Rank: 2/75; Q1, Area: Analytical Chemistry*);

→ Justino C.I.L., Rocha-Santos T.A.P., Duarte A.C., 2010. Review of analytical figures of merit of sensors and biosensors in clinical applications. *Trends in Analytical Chemistry* 29, 1172-1183. (*IF: 6.351; Rank: 2/75; Q1, Area: Analytical Chemistry*).

- Chapter 3 presents the experimental methodologies followed and the results obtained from the comparison on the effectiveness of the dispersion of single-walled carbon nanotubes (SWCNT) through their functionalization with sodium cholate (SC) and dimethylformamide (DMF). The most important variables for SWCNT dispersion were found after statistical analysis of data obtained by the application of an experimental design. The relationships between some experimental conditions related to the main steps (sonication and centrifugation) for the preparation of SWCNT solutions were also determined.

Chapter 3 is partially based on the following published paper:

→ Justino C.I.L., Freitas A.C., Rocha-Santos T.A.P., Duarte A.C., 2012. Screening of single-walled carbon nanotubes by optical fiber sensing. *Talanta* 89, 105-108. (*IF: 3.498; Rank: 12/75; Q1, Area: Analytical Chemistry*).

- Chapter 4 describes the whole experimental methodology and the experimental conditions for the fabrication of various types of FET.

Chapter 4 is partially based on the following published paper:

→ Justino C.I.L., Rocha-Santos T.A.P., Amaral J.P., Cardoso S., Duarte A.C., 2013. Effects of geometry parameters of NTFET devices on the I-V measurements. *Solid-State Electronics* 81, 32-34. (*IF: 1.482; Rank: 88/242; Q2, Area: Engineering, Electrical and Electronics*).

Chapter 5 reports the development of NTFET, with a back-gated and interdigitated configuration, and based on random networks of SWCNT, as immunosensors for the label-free detection of CRP in standard solutions and in clinical samples. Specifically, the assemblage of NTFET with the study of different geometry parameters (distance between electrodes, number of electrodes, and thickness of gold layer) on the device performance is reported, based on the characterization of NTFET by their output characteristics (current-voltage measurements). The selection of the NTFET type for sensing experiments is also reported. The experimental conditions followed and the results obtained from the study for finding the best calibration model obtained through the application of NTFET to CRP standard solutions are also provided. Methodologies tested and results obtained from the separation process of SWCNT networks found in a SWCNT

dispersion by electronic type, that is, in semiconducting and metallic SWCNT is also reported; semiconducting SWCNT were applied for the assemblage of NTFET in order to verify if better performance could be reached, in comparison to the use of SWCNT networks. Furthermore, the methodologies applied for the determination of the CRP concentration by NTFET in clinical samples (blood serum and saliva) and corresponding results are provided, together with the comparison of such results with those obtained from a traditional methodology (ELISA technique), for biosensor validation. Statistical analysis of such results was also performed, and the correlation of CRP with other risk factors such as cholesterol (total, HDL, and LDL), triglycerides, Framingham risk score, and body mass index, as well as with stress, hypertension, dyslipidemia, diabetes *mellitus*, family history of CVD, physical activity, and consumption of tobacco, alcohol, and coffee, was reported.

Chapter 5 is partially based on the following published/submitted papers:

→ Justino C.I.L., Freitas A.C., Amaral J.P., Rocha-Santos T.A.P., Cardoso S., Duarte A.C., 2013. Disposable immunosensors for C-reactive protein based on carbon nanotubes field effect transistors. *Talanta* 108, 165-170. (*IF: 3.498; Rank: 12/75; Q1, Area: Analytical Chemistry*);

→ Justino C.I.L., Rocha-Santos T.A.P., Amaral J.P., Cardoso S., Duarte A.C., 2013. Effects of geometry parameters of NTFET devices on the I-V measurements. *Solid-State Electronics* 81, 32-34. (*IF: 1.482; Rank: 88/242; Q2, Area: Engineering, Electrical and Electronics*);

→ Justino C.I.L., Duarte K., Lucas S., Chaves P., Bettencourt P., Freitas A.C., Pereira R., Cardoso S., Duarte A.C., Rocha-Santos T.A.P., submitted. Assessment of cardiovascular disease risk using immunosensors for determination of C-reactive protein levels in serum and saliva. *Bioanalysis*. (*IF: 3.253; Rank: 15/75; Q1, Area: Analytical Chemistry*).

- Chapter 6 outlines the concluding remarks concerning the various phases of this PhD work, highlighting the advantages of the developed NTFET for the improvement of clinical diagnosis.

Chapter 2

Introduction

In the latest decade, the use of analytical methodologies based on new materials from Nanoscience and Nanotechnology has been increasing and the study of nanostructures such as nanotubes, nanofibres, nanogaps, and quantum dots have contributed to significant advances in Chemistry, Biotechnology and Medicine. Particularly, in Analytical Chemistry, nanostructures have a high potential for the fabrication of sensors as useful and functional devices, due to their capabilities for improved sensitivity, increased speed of analysis, and cost-effectiveness, when compared to traditional devices, such as immunoassays (Lee *et al.*, 2009; Vashist *et al.*, 2011). Furthermore, the association of Nanotechnology with medical diagnostics, therapeutics, treatment, and monitoring has lead to the implementation of the concept of Nanomedicine in Science lexicon. Nanomedicine is related to a wide interdisciplinary scientific area which includes molecular biologists', chemists', physicians', mathematicians', engineers', and computer scientists' knowledge in order to face several analytical challenges (Kranz *et al.*, 2011). In association with the field of Nanotechnology, the microelectronics technology further provides the use of powerful circuits and systems to promote the development of new miniaturized devices for molecular sensing, as reviewed by Carrara (2010) and some of these devices are implantable biosensors, as well as nanosensors for the monitoring of blood glucose (Cash and Clark, 2010) and for DNA detection (Dolatabadi *et al.*, 2011). The incorporation of nanomaterials for the development of versatile tools used as diagnostic devices has been intensively attempted in order to improve healthcare. One of the first examples was the use of nanostructured materials in glucose sensors as a way to support the standard electrochemical detection of glucose, since nanomaterials provide higher surface areas and high electron transfer from enzyme to electrode (Cash and Clark, 2010).

Large improvements in the detection and quantification of compounds such as proteins, neurotransmitters, and cancer biomarkers by biosensors have been reported due to the integration of Nanoscience and Nanotechnology, as reviewed by Justino *et al.* (2010; 2013a). For example, new nanostructured materials with various functional groups such as carboxyl and amine groups, or with metallic nanoclusters such as gold and silver, have been used for the improvement of signal transduction. Specifically, carbon nanotubes (CNT) have been the most used in several modern technologies and devices as transduction components for the improvement of biosensing systems, mainly due to their large surface area, high electrical conductivity, and electron transfer properties (Vashist *et al.*, 2011; Balasubramanian, 2012). The association of CNT, either with other nanomaterials or with polymers in new nanostructured materials, have allowed the

production of new types of biosensors for applications in fields such as healthcare, environmental monitoring, and food safety. Concerning the healthcare field, some examples related to the detection of glucose used the association of CNT with nanoparticles of gold, silver, platinum, and silica and also composites of silica/iron oxide nanoparticles (Justino *et al.*, 2013a) for sensing transducers. Also in this field, the development of biosensors with CNT for detection of diseases at an early stage has been mainly focused in their miniaturization and portability, sensitivity, fast response, real-time diagnosis, reducing sample volume, and non-invasive methods. According to the latest global CNT market report (Patel, 2011), the development of medical and healthcare devices has been one of the reasons for the increase of the production of CNT, which has involved 28 % of the global market demands on nanomaterials. Furthermore, the annual production capacity has been around 2500 t for the ten world major producers of single-walled CNT (SWCNT) and multi-walled CNT (MWCNT), where 44 %, 29 %, and 24 % of such production is accounted for Asia-Pacific, North America and European Union, respectively. According to the same report (Patel, 2011), the CNT production is expected to reach 12800 t in 2016, demonstrating the relevance of these nanomaterials to several known applications.

2.1. Characterization of carbon nanotubes (CNT)

2.1.1. Bonding in carbon materials and structure of CNT

Carbon atoms have the electronic configuration $1s^2 2s^2 2p^2$, and covalent bonds can be formed to produce various allotropic forms of carbon, such as diamond, graphite, graphene, fullerenes and CNT, through hybridization of orbitals due to the transfer of one of the *2s* electrons to the *2p* orbital. Figure 2.1 displays the structural forms of the carbon allotropes.

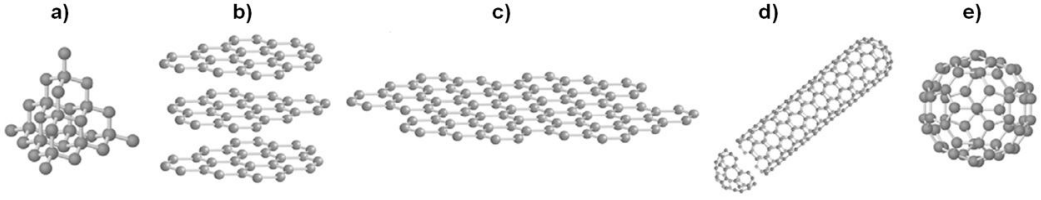

Figure 2.1 Crystal structures of the allotropic forms of carbon: a) diamond, b) graphite, c) graphene, d) CNT, and e) C_{60} (Adapted and reprinted from Materials Today, 10, Katsnelson, Copyright (2007) with permission from Elsevier).

As claimed by Geim and Novoselov (2007), the dimensionality is one of the most defining material parameter, since different orders of the dimensional (D) crystal structure lead to different material properties. Concerning the graphene layer, it can be wrapped up into 0D fullerenes, rolled into 1D CNT, or stacked into 3D graphite, being the graphene itself the 2D form of carbon, as shown in Figure 2.2.

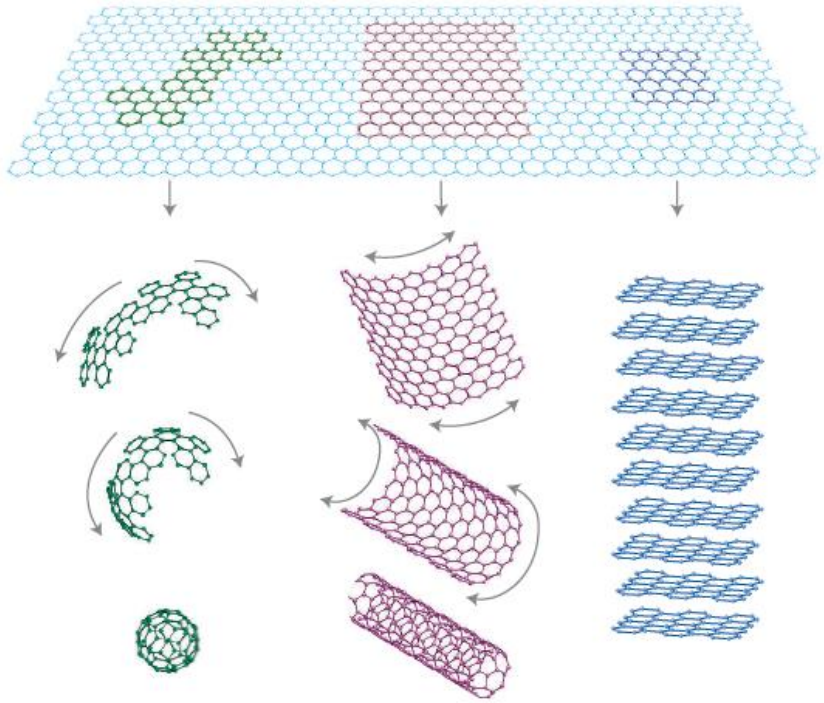

Figure 2.2 Graphene layer as the basis of carbon materials (Reprinted by permission from Macmillan Publishers Ltd: Nature Materials (Geim and Novoselov), copyright (2007)).

Diamond and graphite are the two allotropes of carbon with a 3D configuration. Diamond has carbon atoms in sp^3 hybridization due to the mixing of one *2s* and three *2p* orbitals, producing a transparent, insulating, and rigid structure, and graphite is constituted by carbon atoms in sp^2 hybridization, since one of the *2s* electrons hybridizes with two of the *2p* electrons. Graphite is organized in planar sheets of graphene, with strong σ bonds in graphene layers and weak van der Waals interactions between layers, and it is hexagonally configured having a black, conductive and fragile appearance. Graphene is planar with hexagonal arrangement of carbon atoms. Regarding fullerenes, such as C_{60}, they are stable and approximately spherical structures consisting of tri-coordinated carbon atoms which are interconnected in icosahedral structure, that is, with twelve pentagonal and twenty hexagonal rings. Such spherical curvature produces angle strain which allows fullerenes to undergo characteristic reactions of electrophilic addition at double bonds,

reducing angle strain by changing sp^2- into sp^3-hybridized carbons. Recently, the scientific attention has turned to CNT which have the same hybridization of fullerenes (sp^2 character); three of the four valence electrons of carbon participate in the bond of neighbor carbon (in the σ-orbital), and they do not contribute to the conduction, while the fourth electron is in a π-orbital, corresponding to the valence band, and contributes to the conduction. In a graphene sheet, these π-orbital electrons are distributed in the conduction (high energy band, π*) and valence (low energy band, π) bands (Bandaru, 2007). CNT could be considered as elongated fullerenes (up to 1.5 cm) and with an atomic structure similar to graphene. CNT are rolled in tubular forms, constituting SWCNT with diameters in the range of 1 to 10 nm, or up to fifty concentric CNT sharing a common axis, constituting MWCNT with inner diameters of up to 2 nm and outer diameters in the range of 10 to 50 nm. In MWCNT, adjacent graphene layers are separated approximately by 0.34 nm, which is the interlayer distance in graphite.

The way as the graphene layer is rolled-up affects the properties of resulting SWCNT, as well as their diameter and chirality. Chirality is related to the way as the roll-up of graphene layer is made in relation to the direction of the translational vector (T) axis, which has the same direction than the major axis of resulting SWCNT (Popov, 2004). The schematic representation of a SWCNT is shown in Figure 2.3.

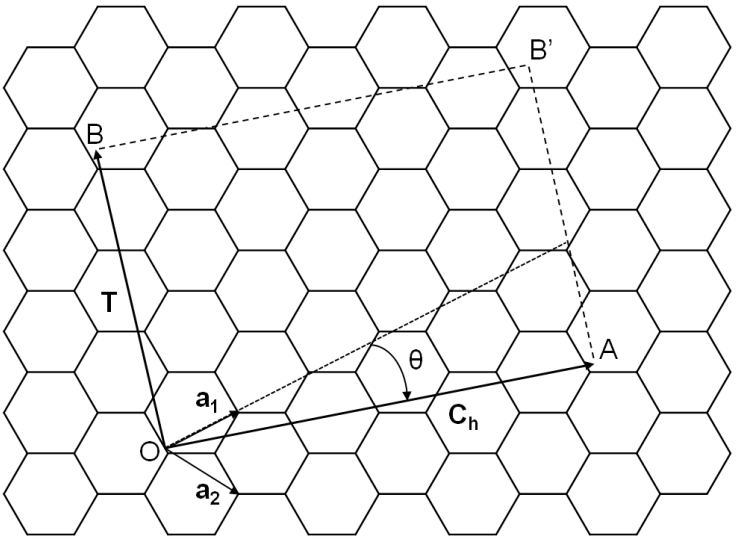

Figure 2.3 Schematic representation of a graphene layer where chiralities of SWCNT are shown based on the relative orientation of the carbon hexagons in relation to CNT axis.

The chirality of a CNT is represented by a pair of indices (*n*,*m*) called the chiral vector C_h, which forms a right angle with the T axis (vector OB), and it is expressed as:

$C_h = n\mathbf{a_1} + m\mathbf{a_2}$, where $\mathbf{a_1}$ and $\mathbf{a_2}$ are the unit cell vectors of the graphene hexagonal structure, and (*n*,*m*) is an integer pair corresponding to the atomic structure of a CNT. T is the smallest graphene lattice vector perpendicular to C_h, and the rectangle defined by vectors T and C_h is called the unit cell for the nanotube. In other words, starting at the (0,0) on the graphene layer, the (*n,m*) point is obtained by moving *n* units in the $\mathbf{a_1}$ direction and *m* units in the $\mathbf{a_2}$ direction. If (0,0) and (*n,m*) points are connected, the chiral vector C_h is defined.

The chiral angle (θ) is the angle between C_h and $\mathbf{a_1}$, and it can vary between 0º and 30º. In this way, there are three possible configurations of CNT, as shown in Figure 2.4, where an example of each configuration is shown: a) when the roll-up in the axis is made with *m*=0 or *n*=0, being θ about 0º, zig-zag nanotubes are produced; b) when *m*=*n* and θ is 30º, armchair nanotubes are produced; and finally, when *m*≠*n* being θ between 0º and 30º, chiral nanotubes are synthesized.

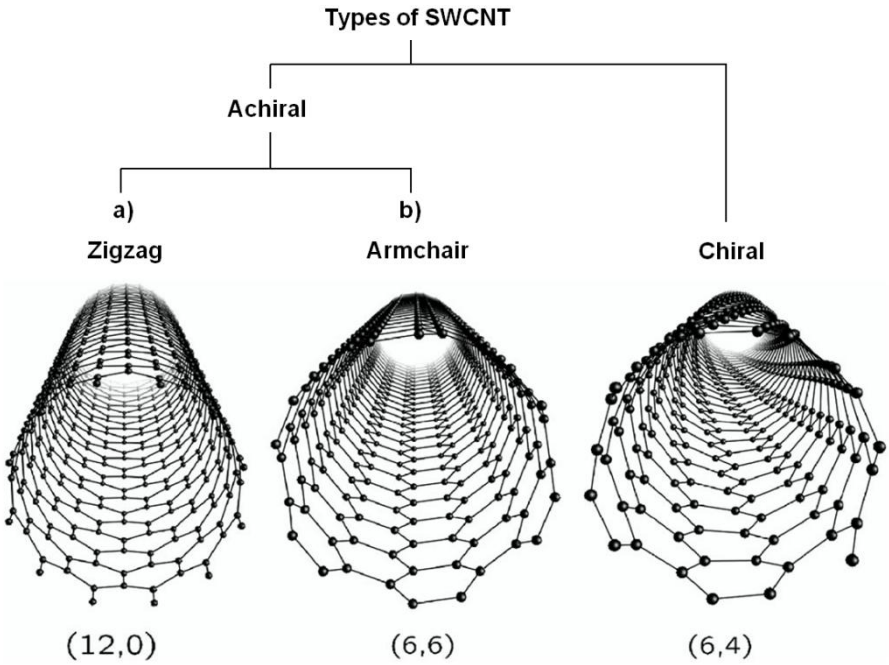

Figure 2.4 Schematic representation of three types of SWCNT produced by the specific orientation of roll-up of the graphene layer: atomic structures of two achiral tubes, that is, a) zigzag tubes (12,0) and b) armchair tubes (6,6), as well as one chiral tube (6,4) (Adapted and reprinted from Charlier *et al.*, Copyright (2007) with permission by The American Physical Society).

The diameter of a CNT can be determined from its (*n,m*) indices according to the following equation (Saito *et al.*, 1992):

$$d = \frac{|C_h|}{\pi} = \frac{a\sqrt{n^2+nm+m^2}}{\pi} \quad [2.1]$$

where '*a'* is the atomic lattice constant of graphene (*a* = 0.246 nm). In the same way, the chiral angle can be calculated by the following equation (Saito *et al.*, 1992):

$$\theta = \tan^{-1}\left[\frac{-\sqrt{3}m}{2n+m}\right] \quad [2.2]$$

As stated above, the chirality is the simplest way to specify the structure of an individual CNT, which is determined by CNT diameter and the relative orientation of the carbon hexagons in relation with the tube axis, and thus, the chirality has important implications on the material properties, with a specific and strong impact on the electronic properties of CNT. The (*n*,*m*) integers determine whether the CNT is metallic (m-CNT) or semiconducting (s-CNT), and a wide range of possible CNT configurations can be mapped, as illustrated in Figure 2.5. All methods of synthesis produce a mixture of m-CNT and s-CNT, called CNT networks; from a statistical point of view, the distribution of C_h vector is uniform as one-third of the probable CNT configurations are metallic with $n - m = 3j$ (*j* being an integer), and two-thirds are semiconducting ($n - m \neq 3j$). Only armchair CNT ($n = m$) are strictly metallic.

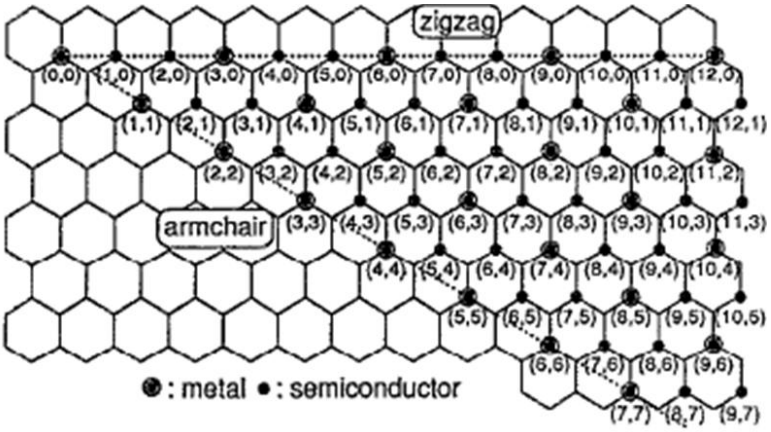

Figure 2.5 Index map with possible configurations for CNT (Reprinted with permission from Saito *et al.*, Applied Physics Letters 60. Copyright (1992), American Institute of Physics).

2.1.2. Synthesis of CNT

In general, all methods of synthesis of CNT require nanoparticles of transition metals, such as Fe, Co, and Ni or their alloys, to function as catalysts for CNT formation, as shown in Figure 2.6. Metal catalysts help to initiate the CNT precipitation at the nucleation stage, and when the CNT growth stops, the metal becomes non-functional. Such metals are commonly chosen due to the high solubility of carbon in these metals at high temperatures, and due to the high carbon diffusion rate into their surface. When the catalysts are in contact with hydrocarbons, for example, methane, ethylene, and acetylene, or even carbon monoxide, such carbon sources are decomposed and the resulting carbon atoms precipitate in a tubular form. As shown in Figure 2.6, the diffusion of carbon atoms occurs through the metal catalyst and when it is fully covered with excess carbon, its catalytic activity finishes and the CNT growth stops.

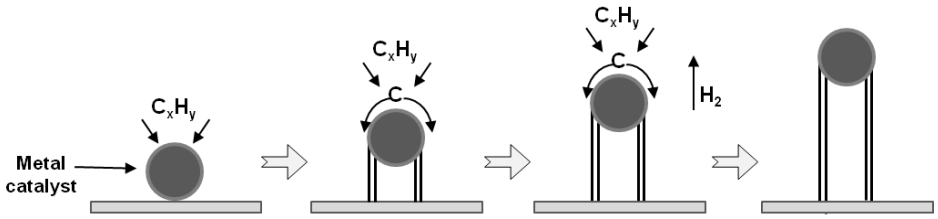

Figure 2.6 General growth mechanisms for synthesis of CNT.

In terms of their large scale production, CNT are currently synthesised by high-temperature processes such as electric arc discharge and laser ablation, and by chemical vapour deposition. Table 2.1 compares the various operational parameters of such synthesis processes, and their schematics.

The arc discharge method is based on the arc discharge between two graphite electrodes at high temperatures (3000 - 4000 ºC) and low pressures of helium or argon (600 mbar) for the formation of CNT on the cathode. Such synthesis can also occur without catalyst, as firstly proposed by Iijima (1991), and in this method, carbon atoms are ejected from the anode and they are deposited at the cathode forming CNT. Although the presence of high quantities of impurities, such as amorphous carbon, and metal clusters coated with carbon is the main disadvantage, the arc discharge method provides high yields of CNT.

The laser ablation consists in the production of SWCNT using a high-power laser beam. The graphite is placed in the middle of an inert quartz tube (with argon) at temperatures up to 1200 ºC which, in turn, is in a furnace, that can reach temperatures

even higher than 1200 ºC. The laser allows the vaporization of graphite and the CNT are grown into a cooled collector, producing a small quantity of long CNT with high purity. It should be highlighted that the quality of synthesised CNT is defined in terms of purity (content of CNT *vs.* amorphous species), and defect density (presence of structural defects on the CNT walls), and thus, when CNT with high quality are synthesised, high purity and low defect density are present. The diameter of CNT produced by either arc discharge or laser ablation is controlled by varying reaction temperatures, and low defect density is attained by these methods. However, the high cost due to the expensive laser is the main limitation of the laser ablation method.

Table 2.1 Operational parameters for the three main processes of production of CNT (Adapted from Trends in Analytical Chemistry, 45, Justino *et al.*, Copyright (2013a), with permission from Elsevier).

	Electric arc discharge	**Laser ablation**	**Chemical vapour deposition**
Temperature	800 - 5000 ºC	Up to 1200 ºC	300 - 1200 ºC
Gas pressure	50 - 700 mbar	Around 670 mbar	Up to 10 atm
Yield	80 %	Up to 70 %	30 - 99 % (MWCNT)
Length/Diameter	Short tubes, 2 - 20 nm Ø	Long tubes, 1 - 2 nm Ø	Long tubes, 0.6 - 4 nm Ø
Main advantage	High production rates	High CNT purity	Control of growth direction
Main limitation	Non-continuous process	Expensive lasers	High defect density of CNT
Schematics of process	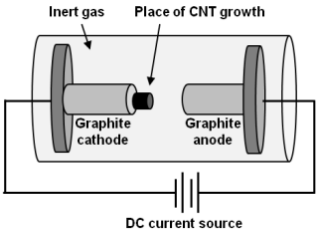	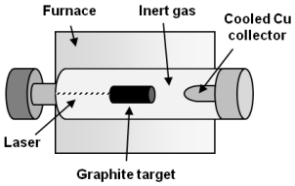	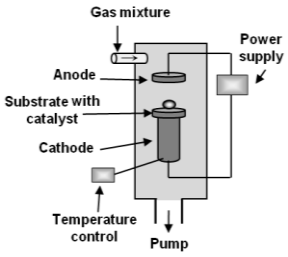

Regarding the chemical vapour deposition, it uses gas-phase molecules based on hydrocarbons which are thermally decomposed using a heated metal catalyst, leading to the CNT growth. When compared with arc discharge and laser ablation methods, the chemical vapour deposition is a simple and economic process of synthesis which has the disadvantage of producing CNT with high defect density, and it has the advantage of the selective growth of CNT. The selective growth is possible due to the control of the place of

growth after the deposition of the metal catalyst onto a substrate such as quartz, silicon, silica, alumina, and magnesium oxide, among others, and depending on the required application of synthesised CNT. Thus, the synthesised CNT on substrates by chemical vapour deposition could be immediately applied, which is not the case with arc discharge and laser ablation methods, where CNT should be collected after their synthesis.

The production of CNT have been improved in order to respond to modern science and process engineering, and variants of the chemical vapour deposition process for the synthesis of CNT have been further developed, such as the processes of high-pressure carbon monoxide reaction (HiPCO) and cobalt-molybdenum catalysis (CoMoCAT). In HiPCO, CO is used as the carbon source to form SWCNT through the reaction with Fe nanoparticles (from iron pentacarbonyl, $Fe(CO)_5$) at 800 - 1200 ºC and 10 atm. During the CNT growth, nanoparticles of Fe provide a nucleation surface for the transformation of CO into carbon. CoMoCAT is a registered method of synthesis forwarded and optimized by Resasco's team, where high purity SWCNT are produced with a narrow distribution of tube diameters (Resasco *et al.*, 2002). In the CoMoCAT process, Co and Mo are used as catalysts, and the SWCNT are grown by the decomposition of CO into C and CO_2, at temperatures between 700 and 950 ºC and at pressures from 1 to 10 atm. The plasma-enhanced chemical vapour deposition (PECVD) is also based on original chemical vapour deposition process, where large quantities of SWCNT or MWCNT are produced by decomposition of a hydrocarbon, as gaseous carbon source, in the presence of a metal catalyst (Ni, Fe or Co) (Melechko *et al.*, 2005). The main difference with original chemical vapour deposition is the activation of the carbon source by electron impact in PECVD, due to the generation of a plasma during the growth process, rather than by thermal energy.

In the synthesis of CNT, several variables such as carbon sources, metal catalyst concentration, gas-flow rate, gas pressure, carrier gas composition (for example, He, Ne, Ar, N_2, and Xe), temperatures, and mixture of catalysts can affect the quantity and the quality of CNT, as well as the mean diameter and the diameter distribution of CNT, thus affecting their properties. For example, Fe is responsible for the production of long CNT with larger diameter (55 nm), while Co is responsible for the production of CNT with the smallest diameter of 20 nm, as studied by Sato (2003).

Commonly, the process of synthesis of CNT is chosen taking into account the required application of CNT. For example, for microelectronics technologies, the chemical vapour deposition is the most used process, since it is based on the simplicity of operation, the possibility of growth control, the energy efficiency, the high yield and purity of CNT, as well as the potential for large scale production (Patel, 2011). Regarding the electronic

applications, such as field emitting devices and field effect arrays, and for the development of sensing devices, CNT can be either grown directly on substrates (*in-situ* growth) through chemical vapour deposition technique, or by depositing pre-grown CNT (Narasimhamurthy and Paily, 2011). For *in-situ* growth, the catalysts are patterned on the substrates where the CNT will grow, as shown in the work of Jiang and Zhang (2010) where MWCNT arrays were produced by chemical vapour deposition process on Ta foils as substrate. In turn, the depositing of pre-grown CNT from a solution can also be considered: the first step is the attachment of CNT to surfactant molecules in aqueous solution, followed by the elimination of residuals in order to obtain the most uniform CNT solution. Such approach was followed by Li *et al.* (2009) where a glucose sensor was based on MWCNT, which were prepared from a CNT suspension in phosphomolybdic acid solution as solvent, with subsequent sonication and centrifugation.

In general, after their synthesis, CNT contain a large content of impurities such as graphite, amorphous carbon, residual meal catalyst, and small fullerenes, but in wide range of quantities depending on the synthesis method, as reviewed by Stetter and Maclay (2004). Thus, the resulting CNT need to be dispersed, purified, and functionalized by different techniques such as chemical oxidation, filtration, centrifugation, and annealing (Haddon *et al.*, 2004) before further applications, as shown in Section 2.2. In addition, and also depending on their potential applications, CNT can be isolated by length, by diameter, or into m-CNT and s-CNT to emphasize their properties (Komatsu and Wang, 2010), as discussed in Section 2.1.4.

2.1.3. Properties and applications of CNT

The peculiar chemical properties as well as the physical properties, that is, mechanical, optical, thermal, and electronic properties of CNT are responsible for the application of CNT in various areas such as in chemical and biological sensors, field emission displays, energy storage devices, drug-delivery devices, and reinforcement of composite materials, as shown in Table 2.2. The interest and importance of CNT could be evaluated by the increasing number of publications in latest years: between 2008 and 2012, the publications related to CNT and to the development of sensors and biosensors with CNT have increased 42 % and 83 %, respectively. The total publications with CNT from 2008 to 2013 were identified in Chemistry (25 %) and Materials Science (23 %), which are the top two main leading subject areas. The other three subject areas are Physics, Science

Technology, and Engineering with 19 %, 14 %, and 7 % of the total publications, respectively. Table 2.2 grouped the areas of applications and the main CNT properties for each of the five main subject areas on CNT research.

Table 2.2 Main subject areas on CNT research, principal areas of application of CNT, and corresponding properties of the applied CNT (Adapted from Trends in Analytical Chemistry, 45, Justino *et al.*, Copyright (2013a), with permission from Elsevier).

Subject areas	Areas of application	CNT properties
Chemistry	Drug-delivery devices	High surface to volume ratio High loadings of therapeutic agents
Materials Science	Reinforcement of CNT in composite materials (for example, polymers, and ceramics, for photovoltaic devices and organic light-emitting diodes)	High tensile strength (≈ 63 GPa, being 50x higher than steel)[a] High Young's elasticity modulus (which is the strength-to-weight ratio, 5x higher than steel)[b] High surface to volume ratio High conductivity
Physics	Field emission displays (for example, development of flat panel displays, and microwave generators)	High surface to volume ratio High thermal conductivity (≈ 3 kW m^{-1} K^{-1}, comparable with that of natural diamond, ≈ 2 kW m^{-1} K^{-1})[c] High electrical conductivity High current density (>1 GA cm^{-2})[c] Chemical stability
Science Technology	Electronic devices (for example, sensors)	Nanoscale dimensions High current density High sensitivity
Engineering	Energy storage devices (for example, as CNT-based solar cells, and in lithium-ion batteries)	Large surface area Low resistivity Good chemical stability High electrical conductivity

[a]Yu *et al.* (2000); [b]Strano *et al.* (2003); [c]Collins and Avouris (2000).

Taking into account the properties of CNT reported in Table 2.2: a) the high electrical conductivity of CNT is due to their tubular configuration, allowing the confinement of electrons around the circumference of the CNT, b) the electronic properties of CNT are due to their small diameter and high length, providing a very large surface to volume ratio, c) the high mechanical, thermal, and chemical stability is due to the covalent and strong C-C bonds, and d) the high Young's modulus promotes a large angle bending without breaking.

Regarding the areas of application of CNT, the development of field emission displays is a current application of CNT requiring large amounts of such nanomaterial, which function as source of field emission electrons and it is used for flat panel displays and microwave generators, since CNT provide stable emission, high surface to volume ratio, long lifetimes, high thermal conductivity, and high current densities. Recently, CNT have also been applied as electron guns for scanning and transmission electron microscopes, where they operate at the highest current density. In Materials Science, the particular mechanical and electronic properties of CNT, that is, their high tensile strength and high conductivity, respectively, are essential for their application as molecular reinforcement in nanocomposites, mainly in ceramic matrix composites, since CNT increase the toughness of composites to energy absorption due to their elastic character. Regarding the Engineering area, CNT have been applied as supercapacitors, lithium-ion batteries, solar and fuel cells due to their capacity for energy storage, considered as an important field in clean energy economy. Such applications are possible due to the good chemical stability and high electrical conductivity. The electronic devices have also been developed using CNT as sensing element due to their high sensitivity leading to lower power consumption, low cost and miniaturized devices. Although controversy continues to exist related to the identification of the long-term effects and the possible toxicity of CNT *in vivo*, the use of CNT for the delivery of therapeutic agents has been found in literature, and the clinical application of CNT for drug-delivery only can be made when such questions will be properly addressed. Thus, the ability of CNT to penetrate in the cells as effective carriers for delivering peptides, proteins, nucleic acids, and small molecular drugs, as well as their drug loading capacity are yet controversial issues. CNT have also been used as transducer elements for biosensing applications mainly due to the presence of all carbon atoms on the entire surface, leading to a potential increase in sensitivity with the neighbouring molecules. Thus, biosensors for the detection of neurotransmitters, biomolecule, tumour biomarkers, and pathogenic bacteria still are a hot research topic.

For this thesis, the understanding of the electronic properties of CNT is important since CNT are a basic element on the transduction mechanism of developed biosensors. The electronic properties of materials are dependent on the separation of the various valence energy states (occupied by electrons) and the conduction states (empty, but that can be occupied by electrons). For example, in metals, the valence and conduction bands are overlapped and then, the conduction is easily performed (without energy gaps, and with conduction bands not fully occupied). In this way, free electrons exist together with partially filled valence bands. In semiconductors, there is an energy gap and additional

energy (from thermal or optical excitation) is need to the movement of electrons to the first available conduction state. In insulators, the filled valence bands and empty conduction bands exist with a large band gap, leading to high resistivity. Regarding the electronic properties of CNT, if a band gap exists between valence and conduction bands, SWCNT are semiconducting. Thus, if any energy gap is present between such bands, and electrons of one energy state can move from valence to conduction band without additional energy, CNT are metallic. CNT display either a metallic or a semiconducting character depending of the (*n,m*) indices: CNT with *n* = *m* are metallic, and quasi-metallic CNT (with a small band gap) have (*n* - *m*) divisible by 3; the other remaining type of CNT are semiconducting. A diagram of electronic density of states (DOS) shows the group of DOS at specific energy levels for a material, which are the states at each energy level that are available to be occupied by electrons. Figure 2.7 shows the diagram of DOS for semiconducting SWCNT (s-SWCNT) and metallic SWCNT (m-SWCNT) where the valence (v_n) and conduction (c_n) bands are represented. DOS are finite for m-SWCNT, since various states are available to be occupied, and they are zero for s-CNT, since no states can be occupied by electrons. The sharp energy peaks in the DOS are known as van Hove singularities, which are discontinuities in the DOS of a solid, usually as result of low dimensionality. The distance between such discontinuities is associated with the energy required to the transition of one electron, and they are dependent of the structure and diameter of CNT.

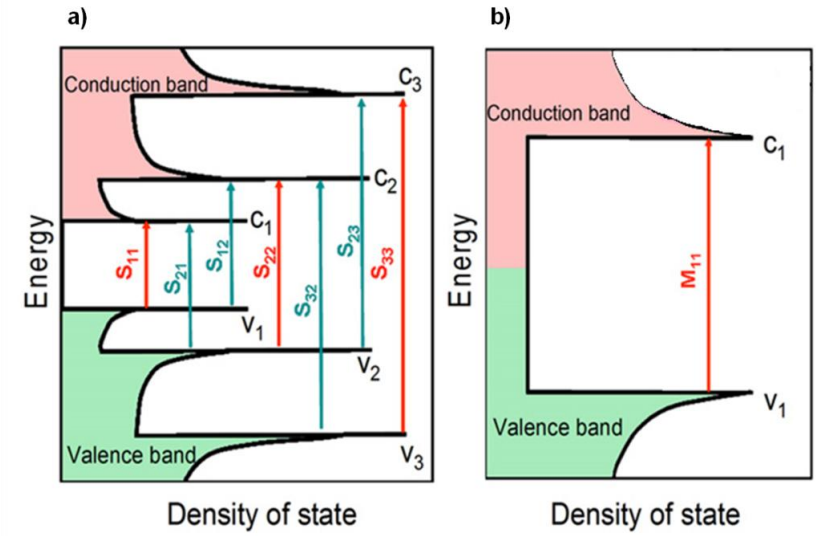

Figure 2.7 Schematic diagram of electronic density of states for: a) s-SWCNT and b) m-SWCNT. The solid arrows depict the optical emission transitions for both m- and s-CNT (Reprinted from Carbon, 50, Battie *et al.*, Copyright (2012), with permission from Elsevier).

The $S_{nn\ (n=1,2,3,\ldots)}$ identifies the energy of electronic transition between the states v_n and c_n, and an expression was found to relate such electronic transition with the diameter of SWCNT (Dresselhaus and Eklund, 2000):

$$S_{nn} = \frac{2\gamma a_{C-C}}{d} \qquad [2.3]$$

where γ is the carbon-carbon (C-C) tight binding overlap energy (2.5-3.2 eV), $a_{c\text{-}c}$ is the distance between C-C bonds (0.144 nm), and d is the diameter of the CNT. In this way, the band gap energy depends only and inversely to the diameter of s-SWCNT, and such band gap in the DOS of m-SWCNT is inexistent, since there is no gap in the DOS between the valence band and the conduction band.

The UV-Vis spectroscopy is the most widely used technique for characterization of the purity and structure of SWCNT, through the evaluation of the singular interband electronic transitions of SWCNT obtained in UV-Vs spectra (Figure 2.8). The absorption bands are due to transitions between spikes in the DOS in the electronic structure of CNT, as reported by Harris (2009). It is important to refer that underneath such absorbance features, a broad and featureless background of π-plasmon absorption exists as a linear sloping baseline due to SWCNT but also due to metal catalysts and carbonaceous impurities derived from the synthesis process, as reported by Haddon *et al.* (2004) and Ryabenko *et al.* (2004). According to Itkis *et al.* (2005), the sloping baseline on which the interband transitions ride can be used to evaluate the intensity of peaks associated with SWCNT, that is, the strength of the characteristic absorbance features compared with the baseline of π-plasmon background provides the measure of the purity of the SWCNT dispersion, as studied by Itkis *et al.* (2005). Figure 2.8 shows the electronic spectrum of SWCNT produced by the electric arc discharge in the work of Itkis *et al.* (2005). As highlighted in the inset of Figure 2.8, the region of S_{22} interband transition was used by Itkis *et al.* (2005) to SWCNT purity evaluation, the AA(S) is the area of the S_{22} spectrum band after linear baseline correction, and AA(T) is the total area of the S_{22} band including SWCNT and carbonaceous impurity contributions. The band of S_{22} was chosen because the absorption of carbonaceous impurities is not reflected, and S_{22} transition is less susceptible to incidental doping, and less sensitive to charge transfer, as explained by Kazaoui *et al.* (1999). In Figure 2.8 it is also shown that it is not yet possible to analytically separate these contributions, and the π-plasmon can be considered as the collective excitation of electrons of π-band in a sample (Pichler *et al.*, 1998).

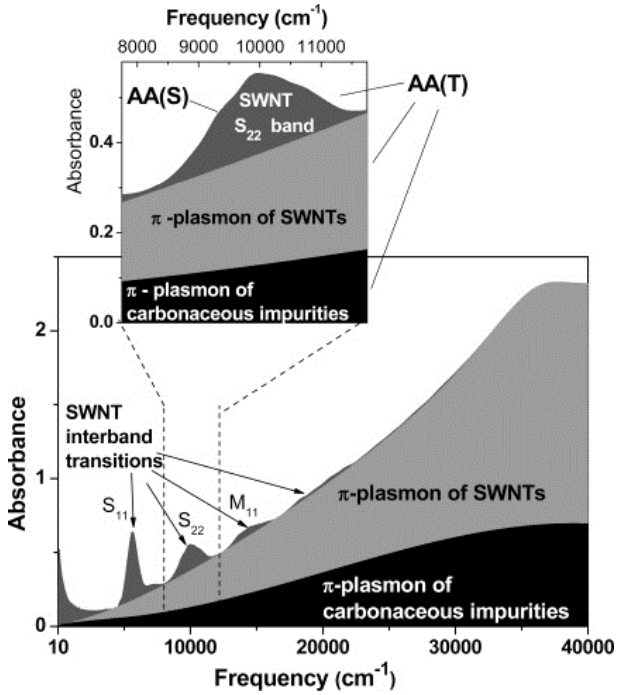

Figure 2.8 Schematic illustration of the electronic spectrum of a typical SWCNT sample with the background π-plasmon location relatively to the absorption features. Inset: region of the S_{22} interband transition used by Itkis *et al.* (2005) for NIR purity evaluation (Reprinted with permission from Itkis *et al.*, Journal of the American Chemical Society 127. Copyright (2005) American Chemical Society).

Other methodologies for the evaluation of m-SWCNT and s-SWCNT have been considered, such as the one forwarded by Landi *et al.* (2005), who based their work in the method proposed by Itkis *et al.* (2005), and concluded that such method leads to an overestimation of SWCNT purity with an average error higher than 24 %, since the metallic portion of SWCNT (in the M_{11} region) is not considered. On the other hand, the uncertainty of the shape and position of background absorption constitutes a limitation together with the variation of the absorbance intensity with the dispersion state, as reported by Ryabenko *et al.* (2004). Then, Landi *et al.* (2005) proposed a nonlinear model, based on the Lorentzian function for the π-plasmon absorption, as a physically based background subtraction, where both the overlap of electronic transitions and the peak broadening are considered. The overlap of electronic transitions is due to the variation of DOS of various SWCNT chiralities and diameters, and the peak broadening is influenced by the structural distortions and defects or bundling effects originated from the van der Waals interactions between the SWCNT. With the model proposed by Landi *et al.* (2005), the accuracy of SWCNT purity assessment was improved with an average error lower

than 7 %, and a physically background subtraction over the entire range of SWCNT electronic transitions is identified.

The interaction of electromagnetic radiation with SWCNT can take place as absorption and as scattering. The light scattering depends on the dimension of scattering particles and the wavelength of radiation. Rayleigh scattering occurs when the diameter of the particle (*d*) is much smaller than one tenth of the wavelength (λ) of the incident beam ($d << \lambda/10$). The amount of Rayleigh scattering (I_s) is inversely proportional to the fourth power of the wavelength of the incident beam ($I_s \propto 1/\lambda^4$) (Haddon *et al.*, 2004), and thus the shorter the wavelength of light, the stronger the scattering. On the other hand, Mie scattering can also occur when the particle size is equal to or greater than the incident wavelength.

Raman spectroscopy can also be used for the characterization of the dispersed SWCNT, in order to identify their electronic and vibrational structures producing typical spectroscopic signatures. Moreover, Raman spectroscopy is effective to obtain qualitative and quantitative information of SWCNT in terms of diameter, electronic structure, and purity, discriminating metallic and semiconducting components (Dresselhaus *et al.*, 2005). This technique is based on the interaction between the incident light in a material and the vibrations of lattice. Since such interaction is done through polarizability variations due to atomic vibrations, it is strongly related to the electronic structure of material. Moreover, this technique is quick, sensitive, non-destructive, and requires little sample preparation. With the exposition of materials to monochromatic radiation, the incoming light interacts with an electron which is excited from the valence energy band to the conduction energy band, that is, it is transferred to higher energy level by absorbing a photon. In those higher energy levels, the interaction with phonons occurs (through electron-phonon coupling) and then the excited electron is scattered by emitting (or absorbing) a phonon, relaxing back to the electronic ground state by emitting a photon leading to the inelastic scattering of photon, as reported by Dresselhaus *et al.* (2005) and by Freiman *et al.* (2008). When the intensity of the scattered light is measured as a function of frequency downshift (losing energy) of the scattered light, Raman spectra are plotted and an accurate measure of the phonon frequencies of the material is obtained (Dresselhaus *et al.*, 2005). Specifically, Raman spectroscopy is based on the light scattering effect: Rayleigh scattering and Raman scattering. The Rayleigh scattering has the same energy (frequency and wavelength) as the incident photons, and the Raman scattering is the inelastic scattering of photons by molecules due to changes in frequency. Figure 2.9 shows the energy level diagram of the states involved in the Raman scattering process, where the energy

difference between the incident photon and the Raman scattered photon is the energy of a vibration of the scattered molecule. Thus, Stokes process occurs with the production of a phonon (phonon emission) and anti-Stokes process occur with annihilating a phonon (phonon absorption) in a material. It should be highlighted that the virtual energy states result from the virtual absorption, which is the absorption that occurs without energy consumption (Long, 2002).

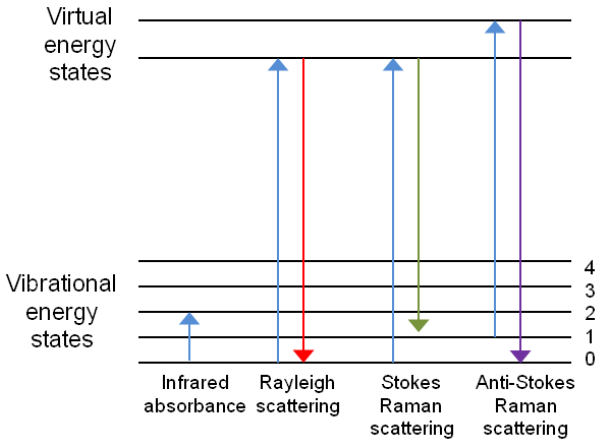

Figure 2.9 Energy level diagrams of the states involved in the Raman signal.

Regarding SWCNT, when the energy of the incident laser is close enough to the energy between the van Hove singularities in the valence and the conduction bands, a strong resonantly enhanced Raman signal of a single SWCNT can be obtained, as stated by Thomsen and Reich (2007). When a bundle or a collection of isolated SWCNT is exposed to the laser line, only those tubes with inter-band transition energies resonant with the excitation energy will contribute strongly to the spectrum.

2.1.4. Methodologies for separation of metallic and semiconducting CNT from CNT networks

The separation of metallic (m-CNT) and semiconducting CNT (s-CNT) from CNT networks is advantageous for many electronic and sensing applications such as the fabrication of conductive films, field effect transistors (FET), and optical devices, as applied by Javey *et al.* (2003), Green and Hersam (2008), and Weisman (2010). The complete separation of CNT into s-CNT is not accomplished, since the synthesis

processes of CNT are not able to synthesise only s-CNT or totally remove m-CNT without damaging s-CNT for functional microfabricated devices. Thus, physical methods such as alternating current dielectrophoresis (Krupke *et al.*, 2003), selective electrical breakdown (Collins *et al.*, 2001), density gradient ultracentrifugation (Arnold *et al.*, 2006; Yanagi *et al.*, 2008), and microwave irradiation, as well as chemical methods such as gel chromatography and selective functionalization are some methodologies employed to isolate m-CNT and s-CNT from a CNT network. For the development of FET with CNT (NTFET), such isolation is needed since the presence of an excessive number of m-CNT can degrade the electrical signal of NTFET on current-voltage curves, decreasing the ON/OFF ratio, which is the extent of current obtained between the lowest and highest voltage applied. It is known that the higher such ratio, the higher the performance of NTFET. However, the application of the CNT network in the NTFET biosensing devices has been reported, for example, by Gui *et al.* (2007), Cid *et al.* (2008a; 2008b), and Villamizar *et al.* (2011) but with resulting low ON/OFF ratios, although in a CNT network, a higher content of s-CNT are present relatively to m-CNT.

Various methodologies have been attempted in order to obtain isolate s-CNT or to enrich them in CNT dispersions, for further application in electronic and biosensing devices. In alternating current dielectrophoresis, the dispersed SWCNT are exposed under an electrical field, and since m- and s-CNT have different dielectric constants under an alternating current (1000 *vs.* 5, respectively), the electronic separation is possible (Krupke *et al.*, 2003; Krupke and Hennrich, 2005). The m-CNT are collected toward the high applied electric field in a microelectrode array, while the s-CNT are left in solvent, which has an dielectric constant of approximately 80, but this process can only be operated at a small-scale. Tanaka *et al.* (2008) also employed electrophoresis but with agarose as the matrix gel (stationary phase) for separation of m-CNT and s-CNT from a CNT dispersion with an aqueous solution of sodium dodecyl sulphate (SDS) as dispersant (mobile phase). In gel electrophoresis, the migration of charged molecules was observed in a gel across an electrical field, sorting analytes by differences in molecular weight (MW). Using this technique, Tanaka *et al.* (2008) verified that, when a constant direct current is applied to the agarose gel, m-CNT coated with negatively charged SDS migrate toward the anode, as shown in Figure 2.10, leaving the enriched s-CNT in the gel.

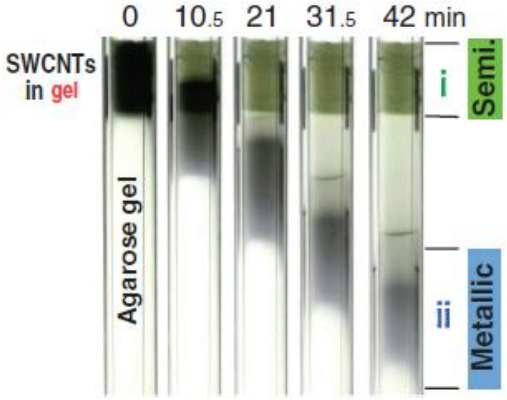

Figure 2.10 Sequential photographs of the separation of SWCNT dispersed by agarose gel electrophoresis (Reproduced from Tanaka *et al.*, Copyright (2008) with permission by The Japan Society of Applied Physics).

As depicted in Figure 2.11, other separation methodologies based on agarose gel were also developed by Tanaka *et al.* (2009), namely: the manual squeezing of the frozen and thawed gel, centrifugation, diffusion, and permeation.

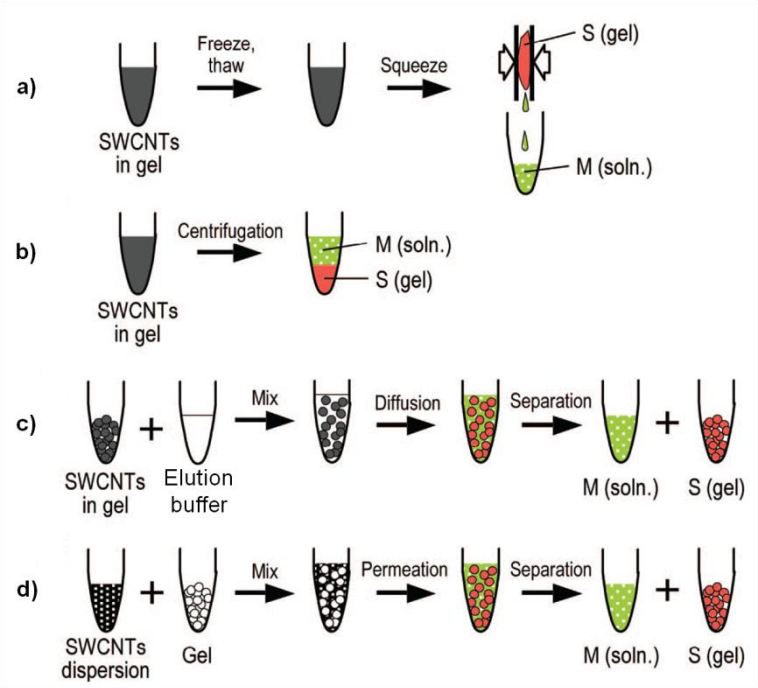

Figure 2.11 Schematic diagrams of separation methodologies based on agarose gel: a) freeze and squeeze, b) centrifugation, c) diffusion, and d) permeation (Adapted and reprinted with permission from Tanaka *et al.*, Nano Letters 9. Copyright (2009), American Chemical Society).

In the squeezing method, the agarose gel is mixed with a SWCNT dispersion and SDS, then, the mixture is frozen, and thawed. The s-SWCNT are selectively adsorbed to the agarose gel matrix, and the m-SWCNT remain in solution with the SDS micelles, as shown in Figure 2.11. In the centrifugation method, the SWCNT mixture is centrifuged and the supernatant becomes enriched with m-SWCNT, while s-SWCNT is precipitated together with the gel. In the diffusion method, the SWCNT in gel are added to an elution buffer, and in the permeation method, the agarose gel is added to a dispersion of SWCNT; then, for both methods, s-CNT and m-CNT are separated with centrifugation. Thin-film transistors (TFT) with separated portions were tested by Fujii *et al.* (2009) and high ON/OFF ratios were observed, although with large hysteresis, which constitutes an experimental problem for NTFET applications, as explained in Section 2.3. In all methods based on agarose gel shown in Figure 2.11, the s-SWCNT are selectively adsorbed in agarose gel. Thus, the separated s-SWCNT/gel should be refluxed in an aqueous solution of 1 % of citric acid at 95 ºC to decompose the agarose gel, and with a brief centrifugation, the s-SWCNT are removed from gel. After that, the separated portion is redispersed in surfactant or solvents such as N-methylpyrrolidone, but this redispersion could introduce structural defects on CNT. Such structural defects are imperfections that change the curvature of CNT, or they occur due to the presence of carbon atoms arranged in pentagons and heptagons embedded in the hexagonal structure of CNT. Finally, the separation process can be significantly improved if an optimization procedure is followed in order to find the optimum values for the gel concentration and the composition of agarose (Li and Li, 2011).

The selective electrical breakdown method is based on the current induced oxidation to selectively eliminate m-SWCNT from SWCNT networks. High currents are applied to the SWCNT networks and the m-SWCNT are selectively removed because they are burned in contact with air. Collins *et al.* (2001) have performed this separation process and used the remaining s-SWCNT for producing FET devices. However, the electrical breakdown is difficult to control, affecting the reproducibility of the process of fabrication, since losses in s-SWCNT could occur limiting the CNT density.

In the density-gradient ultracentrifugation method, CNT are moved in a density gradient solution by the centrifugal force. For example, Arnold *et al.* (2006) have used a non-ionic density gradient agent (iodixanol) to produce density gradients where SWCNT are separated in layers. The s-SWCNT were retained in the upper layer (low density) and the m-SWCNT were located in the lower layer (high density). The iodixanol can constitute a problem due to the presence of iodine atoms, which function as electron acceptor by

SWCNT, degrading the electronic characteristics of s-SWCNT since its conductivity increases. Yanagi *et al.* (2008) also used the density-gradient ultracentrifugation technique, with sucrose as a gradient medium, which does not work as an electron donor/acceptor, and it has a small MW, thus leading to fast removal by centrifugation, and obtaining highly enriched solutions of m-SWCNT and s-SWCNT. According to Izard *et al.* (2008), the density-gradient ultracentrifugation still leaves traces of surfactant and density gradient materials in CNT, which interfere with the performance of FET.

The microwave irradiation method has been used by Shim *et al.* (2009) as a method to obtain separated s-SWCNT. In this technique, the energy is directly applied to the SWCNT by an electromagnetic field, and as the m-SWCNT have higher dielectric constant than the s-SWCNT, they are broken down since the energy absorbed by the m-SWCNT is much higher than that by the s-SWCNT, which makes possible the destruction of m-SWCNT. The limitation of this method is the possible damage of s-SWCNT after the microwave treatment.

The selective reaction is also used for removal of m-SWCNT in order to obtain enriched s-CNT from a SWCNT network. For example, Yang *et al.* (2006) have used fluorine gas to induce stronger electrostatic binding with m-SWCNT due to the presence of more abundant π-electrons near the Fermi level when compared to s-SWCNT. Ghosh and Rao (2009) have employed the selective reaction of a diazonium salt of 4-heptadecafluororooctylaniline with the m-SWCNT to produce covalent aryl bonds, thus extracting electrons from nanotubes and providing high selectivity towards the m-SWCNT. However, the presence of covalent chemical groups degrades the electrical properties and devices performance, and vacuum annealing treatment at 600 ºC is needed for the elimination of such functional groups from the remaining s-SWCNT, which could introduce defects in the CNT walls.

The size exclusion chromatography has been another technique applied for the separation of CNT by electronic type. Liu *et al.* (2011) used Sephacryl S-200 of GE-Healthcare as the size exclusion gel and SDS surfactant solution with a high dispersibility to elute the bound s-SWCNT. In this technique, several chromatography columns are connected in series, and when an excess amount of SWCNT dispersion is applied onto the top of the column, the selective adsorption of s-SWCNT in the various columns occurs due to the different strengths of interaction with the gel. As the m-SWCNT have the lowest interaction with the gel, they are eluted firstly, while the s-SWCNT are adsorbed in gel. However, Liu *et al.* (2011) have found structural defects in the separated s-SWCNT when Raman analysis was used to confirm the electronic structure of the

SWCNT and in order to obtain a scalable separation, a suitable combination between stationary and mobile phases should be found taking into account the different affinities towards the different type of SWCNT.

2.2. Molecular recognition and applications of CNT in sensing devices

The molecular recognition is defined as the energy and the information involved in the selection and binding of an analyte of interest into a recognition molecule due to their complementarity, that is, affinity interaction. In general, the immobilization of biomolecules such as proteins, enzymes, antibodies, and peptides on CNT surface can be made by non-covalent adsorption or covalent bonding of functional groups through reaction with the π-conjugated network of the SWCNT, increasing the specificity and the sensitivity of biosensors, as reported by Zhao and Stoddart (2009), Lei and Ju (2010), and Liu *et al.* (2010). The typical reactions can be based on the formation of covalent bonds, for example with porphyrin-based compounds (Guo *et al.*, 2006), or non-covalent bonds, for example with phospholipid-poly(ethyleneglycol) (Liu *et al.*, 2009). The covalent functionalization of CNT can cause drastic changes on electronic band structures of CNT, since functional groups, such as carboxylic acids at the ends and sidewalls of CNT, contribute with defects on CNT structure, breaking the π-conjugated network on CNT and affecting their properties (Harris, 2009). The incorporation of polymers for CNT functionalization is also used, since polymers protect the CNT surface from unspecific molecules and they are suitable for covalent adsorption of receptor molecules on CNT, obtaining more selective sensors for specific analytes (Katz and Willner, 2004). For example, Star *et al.* (2003) used polyethyleneimine (PEI) and poly(ethyleneglicol) (PEG) as polymers for providing the covalent attachment of amine groups to the receptor molecule in CNT surface (through PEI), and to prevent unspecific adsorption of biomolecules (through PEG).

As CNT display a poor solubility due to their hydrophobicity and strong van der Waals attractions between the nanotubes, the chemical functionalization of CNT surface can also be employed for their dispersion by attaching hydrophilic species, in order to widen their applications, as demonstrated by Star *et al.* (2004), and Zhao and Stoddart (2009). SWCNT can be dispersed in organic and aqueous solutions of surfactants in order to assess the optimal conditions for their surface functionalization, either covalently or non-covalently, as demonstrated by Bandyopadhyaya *et al.* (2002), Nakashima *et al.* (2002),

and Islam *et al.* (2003). The non-covalent functionalization of CNT, which preserves the sp^2 structure of SWCNT without disrupting the CNT structure, can be made through the use of surfactants such as sodium cholate, sodium dodecyl sulphate, and Triton X-100 (Moore *et al.*, 2003), as well as by wrapping CNT in polymers such as polyvinylpyrrolidone and polystyrenesulfonate (Banerjee *et al.*, 2005). Such functionalization employs functional aromatic compounds that have π-π stacking behaviour on the surface of SWCNT, which is a non-covalent interaction between molecules with aromatic structures.

Regarding the application of CNT for the development of sensing devices, biosensors such as immunosensors and genosensors have been reported for the detection and quantification of biomolecules (for example, enzymes and proteins), antibodies/antigens, and DNA sequences, respectively, as studied by Daniel *et al.* (2007), Veetil and Ye (2007), and reviewed by Roman (2010). In immunosensors, the functionalization of CNT surface should occur in order to obtain the immobilization of antibodies (Chen *et al.*, 2003). The incorporation of CNT in point-of-care (POC) biosensors is also a promising research area, due to their sensitivity, their adequate response time, and their fitness for purpose, since POC biosensors can be hand-held and used by patients. As reviewed by Justino *et al.* (2013a), the application of CNT on POC systems has been under consideration for the analysis of biological analytes such as DNA, glucose, proteins, and viruses, and this research area has been expanding due to the increasing demand for rapid diagnostic devices. However, analytical improvements on POC biosensors are greatly needed for the detection of cancer biomarkers for the diagnosis of cancers, and detection of glucose to *diabetes* diagnosis and prognosis. As reviewed by Justino *et al.* (2010), many of the available POC devices are based on electrochemical sensing, and the research in clinical field is likely to progress in this very same direction due to reasons of portability, cost effectiveness, fast response of such biosensors, and high analytical performance provided, mainly in terms of sensitivity and selectivity.

2.2.1. Antibody-antigen interaction and label-free biosensors

Antibodies are glycoproteins with molecular weight (MW) between 140 and 970 kDa, also known as immonuglobulins, and they are secreted by lymphocytes, that is, by the immune system of an organism. Antibodies can be collected from a living organism, separated, and concentrated for use in biosensing applications. In this thesis, the antibodies used are the anti-human C-reactive protein (CRP) and they were obtained from

goat using CRP purified from pooled inflammatory human serum as the immunogen (Sigma-Aldrich Química, Portugal). Biochemically, the structure of an antibody consists of a Y shaped unit, which has polypeptide chains, as shown in Figure 2.12. The polypeptide chains are based on two heavy (H) chains (with 450 amino acid residues and MW of 50 kDa) and two light (L) chains (with 212 amino acid residues and MW of 25 kDa), which are linked by disulphide bonds (-S-S-). Both chains are divided in structural domains based on amino acid sequences. The H chain has four domains (V_H, C_H1, C_H2, and C_H3), and the L chain has two domains (V_L and C_L), which are responsible for the flexibility and globular nature of antibodies (Killard *et al.*, 1995), where V and C are the initials of variable and constant domains, respectively. The variable domains of both chains are the most important in the antibody structure since they determine the variability of antigen interaction.

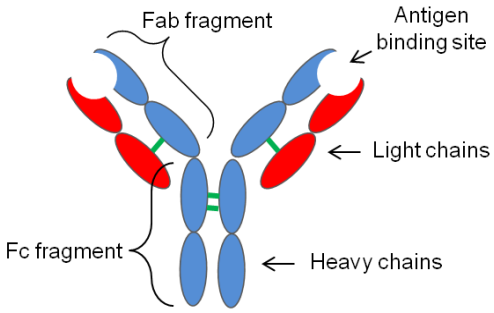

Figure 2.12 Schematic basic structure of an antibody, with typical light chains (red), heavy chains (blue), and disulphide bonds (green).

As also shown in Figure 2.12, the Y shaped structure of an antibody can also be characterized by regions, that is, two regions called Fab (fragment containing antigen binding site) and Fc (fragment that crystallizes) regions. In the Fab domain, a site named epitope is present to bind with the corresponding antigen, and Fab segments provide flexibility to the antibody through rotational and lateral movements of the two Fab segments. The Fc domain is responsible for the linking of the antibody to the receptor molecule.

The antibody-antigen interaction is the detection mechanism used both in immunosensors (sensing devices) and in immunoassays (traditional analytical techniques). Antibodies function as recognition elements in immunoassays and immunosensors, due to their strong specificity and affinity for their equivalent antigens. The immunoassay is an analytical method capable of quantifying the amount of an antigen within a sample through its selective and affinity reaction with a specific antibody.

Normally, antigens are labelled with an enzyme to produce a coloured product which accumulates in the solution for signal detection, which is related to the initial concentration of antigen. The immunosensors are analytical devices where the interaction between antibody and antigen has a non-covalent nature (Moina and Ybarra, 2012), and the analytical signal generated from such interaction is converted through a transducer into a physico-chemical response, for example, based on the variation of optical properties, electric charge, mass or heat, as shown in Table 2.3, where the various categories of immunosensors are identified according to their transduction principle.

Table 2.3 Categories of immunosensors according to their transduction principle.

Immunosensor	Transduction principle	Response
Electrochemical	Amperometry / FET	Current
	Potentiometry	Electrode potential or voltage differences
	Conductimetry	Conductance or resistance
Optical	Surface Plasmon Resonance	Refractive index
	Grating couplers	
	Differential interferometry	Optical path or refractive index
	Reflectrometric interference spectroscopy	
	Resonant mirror (mode coupling)	
Mass sensitive	Surface acoustic wave	Elasticity or density
	Quartz Crystal Microbalance	Mass

For example in electrochemical immunosensors, the response is based on an electrical signal and in optical immunosensors, an optical signal can be generated or a change in optical properties can be monitored. As reviewed by Justino *et al.* (2010), the immunosensors based on surface plasmon resonance, FET, and quartz crystal microbalance are label-free, ease of use, less expensive, with minimal requirements of sample preparation, and the output signal is obtained directly from the sensor software.

The good mechanical and conductive properties of CNT, such as high energy densities and low driving voltages, respectively, can lead to expectable developments in the field of immunosensors. For example, NTFET immunosensors have been already reported as optimal transducers because they are label-free and the biological sensitive elements are immobilised onto the transducer surface also functioning as the electronic part of the

device, as reviewed by Hu *et al.* (2010). Thus, immunosensors have been pointed out as an alternative for immunoassays because they can provide fast screening results, they are small, semi-automated and increasingly portable (Lin and Ju, 2005). Such an increase in portability has been the consequence of improvements in sensor miniaturization.

Usually, immunoassays are analytical techniques used for the validation of a new methodology developed for antigen detection. Various immunoassay formats exist, that is, various types of antibody-antigen interaction are known, such as the capture, sandwich, competition, and inhibition assays. Sandwich assays tend to be more sensitive and robust, and they are the most commonly used together with the competitive binding assay, which are schematically shown in Figure 2.13.

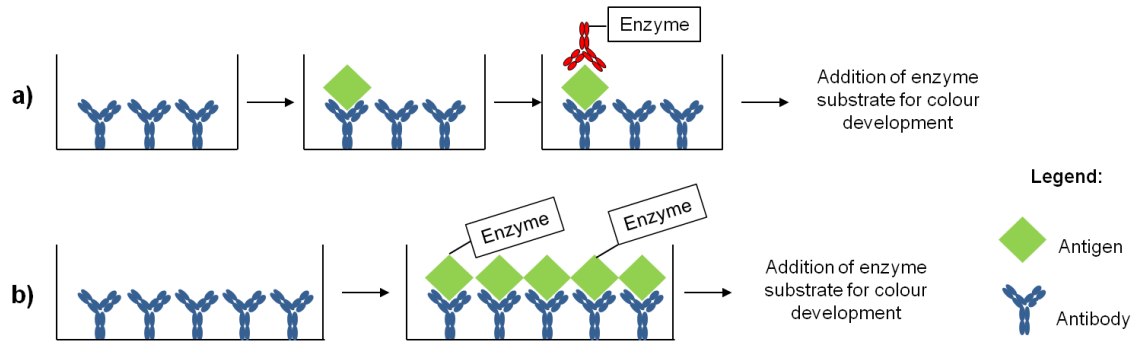

Figure 2.13 Schematic diagrams of the two most commonly used immunoassays: a) sandwich immunoassay and b) competitive binding assay.

In a sandwich immunoassay (Figure 2.13a), two antibodies are used, which bind to different sites in the antigen. The capture antibody is attached to a solid surface and it is specific for antigen. Typically, an enzyme (for example, the horseradish peroxidase) is attached, that is labelled, to the detection antibody in order to react with a substrate responsible for the detection signal. Usually, the colorimetric detection is used, and the signal is proportional to the amount of antigen present in the sample. In a competitive binding assay (Figure 2.13b), a competition between labelled and unlabelled ligand occurs for a limited number of antibody binding sites, and only an antibody is used. A fixed amount of labelled ligand is incubated with the antibody, and with variable amount of unlabeled ligand, being the amount of labelled ligand a function to the total concentration of labelled and unlabelled ligand. The signal is lower with the increase of unlabelled analyte, that is, the signal of immunoassay is inversely proportional to the concentration of analyte in the sample. In this thesis, the capture format was used for the developed

NTFET immunosensors, and the sandwich assay was used for ELISA methodologies for the determination of CRP in saliva and serum samples.

Another classification of biosensors is based on the nature of the molecule detected, that is, they can be classified as label-based or label-free biosensors. In label-based biosensors, the label molecule is detected and it could be radioactive, enzymatic, fluorescent, or redox in nature. In label-free biosensors, any label is used, the analyte of interest is directly detected in its native form, and the intermediate step of tagging is unnecessary. Thus, the reduction of number of steps for the assay is an advantage to the application of such label-free biosensors, since the chemical modifications of biomolecules with labels are not necessary, leading to simplification, higher speed of analysis, increased reliability, and lower cost, as specified by Fan *et al.* (2008). Concerning the transduction technique used in immunosensors, FET devices become successful alternatives to the complex optical sensors due to their low cost, low power consumption, miniaturization, and multiplexing capabilities, as well as due to their simple detection principle based on electrical measurements. In this thesis, the mechanism of transduction of the electrochemical immunosensors is based on the FET principle.

2.3. Operation principles and applications of field effect transistors with carbon nanotubes (NTFET)

Field effect transistors with carbon nanotubes (NTFET) constitute a type of detection systems which use SWCNT as active elements. They were firstly reported by Martel *et al.* (1998), and Tans *et al.* (1998), and they can be made of either a unique SWCNT or a network of SWCNT as studied by Star *et al.* (2003), and Byon and Choi (2006), respectively. Figure 2.14 shows a typical configuration for a NTFET with the electrical associations between the source, drain, and gate contacts. NTFET use the semiconductor characteristic of SWCNT to the construction of sensor devices with an excellent performance in terms of analytical figures of merit, such as low limit of detection, and high sensitivity (Kauffman and Star, 2008). MWCNT can also be used, but the SWCNT are preferable due to their simpler structure, and easier study in terms of chemical and physical properties, as reported by Liang *et al.* (2007).

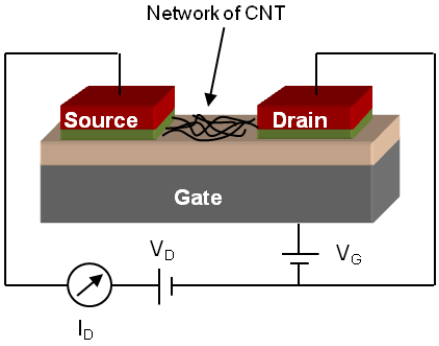

Figure 2.14 Schematic of a typical NTFET (I_D, drain current; V_D, drain voltage; V_G, gate voltage).

As shown in Figure 2.14, a typical NTFET is an electronic device constituted by a source and drain contacts, and a gate contact separated by a thin insulated layer of SiO_2. The gate insulator could also be a double layer of SiO_2-Si_3N_4, SiO_2-Al_2O_3, or SiO_2-Ta_2O_5. NTFET are currently called unipolar transistors due to the use of only one of the two carrier types, holes or electrons, depending on the nature of conduction. NTFET are considered as p-type devices, when the conduction is mostly made through holes, and as n-type when the conduction is made by electrons, as major carriers (McEuen, 2000). For an intrinsic semiconductor, the number of holes is similar to the number of electrons. In electronics, the concept of hole is related to a missing electron in the valence band, and the term electron refers to free electrons in the conduction band. Sometimes FET also show ambipolar behaviour, as studied by Martel *et al.* (2001), when the charge carriers are both holes and electrons in the same device.

In a NTFET, the current flows between the source and the drain contacts, through the CNT channel and it depends of the voltage applied and the resistance of the CNT channel, being modulated by the gate contact (Derycke *et al.*, 2002). When a negative bias voltage is applied to the gate (gate voltage, $V_G < 0$), the hole conduction is induced, and the s-SWCNT are turned ON; then, when the bias is positive ($V_G > 0$), SWCNT are turned OFF. This ON/OFF current ratio is a particular characteristic of each FET device constituting one of its figures of merit. With the decrease of V_G, electrons are pushed away from the CNT and into the contacts, thus increasing the conduction. Increasing the V_G, more electrons are pulled onto the CNT from the contact, polarizing the system and accumulating negative charges, thus stopping the conduction process. In a network of SWCNT, the m-SWCNT have a pronounced effect on the conductance of the “OFF” state (achieved by positive gate voltages), reducing the modulation (difference between the ON and OFF states of the device). Thus, the higher the semiconductor content of the CNT

network, the higher the modulation of current response obtained through the application of gate voltages on NTFET. When a network of SWCNT is used instead of only a single nanotube, the signal monitoring of sensing systems is the average of all signals produced by the CNT network.

In the NTFET, the SWCNT allow the current conduction between contacts (source and drain), contrarily to typical metal-oxide semiconductor FET (MOSFET), a type of transistor where the conduction is controlled by the application of gate voltages at the surface of insulating layer of SiO_2. In a NTFET, the region involving metal contacts and SWCNT interfaces with a region with high electronic density, which generates an electronic valence band, called depletion region, and a potential barrier, called Schottky barrier, which generates an electrical resistance due to the inhibition of holes transmission between SWCNT and the metal. Then, the NTFET behaviour as transistors is based on the transport through the Schottky barrier in the interface of the metal contact/SWCNT, which in turn, depends on the geometry of the interface, the SWCNT diameter, and the type of metal, as studied by Javey *et al.* (2003), and Chen *et al.* (2005).

The hysteresis is an experimental problem which can occur in NTFET due to the interaction of water molecules with SiO_2, when the electrical characterization of NTFET is performed under ambient conditions, or it can be associated with the oxygen-related charge traps in the SiO_2 (Balasubramanian *et al.*, 2004; Kim *et al.*, 2003). Kim *et al.* (2003) suggest that hysteresis is due to the charge trapping by water molecules around the nanotube: when positive V_G values are applied, electrons are slowly trapped near CNT, and CNT have a more negative potential than that simply due to the V_G, and an additional current arises. Such parasitic effect of hysteresis is not present in the NTFET developed in this thesis, being an additional advantage of such devices, as shown in Chapter 5.

Regarding the gate contact of the NTFET, it can have two configurations: the back-gated and the electrolyte-gated, as shown in Figure 2.15.

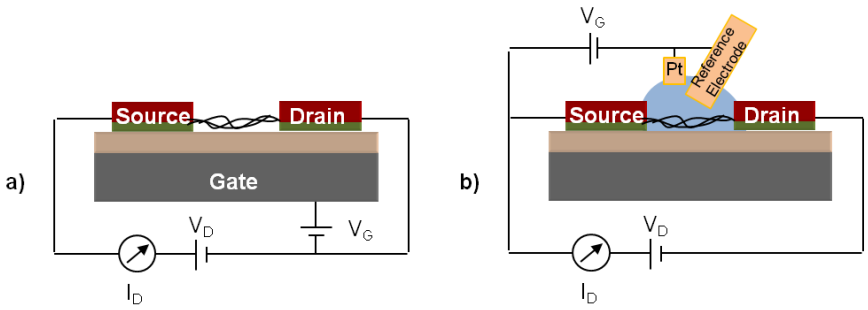

Figure 2.15 Schematic diagrams of different gate configurations for NTFET: a) back-gated configuration and b) electrolyte-gated configuration.

In back-gated configuration (Figure 2.15a), the gate electrode is placed at the back of the devices, and in contact with the SiO_2 layer. In this way, the CNT are in contact with the sample, and the originated signal can be easily related to the presence of the analyte of interest, and measured. Thus, any additional reference and external electrodes are unnecessary. In the electrolyte-gated configuration (Figure 2.15b), an external electrode (usually a Pt electrode, due to its stability) is placed in contact with the aqueous sample solution and the SWCNT. The V_G is applied to the external electrode, and this voltage affects the CNT *via* ions in the electrolyte. The target ion presents in the solution is determined due to the electrostatic potential difference monitored between the CNT and the electrolyte solution, which is due to the various redox reactions occurring at the metal-liquid interface. In the electrolyte-gated configuration, the distance between the gate electrode and the SWCNT channel is short, but the challenge is on the development of reference electrodes at the micrometer scale. Minot *et al.* (2007) have concluded that the potential of the Pt electrode is unstable when proteins bind to its surface, and a reference electrode Ag/AgCl should be used to control the solution potential. In this thesis, the back-gated configuration was applied to the NTFET fabricated, where the silicon wafer, which serves as the basis for the microfabrication, was used as the back-gate.

Regarding the applications of NTFET, they are considered as relatively new devices for the detection and quantification of biomolecules, such as glucose (Besteman *et al.*, 2003), xenobiotic compounds such as bisphenol A (Sánchez-Acevedo *et al.*, 2009), DNA (Star *et al.*, 2006), pathogenic microorganisms such as *Salmonella* Infantis (Villamizar *et al.*, 2008), proteins such as human chorionic gonadotropin and bovine serum albumin, as reported by Chen *et al.* (2004), as well as prostate-specific antigen (Kim *et al.*, 2009). The interaction between such compounds and the SWCNT have various response mechanisms on the NTFET, but the most reported is the variation of electrical properties, that is, the transference of charges, or the modification of Schottky barrier, as proposed by Chen *et al.* (2005) and Wang (2005), as well as the scattering potential for mobile charges or charge scattering caused by local deformation, as stated by Heller *et al.* (2008).

Although the performance of various NTFET, when applied to environmental quality and clinical diagnosis, have been highlighted as reported by Kauffman and Star (2008), and Burghard *et al.* (2009), the incorporation of CNT and other nanomaterials in sensors and biosensors still shows some limitations which hinder their wider potential applications. Some characteristics of nanomaterials such as CNT density, diameter, and chiralities may cause considerable variability on the devices properties affecting the analytical performance of the sensing systems, as shown in Figure 2.16. For example, Ishikawa *et*

al. (2010) studied the effect of the density of SWCNT network on the analytical performance of FET devices for streptavidin detection, and concluded that, when the density of CNT is lower, the sensitivity is higher in terms of both limit of detection (LOD) and the magnitude of analytical response (defined as normalized conductance), and the reproducibility of such biosensors is better. The enhanced sensitivity associated with a low density of SWCNT is partly explained by the elimination of direct metallic nanotube pathways, enhancing the semiconductor behaviour of nanotubes and providing strong gate dependence, lower capacitance, and high ON/OFF ratios, while the high density of SWCNT reflects their quasi-metallic behaviour. Fu and Li (2010) also reported a ultrasensitivity of FET biosensors with SWCNT networks for detection of DNA molecules (0.1 fM) when lower density of CNT were applied: ON/OFF ratio and LOD have been improved three and five orders of magnitude, respectively.

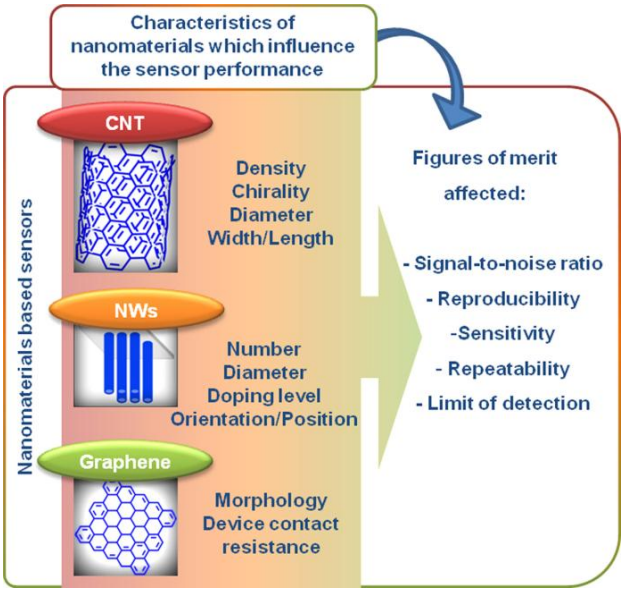

Figure 2.16 Characteristics of the nanomaterials that can influence the analytical performance of chemical and biological sensors (Reprinted from Trends in Analytical Chemistry, 47, Justino *et al.*, Copyright (2013b), with permission from Elsevier).

2.4. C-reactive protein (CRP): characterization, clinical importance, and methodologies for its quantification

Cardiovascular diseases (CVD), for example, cerebral vascular accident and coronary heart disease are among the major causes of ill health, invalidity, and death in Portugal, according to the latest Portuguese National Health Plan for 2012-2016 (PNHP, 2012) and the National Programme for Prevention and Control of the Cardiovascular Diseases (NPPCCD, 2006). Such diseases are mainly associated with smoking, high blood pressure, high cholesterol levels, and sedentary habits, and then the prevention of such risk factors should be taken into consideration. In Europe, there is a similar pattern and CVD cause nearly half of all deaths (48%), according to the latest European Cardiovascular Diseases Statistics (Nichols *et al.*, 2012), also being the main cause of death worldwide (Roger *et al.*, 2012).

In the biomedical area, the determination of specific blood compounds (biomarkers) has been suggested as a tool for the identification of high-risk patients in terms of the CVD risk (Vasan, 2006). According to Packard and Libby (2008) the diagnosis of such compounds, such as C-reactive protein (CRP), interleukin 18, matrix metalloproteinase 9, adiponectin, and soluble CD40 ligand, in real-time and with rapid analysis is required for the adequate evaluation and prediction of CVD risk. CRP is currently considered the best validated inflammatory biomarker (Packard and Libby, 2008), and functions as an acute-phase protein, since it is found at trace levels in serum and increases dramatically during tissue damage, infection, and inflammatory processes. According to Mitaka (2005), the CRP has a plasma half-life of 19 hours, and even after a single stimulus, it may take several days to return to the baseline. Thus, as the CRP levels keep relatively stable without significant diurnal variation, this parameter is quite amenable to its correct quantification (Macy *et al.*, 1997). The name of such protein, called fraction C when discovered by Tillet and Francis (1930), is due to its precipitation with the C-polysaccharide of pneumococcus in the acute-phase pneumococcal pneumonia.

Chemically, the CRP is composed by five identical non-glycosylated (without attached glycans) polypeptide subunits, and each of them has approximately 23 kDa. As displayed in Figure 2.17, the subunits are non-covalently associated in an annular configuration, each of them containing two calcium ions in the ligand-binding sites. Due to its cyclic pentameric configuration, the CRP belongs to the family of pentraxins (acute-phase reactants characterized by a cyclic structure) which are a group of proteins that are expressed with infection, systemic inflammation, and tissue damage.

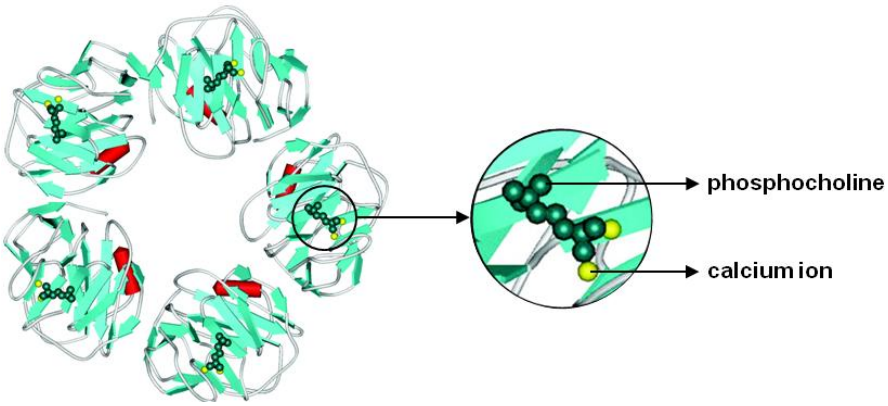

Figure 2.17 Molecular structure of CRP (Reproduced from Black *et al.*, Copyright (2004) with permission by The American Society for Biochemistry and Molecular Biology). In zoom: the ligand-binding site of CRP with the calcium ions (yellow) complexed with phosphocholine (green) of a damaged cell.

The CRP is synthesized in the serum by the hepatocytes and its production can be regulated by inflammatory cytokines, mainly by interleukin-6 (Bucova *et al.*, 2008). The CRP, through its calcium ligands, binds to phosphocholine, which is a component of phospholipids on cell membranes and plasma lipoproteins (Thompson *et al.*, 1999). The complexed CRP activates the complement system, and a range of processes, such as phagocytosis and lysis of invading cells is initiated. Biochemically, the complement system is constituted by approximately 35 proteins, which become activated through sequential proteolytic cleavages in response to endogenous ligands, such as immunoglobulins or pentraxins, among others (Tulamo *et al.*, 2010).

The monitoring of CRP levels is important to predict the risk of atherosclerotic diseases, including CVD, and various epidemiologic studies have demonstrated the association of CRP with the increase of cardiovascular risk, as reviewed by Calabró *et al.* (2009), and Silva and Lacerda (2012). The risk of CVD has been considered low if the levels of CRP in serum are below 1.0 mg L^{-1} and, in turn, it becomes elevated when levels of CRP are higher than 3.0 mg L^{-1}. When levels of CRP are higher than 3.0 mg L^{-1} and up to 10 mg L^{-1}, it functions as an indicator for significant risk of chronic CVD including acute coronary syndromes. Very high levels between 10 and 50 mg L^{-1} can also be found in late pregnant women and viral infections, and even higher levels, between 50 and 200 mg L^{-1}, are related to bacterial infections and active inflammation (Clyne and Olshaker, 1999). Thus, and according to FDA (2005), patients with CRP levels higher than 10 mg L^{-1} should be checked for infection and inflammation, other than CVD. Therefore, biosensing systems as well as other analytical techniques fit for purpose should cover the whole

concentration range of interest, that is, they may be capable of evaluating levels of CRP lower than 1.0 mg L^{-1} and higher than 50 mg L^{-1}.

The CRP has been considered as an immunogenic protein, since it has a MW greater than 5 kDa (Vo-Dinh and Cullum, 2000), suggesting high recognition and antibody binding with very high specificity. Then, in all methodologies used for the detection and quantification of CRP, the interaction between antibody and antigen is applied due to the high specificity and affinity of antibodies to the target molecules. Clinical immunochemical methods based on high sensitivity assays, that is, immunoturbidimetric, immunochemiluminometric, and immunonephelometric assays, as well as enzyme linked immunosorbent assays have been traditionally used to the detection of CRP in blood serum with LOD ranging from 0.03 to 0.2 mg L^{-1} and detection range between 5 and 10 mg L^{-1} of CRP (Dominici *et al.*, 2004; FDA, 2005). Immunoassays, which are biochemical tests for quantifying a substance based on its ability to bind to an antibody (immunoreaction), require expensive instrumentation, sample pre-treatment protocols, laborious work, and rigid operational procedures. Besides, they are time-consuming, and the detection is indirect, since they are based on optical transduction and one of the reagents is labelled. In the 1990s, the CRP concentration in patient serum was determined by nephelometric assays measuring the formation of antibody-antigen complexes (ICSH, 1988), and such test would take 30 minutes with an analytical sensitivity of 0.04 mg L^{-1}. Nowadays, the CRP quantification method used in routine clinical laboratories is the high-sensitivity CRP test based on the enzyme-linked immunosorbent assay (ELISA assay) (Rifai and Ridker, 2001), an immunoanalytical method which became a traditional technique to quantify the amount of CRP in blood serum with a sensitivity in the order of ng L^{-1}.

In the field of the development of electrochemical immunosensors for CRP detection, Meyer *et al.* (2007) developed a magnetic immunosensor with acceptable values for LOD (2.5×10^{-2} mg L^{-1}) on a large dynamic linear range (2.5×10^{-2} - 2.5 mg L^{-1}). However, Meyer *et al.* (2007) pointed out some disadvantages in the magnetic immunosensor, such as the high sample size (0.5 mL) and large time required for measurement (30 minutes). Bini *et al.* (2008) proposed an optical RNA-based aptasensor based on the surface plasmon resonance method, with a lower LOD (5 µg L^{-1}) than that obtained by Meyer *et al.* (2007); however, the method is labour intensive and required expensive equipment for measurement of CRP. Sohn and Kim (2008) have developed a BioFET where the CRP was linked to an antibody which in turn was bound to a cystein-tagged protein G. The signal produced by the binding of the protein G with the CRP was similar to the application

of a negative gate voltage to MOSFET with a decrease in the channel conductance. Sohn and Kim (2008) obtained a linear sensor response in a concentration range between 3 and 20 mg L^{-1} of CRP. In turn, Yang *et al.* (2009), and Quershi *et al.* (2009) proposed biosensing systems based on magnetic principles, that is, a microfluidic system and a capacitive immunosensor, with LOD of $1.25x10^{-2}$ and $2.5x10^{-2}$ mg L^{-1}, respectively. Therefore, disposable, rapid, simple, and low-cost biosensing instrumentation for CRP has not yet been reported.

Regarding biosensing systems with nanomaterials for the determination of CRP, a few examples can be found in literature. For example, Buch and Rishpon (2008) developed an electrochemical immunosensor based on MWCNT-modified screen printed electrodes, and more recently, Ibupoto *et al.* (2012) proposed a potentiometric sensor with ZnO nanotubes, with LOD of $5x10^{-4}$, and 10^{-3} mg L^{-1}, respectively. In Section 5.2, the analytical performance of NTFET developed in this thesis for the determination of CRP will be compared to other biosensors.

References

Arnold M.S., Green A.A., Hulvat J.F., Stupp S.I., Hersam M.C., 2006. Sorting carbon nanotubes by electronic structure using density differentiation. *Nat. Nanotechnol.* 1, 60-65.

Balasubramanian K., Sordan R., Burghard M., Kern K., 2004. A selective electrochemical approach to carbon nanotube field-effect transistors. *Nano Lett.* 4, 827-830.

Balasubramanian K., 2012. Label-free indicator-free nucleic acid biosensors using carbon nanotubes. *Eng. Life Sci.* 12, 121-130.

Bandaru P.R., 2007. Electrical properties and applications of carbon nanotube structures. *J. Nanosci. Nanotechnol.* 7, 1-19.

Bandyopadhyaya R., Nativ-Roth E., Regev O., Yerushalmi-Rozen R., 2002. Stabilization of individual carbon nanotubes in aqueous solutions. *Nano Lett.* 2, 25-28.

Banerjee S., Hemraj-Benny T., Wong S.S., 2005. Covalent surface chemistry of single-walled carbon nanotubes. *Adv. Mater.* 17, 17-29.

Battie Y., Jamon D., Lauret J.-S., En Naciri A., Broch L., Loiseau A., 2012. Optical anisotropy of single walled carbon nanotubes investigated by spectroscopic ellipsometry. *Carbon* 50, 4673-4679.

Besteman K., Lee J.O., Wiertz F.G.M., Heering H.A., Dekker C., 2003. Enzyme-coated carbon nanotubes as single-molecule biosensors. *Nano Lett.* 3, 727-730.

Bini A., Centi S., Tombelli S., Minunni M., Mascini M., 2008. Development of an optical RNA-based aptasensor for C-reactive protein. *Anal. Bioanal. Chem.* 390, 1077-1086.

Black S., Kushner I., Samols D., 2004. C-reactive protein. *J. Biol. Chem.* 279, 48487-48490.

Buch M., Rishpon J., 2008. An electrochemical immunosensor for C-reactive protein based on multi-walled carbon nanotube-modified electrodes. *Electroanalysis* 20, 2592-2594.

Bucova M., Bernadic M., Buckingham T., 2008. C-reactive protein, cytokines and inflammation in cardiovascular diseases. *Bratisl. Lek. Listy* 109, 333-340.

Burghard M., Klauk H., Kern K., 2009. Carbon-based field-effect transistors for nanoelectronics. *Adv. Mater.* 21, 2586-2600.

Byon H.R., Choi H.C., 2006. Network single-walled carbon nanotube-field effect transistors (SWNT-FETs) with increased Schottky contact area for highly sensitive biosensor applications. *J. Am. Chem. Soc.* 128, 2188-2189.

Calabró P., Golia E., Yeh E.T.H., 2009. CRP and the risk of atherosclerotic events. *Semin. Immunopathol.* 31, 79-94.

Carrarra S., 2010. Nano-bio-technology and sensing chips: new systems for detection in personalized therapies and cell biology. *Sensors* 10, 526-543.

Cash K.J., Clark H.A., 2010. Nanosensors and nanomaterials for monitoring glucose in diabetes. *Trends Mol. Med.* 16, 584-593.

Charlier J.-C., Blase X., Roche S., 2007. Electronic and transport properties of nanotubes. *Rev. Mod. Phys.* 79, 677-732.

Chen R.J., Bangsaruntip S., Drouvalakis K.A., Kam N.W.S., Shim M., Li Y., Kim W., Utz P.J., Dai H., 2003. Noncovalent functionalization of carbon nanotubes for highly specific electronic biosensors. *Proc. Nat. Acad. Sci.* 100, 4984-4989.

Chen R.J., Choi H.C., Bangsaruntip S., Yenilmez E., Tang X., Wang Q., Chang Y.-L., Dai H., 2004. An investigation of the mechanisms of electronic sensing of protein adsorption on carbon nanotube devices. *J. Am. Chem. Soc.* 126, 1563-1568.

Chen Z., Appenzeller J., Knoch J., Lin Y.M., Avouris P., 2005. The role of metal-nanotube contact in the performance of carbon nanotube field-effect transistors. *Nano Lett.* 5, 1497-1502.

Cid C.C., Riu J., Maroto A., Rius F.X., 2008a. Detection of human immunoglobulin G at physiological conditions with chemically functionalizated carbon nanotube field effect transistors. *Curr. Nanosci.* 4, 314-317.

Cid C.C., Riu J., Maroto A., Rius F.X., 2008b. Carbon nanotube field effect transistors for the fast and selective detection of human immunoglobulin G. *Analyst* 133, 1005-1008.

Clyne B., Olshaker J.S., 1999. The C-reactive protein. *J. Emerg. Med.* 17, 1019-1025.

Collins P.G., Avouris P., 2000. Nanotubes for electronics. *Sci. Am.* 2000, 62-69.

Collins P.G., Arnold M.S., Avouris P. 2001. Engineering carbon nanotubes and nanotube circuits using electrical breakdown. *Science* 292, 706-709.

Daniel S., Rao T.P., Rao K.S., Ran S.U., Naidu G.R.K., Lee H.-Y., Kawai T., 2007. A review of DNA functionalized/grafted carbon nanotubes and their characterization. *Sens. Actuat. B* 122, 672-682.

Derycke V., Martel R., Appenzeller J., Avouris P., 2002. Controlling doping and carrier injection in carbon nanotube transistors. *Appl. Phys. Lett.* 80, 2773-2775.

Dolatabadi J.E.N., Mashinchian O., Ayoubi B., Jamali A.A., Mobed A., Losic D., Omidi Y., Guardia M., 2011. Optical and electrochemical DNA Nanobiosensors. *Trends Anal. Chem.* 30, 459-472.

Dominici R., Luraschi P., Franzini C., 2004. Measurement of C-reactive protein: two high sensitivity methods compared. *J. Clin. Lab. Anal.* 18, 280-284.

Dresselhaus M.S., Eklund P.C., 2000. Phonons in carbon nanotubes. *Adv. Phys.* 49, 705-814.

Dresselhaus M.S., Dresselhaus G., Saito R., Jorio A., 2005. Raman spectroscopy of carbon nanotubes. *Phys. Rep.* 409, 47-99.

Fan X., White I.M., Shopova S.I., Zhu H., Suter J.D., Sun Y. 2008. Sensitive optical biosensors for unlabeled targets: a review. *Anal. Chim. Acta* 620, 8-26.

FDA, Food and Drug Administration, Guidance for industry - review criteria for assessment of C-reactive protein (CRP), high sensitivity C-reactive protein (hsCRP) and cardiac C-reactive protein (cCRP) assays, 2005. Available at: <http://www.fda.gov/downloads/MedicalDevices/DeviceRegulationandGuidance/GuidanceDocuments/UCM071017.pdf> [Last access: 17 August 2013].

Freiman S., Hooker S., Migler K., Sivaram A., Arepalli S., Measurement issues in single wall carbon nanotubes, National Institute of Standard and Technology, 2008. Available at: <http://www.nist.gov/customcf/get_pdf.cfm?pub_id=852726> [Last access: 17 August 2013].

Fu D., Li L.-J., 2010. Label-free electrical detection of DNA hybridization using carbon nanotubes and graphene. *Nano Rev.* 1, 5354 (1-9).

Fujii S., Tanaka T., Nishiyama S., Kataura H., 2009. High performance thin-film transistors using moderately aligned semiconducting single-wall carbon nanotubes. *Phys. Stat. Sol. B* 248, 2692-2696.

Geim A.K., Novoselov K.S., 2007. The rise of graphene. *Nat. Mater.* 6, 183-191.

Ghosh S., Rao C.N.R., 2009. Separation of metallic and semiconducting single-walled carbon nanotubes through fluorous chemistry. *Nano Res.* 2, 183-191.

Green A.A., Hersam M.C., 2008. Colored semitransparent conductive coatings consisting of monodisperse metallic single-walled carbon nanotubes. *Nano Lett.* 8, 1417-1422.

Gui E.L., Li L.-J., Zhang K., Xu Y., Dong X., Ho X., Lee P.S., Kasim J., Shen Z.X., Rogers J.A., Mhaisalkar S.G. 2007. DNA sensing by field-effect transistors based on networks of carbon nanotubes. *J. Am. Chem. Soc.* 129, 14427-14432.

Guo Z., Du F., Ren D., Chen Y., Zheng J., Liu Z., Tian J., 2006. Covalently porphyrin-functionalized single-walled carbon nanotubes: a novel photoactive and optical limiting donor–acceptor nanohybrid. *J. Mater. Chem.* 16, 3021-3030.

Haddon R.C., Sippel J., Rinzler A.G., Papadimitrakopoulos F., 2004. Purification and separation of carbon nanotubes. *MRS Bull.* 29, 252-259.

Harris P.J.F., Carbon nanotube science - synthesis, properties and applications. Cambridge University Press, Cambridge, 2009.

Heller I., Janssens A.M., Männik J., Minot E.D., Lemay S.G., Dekker C., 2008. Identifying the mechanism of biosensing with carbon nanotube transistors. *Nano Lett.* 8, 591-595.

Hu P.A., Zhang J. Li L., Wang Z., O'Neill W., Estrela P., 2010. Carbon nanostructure-based field-effect transistors for label-free chemical/biological sensors. *Sensors* 10, 5133-5159.

Ibupoto Z.H., Jamal N., Khun K., Willander M, 2012. Development of a disposable potentiometric antibody immobilized ZnO nanotubes based sensor for the detection of C-reactive protein. *Sens. Actuators B* 166, 809-814.

ICSH - International Committee for Standardization in Haematology, 1988. Guidelines on selection of laboratory tests for monitoring the acute phase response. *J. Clin. Pathol.* 41, 1203-1212.

Iijima S., 1991. Helical microtubes of graphitic carbon. *Nature* 354, 56-58.

Ishikawa F.N., Curreli M., Olson C.A., Liao H.-I., Sun R., Roberts R.W., Cote R.J., Thompson M.E., Zhou C., 2010. Importance of controlling nanotube density for highly

sensitive and reliable biosensors functional in physiological conditions. *ACS Nano* 4, 6914-6922.

Islam M.F., Rojas E., Bergey D.M., Johnson A.T., Yodh A.G., 2003. High weight fraction surfactant solubilization of single-wall carbon nanotubes in water. *Nano Lett.* 3, 269-273.

Itkis M.E., Perea D.E., Jung R., Niyogi S., Haddon R.C., 2005. Comparison of analytical techniques for purity evaluation of single-walled carbon nanotubes. *J. Am. Chem. Soc.* 127, 3439-3448.

Izard N., Kazaoui S., Hata K., Okazaki T., Saito T., Iijima S., Minami N., 2008. Semiconductor-enriched single wall carbon nanotube networks applied to field effect transistors. *Appl. Phys. Lett.* 92, 243112 (1-3).

Javey A., Guo J., Wang Q., Lundstrom M., Dai H., 2003. Ballistic carbon nanotube field-effect transistors. *Nature* 424, 654-657.

Jiang L.-C., Zhang W.-D., 2010. A highly sensitive nonenzymatic glucose sensor based on CuO nanoparticles-modified carbon nanotube electrode. *Bios. Bioelectron.* 25, 1402-1407.

Justino C.I.L., Rocha-Santos T.A., Duarte A.C., 2010. Review of analytical figures of merit of sensors and biosensors in clinical applications. *Trends Anal. Chem.* 10, 1172-1183.

Justino C.I.L., Rocha-Santos T.A.P., Duarte A.C., 2013a. Advances in point-of-care technologies with biosensors based on carbon nanotubes. *Trends Anal. Chem.* 45, 24-36.

Justino C.I.L., Rocha-Santos T.A.P., Cardoso S., Duarte A.C., 2013b. Strategies for enhancing the analytical performance of nanomaterial-based sensors. *Trends Anal. Chem.* 47, 27-36.

Katsnelson M.I., 2007. Graphene: the carbon in two dimensions. *Mater. Today* 10, 20-27.

Katz E., Willner I., 2004. Biomolecule-functionalized carbon nanotubes: applications in nanobioelectronics. *Chem. Phys. Chem.* 5, 1084-1104.

Kauffman D.R., Star A., 2008. Electronically monitoring biological interactions with carbon nanotube field-effect transistors. *Chem. Soc. Rev.* 37, 1197-1206.

Kazaoui S., Minami N., Jacquemin R., 1999. Amphoteric doping of single-wall carbon-nanotube thin films as probed by optical absorption spectroscopy. *Phys. Rev. B* 60, 13339-13432.

Killard A.J., Deasy B., O'Kennedy R., Smyth M.R., 1995. Antibodies: production, functions and applications in biosensors. *Trends Anal. Chem.* 14, 257-266.

Kim O.-K., Je J., Baldwin J. W., Kooi S., Pehrsson P.E., Buckley L.J., 2003. Solubilization of single-wall carbon nanotubes by supramolecular encapsulation of helical amylose. *J. Am. Chem. Soc.* 125, 4426-4427.

Kim S.K., Cho H., Park H.-J., Kwon D., Lee J.M., Chung B.H., 2009. Nanogap biosensors for electrical and label-free detection of biomolecular interactions. *Nanotechnol.* 20, 455502 (1-7).

Komatsu N., Wang F. 2010. A comprehensive review on separation methods and techniques for single-walled carbon nanotubes. *Materials* 3, 3818-3844.

Kranz C., Eaton D.C., Mizaikoff B., 2011. Analytical challenges in nanomedicine. *Anal. Bioanal. Chem.* 399, 2309-2311.

Krupke R., Hennrich F., Löhneysen H., Kappes M.M., 2003. Separation of metallic from semiconducting single-walled carbon nanotubes. *Science* 301, 344-347.

Krupke R., Hennrich F., 2005. Separation techniques for carbon nanotubes. *Adv. Eng. Mater.* 7, 111-116.

Landi B.J., Ruf H.J., Evans C.M., Cress C.D., Raffaelle R.P., 2005. Purity assessment of single-wall carbon nanotubes, using optical absorption spectroscopy. *J. Phys. Chem. B* 109, 9952-9965.

Lee M. Baik K.Y., Noah M., Kwon Y.-K., Lee J.-O., Hong S., 2009. Nanowire and nanotube transistors for lab-on-a-chip applications. *Lab Chip* 9, 2267-2280.

Lei J., Ju H. 2010. Nanotubes in biosensing. *WIREs Nanomed. Nanobiotechnol.* 2, 496-509.

Li H., Li Q., Selective separation of single-walled carbon nanotubes in solution, In: Marulanda J.M (Ed.) Electronic properties of carbon nanotubes, InTech, 2011. Available at: <http://www.intechopen.com/books/electronic-properties-of-carbon-nanotubes/selective-separation-of-single-walled-carbon-nanotubes-in-solution> [Last access: 17 August 2013].

Li X., Zhu Q., Tong S., Wang W., Song W., 2009. Self-assembled microstructure of carbon nanotubes for enzymeless glucose sensor. *Sens. Actuat. B* 136, 444-450.

Liang X**.**L**.**, Wang S**.**, Duan X**.**J**.**, Zhang Z**.**Y**.**, Chen Q**.**, Zhang J**.**, Peng L.M., 2007. A comparative study on SWCNT and DWCNT field-effect transistors. *J. Nanosci. Nanotechnol.* 7, 1568-1572.

Lin J., Ju H., 2005. Electrochemical and chemiluminescent immunosensors for tumor markers. *Bios. Bioelectron.* 20, 1461-1470.

Liu Z., Tabakman S.M., Chen Z., Dai H., 2009. Preparation of carbon nanotube bioconjugates for biomedical applications. *Nat. Prot.* 4, 1372-1382.

Liu S., Shen Q., Cao Y., Gan L., Wang Z., Steigerwald M. L., Guo X., 2010. Chemical functionalization of single-walled carbon nanotube field-effect transistors as switches and sensors. *Coord. Chem. Rev.* 254, 1101-1116.

Liu H., Nishide D., Tanaka T., Kataura H., 2011. Large-scale single-chirality separation of single-wall carbon nanotubes by simple gel chromatography. *Nature Commun.* 2, 309 (1-8).

Long D.A., The Raman effect. A unified treatment of the theory of Raman scattering by molecules. John Wiley and Sons Ltd, England, 2002.

Macy E.M., Hayes T.E., Tracy R.P., 1997. Variability in the measurement of C-reactive protein in healthy subjects: implications for reference intervals and epidemiological applications. *Clin. Chem.* 43, 52-58.

Martel R., Schmidt T., Shea H., Hertel T., Avouris P., 1998. Single- and multi-wall carbon nanotube field-effect transistors. *Appl. Phys. Lett.* 73, 2447-2449.

Martel R., Derycke V., Lavoie C., Appenzeller J., Chan K.K., Tersoff J., Avouris P., 2001. Ambipolar electrical transport in semiconducting single-wall carbon nanotubes. *Phys. Rev. Lett.* 87, 256805 (1-4).

McEuen P.L., 2000. Single-wall carbon nanotubes. *Phys. World* 2000, 31-36.

Melechko A.V., Merkulov V.I., McKnight T.E., Guillorn M.A., Klein K.L., Lowndes D.H., Simpson M.L., 2005. Vertically aligned carbon nanofibers and related structures: controlled synthesis and directed assembly. *J. Appl. Phys.* 97, 041301 (1-39).

Meyer M.H.F., Hartmann M., Krause H.J., Blankenstein G., Mueller-Chorus B., Oster J., Miethe P., Keusgen M., 2007. CRP determination based on a novel magnetic biosensor. *Bios. Bioelectron.* 22, 973-979.

Minot E.D., Janssens A.M., Heller I., Heering H.A., Dekker C., Lemay S.G., 2007. Carbon nanotubes biosensors: the critical role of reference electrode. *Appl. Phys. Lett.* 91, 093507 (1-3).

Mitaka C., 2005. Clinical laboratory differentiation of infectious versus non-infectious systemic inflammatory response syndrome. *Clin. Chim. Acta* 351, 17-29.

Moina C., Ybarra G., 2012. Fundamentals and applications of immunosensors. In: Chiu N.H.L. (Ed.) Advances in immunoassay technology, InTech. Available at: <http://www.intechopen.com/books/advances-in-immunoassay-technology/fundamentals-and-applications-of-immunosensors> [Last access: 17 August 2013]

Moore V.C., Strano M.S., Haroz E.H., Hauge R.H., Smalley R.E., 2003. Individually suspended single-walled carbon nanotubes in various surfactants. *Nano Lett.* 3, 1379-1382.

Nakashima N., Tomonari Y., Murakami H., 2002. Water-soluble single-walled carbon nanotubes via noncovalent sidewall-functionalization with a pyrene-carrying ammonium ion. *Chem. Lett.* 2002, 638-639.

Narasimhamurthy K.C., Paily R., 2011. Fabrication of carbon nanotube field effect transistor. *IETE Tech. Rev.* 28, 57-69.

Nichols M., Townsend N., Scarborough P., Rayner M., Leal J., Luengo-Fernandez R., Gray A European cardiovascular disease statistics. European Heart Network, Brussels, 2012.

NPPCCD - National Programme for Prevention and Control of the Cardiovascular Diseases, Ministry of Health, Lisbon, 2006.

Packard R.R., Libby P., 2008. Inflammation in atherosclerosis: from vascular biology to biomarker discovery and risk prediction. *Clin. Chem.* 54, 24-38.

Patel V., 2011. Global carbon nanotubes market outlook: industry beckons. *Nanotech. Insights* 2, 31-35.

Pichler T., Knupfer M., Golden M.S., Fink J., Rinzler A., Smalley R.E., 1998. Localized and delocalized electronic states in single-wall carbon nanotubes. *Phys. Rev. Lett.* 80, 4729-4732.

Popov V.N., 2004. Carbon nanotubes: properties and application. *Mater. Sci. Eng. R* 43, 61-102.

PNHP - Portuguese National Health Plan 2012-2016, Ministry of Health, Lisbon, 2012.

Quershi A., Gurbuz, Y., Krag W.P., Davidson J.L., 2009. A novel interdigitated capacitor based biosensor for detection of cardiovascular risk marker. *Bios. Bioelectron.* 25, 877-882.

Resasco D.E., Alvarez W.E., Pompeo F., Balzano L., Herrera J.E., Kitiyanan B., Borgna A., 2002. A scalable process for production of single-walled carbon nanotubes (SWNTs) by catalytic disproportionation of CO on a solid catalyst. *J. Nanopart. Res.* 4, 131-136.

Rifai N., Ridker P.M., 2001. High-sensitivity C-reactive protein: a novel and promising marker of coronary heart disease. *Clin. Chem.* 47, 403-411.

Roger V.L., Go A.S., Lloyd-Jones D.M., Benjamin E.J., Berry J.D., Borden W.B., Bravata D.M., Dai S., Ford E.S., Fox C.S., Fullerton H.J., Gillespie C., Hailpern S.M., Heit J.A., Howard V.J., Kissela B.M., Kittner S.J., Lackland D.T., Lichtman J.H., Lisabeth L.D., Makuc D.M., Marcus G.M., Marelli A., Matchar D.B., Moy C.S., Mozaffarian D., Mussolino M.E., Nichol G., Paynter N.P., Soliman E.Z., Sorlie P.D., Sotoodehnia N., Turan T.N., Virani S.S., Wong N.D., Woo D., Turner M.B., 2012. Heart disease and

stroke statistics - 2012 update. A report from the American Heart Association. *Circulation* 125, 2-220.

Roman C., Helbling T., Hierold C., Single-walled carbon nanotube sensor concepts. In: Bushan B. (Ed.) Springer Handbook of Nanotechnology Part B, Springer, 2010.

Ryabenko A.G., Dorofeeva T.V., Zvereva G.I., 2004. UV–VIS–NIR spectroscopy study of sensitivity of single-wall carbon nanotubes to chemical processing and van-der-Waals SWNT/SWNT interaction. Verification of the SWNT content measurements by absorption spectroscopy. *Carbon* 42, 1523-1535.

Saito R., Fujita M., Dresselhaus G., Dresselhaus M.S., 1992. Electronic structure of chiral graphene tubules. *Appl. Phys. Lett.* 60, 2204-2206.

Sánchez-Acevedo Z.C., Riu J., Rius F.X., 2009. Fast picomolar selective detection of bisphenol A in water using a carbon nanotube field effect transistor functionalized with estrogen receptor-α. *Bios. Bioelectron.* 24, 2842-2846.

Sato H., 2003. Vertically aligned carbon nanotubes grown by plasma enhanced chemical vapor deposition. *J. Vac. Sci. Technol. B Microelectron. Nanometer Struct.* 21, 2564-2568.

Shim H.C., Song J.-W., Kwak Y.K., Kim S., Han C.-S., 2009. Preferential elimination of metallic single-walled carbon nanotubes using microwave irradiation. *Nanotechnol.* 20, 065707 (1-5).

Silva D., Lacerda A.P., 2012. High-sensitivity C-reactive protein as a biomarker of risk in coronary artery disease. *Rev. Port. Cardiol.* 31, 733-745.

Sohn Y.-S., Kim Y.T., 2008. Field-effect-transistor type C-reactive protein sensor using cysteine-tagged protein G. *Electron. Lett.* 44, 955-956.

Star A., Gabriel J., Bradley K., Grüner G., 2003. Electronic detection of specific protein binding using nanotube FET devices. *Nano Lett.* 3, 459-463.

Star A., Han T.-R., Joshi V., Stetter J.R., 2004. Sensing with nafion coated carbon nanotube field-effect transistors. *Electroanalysis* 16, 108-112.

Star A., Tu E., Niemann J., Gabriel J.C.P., Joiner C.S., Valcke C., 2006. Label-free detection of DNA hybridization using carbon nanotube network field-effect transistors. *Proc. Nat. Acad. Sci.* 103, 921-926.

Stetter J.L., Maclay G.J., Carbon nanotubes and sensors: a review. In: Baltes H., Brand O., Fedder G.K., Hierold C., Korvink J., Tabata O. (Eds.) Advanced micro and nanosystems, Wiley-VCH, 2004.

Strano M.S., Doorn S.K., Haroz E.H., Kittrell C., Hauge R.H., Smalley R.E., 2003. Assignment of (n,m) Raman and optical features of metallic single-walled carbon nanotubes. *Nano Lett.* 3, 1091-1096.

Tanaka T., Jin H., Miyata Y., Kataura H., 2008. High-yield separation of metallic and semiconducting Single-Wall Carbon Nanotubes by Agarose Gel Electrophoresis – *Appl. Phys. Express* 1, 114001 (1-3).

Tanaka T., Jin H., Miyata Y., Fujii S., Suga H., Naitoh Y., Minari T., Miyadera T., Tsukagoshi K., Kataura H., 2009. Simple and scalable gel-based separation of metallic and semiconducting carbon nanotubes. *Nano Lett.* 9, 1497-1500.

Tans S.J., Verschueren A.R.M, Dekker C. 1998. Room-temperature transistor based on a single carbon nanotube. *Nature* 393, 49-52.

Thomsen C., Reich S., Raman scattering in carbon nanotubes. In: Cardona M., Merlin R. (Eds.) Light Scattering in Solid IX. Topics Applied Physics 108, Springer, 2007.

Thompson D., Pepys M.B., Wood S P., 1999. The physiological structure of human C-reactive protein and its complex with phosphocholine. *Structure* 7, 169-177.

Tillet W.S., Francis T., 1930. Serological reactions in pneumonia with a nonprotein somatic fraction of pneumococcus. *J. Exp. Med.* 52, 561-571.

Tulamo R., Frösen J., Junnikkala S., Paetau A., Kangasniemi M., Peáez J., Hernesniemi J., Niemela M., Meri S., 2010. Complement system becomes activated by the classical pathway in intracranial aneurysm walls. *Lab. Investig.* 90, 168-179.

Vasan R.S., 2006. Biomarkers of cardiovascular disease: molecular basis and practical considerations. *Circulation* 113, 2335-2362.

Vashist S.K., Zheng D., Al-Rubeaan K., Luong J.H.T., Sheu F.-S., 2011. Advances in carbon nanotube based electrochemical sensors for bioanalytical applications. *Biotechnol. Adv.* 29, 169-188.

Veetil J.V., Ye K., 2007. Development of immunosensors using carbon nanotubes. *Biotechnol. Progress* 23, 517-531.

Villamizar R.A., Maroto A., Rius F.X., Inza I., Figueras M.J., 2008. Fast detection of Salmonella infantis with carbon nanotube field effect transistors. *Bios. Bioelectron.* 24, 279-283.

Villamizar R.A., Maroto A., Rius F.X., 2011. Rapid detection of Aspergillus flavus in rice using biofunctionalized carbon nanotube field effect transistors. *Anal. Bional. Chem.* 399, 119-126.

Vo-Dinh T., Cullum B., 2000. Biosensors and biochips: advances in biological and medical diagnostics. *Fres. J. Anal. Chem.* 366, 540-551.

Wang J., 2005. Carbon-nanotube based electrochemical biosensors: a review. *Electroanalysis* 17, 7-14.

Weisman R.B., 2010. Fluorimetric characterization of single-walled carbon nanotubes. *Anal. Bioanal. Chem.* 396, 1015-1023.

Yanagi K., Iitsuka T., Fujii S., Kataura H., 2008. Separations of metallic and semiconducting carbon nanotubes by using sucrose as a gradient medium. *J. Phys. Chem. C* 112, 18889-18894.

Yang C.-M., An K.H., Park J.S., Park K.A., Lim S.C., Cho S.-H., Lee Y.-S., Park W., Park C.Y., Lee Y.H., 2006. Preferential etching of metallic single-walled carbon nanotubes with small diameter by fluorine gas. *Phys. Rev. B* 73, 075419 (1-7).

Yang Y.-N., Lin H.-I., Wang J.-H., Shiesh S.-C., Lee G.-B., 2009. An integrated microfluidic system for C-reactive protein measurement. *Bios. Bioelectron.* 24, 3091-3096.

Yu M.F., Files B.S., Arepalli S., Ruoff R.S., 2000. Tensile loading of ropes of single wall carbon nanotubes and their mechanical properties. *Phys. Rev. Lett.* 84, 5552-5555.

Zhao Y.-L., Stoddart J.F., 2009. Noncovalent functionalization of single-walled carbon nanotubes. *Acc. Chem. Res.* 42, 1161-1171.

Chapter 3

Dispersion of Single-Walled Carbon Nanotubes (SWCNT): screening of the most important variables and characterization

3.1. Introduction

The dispersion of carbon nanotubes (CNT) results from the unbalancing between the van der Waals forces responsible for the aggregation and bundling of synthesised CNT, which is enhanced by the mechanical energy provided by the sonication. The sonication of CNT is affected by dispersant properties and concentration, characteristics of ultrasonic bath, such as the water volume, the ultrasonic frequency, time and temperature of sonication. The geometry and position of the vessel in ultrasonic baths are also other factors which interfere in the performance of sonication, as reviewed by Hilding *et al.* (2003).

Concerning the dispersants, the surfactants are the most used through non-covalent functionalization, preserving the sp^2 structure of SWCNT and minimizing defects along with their electronic properties. The surfactants are amphiphilic molecules, that is, they have both polar and apolar groups, which constitute the hydrophilic (polar head group) and the hydrophobic (tail with hydrocarbon chains) regions, respectively. Thus, hydrophobic groups face toward the CNT surface while the hydrophilic groups face toward the aqueous phase. The surfactants are classified according to the charge of their head groups, being non-ionic, anionic and cationic. For example, the Triton X-100 ($C_{14}H_{22}O(C_2H_4O)_n)_{(n\ =\ 9\text{-}10)}$ is non-ionic, the sodium cholate ($C_{24}H_{39}NaO_5$), the sodium dodecyl sulphate ($NaC_{12}H_{25}SO_4$), and the sodium benzoate ($NaC_6H_5CO_2$) are anionic, and the cetyltrimethylammonium bromide ($C_{19}H_{42}BrN$) is cationic. It has been proposed that the surfactants with benzene rings and naphthenic groups are responsible for the high dispersing ability of CNT through the π-π stacking interactions of the benzene ring onto the CNT surface (Vaisman *et al.*, 2006). In this thesis, two surfactants (sodium cholate and sodium dodecyl sulphate), a polymer (sodium alginate) and an organic solvent (dimethylformamide) were compared in respect to their efficiency in dispersing SWCNT.

3.2. Experimental methods

3.2.1. Dispersion of SWCNT on dimethylformamide (DMF) and sodium cholate (SC) and spectroscopic characterization

The comparison of the effectiveness on dispersion of SWCNT by a polar aprotic solvent (dimethylformamide, DMF, C_3H_7NO, Sigma-Aldrich) and an anionic surfactant

(sodium cholate, SC, Sigma-Aldrich) is reported in this section. The SC is the dispersant recommended by Sigma-Aldrich for the dispersion of commercial SWCNT and, as shown in Figure 3.1a, it has a naphthenic structure constituted by three C_6 rings and one C_5 ring contributing to the dispersing efficiency. In the case of DMF, which molecular structure is shown in Figure 3.1b, it is characterized by a high value for electron pair donation (which describes the ability of the solvent to donate a pair of non-bonding electrons to another molecule in order to form a coordinate bond) and with a negligible value for hydrogen bond donation parameter of Taft and Kamlet (which describes the ability of a solvent to accept an electron pair), enabling the good dispersion of CNT, as reported by Ausman *et al.* (2000), and it does not have aromatic rings.

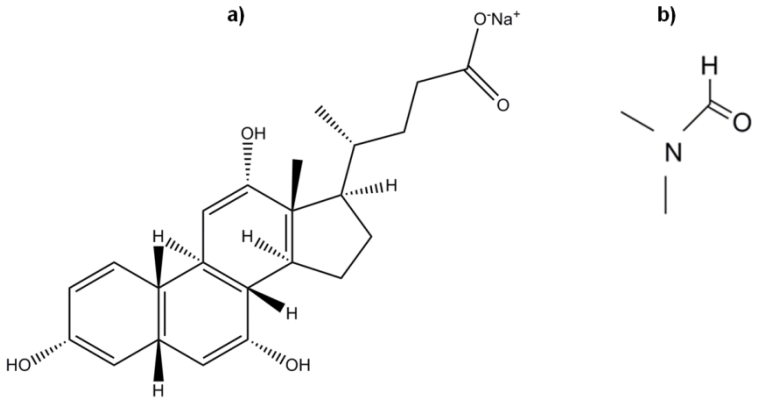

Figure 3.1 Molecular structures of a) sodium cholate (SC) and b) dimethylformamide (DMF).

The SWCNT (#704113, Sigma-Aldrich, Portugal) used in the experiments were synthesised through cobalt-molybdenum catalysis (CoMoCAT, Southwest Nanotechnologies). For their dispersion as a non-covalent functionalization, SWCNT samples were prepared through dispersion of 4 mg of SWCNT in 14 mL of aqueous solution of SC (0.2 % w/v) according to published protocol (AL-265 Technical Information Bulletin, Sigma-Aldrich), or through dispersion of 3 mg of SWCNT in 20 mL of DMF, according to the procedures followed by Xiao *et al.* (2010). The SWCNT samples were maintained in a water bath ultrasonicator (Ultrasonik 57H Ney, 400W, 50/60 Hz) for periods of 40, 60, and 100 minutes, in order to compare the influence of sonication time for obtaining stable and uniform SWCNT dispersions. All experiments in the water bath ultrasonicator were made in round-bottom flasks, and in each sonication step, only one flask was used at the centre of the ultrasonic bath, in order to provide the same sonication characteristics for each sample. Besides the sonication, the effects of different centrifugation programs were also assessed. The centrifugation of SWCNT samples was

performed at a relative centrifugal force (RCF) of 2000 × g, and 10000 × g during 5 minutes at 20 ºC with a centrifuge Medifriger BL-S (JP Selecta, Spain) in order to remove graphite, residual catalyst, and amorphous carbon, and approximately 70 % fraction of supernatant was collected for subsequent analysis. It is important to note that the centrifugation speed can be expressed in RCF or rotations *per* minute (RPM). In this thesis, RCF was employed as the correct rotational unit, since RPM unit is dependent of the rotational radius of the centrifuge, and thus RPM conditions are not the same with different centrifuges, while RCF, referred as g-force, is acceleration constant, and it can be exchanged between centrifuges for obtaining equivalent results. RPM and RCF are convertible using the following equation (Frei, 2011):

$$\mathrm{RCF} = \left[11.2 \times \text{centrifuge radius (in cm)} \times \left(\frac{\mathrm{RPM}}{1000}\right)^2\right] \qquad [3.1]$$

As SWCNT strongly absorb from the UV to the NIR regions, the SWCNT dispersions in DMF and SC were analyzed by UV-Vis spectroscopy in order to obtain adequate information about the SWCNT purity and structure through the evaluation of the singular interband electronic transitions of SWCNT, as studied by Itkis *et al.* (2005), and Jeong *et al.* (2008). In order to provide such typical spectroscopic signature of SWCNT, UV-Vis optical absorption spectra (200 - 800 nm) were recorded in a spectrophotometer (GBC/Cintra10e) using a quartz optical cell with a path length of 10 mm. The spectrophotometer comprised a light source with a wavelength range between 190 and 1000 nm, providing an accuracy of 0.08 nm in the UV-Vis region, and 0.3 nm in the IR region, a monochromator for precise wavelength selection due to the diffraction grating incorporated, and a detector (silicon photodiode and photomultiplier tube). The UV-Vis instrument is a double beam UV-Vis spectrometer, and it is equipped with two optical sources: the tungsten iodine lamp (for wavelengths higher than 300 nm), and the deuterium lamp for wavelengths below 300 nm.

In this thesis, Raman spectra (90 - 1900 cm^{-1}) were also obtained for the SWCNT sample dispersed in SC, with a Bruker RFS/100S Raman-FT spectrophotometer. The spectrophotometer has a Nd:YAG (from neodymium-doped yttrium aluminium garnet, $Nd:Y_3Al_5O_{12}$) laser of 1064 nm (in IR region), and the spectra were obtained at 100 mW power, with a spectral resolution of 4 cm^{-1}, and 1500 scans.

3.2.2. Experimental design for screening the dispersion conditions of SWCNT in sodium cholate (SC)

An experimental design based on a 2^3 factorial design with 2 replicates, and involving 16 experimental runs, was applied to identify the factors which may affect the dispersion of SWCNT as well as to evaluate the effects of various factors, and to understand the interactions between the factors on the main steps of preparation of SWCNT dispersion, that is, sonication and centrifugation. The main effects and interactions of 3 quantitative variables (sonication time – factor A, centrifugation time – factor B, and RCF – factor C) on the dispersion of SWCNT were assessed by UV-Vis spectroscopy at 500 nm, which is the wavelength frequently selected to quantify different SWCNT dispersions, for example in the works of Bahr *et al.* (2001), Kim *et al.* (2003), and Sinani *et al.* (2005). The SWCNT samples were dispersed in aqueous solutions of surfactant by adding 4 mg of SWCNT to 14 mL of a sodium cholate (SC) aqueous solution (0.2% w/v). Such samples were sonicated for 60 and 100 minutes, and centrifuged during 5 and 10 minutes at 2000 × g and 10000 × g, which correspond to the low and high levels for each factor, respectively.

3.2.3. Comparison of the dispersion of SWCNT in sodium cholate (SC), sodium dodecyl sulphate (SDS), and sodium alginate (SA)

Dispersion assays with another surfactant than SC, that is the sodium dodecyl sulphate (SDS), and a polymer, that is, the sodium alginate (SA) were also performed to compare the dispersing efficiency of SWCNT in SDS and SA with that obtained in SC. The SDS is an anionic surfactant since it has a sulphate ion in its head group, as shown in Figure 3.2a, and the SA, which monomer is shown in Figure 3.2b, is a water-soluble polymer which becomes negatively charged in aqueous solution. Both the SDS and the SA were prepared in the same way as the SC, that is, at 0.2 % in distilled water.

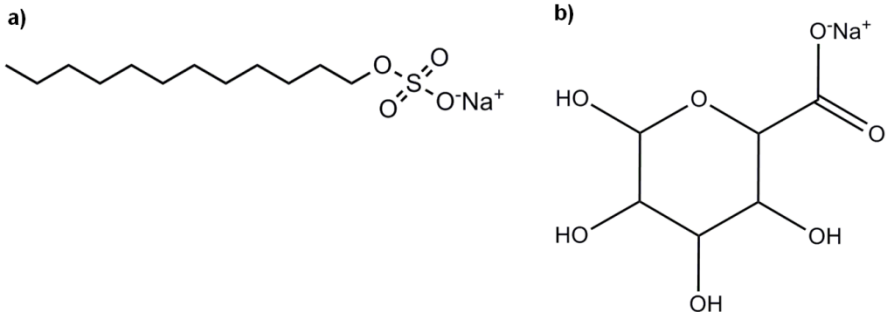

Figure 3.2 Molecular structures of a) sodium dodecyl sulphate (SDS) and b) sodium alginate (SA).

3.2.4. Effect of the concentration of the SWCNT in their optical properties

According to O'Connell *et al.* (2002), the UV-Vis spectroscopy is sensitive to SWCNT bundles, to effects of charge transfer, and to the SWCNT concentration. Thus, the effect of the concentration on the optical properties of SWCNT was assessed by measuring the absorbance at 500 nm of six samples of different concentrations of SWCNT diluted in SC. Aliquots of a SWCNT solution at a concentration of 0.28 g L^{-1} were pippeted out, and diluted with fresh SC (0.2%, w/v) to reach concentrations of 0.25, 0.20, 0.15, 0.10, 0.05, and 0.01 g L^{-1} in SWCNT. Such dilutions were used to prepare a calibration curve by measuring the absorbance values at 500 nm against the different SWCNT concentrations, as well as to verify the influence of SWCNT concentration on the efficiency of dispersion process. The values of the absorbance at x = 0 g L^{-1} and x = 0.28 g L^{-1} in the calibration plot correspond to the absorbance values for the solution without SWCNT (only with SC), and for the SWCNT solution used to prepare dilutions, respectively.

3.3 Results and discussion

3.3.1. Dispersion of SWCNT on DMF and SC and spectroscopic characterization

Figure 3.3 shows sets of SWCNT samples prepared in DMF and SC, after sonication and centrifugation. After sonication and centrifugation, the homogeneous gray suspensions of SWCNT in SC stayed under the form of stable colloidal solutions. It is known that when SWCNT are exfoliated, they are maintained dispersed and do not settle, and when they are bundled, they phase separate with the other impurities such as graphite, amorphous carbon, and catalysts, as verified by Bandyopadhyaya *et al.* (2002). In the experiments of this thesis, even after two months, the suspension was still stable without occurring coagulation and precipitation of particles at the bottom of the flasks. As also shown in Figure 3.3, when dispersed in DMF, the SWCNT settled down after centrifugation, with a resulting quasi-transparent supernatant with very few suspended particles and a precipitate.

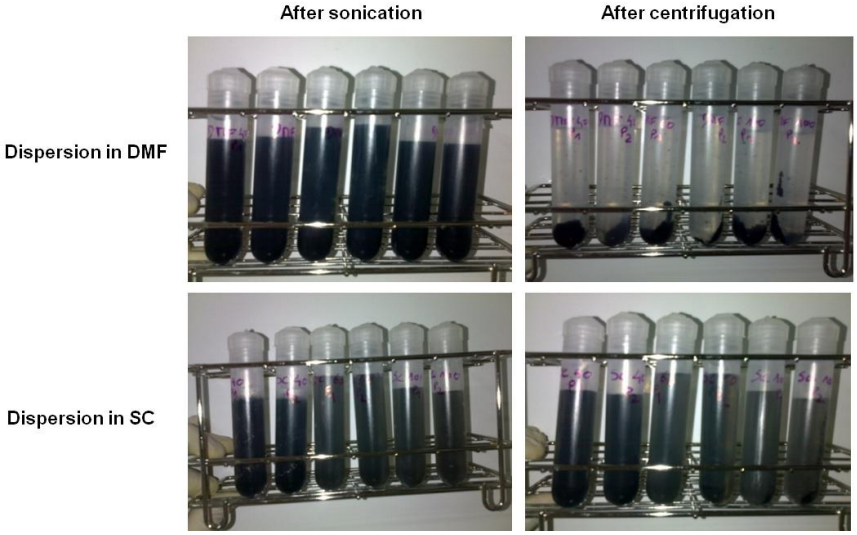

Figure 3.3 Dispersions of SWCNT in DMF and SC, after sonication and centrifugation.

Figure 3.4a and Figure 3.4c display the absorbance spectra of the prepared SWCNT samples in SC and in DMF, respectively, in order to characterize dispersed SWCNT in terms of their interband electronic transitions. As shown in Figure 3.4a, the absorbance spectrum of SC is transparent in the entire range of wavelength from 250 nm to 800 nm, thus allowing the observation of the characteristic electronic transitions of the SWCNT, and ensuring that all spectroscopic features observed in the spectra of dispersed SWCNT in SC are due only to the addition of SWCNT. At lower wavelength, in the UV region ($\lambda < 400$ nm), broad absorptions are due to plasmon resonances in the free electron cloud of the CNT π-electrons; the π-plasmon is associated with collective excitation of π-electrons, at around 155 - 310 nm, and it has no practical significance in the interpretation of SWCNT absorption spectra, as firstly discussed by Kataura *et al.* (1999). Also shown in Figure 3.4a, the most pronounced peaks are observed at 455, 510, 570, and 655 nm. As shown in Figure 3.4c, DMF is not suitable for dispersing SWCNT, as also verified by Maeda *et al.* (2006) since there are no discriminative features between the spectra of SWCNT dispersed in DMF, and the DMF spectrum. The DMF as dispersing agent has lead to ambiguous conclusions: some works attribute to DMF a high potential for dispersing SWCNT, as reported by Ausman *et al.* (2000), and Krupke (2003), while others claim that is unsuitable since it can damage the SWCNT through the modification of the π*-states of carbons in SWCNT structure, as reported by Monthioux *et al.* (2001), and Costa *et al.* (2008).

The variation of the mean values of absorbance obtained from the most pronounced peaks in a SWCNT sample dispersed in SC as a function to the sonication time and for the two RCF values is shown in Figure 3.4b, where the absorbance values are higher when the SWCNT samples are subjected to lower RCF for the same sonication time.

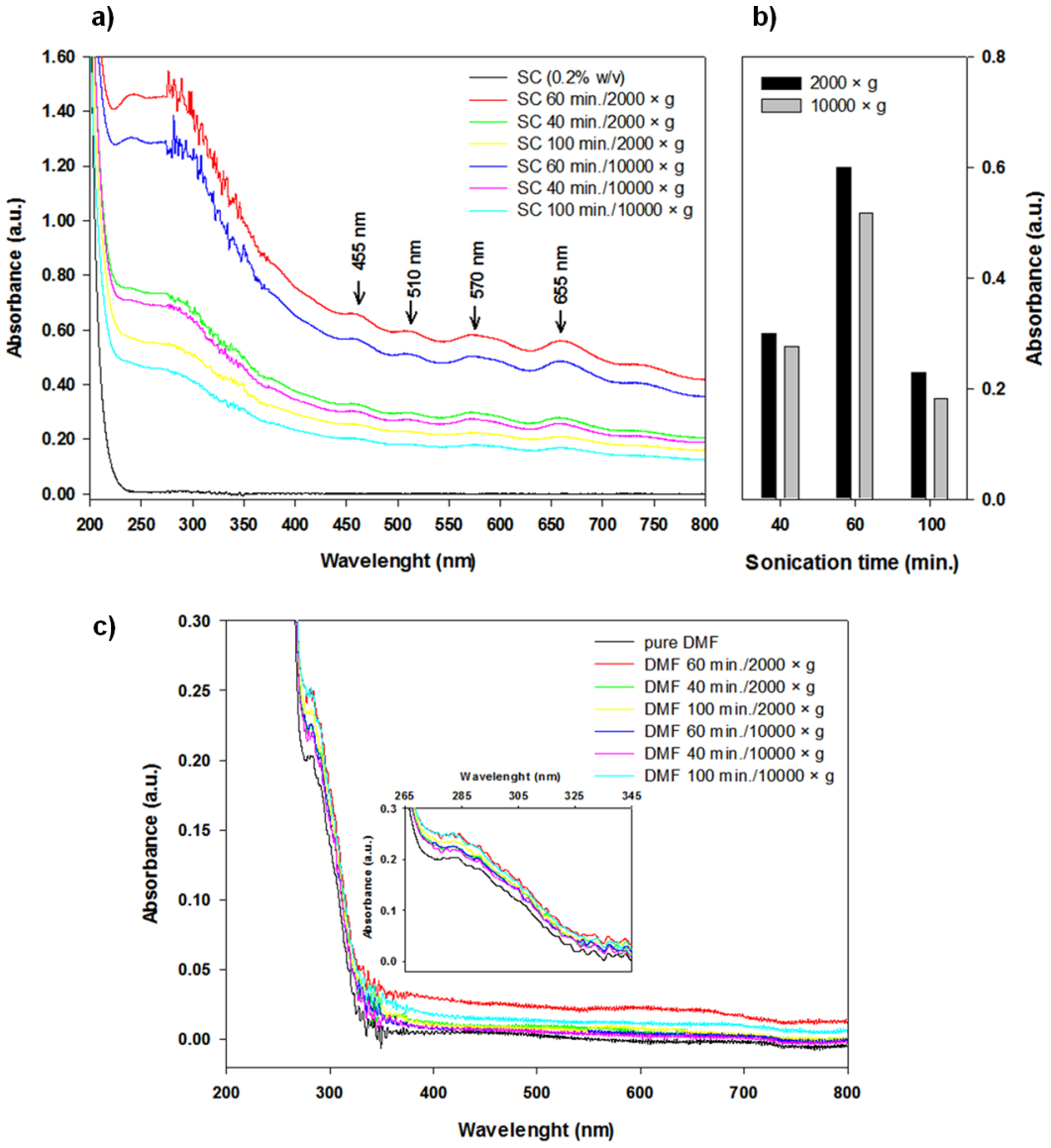

Figure 3.4 a) Absorbance spectra of dispersed SWCNT in SC, at different sonication times (40, 60, and 100 minutes) and RCF (2000 × g and 10000 × g), b) Variation of the mean absorbance values obtained from the most pronounced peaks in a SWCNT sample dispersed in SC in function of the sonication time, and for the two RCF values, and c) Absorbance spectra of dispersed SWCNT in DMF, at different sonication times (40, 60, and 100 minutes) and RCF (2000 × g and 10000 × g).

As shown in the Technical Bulletin of Sigma-Aldrich (AL-265), and also in the works of Maeda *et al.* (2006) and Strano *et al.* (2009), the UV-Vis absorbance spectra are usually normalized by the absorbance value at 780 nm in order to enhance the characteristic absorption bands of SWCNT. Effectively, as it can be seen in Figure 3.5a, the interband electronic transitions of SWCNT are highlighted using this procedure, and the effect of experimental conditions tested for the dispersion of SWCNT are more pronounced at 550 - 600 nm and at 640 - 680 nm. The normalized absorbance spectra, shown in Figure 3.5a, corresponds to the same samples of dispersed SWCNT in SC used in Figure 3.4a, and only in the range of 400 to 800 nm (visible and NIR regions), since those ranges include the optical interband transitions of m-SWCNT and s-SWCNT, such as M_{11} and S_{22}. According to O'Connell *et al.* (2002), the electronic transitions between 400 and 600 nm are assigned to the m-SWCNT (M_{11} interband, corresponding to the absorbance feature $v_1 \rightarrow c_1$), and the absorbance features between 550 and 800 nm are assigned to the s-SWCNT (S_{22} interband, corresponding to the absorbance feature $v_2 \rightarrow c_2$). A slightly overlapping of bands is observed between 550 and 600 nm, which could difficult the correct assignment of bands to m-SWCNT or to s-SWCNT. However, in this work, it is considered that absorbance between 550 and 600 nm is associated with s-SWCNT, since Henrich *et al.* (2005), and Zheng and Semke (2007) have observed the S_{22} transition with higher absorbance at 576 nm and 574 nm for CoMoCAT SWCNT, respectively, which are SWCNT produced by the same synthesis method as used in this work, which means, that properties are expected to be identical. Thus, the S_{22} is considered to begin at approximately 550 nm.

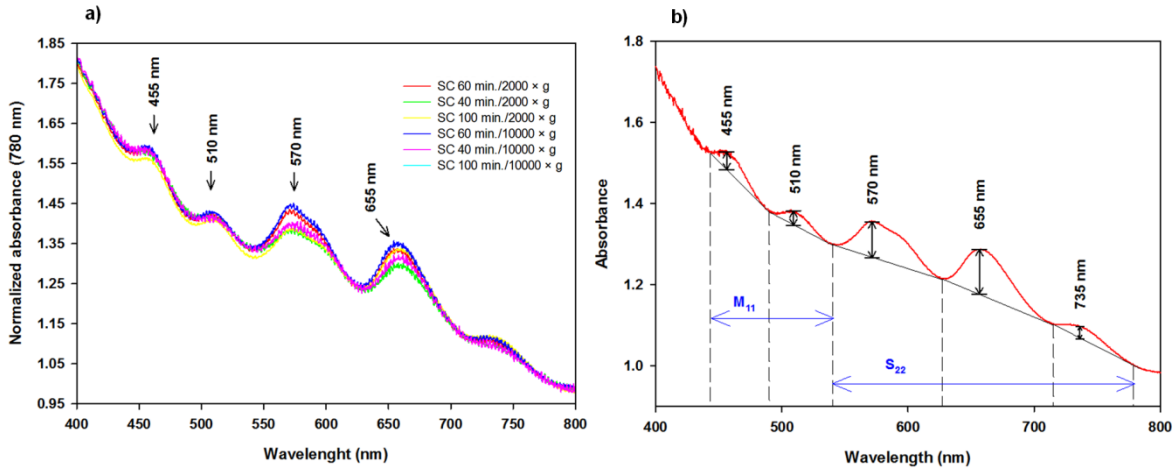

Figure 3.5 a) Normalized absorbance spectra of dispersed SWCNT in SC in the range from 400 to 800 nm and b) Methodology used in this thesis for the quantitative determination of the s-SWCNT and m-SWCNT.

The networks of SWCNT synthesized by various methods are mixtures of nanotubes with typical ratios of 1/3 of m-SWCNT and 2/3 of s-SWCNT, as shown for example in the work of Dresselhaus *et al.* (2005). Thus, for the SWCNT samples obtained in this work, the ratio between m-SWCNT and s-SWCNT was calculated from the absorbance spectra by subtracting the value of each peak by the corresponding values of the background feature above the peak, as demonstrated in Figure 3.5b. A baseline was drawn at the points at either side of each peak and the height of the peak up to the baseline was measured. Specifically, the expression $\frac{A_{455}+A_{510}}{A_{455}+A_{510}+A_{570}+A_{655}+A_{735}} \times 100$ was considered (where *A* is absorbance value at a specific wavelength) in order to calculate the % m-SWCNT = $\frac{M_{11}}{M_{11}+S_{22}} \times 100$, and the % s-SWCNT = 100–(% m-SWCNT). In this way, m-SWCNT was about 27.9 %, and s-SWCNT was about 72.1 %, being the ratio between s-SWCNT and m-SWCNT of 2.6, which is accordance to the ratio of 3 expected for a random chirality distribution.

Figure 3.6 shows the baseline corrected Raman spectrum obtained from the SWCNT dispersed in SC with the Bruker RFS/100S Raman-FT spectrophotometer.

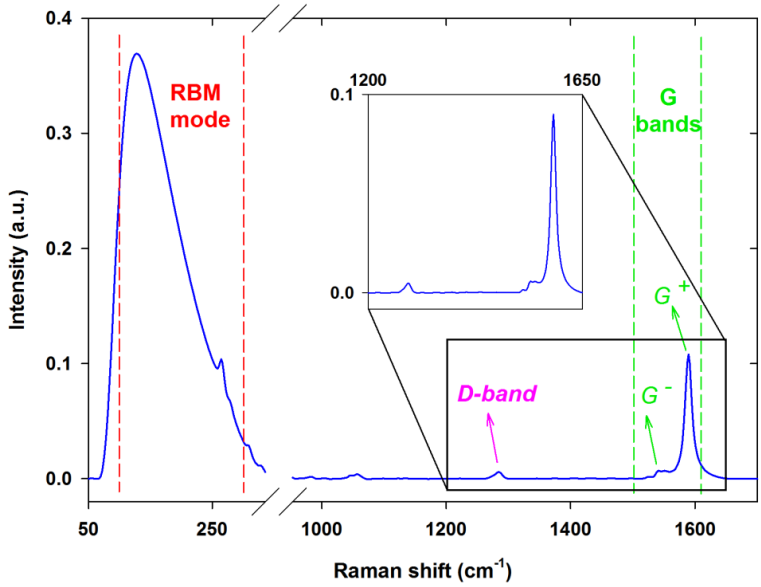

Figure 3.6 Baseline corrected Raman spectrum of SWCNT dispersed in SC (Reprinted from Talanta, 108, Justino *et al.*, Copyright (2013), with permission from Elsevier).

The two active Raman modes of SWCNT are present as first-order features, thus the low frequency radial breathing mode (RBM) is displayed between 100 and 300 cm^{-1}, and the high frequency G-bands are shown between 1550 and 1605 cm^{-1}.

The frequency of the RBM mode (ω_{RBM}), which is the feature of primary interest for SWCNT, allowed the determination of the average diameter of the SWCNT (d) as 1.8 nm, by following the relation established by Dresselhaus *et al.* (2005):

$$\omega_{\mathrm{RBM}}(\mathrm{cm}^{-1}) = \left(\frac{234\mathrm{cm}^{-1}\mathrm{nm}}{\mathrm{d}}\right) + 10\mathrm{cm}^{-1} \qquad [3.2]$$

The G-band has two main components, the high (G^+) and the low (G^-) frequency components, which are due to the curvature of the sheet of graphene. In contrast to the graphite G-band, which is present only at approximately 1580 cm^{-1} due to the tangential mode vibrations of C atoms, the G-band of CNT is composed of several tangential modes due to the vibrations of stretching of the SWCNT sidewall C-C bonds (Itkis *et al.*, 2005), and it is not affected by the defects on the SWCNT structure. The G^+ feature is observed at 1590 cm^{-1} due to in-plane vibrations along the nanotube axis, while the G^- feature at 1570 cm^{-1} is attributed to in-plane vibrations along the circumferential direction. On the other hand, the line shape of the G-band can be used to differentiate the m-SWCNT from the s-SWCNT, as reported in Dresselhaus *et al.* (2002). The pattern shown in Figure 3.6 can be compared to that present in the works of Dresselhaus and Eklund (2000), and Dresselhaus *et al.* (2005) where the peak at 1590 cm^{-1}, narrow and symmetric, is associated with s-SWCNT. In turn, the weak frequency peak at ~1570 cm^{-1} (G^- band), with its commonly called Breit-Wigner-Fano line shape, is originated from the electron-phonon interactions in the m-SWCNT.

An additional feature at about 1300 cm^{-1} (D-band) is attributed to a second-order Raman scattering process, which characterizes the structural disorder of the sp^2-hybridized carbon. In Figure 3.6, such a band is very small which means that the impurities (for example, carbonaceous materials), defects, and disorder effects are minimal. On the other hand, the very low value of D/G^+ intensity ratio (~ 0.02) is an indicator of the quality of the dispersed SWCNT, as reported in Dresselhaus *et al.* (2005).

The Raman spectrum obtained in this thesis is in accordance with the typical spectra for the SWCNT. However, it is known that the spectral profiles depend on the laser excitation energy used in the spectrophotometer, with variations in the intensity of peaks but not influencing the peak position (same wavenumbers), as reported by Rao *et al.* (1997) and shown in Figure 3.7. Ouyang *et al.* (2008) have also observed that D/G^+ intensity ratio hardly decreases with increasing laser excitation energy from 325 nm to 514.5 nm and to 1064 nm.

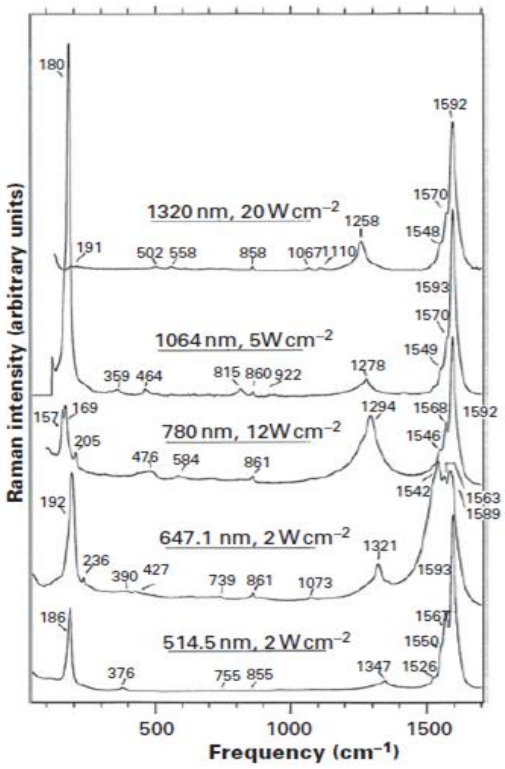

Figure 3.7 Raman spectra at five different laser excitations (from Rao *et al.*, Science, 275, Copyright (1997). Reprinted with permission from The American Association for the Advancement of Science).

According to Harris (2009), the Raman spectroscopy has been of less value when applied to MWCNT, due to their large diameter (which is equivalent to weak RBM signals) and the non-observation of the splitting of the G-band observed in SWCNT.

3.3.2. Experimental design for screening the dispersion conditions of the SWCNT in sodium cholate (SC)

The details of the experimental design followed, as well as the results obtained are depicted in Table 3.1, and Table 3.2 displays the statistics associated with the main effects, the two-way and three-way interactions, and the coefficients for the response model obtained using Minitab software (Minitab Inc., 2010).

Table 3.1 Experimental plan and response of the 2^3 factorial design with 2 replicates (Reprinted from Talanta, 89, Justino *et al.*, Copyright (2012), with permission from Elsevier).

Run order	A (Sonication time, min.)	B (Centrifugation time, min.)	C (RCF, × g)	Y (Abs_{500})
1	100	10	10000	0.6380
2	60	10	10000	0.9130
3	100	10	2000	0.9940
4	100	5	2000	1.1037
5	60	10	2000	1.3039
6	60	5	10000	1.0725
7	100	5	10000	0.7756
8	100	10	10000	0.6488
9	60	10	2000	1.2871
10	60	5	10000	0.9901
11	100	5	2000	1.0946
12	60	5	2000	1.4506
13	100	5	10000	0.7789
14	100	10	2000	0.9633
15	60	10	10000	1.0570
16	60	5	2000	1.4172

Table 3.2 Main effects, interactions and regression coefficients (including respective standard error, SE) for the response model (Reprinted from Talanta, 89, Justino *et al.*, Copyright (2012), with permission from Elsevier).

Term	Effect	Regression coefficients	SE	*t* value	*p* value
Constant		1.0305	0.0108	95.07	0.000
A	-0.3118	-0.1559	0.0108	-14.38	0.000
B	-0.1098	-0.0549	0.0108	-5.06	0.001
C	-0.3426	-0.1713	0.0108	-15.80	0.000
A*B	-0.0174	-0.0087	0.0108	-0.80	0.445
A*C	0.0140	0.0070	0.0108	0.65	0.537
B*C	0.0197	0.0098	0.0108	0.91	0.390
A*B*C	-0.0264	-0.0132	0.0108	-1.22	0.259

SE – Standard errors for regression coefficients.

According to Table 3.2, the main effects due to the individual factors A, B and C are statistically significant (p < 0.05), and the factorial design fitting is acceptable for the interpretation of future results with high determination coefficients (R^2 = 0.9838, and adjusted R^2 = 0.9696). On the other hand, the three two-way interactions (A*B, A*C, and B*C), and the three-way interaction (A*B*C) are not significant (p > 0.05), which means that the factors (that is, sonication time, centrifugation time, and RCF) affect the response only in an independent way, and not interactively. The normal probability plot and the Pareto chart of the standardized effects are displayed in Figure 3.8 in order to highlight the statistical significance of the main effects of the 3 factors and respective interactions on the response measured as the absorbance at 500 nm.

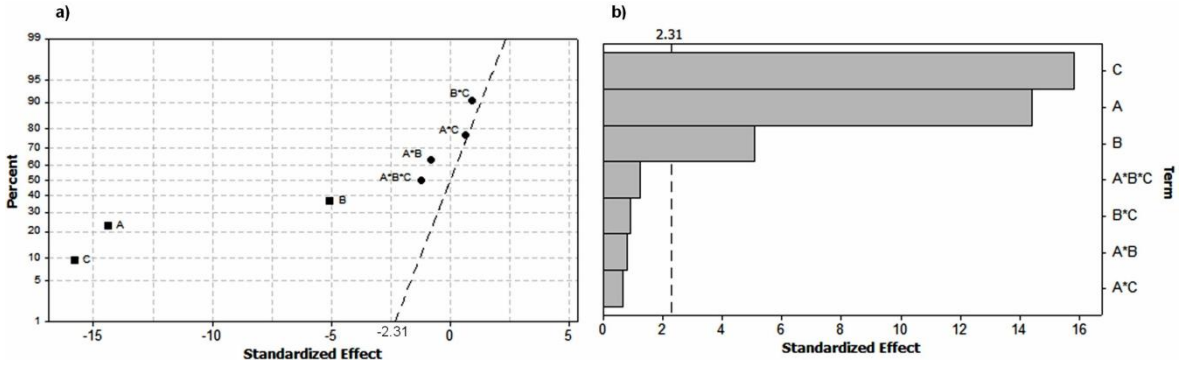

Figure 3.8 a) Normal probability plot (■ Significant effect; ● Not significant effect), and b) Pareto chart of the standardized effects at 95% confidence interval (the absolute value of point 2.31 is the minimum statistically significant effect) (Reprinted from Talanta, 89, Justino *et al.*, Copyright (2012), with permission from Elsevier).

The normal probability plot (Figure 3.8a) shows the statistical significance and the magnitude of both main and interaction effects at a significance level of 5 %, and through standardized values in x-axis (such values are the t statistics shown in Table 3.2, and they are calculated by dividing each coefficient by its standard error, also shown in Table 3.2). The points near the dashed line within -2.31 and 2.31 are the points expected to fall when the respective effect is not significant. The points which do not fall close to this dashed line, that is, those corresponding to the factors A, B, C are active effects, and they have a significant effect on the response. Moreover, factor C (RCF) has the largest main effect, higher than the other two factors (factor A – sonication time, and factor B – centrifugation time), while the factor A also has the second most important effect.

The Pareto chart (Figure 3.8b) is another type of plot which provides the relative magnitude and significance of both individual and interaction effects, with the same standardized effects values that those of the normal probability plot. However, in the

Pareto chart, the *x*-axis contains the absolute values, and the factors studied as well as their interactions are in the *y*-axis, providing a quick and easy graphical method to identify the main effects on the response model. The vertical line of Pareto chart at a standardized effect of 2.31 has the same interpretation of the dashed line of the normality plot (Figure 3.8a) and indicates the minimum statistically significant effect at a significance level of 5 %.

Also from the Table 3.2, the column “Effect” provides information about the relative strength of the effects through its absolute value, and such value to RCF factor (C) provides the highest effect on the response. Finally, the negative sign associated with each effect value means that when the factor level changes from low level to high level, the response decreases, which allows to conclude that the conditions of 60 minutes of sonication and centrifugation during 5 min at 2000 × g will allow to obtain a SWCNT solution most adequate for further studies.

3.3.3. Comparison of the dispersion of SWCNT in sodium cholate (SC), sodium dodecyl sulphate (SDS), and sodium alginate (SA)

The UV-Vis spectra of the SDS and SA are shown in Figure 3.9, in order to compare their effectiveness on the dispersion of SWCNT with that obtained with SC.

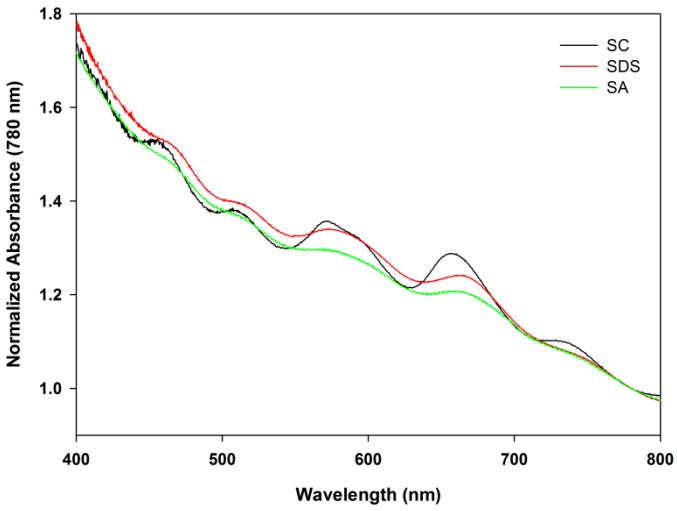

Figure 3.9 UV-Vis spectra obtained from SWCNT dispersed on sodium dodecyl sulphate (SDS) and sodium alginate (SA), together with the UV-Vis spectrum of SWCNT dispersed on SC.

For samples of SWCNT dispersed in SDS and SA, less-resolved features were observed, that may be due to a loss of the typical interband electronic transitions. Li *et al.* (2005) have found that the SDS coated on the SWCNT appear to be relatively unstable, and as the SC is a bile salt molecularly more rigid than the SDS, the SC becomes more stable in aqueous solutions, as reported by Arnold *et al.* (2006). On the other hand, the SDS could not cover the surface of CNT uniformly, since the simple alkyl chains of the SDS could form non-specific hydrophobic interaction with CNT, as reported by O'Connell *et al.* (2002) and Tummala and Striolo (2009). Relatively to the polymer SA, it is known that interactions with mechanically rigid SWCNT may force them into energetically unfavourable conformations, thus providing some problems in efficient dispersion of SWCNT, as shown by Hu *et al.* (2009).

3.3.4. Effect of the concentration of the SWCNT in their optical properties

Figure 3.10 shows the absorbance spectra of the various SWCNT dispersions with different concentrations. At lower concentrations, there is a decrease of absorbance intensity, which means that lower SWCNT content is present, due to the loss of van Hove singularities.

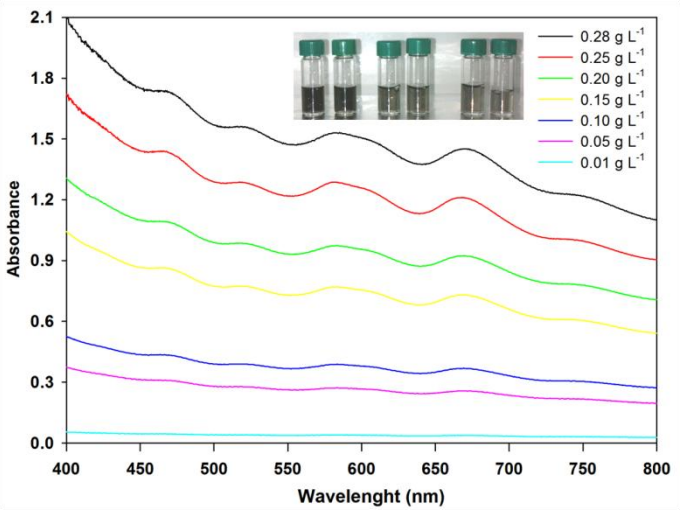

Figure 3.10 Absorbance spectra of dispersed SWCNT at different concentrations (Inset: photograph of SWCNT dilutions).

The absorbance at the wavelength of 500 nm was plotted against the concentration of SWCNT, as shown in Figure 3.11. A high correlation is observed between the absorbance

(*y*) values recorded at 500 nm, and the concentration of different SWCNT concentrations (*x*), given by the high correlation coefficient (*R* = 0.9992), in a determination range from 0 to 0.28 g L^{-1}. The limit of detection (LOD), calculated as three times the standard error of the estimate (Miller and Miller, 2005) was 1.2x10^{-2} g L^{-1}.

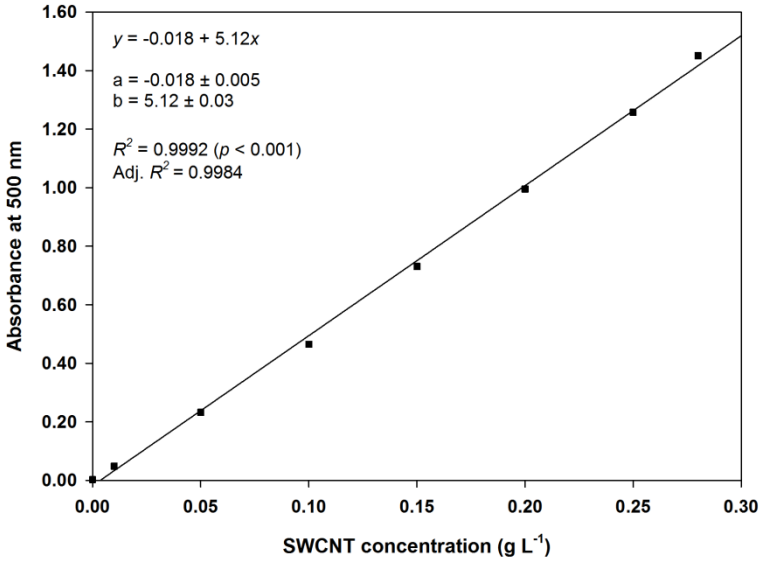

Figure 3.11 Calibration plot of absorbance values at 500 nm for different SWCNT concentrations.

As the length of quartz cell used for the spectra acquisition was of 1 cm, the absorbance and concentration are directly proportional to the absorption coefficient ε, as defined by the Beer-Lambert law (A = εLc), which corresponds to the slope of the fitted line. Thus, an absorption coefficient for the dispersed SWCNT was found as 5.12 mL mg^{-1} cm^{-1}. However, it should be considered that to follow the Beer-Lambert law, the plot should be passing through the origin. Thus, a little modification of the determined absorption coefficient was observed, which was of 5.04 mL mg^{-1} cm^{-1} (with R^2 = 0.9996, and adj. R^2 = 0.9736), corresponding to a difference of 2%. In the literature, only absorption coefficients for MWCNT are reported, where values between 17.9 and 39.9 mL mg^{-1} cm^{-1} were obtained by Li *et al.* (2006).

3.4 Conclusions

In this Chapter 3, it was found that the sodium cholate (SC) is the dispersant more effective in the dispersion of SWCNT since UV-Vis spectroscopic features are well

defined, and in accordance to the literature. From an experimental design based on a 2^3 factorial design, it was found that a dispersion of SCWNT obtained after 60 minutes of sonication and after 5 minutes of centrifugation at RCF of 2000 × g is the most adequate. The results obtained in this Chapter also showed that a typical SWCNT dispersion in SC applying such experimental conditions have a content of approximately 72 % of s-SWCNT, and with a ratio between s-SWCNT and m-SWCNT of 2.6, which is similar to the expected value of 3. Thus, the experimental conditions found for dispersion of SWCNT in SC were used in further work, in order to obtain uniform dispersions of SWCNT for application as a component of transduction mechanism in biosensors, as shown in Chapter 5.

References

AL-265 Technical Bulletin, Exfoliation and debundling procedure, Sigma-Aldrich. Available at: <http://www.sigmaaldrich.com/etc/medialib/docs/Aldrich/Instructions/1/al-265bul-08-10-1.Par.0001.File.tmp/al-265bul-08-10-1.pdf> [Last access: 18 August 2013].

Arnold M.S., Green A.A., Hulvat J.F., Stupp S.I., Hersam M.C., 2006. Sorting carbon nanotubes by electronic structure using density differentiation. *Nat. Nanotechnol.* 1, 60-65.

Ausman K.D., Piner R., Lourie O., Ruoff R.S., Korobov M., 2000. Organic solvent dispersions of single-walled carbon nanotubes: toward solutions of pristine nanotubes. *J. Phys. Chem. B* 104, 8911-8915.

Bahr J.L., Mickelson E.T., Bronikowski M.J., Smalley R.E., Tour J., 2001. Dissolution of small diameter single-wall carbon nanotubes in organic solvents? *Chem. Commun.* 2001, 193-194.

Bandyopadhyaya R., Nativ-Roth E., Regev O., Yerushalmi-Rozen R., 2002. Stabilization of individual carbon nanotubes in aqueous solutions. *Nano Lett.* 2, 25- 28.

Costa S., Tripisciano C., Borowiak-Palen E., Kalenczuk R.J., 2008. Comparative study on purity evaluation of singlewall carbon nanotubes. *Energy Convers. Manag.* 49, 2490-2493.

Dresselhaus M.S., Eklund P.C., 2000. Phonons in carbon nanotubes. *Adv. Phys.* 49, 705-814.

Dresselhaus M.S., Dresselhaus G. Jorio A., Souza Filho A.G., Saito R., 2002. Raman spectroscopy on isolated single wall carbon nanotubes. *Carbon* 40, 2043-2061.

Dresselhaus M.S., Dresselhaus G., Saito R., Jorio A., 2005. Raman spectroscopy of carbon nanotubes. *Phys. Rep.* 409, 47-99.

Frei M., 2011. Centrifugation basics. BioFiles 6, 4-5. Available at: <http://www.sigmaaldrich.com/content/dam/sigma-aldrich/articles/biofiles/biofiles-pdf/biofiles_v6_n5.pdf> [Last access: 18 August 2013].

Harris P.J.F., Carbon nanotube science - synthesis, properties and applications. Cambridge University Press, Cambridge, 2009.

Henrich F., Krupke R., Lebedkin S., Arnold K., Fischer R., Resasco D.E., Kappes M.M., 2005. Raman spectroscopy of individual single-walled carbon nanotubes from various sources, *J. Phys. Chem. B* 109, 10567-10573.

Hilding J., Grulke E.A., Zhang Z.G., Lockwood F., 2003. Dispersion of carbon nanotubes in liquids. *J. Dispers. Sci. Technol.* 24, 1-41.

Hu C.-Y., Xu Y.-J., Duo S.-W., Zhang R.-F., Li M.-S., 2009. Non-covalent functionalization of carbon nanotubes with surfactants and polymers. *J. Chin. Chem. Soc. 56*, 234-239.

Itkis M.E., Perea D.E., Jung R., Niyogi S., Haddon R.C., 2005. Comparison of analytical techniques for purity evaluation of single-walled carbon nanotubes. *J. Am. Chem. Soc.* 127, 3439-3448.

Jeong M.S., Byeon C.C., Cha O.H., Jeong H., Han J.H., Choi Y.C., An K.H., Oh K.H., Kim K.K., Lee Y.H., 2008. Purity measurement of single-walled carbon nanotubes by UV-VIS-NIR absorption spectroscopy and thermogravimetric analysis. *NANO: Brief Rep. Rev.* 3, 101-108.

Justino C.I.L., Freitas A.C., Rocha-Santos T.A.P., Duarte A.C., 2012. Screening of single-walled carbon nanotubes by optical fiber sensing. *Talanta* 89, 105-108.

Justino C.I.L., Freitas A.C., Amaral J.P., Rocha-Santos T.A.P., Cardoso S., Duarte A.C., 2013. Disposable immunosensors for C-reactive protein based on carbon nanotubes field effect transistors. *Talanta* 108, 165-170.

Kataura H., Kumazawa Y., Maniwa Y., Umezu I., Ohtsuk S.Y., Achiba Y., 1999. Optical properties of single-wall carbon nanotubes. *Synthetic Met.* 103, 2555-2558.

Kim O.-K., Je J., Baldwin J. W., Kooi S., Pehrsson P.E., Buckley L.J., 2003. Solubilization of single-wall carbon nanotubes by supramolecular encapsulation of helical amylose. *J. Am. Chem. Soc.* 125, 4426-4427.

Krupke R., Hennrich F., Hampe O., Kappes M.M., 2003. Near-infrared absorbance of single-walled carbon nanotubes dispersed in dimethylformamide. *J. Phys. Chem. B* 107, 5667-5669.

Li L.-J., Nicholas R.J., Chen C.-Y., Darton R.C., Baker S.C., 2005. Comparative study of photoluminescence of single-walled carbon nanotubes wrapped with sodium dodecyl sulphate, surfactin and polyvinylpyrrolidone. *Nanotechnol.* 16, 202-205.

Li Z.F., Luo G.H., Zhou W.P., Wei F., Xiang R., Liu Y.P., 2006. The quantitative characterization of the concentration and dispersion of multi-walled carbon nanotubes in suspension by spectrophotometry. *Nanotechnol.* 17, 3692-3698.

Maeda Y. Kanda M., Hashimoto M., Hasegawa T., Kimura S., Lian Y., Wakahara T., Akasaka T., Kazaoui S., Minami N., Okazaki T., Hayamizu Y., Hata K., Lu K., Nagase S., 2006. Dispersion and separation of small-diameter single-walled carbon nanotubes. *J. Am. Chem. Soc.* 128, 12239-12242.

Miller J.N., Miller J.C., Statistics and chemometrics for Analytical Chemistry, 5th ed., Pearson Prentice Hall, New York, 2005.

Minitab Inc., Minitab 16 Statistical Software, 2010, Version 16.2.1.0.

Monthioux M., Smith B.W., Burteaus B., Claye A., Fischer J.E., Luzzi D E., 2001. Sensitivity of single-wall carbon nanotubes to chemical processing: an electron microscopy investigation. *Carbon* 39, 1251-1272.

O'Connell M.J., Bachilo S.M., Huffman C.B., Moore V.C., Strano M.S., Haroz E.H., Rialon K.L., Boul P.J., Noon W.H., Kittrell C., Ma J., Hauge R.H., Weisman R.B., Smalley R.E., 2002. Band gap fluorescence from individual single-walled carbon nanotubes. *Science* 297, 593-596.

Ouyang Y., Cong L.M., Chen L., Liu Q.X., Fang Y., 2008. Raman study on single-walled carbon nanotubes and multi-walled carbon nanotubes with different laser excitation energies. *Physica E* 40, 2386-2389.

Rao A.M., Richter E., Bandow S., Chase B., Eklund P.C., Williams K.A., Fang S., Subbaswamy K.R., Menon M., Thess A., Smalley R.E., Dresselhaus G., Dresselhaus M.S., 1997. Diameter-selective Raman scattering from vibrational modes in carbon nanotubes. *Science* 275, 187-191.

Sinani V.A., Gheith M.K., Yaroslavov A.A., Rakhnyanskaya A.A., Sun K., Mamedov A. A., Wicksted J.P., Kotov N.A., 2005. Aqueous dispersions of single-wall and multiwall carbon nanotubes with designed amphiphilic polycations. *J. Am. Chem. Soc.* 127, 3463-3472.

Strano M.S., Boghossian A.A., Kim W.-J., Barone P.W., Jeng E.S., Heller D.A., Nair N., Jin H., Sharma R., Lee C.Y., 2009. The chemistry of single-walled nanotubes. *MRS Bull.* 34, 950-961.

Tummala N.R., Striolo A., 2009. SDS surfactants on carbon nanotubes: aggregate morphology. *ACS Nano* 3, 595-602.

Vaisman L., Wagner H.D., Marom G., 2006. The role of surfactants in dispersion of carbon nanotubes. *Adv. Colloid Interface Sci*. 128-130, 37-46.

Xiao Z., Sharma H., Zhu M. Y., Pearson T. 2010. Dielectrophoresis-assisted deposition and alignment of single-walled carbon nanotubes for electronic-device fabrication. *J. Vac. Sci. Technol. A* 28, 750-754.

Zheng M., Semke E.D., 2007. Enrichment of single chirality carbon nanotubes. *J. Am. Chem. Soc.* 129, 6084-6085.

Chapter 4

Microfabrication of Field Effect Transistors (FET)

In this Chapter 4, the microfabrication of field effect transistors (FET) is reported together with the description of each processing step and equipments used. The microfabrication consists in the process of manufacturing individual devices in micrometre sizes. The reported work of microfabrication of FET was developed at INESC-MN (*Instituto de Engenharia de Sistemas e Computadores - Microsistemas e Nanotecnologias*, Lisbon, *www.inesc-mn.pt*) in cleanroom facilities in order to avoid any contamination of the microfabricated devices. In a cleanroom, a controlled and dust-free environment is achieved through high-efficiency particulate air filters, maintaining low levels of environmental pollutants such as airborne particles, and chemical vapours, as well as acoustic noise, vibrations, and electromagnetic interferences. The controlled level of contamination is specified by the number of particles *per* volume of air at a specified particle size, thus defining various classes of cleanrooms. For example, the classes 10, 100, and 10000 are those existing in the INESC-MN cleanroom, as depicted in Figure 4.1a, where the limits of each class are associated with the maximum number of particles *per* cubic feet with size equal to and larger than 0.5 µm. Moreover, constant temperature and relative humidity are maintained, and the operators are required to use special garments such as hoods, gloves, boots, and coveralls, as shown in Figure 4.1b and 4.1c, to function as a barrier to particles and chemicals.

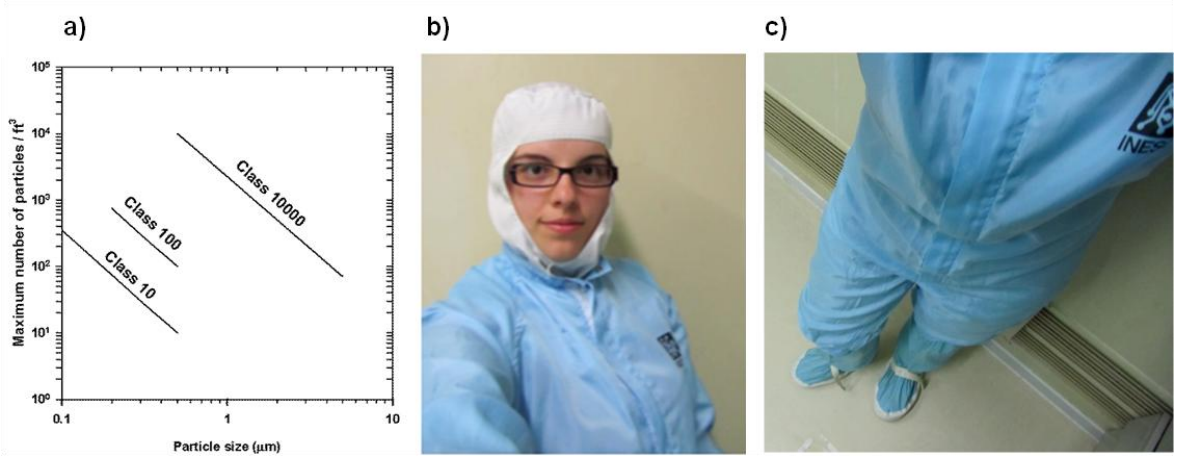

Figure 4.1 a) Classification of cleanrooms (according to data of FED STD 209E, 1992), b) and c) Details of cleanroom garments used during microfabrication.

The microfabrication of FET has aimed at the definition of an interdigitated architecture configuration, where each defined electrode has 1.5 µm of width and 1000 µm of length, as shown in Figure 4.2k. The architecture of interdigitated electrodes was chosen due to their large surface area which increases the probability of contacting multiple carbon

nanotubes in each device. FET with different geometry parameters, such as with different distances between electrodes, number of electrodes, and thickness of gold layer, were fabricated as explained in Section 4.1.3, in order to study the effect of such variation on device performance, that is, through the electrical device characteristics (current-voltage measurements), as reported in the Section 5.1 where the assemblage of FET with single-walled carbon nanotubes is reported.

4.1. Experimental equipment and microfabrication process

Two commercial *p*-type silicon wafers (diameter of 3 inch, and thickness of 0.5 mm, Sigma-Aldrich Química, Portugal) were used as substrate of FET, in order to study the influence of the thickness of the gold layer (40 and 100 nm, respectively, in wafers #1 and #2) in the sensor response. The schematics of the overall microfabrication process and the final FET architecture are shown in Figure 4.2.

4.1.1. Oxide deposition

After cleaning with a blow of nitrogen, the substrates were passivated with an insulating layer of 400 nm-thick SiO_2 by plasma-enhanced chemical vapour deposition (PECVD, Electrotech Delta 201 CVD System), according to the conditions identified in Table 4.1.

Table 4.1 Conditions used in oxide deposition for passivation.

RF Power (W)	Pressure (mTorr)	SiH_4 flow (sccm)	N_2O flow (sccm)	Temperature
430	700	125	2500	350ºC

sccm - standard cubic centimetres *per* minute

This technique consists on the deposition of thin films of SiO_2 from vapour gases, that is, SiH_4 and N_2O to provide electrical insulation, through following reactions: $SiH_4 + O_2 \rightarrow SiO_2 + 2\ H_2$, and $SiCl_2H_2 + 2\ N_2O \rightarrow SiO_2 + 2\ N_2 + 2\ HCl$, respectively. Such chemical reactions occur after the production of a plasma of reactive gases, by a direct-current (DC) discharge at 700 mTorr between two electrodes.

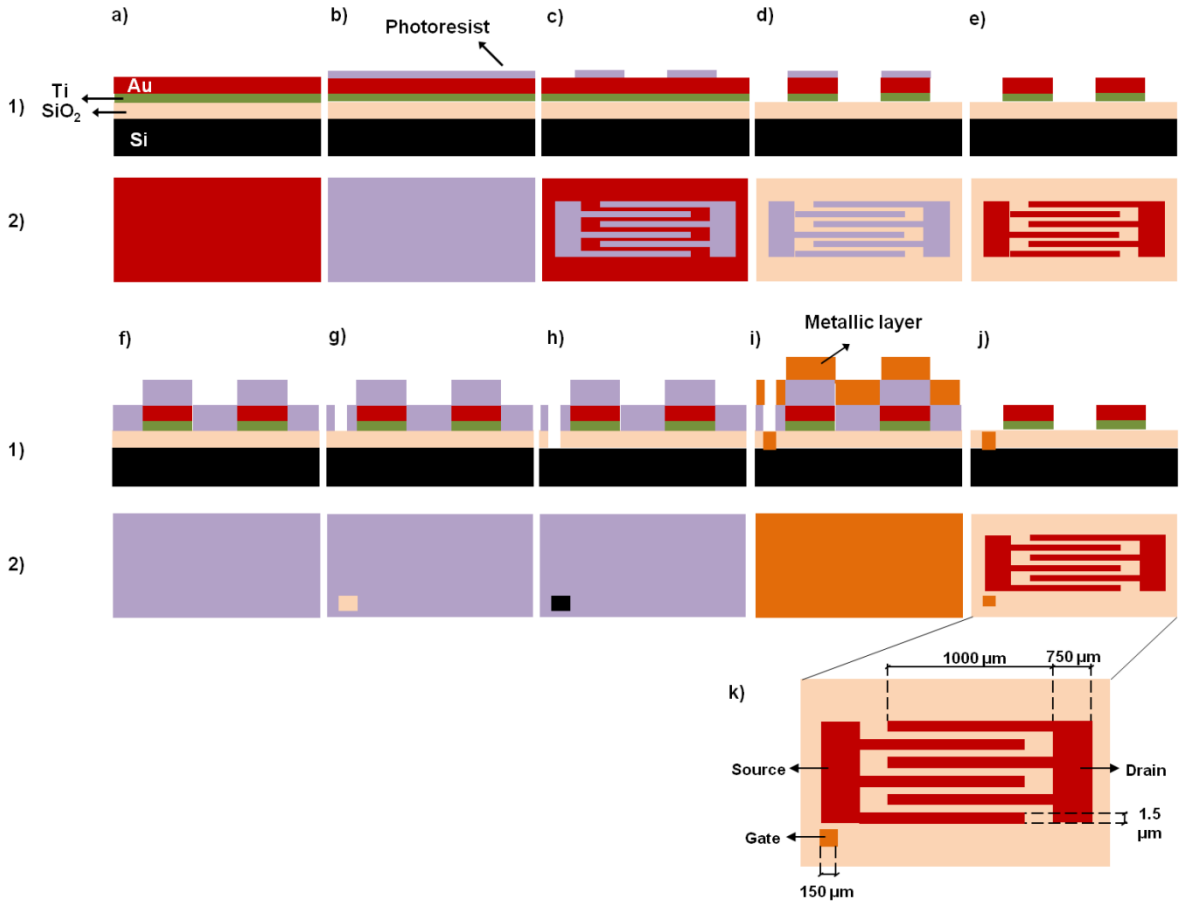

Figure 4.2 Schematic 1) cross views and 2) top views of microfabrication steps of FET: a) SiO_2 and Ti/Au depositions, b) Coating with photoresist, c) Lithography (inverted mask, resist mask defining the contacts), d) Ion milling Ti/Au films to remove undesired zones, e) Resist strip, f) Coating with photoresist, g) Lithography for opening contact *via* (non-inverted mask, resist all over, except in 150x150 μm^2 holes), h) Reactive ion etching of SiO_2, i) Metallic layer deposition (Cr/Au for wafer #1 and Ru for wafer #2), j) Lift-off, and k) final FET architecture.

4.1.2. Ti/Au deposition

The insulation by oxide deposition was followed by the deposition of a thin layer of Au (40 and 100 nm, respectively, in wafers #1 and #2), with a 10 nm-thick adhesion layer of Ti underneath, on SiO_2 (step depicted in Figure 4.2a) through physical vapour deposition (PVD) by sputtering (Alcatel Magnetron Sputtering System), which is the most often used technique for depositing Ti and Au films on substrates. The conditions used for the PVD are identified in Table 4.2. The deposition of a Ti film is required prior to the Au deposition to assure film adhesion, as Au tends to delaminate from all surfaces (Cr is also often used).

Table 4.2 Conditions used in the Alcatel Magnetron sputtering system.

Wafer designation	Films thickness (nm)	Deposition conditions				
		Time (min.)	DC Power (W)	RF Power (W)	Pressure (mTorr)	Gas flow (sccm Ar)
#1	Ti: 10; Au: 40	8	20	20	3.1	20
#2	Ti: 10; Au: 100	19				

DC – Direct-current; RF – Radio-frequency.

In the sputtering technique, which occurs in a vacuum chamber, the metal atoms are ejected from a target material by high energy ion bombardment provided by direct-current (DC) and radio-frequency (RF) power supplies, and sputtered atoms can condense on a substrate as thin films.

4.1.3. Coating with photoresist and lithography for contact definition

The Ti/Au film was coated with a 1.5 µm-thick layer of a photosensitive polymer called positive photoresist (PFR 7790G-27cP, JSR Corporation), as depicted in Figure 4.2b, by a standard spin coating system (Silicon Valley Group, SVG), with a spin speed of 2800 RPM for 40 s. The resist thickness was confirmed with a profilometer (Dektak 3030ST Surface Texture Analysis System), which has a piezo-resistive sensor able to detect any changes in the topography of samples, with minimum vertical resolution of 10 nm. Spin coating consists in the deposition of the photoresist onto the wafer that is spun to produce an uniform thin layer. The photoresist used in this work is a positive photoresist; the basis of its chemical composition is a resin and a photo-reactive component dissolved in a solvent which is a dissolution inhibitor. Such component becomes soluble when exposed to ultraviolet light ($\lambda \sim 442$ nm). Due to the breaking of polymer chemical bonds, the regions in the wafer with a resist mask are defined, while the remaining surface is cleaned. In this way, the optical lithography is performed by a Direct Write Laser 2.0 Litography System (DWL, 120 mW, Heidelberg Instrument) to define the source (S) and drain (D) metal contacts, as depicted in Figure 4.2c. The lithography process, which uses a 442 nm HeCd laser, consists in the transfer of a geometric pattern (photomask) to the light-sensitive polymer (photoresist), with a resolution of 0.8 µm, which is the minimum feature resolved by DWL.

The shape of the geometric pattern was produced by computer-assisted design software (AutoCAD). The DWL machine has the capability to convert the AutoCAD format file (.dxf) in adequate DWL machine language (.gdsii format) and each photomask layout

or layer correspond to a microfabrication process step. In this thesis, the resulting file (photomask) corresponds to an individual die, as shown in Figure 4.3b, which was automatically repeated in order to have a total of 30 dies in each wafer, as shown in Figure 4.3a.

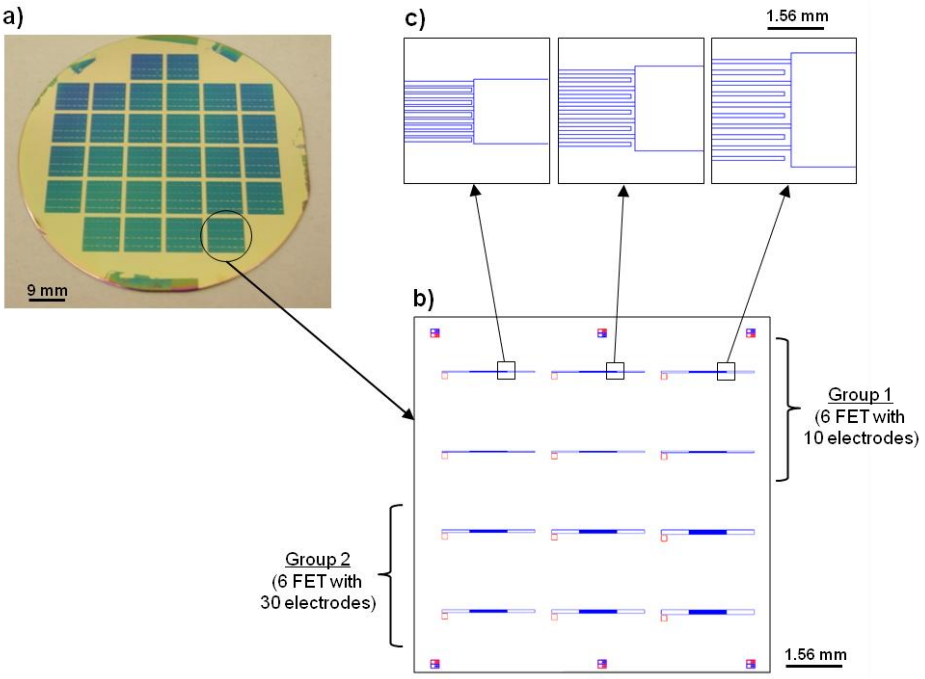

Figure 4.3 a) Silicon wafer (substrate) with 30 repeated dies, b) final pattern geometry (die with 12 FET) designed by AutoCAD software, and c) example of three FET with different distance between electrodes.

As shown in Figure 4.3b, the file image has two colours, which corresponds to different layouts, that is, the blue layer is associated with the FET pattern (selecting that, the lithography only develop such layer), and the red layout is associated with the 150 x 150 μm^2 hole (for third contact definition, which is reported in Section 4.1.6). In Figure 4.3b, it can be observed that in a die, two groups of FET were repeated depending on the number of electrodes. The first group (first two rows of FET) consists of six individual FET, each of them with 10 electrodes. The second group (last two rows of FET) consists of six FET, each of them with 30 electrodes. The distance between the electrodes will also be optimized for the sensor response, and thus, each die was divided into three columns of FET. Each column is constituted by FET with different distances between electrodes, that is, 0.8, 1.5 or 2.5 µm, respectively for each column. FET with 0.8 µm as distance between electrodes, both with 10 and 30 electrodes were not used in this thesis, since they were not well defined by optical lithography. Figure 4.3c depicts the

photomask layer for the area of 3 FET with the interdigitated electrodes on the left hand zone of each picture, and the drain of each FET on the right hand zone of each picture. The wafers were observed at an optical microscope (BH3-MJL, Olympus Optical) to verify the correct spacing between the electrodes and the appropriate dimensions of the electrodes and contacts, and Figure 4.4 shows examples of the optical microscopy images of FET corresponding to the FET shown in Figure 4.3c.

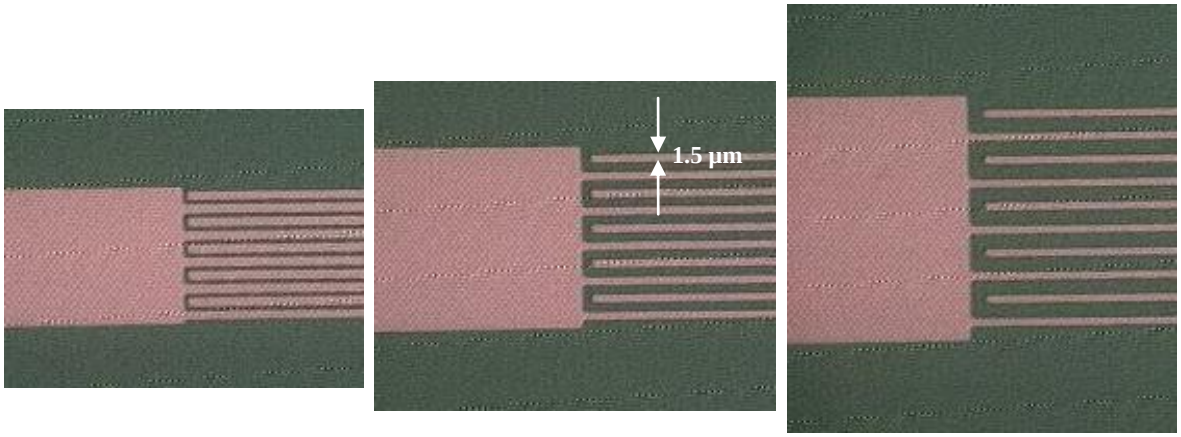

Figure 4.4 Magnified images of FET (wafer #2) after lithography process, corresponding to zoomed pictures of Figure 4.3c (500x images from optical microscope BH3-MJL, Olympus Optical).

4.1.4. Ion beam etching

The ion beam etching removes material from the target through the bombardment of high energy Ar ions. The plasma of Ar ions is not produced inside the vacuum chamber, as it happens in the sputtering system, but it is produced inside the gun through a RF antenna ion source. As the whole substrate surface was exposed to the UV laser (inverted mask), the uppermost layer of the substrate that is not protected by photoresist was removed by ion beam etching using an automated ion beam system (Nordiko 3000 Series), as depicted in Figure 4.2d. In this microfabrication step, the etchings have removed 50 nm (10 nm of Ti, plus 40 nm of Au) or 110 nm (10 nm of Ti, plus 100 nm of Au) of material in wafers #1 and #2, respectively, and the specific experimental conditions are identified in Table 4.3. These conditions are also observed in the user interface of the program of Nordiko 3000 in the characteristics of the assist gun, as shown in Figure 4.5. The user interface of the program of Nordiko 3000 also displays the running time for the etching process, as well as the characteristics observed instantly for each component of the equipment. As shown in Figure 4.5, the characteristics of the deposition gun and the

assist gun are observed, since they are the two ion sources of this system, called ion beam guns: the deposition gun for deposition of thin films in substrates from targets, and the assist gun for ion milling directly to the substrate. However, the deposition gun is inactive since, for that microfabrication step, the Nordiko 3000 was only used for ion etching.

Table 4.3 Conditions used in the Nordiko 3000 system for the Assist Gun.

RF Power (W)	(V^+) Voltage (V)	(I^+) Current (mA)	(V^-) Voltage (V)	(I^-) Current (mA)	Ar flow (sccm)	Pressure (Torr)
59	488.0	30.1	193.5	1.8	7.9	$1.7x10^{-4}$

V^+ – acceleration voltage; V^- – deceleration voltage.

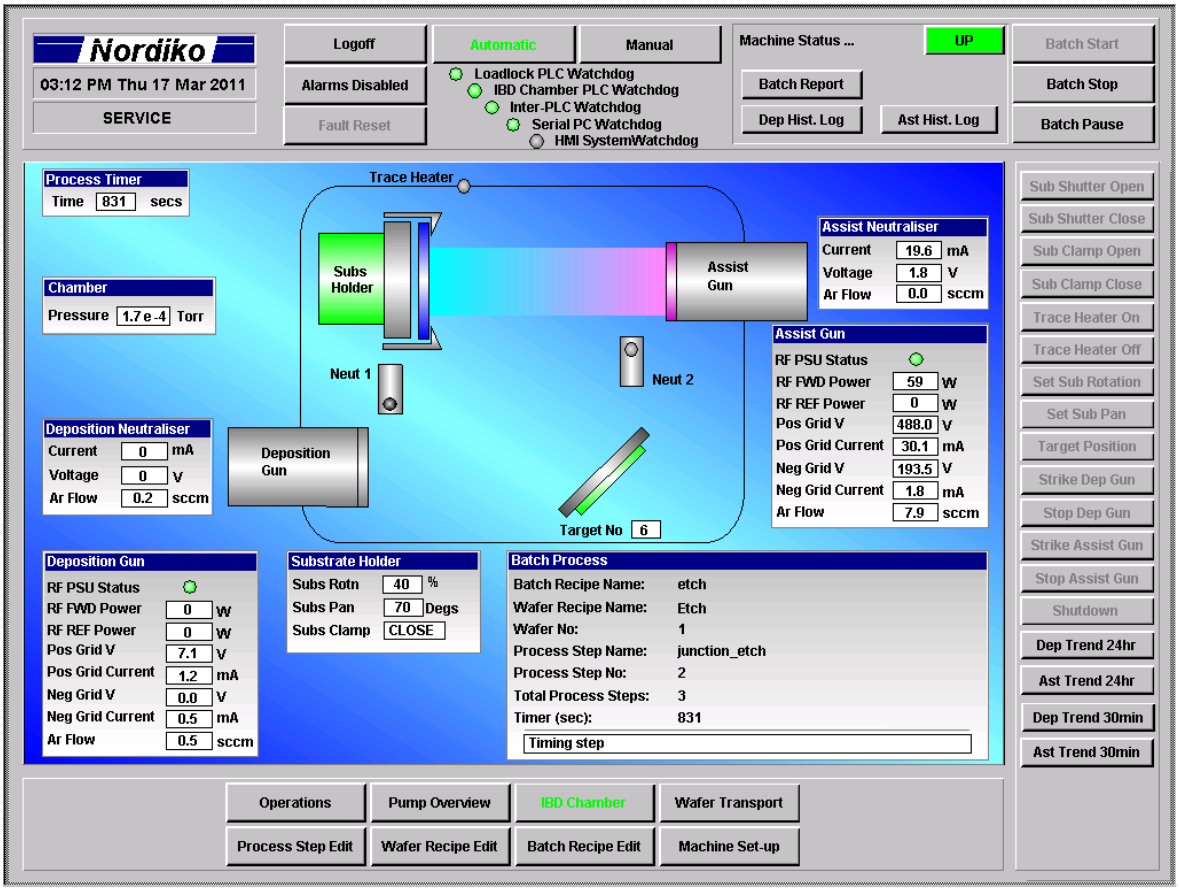

Figure 4.5 User interface of Nordiko 3000 system of INESC-MN.

4.1.5. Photoresist strip

The remaining photoresist on the surface of sensor structures was removed (step depicted in Figure 4.2e) through immersion of the wafer in a stripper solution (Microstrip® 2001, Fujifilm) which functions as photoresist solvent at 65ºC. The stripper solution is an organic mixture of 2-(2-aminoethoxy)ethanol (40-55%) with N-methyl-2-pyrrolidone (45-55%) as the solvent. The wafers were then cleaned with isopropanol and distilled water, and finally dried with nitrogen in a wet bench, which is a station for cleaning the wafers and devices.

4.1.6. Lithography for opening contact *via* (for third contact definition) and reactive ion etching of SiO_2

The final step of FET microfabrication was the definition of the third contact (gate) to reach to FET with back-gated configuration. The silicon substrate was used as the back gate electrode; for that, the wafers (substrate) were coated with a photoresist film (1.5 µm) as depicted in Figure 4.2f, and the second mask (red layout with 150 x 150 μm^2, as shown in Figure 4.3b) was defined by optical lithography with a DWL system, as depicted in Figure 4.2g. Here, the mask is non-inverted, so that only an opening is defined in the resist by etching the oxide through the resist. In this way, 400 nm SiO_2 were removed by reactive ion etching through a LAM Rainbow plasma etcher (LAM Rainbow 4400 System) as depicted in Figure 4.2h, and following the conditions shown in Table 4.4.

Table 4.4 Deposition parameters used in the LAM Plasma Etcher.

Time (sec.)	RF Power (W)	Pressure (mTorr)	CF_4 flow (sccm)	Ar flow (sccm)
3x150	100	140	100	200

This technique uses chemically reactive plasma to remove material deposited on the wafer through high energy ions from plasma, which has been produced inside a grounded vacuum chamber, combining physical and chemical etchings. The sulphur hexafluoride is commonly used for silicon etching, exactly as it was used in this thesis.

4.1.7. Metal deposition and resist strip (lift-off)

Keeping the same resist mask, Cr/Au 100 nm-thick (wafer #1) and Ru 50 nm-thick (wafer #2) films were deposited by ion beam deposition/milling (Nordiko 3000 Series) following the step depicted in Figure 4.2i, and immediately after ion beam etching. The same ion beam system Nordiko 300 used in step 4.1.4 was also used for milling, that is, for the deposition of material through the bombardment of high energy Xe ions in the deposition gun.

Finally, the photoresist and the Cr/Au or Ru films were removed by lift-off (step depicted in Figure 4.2j), immersing the wafers in a microstrip solution (Microstrip® 2001, Fujifilm) at 65ºC. Ultrasounds were also used to accelerate the action, and as the Microstrip reacts with the photoresist also under the metallic layers, such material is also lifted-off. The wafers were then cleaned with isopropanol and distilled water, and finally dried with nitrogen in a wet bench.

Figure 4.6 shows images obtained by optical microscopy of various FET at different microfabrication steps, that is, before and after the etching (reported in Section 4.1.4) and after Microstrip treatment (reported in this Section). It is possible to observe the effect of etching and the action of Microstrip by a visual inspection of FET and SiO_2, which appears as green after etching and before Microstrip treatment. On the other hand, the metal electrodes after Microstrip treatment are well defined, due to the removal of photoresist layer.

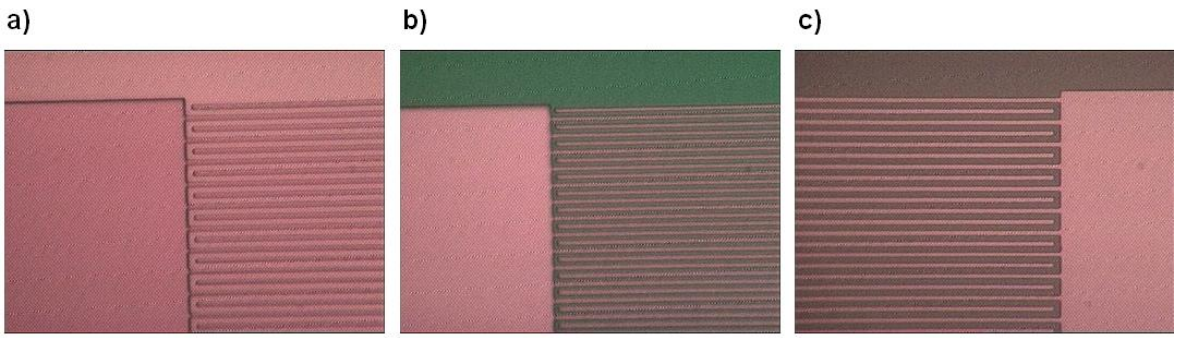

Figure 4.6 a) Wafer #1 before etching, b) wafer #2 after etching, and c) wafer #1 after Microstrip treatment (100x images from optical microscope BH3-MJL, Olympus Optical).

4.1.8. Wafer dicing

In order to have individualized FET, the wafers were cut with an automatic dicing saw system (DISCO DAD 321) into their dies and then into individualized FET, as shown in Figure 4.7a. A previous layout was made according to the final dimensions required for the FET, as shown in Figure 4.7b. Each individualized FET (Figure 4.7c) has dimensions of approximately 3 x 2 mm^2 and they have back-gated geometry and interdigitated architecture configuration which allows a large surface area for sensing.

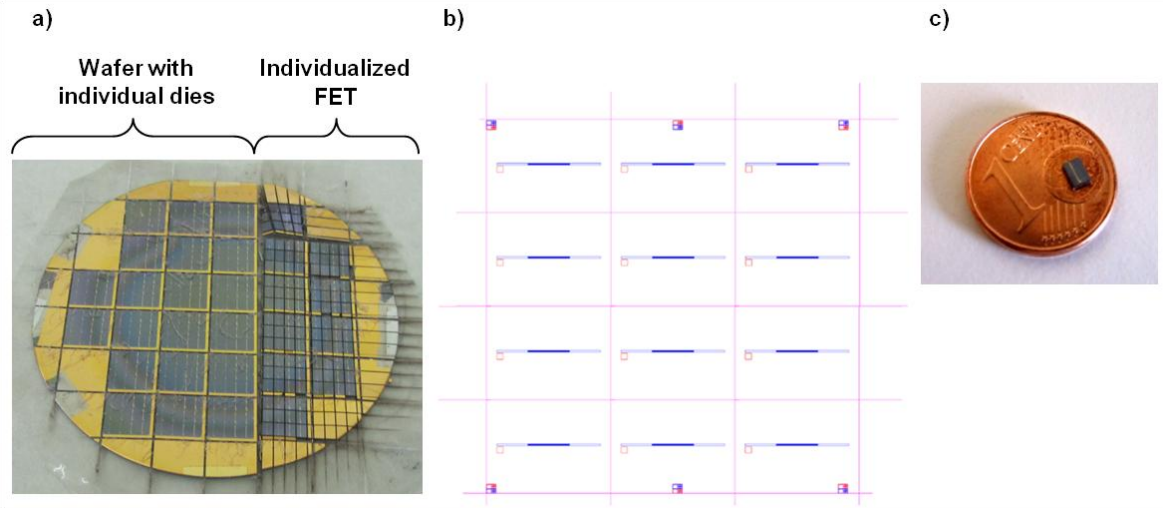

Figure 4.7 a) Diced wafer into individual dies and individualized FET, b) Layout of dimensions for the dicing, and c) Individualized FET (2975 x 2150 μm^2).

Visual inspection was enough to check whether some of FET were not defined because the DWL system for photolithography have a resolution of 0.8 µm, which is exactly the distance between electrodes. Thus, the FET existing closer to the edge of the wafer are not well defined, and consequently they were not used. Figure 4.8 shows two of these FET containing such defects and making them unfit for further use.

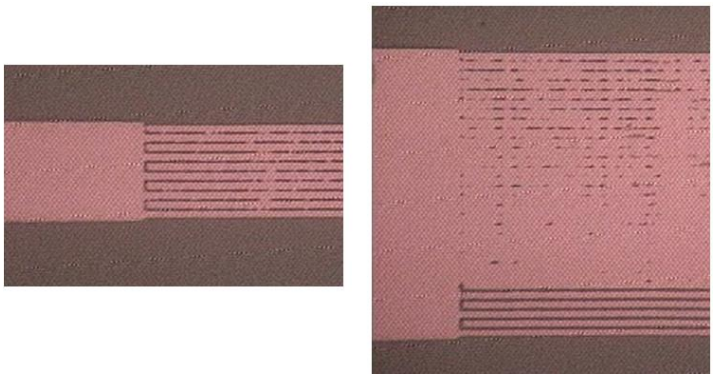

Figure 4.8 Magnified images of FET (wafer #1) with non defined areas (500x images from optical microscope BH3-MJL, Olympus Optical).

4.1.9. FET mounting

Individualized FET were washed with acetone and distilled water, and dried with nitrogen, as well as mounted to a printed circuit board (PCB). The PCB pattern was obtained by AutoCAD software, as shown in Figure 4.9a. The role of PCB strip is to allow the connection of the contacts (source, drain, and gate) of each FET to soldered pins. The FET were fixed on the PCB with acrylate-based glue (super-glue), and they were wire-bonded with aluminium wires (25 µm Ø). For each FET, three chromium strips were defined and a pin was soldered at the end of each of them, in order to make the connections which would allow the characterization of sensors by measuring the electrical output signals, in further experiments. Finally, the wirebondings were protected by a silicon gel (Elastosil E41, Wacker) which also allows to open a chamber (~1 mm ø) for further sensing experiments, as shown in the zoom image of Figure 4.9c, and the resulting PCB strips are shown in Figures 4.9b, and 4.9c, with three bounded FET in each of them.

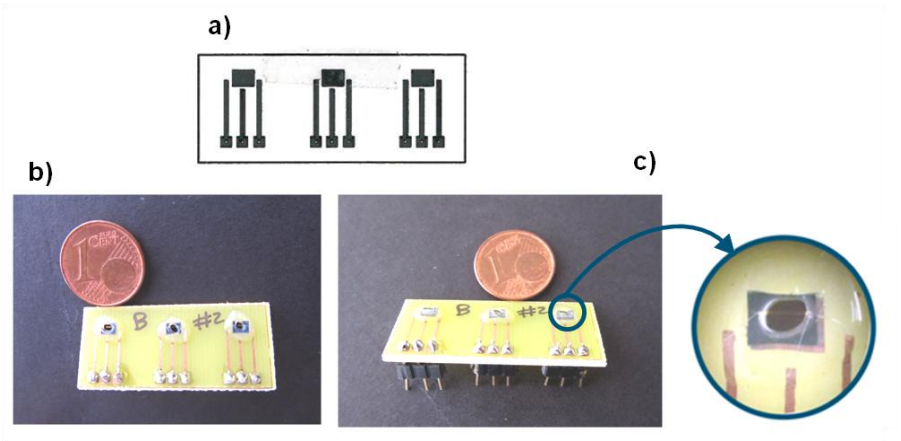

Figure 4.9 a) PCB pattern used to fabricate PCB strip, b) PCB with three individualized FET with a silicone cell, and the three chromium strips to the soldering of pins, for each FET, and c) lateral view of PCB with mounted FET, showing the soldered pins, and a zoom image of the silicone chamber where the sensing experiments were performed.

In order to verify the correct structure of the microfabricated FET after their mounting in the PCB, images from scanning electron microscopy (SEM) were taken, as shown in Figure 4.10. In SEM imaging, a high beam of primary electrons with typical energies of 1 to 40 keV is scanned over a sample, rather than photons as in optical microscopy, producing secondary electrons. Such electrons are generated and emitted in a series of signals producing a topographic image as final result. For the SEM visualization of the FET, no coating was deposited, since the microfabricated structures were already

conductive. In Figure 4.10, the contrast between Au electrodes and SiO_2 surface is clearly highlighted.

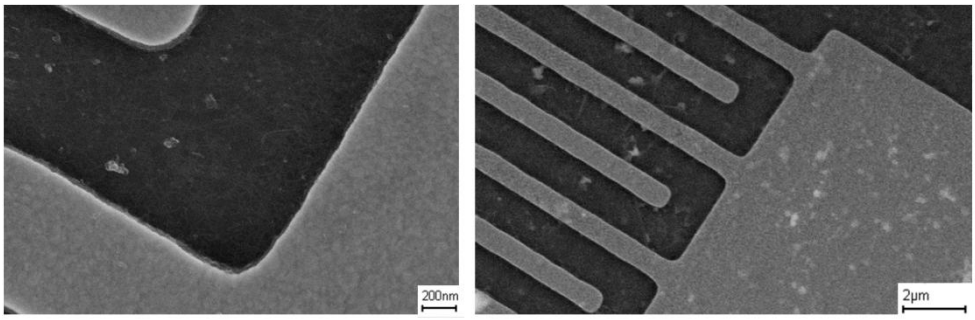

Figure 4.10 SEM images of different zones of the FET after their mounting in the PCB (obtained with RAITH 150 SEM).

4.2 Conclusions

In this Chapter 4, the microfabrication of FET was demonstrated, being an important step for the aim of this thesis, since FET are the basis for the transducer mechanism of the biosensors developed, as shown in Chapter 5. Thus, various microfabrication steps were followed to obtain disposable FET with simple electric circuit.

References

FED STD 209E cleanroom classes – Federal Standard 209E, airborne particulate cleanliness classes in cleanrooms and clean zones. Institute of Environmental Sciences, 1992. Available at: <http://www.set3.com/papers/209e.pdf> [Last access: 18 August 2013].

Chapter 5

Development of Field Effect Transistors with Single-Walled Carbon Nanotubes (NTFET) for C-Reactive Protein (CRP) Detection

5.1. Assemblage of NTFET and effects of their geometry parameters on the I-V measurements

This section reports the assemblage of NTFET with different geometry parameters by means of direct deposition for as-prepared network SWCNT dispersion, and their characterization by current-voltage (I-V) measurements. From I-V measurements, the resistance for each NTFET was also calculated in order to evaluate the NTFET performance. Based on the study of different geometry parameters, the NTFET type with lower resistance was selected for further sensing experiments due to its enhanced device performance.

5.1.1. Introduction

The NTFET approach is considered essentially for sensing applications due to the particular mechanical and electronic properties of SWCNT, since the nanometric dimensions of SWCNT together with the carbon atoms over their entire surface allows high electron transfer reactivity (Balasubramanian and Burghard, 2005). The need for a low sample volume, a quick response, the miniaturization, and the label-free process make the nano- and microfabrication of low-cost devices, such as NTFET, even more attractive and advantageous in the field of Analytical Chemistry.

NTFET are usually fabricated on Si/SiO_2 substrates based on several device architectures using dispersed SWCNT or SWCNT directly grown in substrates. In both cases, the main challenge is the control and enhancement of the SWCNT output, and consequently the improvement of the electronic characteristics of the devices. For such an accomplishment, the complete control of the process of synthesis of SWCNT is demanded for decreasing their defects and impurities and to allow a higher production yield of individual or networks of SWCNT.

Simple circuits based on NTFET have already been demonstrated with networks of SWCNT (Snow *et al.*, 2003; Hong and Myung, 2007). Although the device performance can be compromised due to the mixture of SWCNT, leading to the high resistance of electronic devices from intertube junctions (Hecht *et al.*, 2006), Martel *et al.* (2001) have referred that the combined properties of both kinds of nanotubes can produce a particular type of “building block” for electronics.

5.1.2. Experimental methods

Before every experiment, the FET surface was washed with acetone and 1-propanol to remove any traces of grease, rinsed twice with distilled water, and finally dried under a N_2 flow. A 1.2 µL droplet of the SWCNT dispersion (0.28 mg L^{-1}), based on a random network of SWCNT, was placed over the microfabricated FET surface. After a delay of 5 minutes, the liquid of droplet was blown off using a N_2 flow in order to produce a SWCNT network bridging the FET electrodes. As the solution was dried, the SWCNT diffused to the surface and adhered through strong van der Waals interactions (Lay *et al.*, 2004). This same approach based on placing the SWCNT from liquid suspensions onto fabricated substrates has been already used after the definition of the metallic electrodes (Javey *et al.*, 2002; Lim *et al.*, 2010). However, the deposition of SWCNT before the definition of metal contacts through physical techniques, such as drop casting or annealing have been also used (Wind *et al.*, 2002). The amount of the SWCNT was previously determined as the ideal to have the I-V characteristics typical for NTFET. Various volumes of SWCNT dispersion were placed on the NTFET surface with subsequent washing with distilled water, and the volume above mentioned was the minimum volume to have an ohmic behaviour on the NTFET. Volumes higher than that lead to degradation of signal, and therefore they were considered unsuitable. The SWCNT were observed at micrometer scale by Scanning Electron Microscopy (SEM, FE-SEM Hitachi SU-70) giving an idea about the density and uniformity of the individual SWCNT used for application on the NTFET. For that, the samples (NTFET) required a little pre-treatment with an ultrathin coating of graphite obtained from a Carbon Evaporator (Emitech K950x) to be electrically conductive samples, and Figure 5.1 shows the difference on the printing circuit board (PCB) surface, before and after such exposition.

Figure 5.1 Printing circuit board (PCB) surface before and after the graphite exposition.

The SWCNT dispersion was prepared through non-covalent functionalization of commercial SWCNT with an anionic surfactant (sodium cholate) after 60 minutes of sonication, and 5 minutes of centrifugation (2000 × g) at 20 ºC. The suitable experimental

conditions were found by application of an experimental design as published elsewhere (Justino *et al.*, 2012) and reported in Chapter 3.

The electrical characterization of the disposable NTFET was performed at room temperature, in air, and in real-time, using a semiconductor parameter analyzer (HP4155C, Japan). The normal laboratory conditions used for electrical characterization can cause an inherent variability in the experimental conditions but it also simulates real conditions in non-controlled environments. The parameter analyser was linked to a test fixture (Agilent 16442A, Japan) which is a closed box where the devices were positioned, and the drain, the gate, and the source of each FET were connected to respective terminals to provide the appropriate electrical circuit for sensing measurements. The software Desktop EasyExpert from Agilent was used for the acquisition of data and also for the control of the experiments through an USB/GPIB interface. The NTFET were characterized in terms of their drain current (I_D) as a function of the applied drain voltage (V_D), and the gate voltage (V_G) to obtain the output and the transfer characteristics, respectively. In order to obtain an accurate estimate of the instrumental variability, all the measurements were carried out three times.

As described in Chapter 4, the microfabrication process allowed fabricating FET with the same configuration, that is, with an interdigitated architecture, which allows a large surface area due to the interdigitated electrodes, leading to a simple and rapid analysis. Figure 5.2 shows the configuration of the FET devices (Figure 5.2b) with the main components (source, drain and gate), and the corresponding top view (Figure 5.2a). In the fabricated FET, the source and drain contact electrodes (constituted by Ti/Au layers) are positioned on the Si/SiO_2 surface. The Si substrate is the back gate (third contact of the FET configuration) and the SiO_2 is the insulating layer, with the role of isolating the SWCNT from the Si layer. It is important to refer that the leakage current, that is, the current recorded through the insulating region, was considered as negligible from I-V measurements performed without the SWCNT. In other words, the SiO_2 was perfectly deposited, since insulator characteristics were experimentally observed.

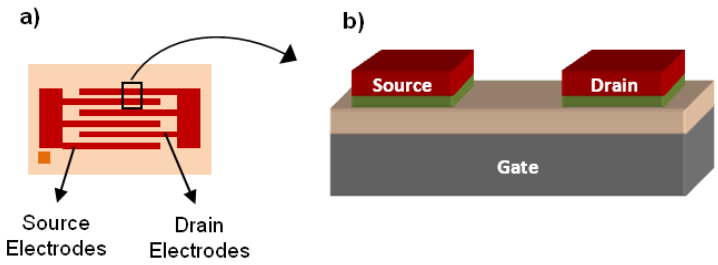

Figure 5.2 Schematic diagram of a) the top view of fabricated FET and b) the FET configuration.

As reported in Section 4.1.3, the dies of silicon wafers have FET with different geometry parameters. The influence of such geometry parameters on the electrical properties of devices was then assessed, by testing different values of thickness of gold (40 and 100 nm), distance between the electrodes (0.8, 1.5, and 2.5 µm), and number of electrodes (10 and 30). As the FET with 0.8 µm as distance between electrodes were not used, as also explained in Section 4.1.3, a total of eight types of FET were used to compare their electrical characteristics. Table 5.1 shows the employed designation of the tested FET according to their geometry characteristics. Thus, in the FET with general designation of "**#Y-Z$_n$**", **Y** is associated with the thickness of gold layer, that is, **1** corresponds to 40 nm of gold and **2** corresponds to 100 nm of gold, **Z** is associated with the distance between electrodes, that is, **A** corresponds to 1.5 µm and **B** corresponds to 2.5 µm, and **n** is associated with the number of electrodes, that is, **10** or **30** electrodes. In Figure 5.3, a layout of such types of FET is shown on a die of silicon wafer.

Table 5.1 Geometry parameters tested on the various experiments with FET.

Experiments	Geometry parameters		
	Thickness of gold layer (nm)	Distance between electrodes (µm)	Number of electrodes
#1-A_{10}	40	1.5	10
#1-A_{30}	40	1.5	30
#1-B_{10}	40	2.5	10
#1-B_{30}	40	2.5	30
#2-A_{10}	100	1.5	10
#2-A_{30}	100	1.5	30
#2-B_{10}	100	2.5	10
#2-B_{30}	100	2.5	30

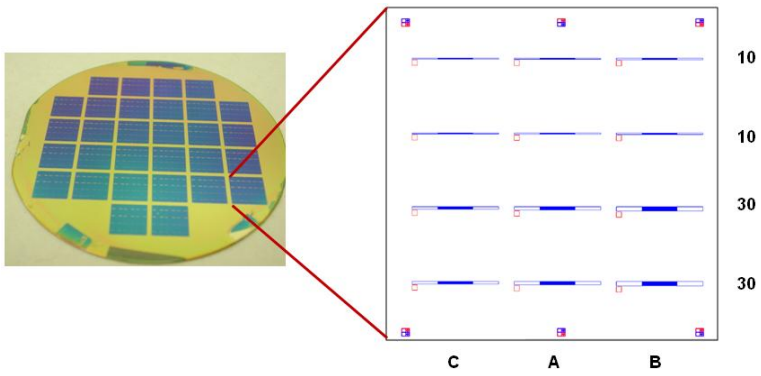

Figure 5.3 Layout of the various FET on a die of silicon wafer (lines 10 and 30 correspond to the number of electrodes and columns C, A, and B correspond to the distance between electrodes: C - 0.8 µm, B - 1.5 µm, and A - 2.5 µm).

5.1.3. Results and discussion

Figure 5.4 shows a SEM image of the surface of a typical NTFET (Figure 5.4a) where a dense network of SWCNT was observed, as well as the output characteristics (I_D-V_D graph) obtained (Figure 5.4b) where various V_G curves (between -5 to +5 V) were plotted as the means of three successive measurements.

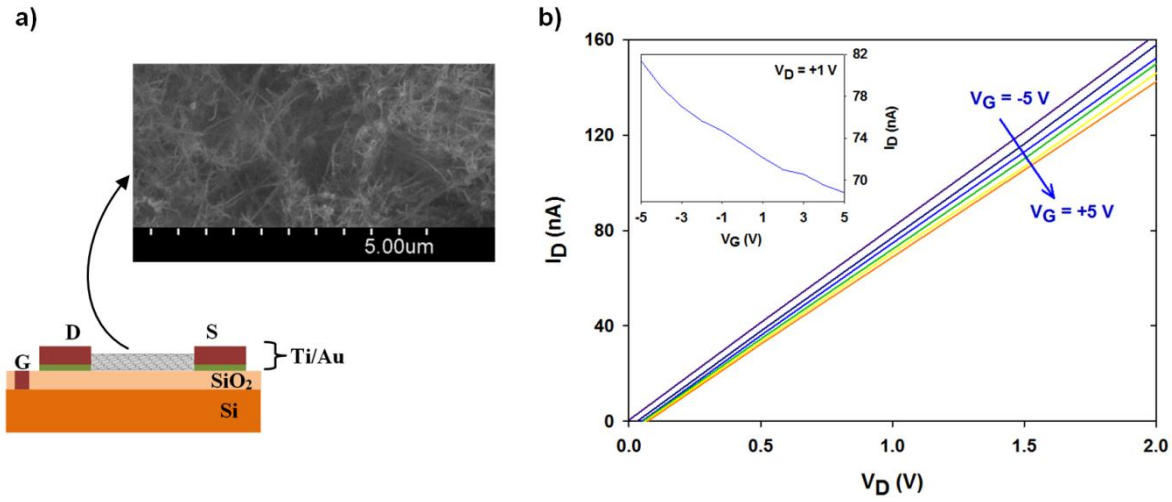

Figure 5.4 a) Schematic cross section of a typical NTFET with a zoom SEM image of the SWCNT network (image obtained with FE-SEM Hitachi SU-70), and b) Output characteristics (for V_G curves between -5 and +5 V) for one typical NTFET (inset: corresponding transfer characteristics for V_D curves between 0 and +1 V).

As shown in Figure 5.4b, there is a strong linear dependence between the measured I_D and the applied V_D, suggesting the achievement of ohmic contacts and the potential of transistor behaviour for sensing devices, since the current decreases with increasing gate voltages, being modulated linearly by the gate voltage. Such decreasing pattern is clearly observed in the inset of Figure 5.4b, where for increasing values of V_G from -5 to +5 V, the I_D values decreased from 81.4 to 68.8 nA at V_D = +1 V, also suggesting that the conduction process corresponds to hole transport as usually observed in the SWCNT (Teker *et al.*, 2006). In other words, s-SWCNT present in the NTFET have a p-type electrical behaviour in air, being the conduction made through holes (positive carriers) instead of electrons (negative carriers). Commonly, two main theories have been proposed to explain such p-type behaviour as suggested by Collins and Avouris (2000) and Derycke *et al.* (2001), that is, the p-type behaviour of NTFET could be due to the absorption of oxygen on SWCNT with the withdrawn of electrons from SWCNT surface, or

due to the metal contacts nature, respectively, but a consistent theory has not yet been well established. In the Figure 5.4b, it has been also shown that the ON/OFF ratio of 1.2, calculated from I_D values between the lower and higher V_G values at V_D = +1 V, was as low as reported in other studies with biosensors based on SWCNT networks, for example, in the works of Cid *et al.* (2008a; 2008b), and Villamizar *et al.* (2011). These low values of ON/OFF ratios are due to the presence of m-SWCNT in the SWCNT network, as also reported in the works of Hone *et al.* (2004), and Villamizar *et al.* (2009). Therefore, the random network of the SWCNT used as the conducting channel in the FET configuration displays the tolerance of individual SWCNT breakdown, since the average over a large number of SWCNT is considered (Peng *et al.*, 2008; Lim *et al.*, 2010), and they exhibit the averaged properties of a large number of random individual SWCNT (Cao and Rogers, 2008). According to Kreupl (2008), low ON/OFF ratios could be due to the parallel connection of m-SWCNT and small band gap SWCNT together with the s-SWCNT. For the different types of NTFET, the range of the ON/OFF ratio values is between 1.1 and 2.4, also confirmed by the transfer characteristics (I_D-V_G graph) observed in the inset of Figure 5.4b, where a weak dependence of I_D on the V_G was observed. It should be highlighted that in Figure 5.4, the V_D value is about +1 V, since it provides a better modulation of the NTFET electrical signal, that is, at such value the ON/OFF ratio is higher than with other V_D values. Thus, along this thesis, such value will also be used in the different sensing experiments.

Also from Figure 5.4b, the resistance values of the conducting channel made of a SWCNT network can be extracted as the inverse slope of the I_D-V_D curve in the linear range between 0 and +2 V at a fixed V_G value of 0 V for each type of NTFET, as suggested by Cid *et al.* (2010), in order to evaluate the NTFET performance. Table 5.2 reports the calculated resistance values obtained from the different types of NTFET; for each type of FET, five individual devices were used to assess the variability which was determined as coefficient of variation (CV). It was found that the experiments exhibited an adequate repeatability, since a variation between 0.6 and 4.9 % of the resistance values was observed when performing three successive measurements on the same NTFET. Curutchet *et al.* (2008) and Villamizar *et al.* (2008) obtained variations on the electrical current of 5 %, and up to 10 %, respectively, when successive measurements were carried out, which means that the low variability obtained in this work is quite acceptable. Curutchet *et al.* (2008) suggest that this behaviour is related to the influence of the environment since the devices are not passivated, which also happened with our tested devices.

Table 5.2 Resistance values obtained by the NTFET as function of various geometry parameters.

FET type	Geometry parameters			Device performance	
	Thickness of gold layer (nm)	Distance between electrodes (μm)	Number of electrodes	Resistance (MΩ)	CV (%)
#1-A_{10}	40	1.5	10	893	6.2
#1-A_{30}	40	1.5	30	483	8.9
#1-B_{10}	40	2.5	10	15.3	18.1
#1-B_{30}	40	2.5	30	179	16.5
#2-A_{10}	100	1.5	10	3.84	13.8
#2-A_{30}	100	1.5	30	53.9	11.2
#2-B_{10}	100	2.5	10	2.53	9.5
#2-B_{30}	100	2.5	30	28.3	10.3

From Table 5.2, the resistance values are in accordance with the typical resistance values range, that is, in the order of MΩ, as reported by Cid *et al.* (2010), and the variability of the resistance values for the five devices of each type of NTFET varied between 6.2 % and 18.1 %. Karp *et al.* (2009) referred that the variability on different devices can be associated with the structural properties of the deposited CNT, affecting considerably the conductance of devices with same characteristics. Justino *et al.* (2013c) have recently reviewed the main strategies for the enhancement of analytical performance of sensors using nanomaterials, particularly nanowires and carbon-based materials, emphasizing the way to overcome the problem of device-to-device variation, and discussing the influence of nanomaterial characteristics, sensor dimensions and operational conditions on sensing performance,

A three-way analysis of variance (ANOVA) was performed with the results reported in Table 5.2 in order to test whether differences exist between the levels of each parameter, that is, the thickness of gold layer, the distance between electrodes, and the number of electrodes on the response (resistance). As the normality test have failed ($p < 0.05$), the Holm-Sidak method has been performed for pairwise comparison, and an estimated statistically significant difference was found between the various types of NTFET ($p < 0.001$), that is, between NTFET with different thickness of gold layer, distance between electrodes, and number of electrodes. Specifically, the variation in geometry parameters affects the obtained resistance values of the various NTFET, and some considerations could be stated, as follows:

a) there is a statistically significant difference between the two levels (40 and 100 nm) of the factor thickness of gold layer ($p < 0.001$). Thus, by changing the thickness from 40 to 100 nm, the resistance values decrease between 0.84X and 1X, since the lower resistances are provided with 100 nm of gold layer;
b) there is a statistically significant difference between the two levels (1.5 to 2.5 µm) of the factor distance between electrodes ($p < 0.001$). Thus, when increasing the distance from 1.5 to 2.5 µm, the electrical resistance decreases for all NTFET devices between 0.34X and 0.98X, and this could be due to the higher conduction channels which provide lower resistances. On the other hand, the higher the surface area between the electrodes of devices, the higher will be the sensitivity of devices to the receptor molecules when such devices will be applied for sensing; and,
c) there is a statistically significant difference between the two levels (10 and 30) of the factor number of electrodes ($p < 0.001$). Thus, when increasing the number of electrodes from 10 to 30, the largest impact was recorded in the obtained resistance values, that is, the resistance values increased from 10.2X to 13.0X, which is also related to the large increase of NTFET dimensions with the increase of the number of electrodes. However, an exception was observed for NTFET with 40 nm-thick gold, and 1.5 µm where a small decrease of resistance values of 0.46X was recorded.

Taking into account the considerations above mentioned, the type of NTFET with 100 nm gold-thick, 2.5 µm of distance between electrodes, and with 10 electrodes (that is, 5 source and 5 drain electrodes), leads to lower resistance values and it was selected for further sensing experiments.

5.2. Calibration of the NTFET with CRP standard solutions

After their assemblage, the NTFET with 100 nm-thick of gold, a distance between the electrodes of 2.5 µm, and 10 electrodes were found to be the most suitable for further sensing experiments, and the calibration of the NTFET was performed with standards solutions of CRP, as reported in this Section.

5.2.1. Experimental methods

5.2.1.1. Immobilization of the specific antibody for the CRP (the anti-CRP)

Due to the affinity of the SWCNT with amino groups of antibodies, as reported by Wang *et al.* (2003) and Bradley *et al.* (2004), the immobilization of antibodies specific to the CRP (the anti-CRP produced in goat, Sigma-Aldrich Química, Portugal) on the SWCNT surface was directly processed through a non-covalent adsorption, since this method preserves the structure of the SWCNT and consequently their mechanical and electronic properties (Allen *et al.*, 2007). Thus, a 1 µL droplet of the anti-CRP was pippeted onto the surface of the NTFET, which were stored overnight at 4 ºC. The anti-CRP solution of 1 g L^{-1} has been previously prepared by adding 62.1 µL of the purchased anti-CRP in a volumetric flask of 5 mL, using Dulbecco's phosphate buffered (pH 7.4) saline solution (PBS). In order to prevent evaporation of the anti-CRP solution, each one of the NTFET were placed in a small Petri dish (10 cm Ø) hermetically sealed with parafilm. Any unbound molecules were then washed from the NTFET with the PBS and distilled water, and finally dried with nitrogen for further electrical characterization.

It is known that the concentration of the antibody on the CNT is associated with the number of antibodies available for interaction with the target analyte. Thus, the most suitable value of concentration of anti-CRP immobilized on the NTFET surface (1 g L^{-1}) was previously found by comparing the electrical signal (current) of four anti-CRP solutions with concentrations of 0.01, 0.1, 1, and 10 g L^{-1}. The solutions of 0.01 and 0.1 g L^{-1} were obtained through dilution of the anti-CRP stock solution (1 g L^{-1}), and the solution of 10 g L^{-1} was prepared by adding 621.1 µL of purchased anti-CRP in a volumetric flask of 5 mL using PBS as solvent.

5.2.1.2. Control experiments for determining the nonspecific binding and specificity of the NTFET

Two control assays were performed in parallel experiments in order to ascertain the nonspecific binding of other compounds and possible interferences on the SWCNT, as well as to study the specificity of the fabricated NTFET to the CRP analyte. Nonspecific binding of biomolecules is not desirable in an immunoassay, since false positive signals can be produced, and such unwanted interactions and consequent analytical artefacts

should be avoid in the process of the development of biosensors. Therefore, in order to prevent the nonspecific binding of other compounds (such as bovine serum albumin, BSA) and avoiding possible interferences on the SWCNT, a Tween 20 solution was used as blocking agent, by dropping 1 µL of 0.5 % Tween 20 in PBS on the surface of the NTFET without anti-CRP for one hour, since it is commonly used to block the CNT surface of nonspecific molecules (Chen *et al.*, 2004; Star *et al.*, 2003; Shim *et al.*, 2009). The devices were washed with PBS and distilled water, and dried with a stream of nitrogen. Then, a high concentration of CRP (100 mg L^{-1}) was deposited on the NTFET surface to evaluate the analytical response. This control experiment confirmed that the change of drain current (I_D) values when the CRP was dropped onto the NTFET surface is only due to the detection of the CRP by immunoreaction. The 100 mg L^{-1} CRP solution was the CRP stock solution considered along this thesis, and it was prepared by adding 217.5 µL of purchased CRP (human CRP, Sigma-Aldrich, Portugal) in a volumetric flask of 5 mL using PBS as solvent. For the specificity test, NTFET were exposed to BSA (1 µL of 10 mg L^{-1}) during one hour at room temperature, after the immobilization of the anti-CRP (1 µL of 1 g L^{-1}) on the blocked CNT. This assay allowed to assess the specificity of the fabricated NTFET to the CRP analyte. Since the serum albumin is the most common protein in blood serum, many studies tested the specificity of biosensing devices to the BSA, which has an amino acid sequence very similar to the human serum albumin. Then, the obtained results help to confirm the specific interaction of the CRP with its respective antibody.

5.2.1.3. Detection of CRP standard solutions

For the detection of CRP, 1 µL of each CRP solution at concentrations from 10^{-4} to 10^{2} mg L^{-1} were introduced into the silicone chamber of three individual NTFET, and incubated 15 minutes at room temperature. The NTFET were washed with distilled water, dried with nitrogen, and their electrical characterization was immediately processed. Since the FET devices are easily affected by ionic strength, as reported by Cid *et al.* (2008a), and Villamizar *et al.* (2011), the electrical measurements were carried out under dry conditions, after rinsing and evaporating the remaining antigen solution, in order to eliminate the influence of ions present in aqueous solutions which could promote noise in the electrical signal of FET, and which are no longer of concern in a dry environment. On the other hand, Ah *et al.* (2012) have obtained an enhancement of the electrical signal of

FET in dry conditions applied for the biosensing of small molecules (< 400 kDa), through an increase of two orders of magnitude of the electrical current in comparison to measurements in solution systems. Moreover, the Debye screening length, which is a screening distance where charge carriers of a molecule in buffer solution are unaffected by other charges, is absent in the dry state, being measurements more sensitive, as concluded by Kim *et al.* (2012) when they have studied label-free FET biosensors for avian influenza in both aqueous and dry environments. In this thesis, the electrical signal for both anti-CRP and CRP expositions were determined under dry conditions, following closely the works of Star *et al.* (2003; 2004).

The drain current (I_D) was measured as a function of the drain voltage (V_D), between 0 and +2 V, to find the output characteristics of the NTFET, after SWCNT deposition, antibody immobilization, and introduction of each CRP solution at various concentrations. The experiments in each condition were repeated three times. The reproducibility was evaluated performing all measurements in three individual FET devices. The transfer characteristics of such NTFET were also assessed by measurement of the I_D values against the back-gate voltage (V_G), between -5 and +5 V, at a fixed drain voltage (V_D = +1 V). The changes in I_D values in each NTFET after the exposure of any solution on the CNT surface are due to the variation of the flow of electrons through the nanotubes between the source and the drain of each NTFET, as reported by Kamahori *et al.* (2007).

As the detection of the CRP antigen (I_{CRP}) depends on the interaction with its specific antibodies (anti-CRP) and in turn, with the extent of binding of the anti-CRP onto the SWCNT ($I_{anti\text{-}CRP}$), the analytical response (current change, ΔI_{CRP}) for the sensing experiments with the fabricated NTFET was considered as the change in I_D values for each CRP concentration after their interaction with antibody ($I_{CRP} - I_{anti\text{-}CRP}$). The analytical response from various NTFET was then plotted against the values of the CRP concentration between 10^{-4} and 10^{2} mg L^{-1} to obtain the calibration curve. Due to the high stability of the interaction between the antibody and the antigen, the majority of immunosensors are of single-use, that is, they are disposable, and such configuration was also considered for the NTFET developed in this thesis. In addition to such strong interaction, there is also a very difficult regeneration of the devices, which is based in the obtaining of free antibody capturing sites by dissociation of antibody and antigen, and in the removal of antibodies from the CNT, which in turn are immobilized on the FET surface. Moreover, such regeneration should be done on each individual device, leading to expensive and time-consuming tasks.

5.2.2. Results and discussion

5.2.2.1. Immobilization of the anti-CRP

Figure 5.5 shows the variation of the drain current (electrical signal) as a function of the drain voltage (V_D) in the NTFET only with the SWCNT and in the NTFET with solutions of anti-CRP at concentrations of 0.01, 0.1, 1, and 10 g L^{-1}.

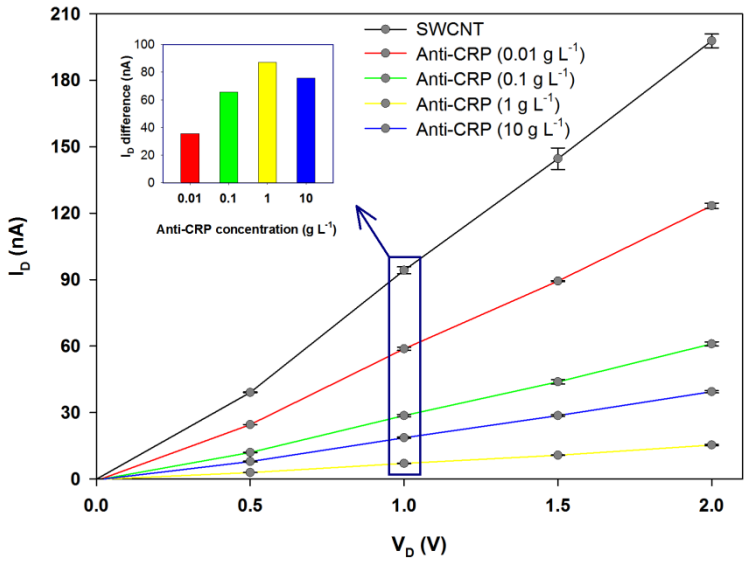

Figure 5.5 Variation of the drain current (I_D) as a function of the drain voltage (V_D) obtained for the four anti-CRP concentrations in comparison with that of SWCNT (at V_G = +1 V) (Inset: I_D difference values between SWCNT and each anti-CRP concentration at V_D = +1 V). The error bars show the standard deviation of three successive measurements.

Figure 5.5 shows that after the immobilization of the anti-CRP, the current decreases when compared to the drain current observed for NTFET only with SWCNT. As reported in the work of Teker *et al.* (2006), where a decrease in the current of the NTFET has occurred after the exposure of the antibody molecules on the CNT channel, the amine groups of antibodies provide electrons for the nanotubes, reducing the number of holes as major charge carriers, and consequently also reducing the drain current. On the other hand, it is also observed that when the antibody concentration increases, the current decreases for all V_D values, since more molecules are adsorbed onto the SWCNT surface. However, an exception is observed for the electrical response obtained when the anti-CRP concentration of 10 g L^{-1} was applied on the NTFET surface, that is, the current is higher than that obtained with a concentration of 1 g L^{-1}, which could mean that an

excess of antibodies is certainly present retarding the electron transfer on the NTFET surface and thus NTFET are not sensitive to antibody concentration above 1 g L^{-1}. With an antibody concentration of 1 g L^{-1}, the difference between the SWCNT and the anti-CRP response is higher than the differences with other antibody concentrations, as shown in the inset of Figure 5.5, where the differences between the drain current obtained for NTFET only with SWCNT and the drain current obtained for NTFET with the various solutions of anti-CRP are plotted. In this way, the antibody concentration of 1 g L^{-1} was chosen to be used in the biosensing experiments, due to the enhanced change of current signal provided relatively to the current observed for NTFET only with SWCNT, and also providing the more effective number of anti-CRP immobilized on SWCNT surface.

Figure 5.6 shows the output characteristics of a typical NTFET device (at V_G = +1 V) before (that is, only for the SWCNT) and after the modification of the NTFET surface with specific antibodies for the CRP, that is, the anti-CRP of 1 g L^{-1}. The V_G value of +1 V was chosen, since it allows a higher correlation between I_D and V_D, as studied in the preliminary work, with a set of NTFET.

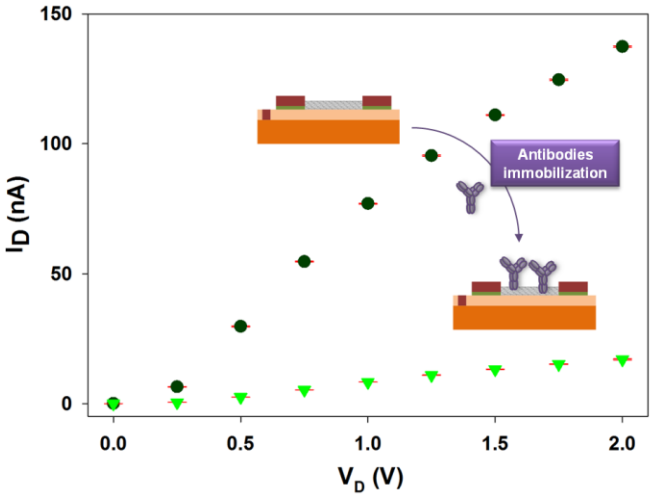

Figure 5.6 Change in output characteristics (at V_G = +1 V) of a typical NTFET before (●) and after (▼) the incubation of anti-CRP (1 g L^{-1}) for one hour. The error bars show the standard deviation of three successive measurements.

The direct charge transfer is one of the proposed mechanisms about how the immobilization of the charged analytes can affect the conductance of the SWCNT, as studied by Gruner (2006). Thus, and according to the experimental data shown in Figure 5.6, the adsorption of a charged biomolecule (the anti-CRP) at the nanotubes surface leads to a decrease of I_D values of 88 % (calculated from the difference between output

curves before and after the incubation of the anti-CRP at V_D = +1 V), which means that the immobilization of the anti-CRP onto the SWCNT has occurred. As above mentioned, the decrease of the drain current is associated with the reducing of the number of holes as major charge carriers in NTFET after the immobilization of the antibody molecules onto SWCNT.

5.2.2.2. Control experiments for determining the specificity and the nonspecific binding of the NTFET

One of the two control experiments was performed to determine the specificity of NTFET and Figure 5.7a shows the results obtained, that is, the change of NTFET response after the introduction of BSA. The nonspecific binding of NTFET was also tested and Figure 5.7b shows the obtained results from the control assay with Tween 20. As shown in Figure 5.7a, no decrease of the BSA signal is shown in comparison to the signal of the anti-CRP signal being only slightly higher. It means that no specifically binding of BSA occurred in the NTFET after one hour of incubation, that is, BSA did not bind to antibodies specific to CRP, as also verified by Quershi *et al.* (2009). The PBS signal on the NTFET was also determined, being lower than that of BSA, which demonstrates that the buffer used for the preparation of solutions do not influences the final response (I_D values).

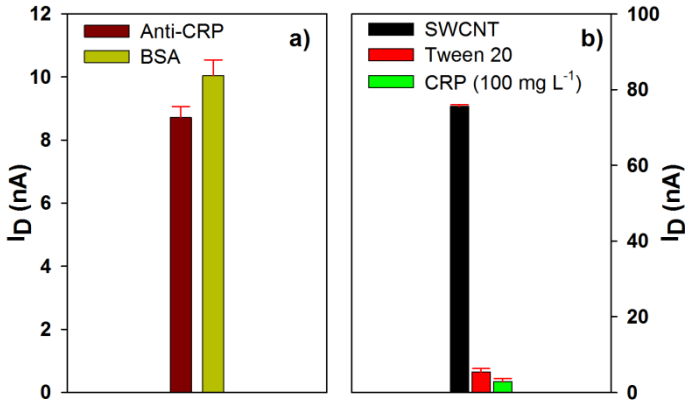

Figure 5.7 a) Control assay showing the effect of the BSA on the NTFET response, and b) response change before and after the exposure of Tween 20 to a typical NTFET (at V_G = +1 V and V_D = +1 V). The errors bars show the standard deviation of three assays.

In order to confirm that the change in drain current (I_D) is due to the interaction between the anti-CRP (the receptor) and the CRP (the analyte), an additional control assay was

performed by blocking the CNT free sites with Tween 20, without the previous exposure to the anti-CRP. The NTFET was then exposed to the high concentration of the CRP (100 mg L^{-1}), and a weak decrease in I_D values has occurred after the exposure of CRP on NTFET with Tween 20, as shown in Figure 5.7b. Based on such results, it is considered that Tween 20 blocks the CNT sites, and without the anti-CRP, the devices do not respond to the CRP, being the interaction between the anti-CRP and the CRP unique for the NTFET response.

5.2.2.3. Analytical response for the CRP standard solutions

After the characterization of the electrical behaviour of the NTFET through I-V measurements (Figures 5.4b and 5.6) and performing the control experiments, the NTFET were tested for their sensing features towards the CRP. The detection of CRP standard solutions of concentrations ranging from 10^{-3} to 10^{2} mg L^{-1} was carried out through the measurement of the drain current at V_G = +1 V and V_D = +1 V on three individual NTFET for each of the CRP concentrations. The plot of the analytical response (current change, that is, ΔI_{CRP}) is shown in Figure 5.8, where each vertical bar represents an average value based on three successive measurements, and the respective standard deviation is reflected in each error bar. The analytical response ΔI_{CRP} was considered as the change in drain current of NTFET by the interaction of CRP with their specific antibody ($\Delta I_{CRP} = I_{CRP} - I_{anti\text{-}CRP}$).

As shown in Figure 5.8, the current change decreases from 6.4 to 0.9 nA as the CRP concentrations increase from 10^{-3} to 10^{2} mg L^{-1}, since as the concentration of CRP increases, more binding sites are occupied which limits the interaction between the anti-CRP and the CRP molecules, thus leading to a larger decrease in the analytical response (ΔI_{CRP}). As a result of the binding events, that is, the antibody-antigen interactions, a geometrical deformation of nanotubes could occur, thus increasing the scattering centres among them, and decreasing the current, as studied by Star *et al.* (2003). Moreover, Gruner *et al.* (2006) suggest that the decrease of current after binding events could be due to a potential scattering which leads also to a decrease on the mobility of holes, which are the major charge carriers of the NTFET.

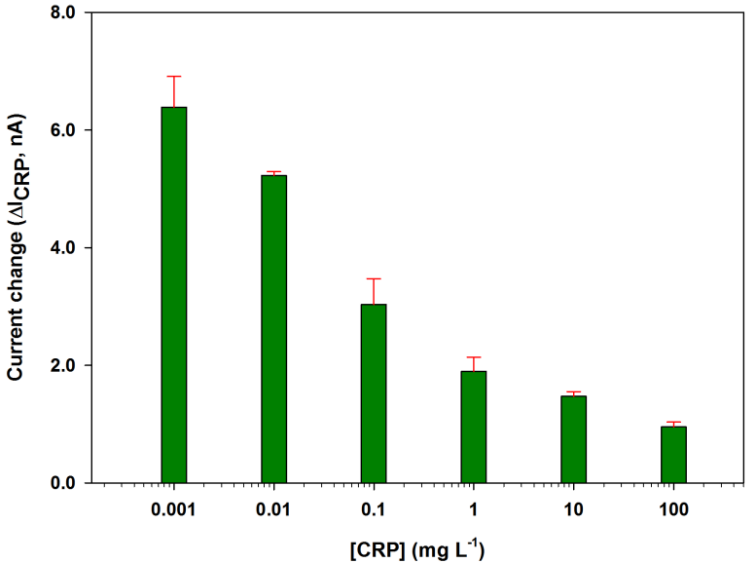

Figure 5.8 Variation of the analytical response obtained from three individual NTFET for each of the CRP concentrations between 10^{-3} and 10^{-2} mg L^{-1} (error bars show the standard deviation of three individual NTFET).

The variability of the current change for the three individual NTFET was assessed as coefficient of variation (CV), and the following results were obtained for the successive decimal concentrations of CRP between 10^{-3} and 10^{2} mg L^{-1}, respectively, 8.2, 1.4, 14.5, 12.9, 5.6, and 8.8 % with an average CV of 8.6 %. Such variability may be due to: a) the random nature of the nanotubes networks in terms of their chirality and their diameter, b) the variations in the SWCNT networks, c) the density of the SWCNT bundles, and d) different ratio of m-CNT and s-CNT, as stated by Tey *et al.* (2009), who obtained a variability between 10 and 15 % in current measurements when poly-L-lisine was detected with CNT-based biosensors. Such physical features can affect the electronic structure of the SWCNT and consequently their mobility and the current on each device. However, the ANOVA applied to the experimental data showed that there is no statistically significant difference (p = 0.958) between the various NTFET for the same concentration of CRP.

Based on the response of the NTFET to the different concentrations of CRP, as shown in Figure 5.8, the best calibration model was sought for fitting the experimental data. In a first attempt, a logistic regression model based on a four-parameter logistic (4PL) curve was applied to the experimental data, since such calibration curve has been recommended for limited reagent immunoassay (Little, 2004), and this is the most used calibration model for immunoassays (Robison-Cox, 1995). Figure 5.9 shows the 4PL

curve applied to calibrate the NTFET, and Table 5.3 contains the parameters of the model obtained by SigmaPlot software (SigmaPlot, 2008).

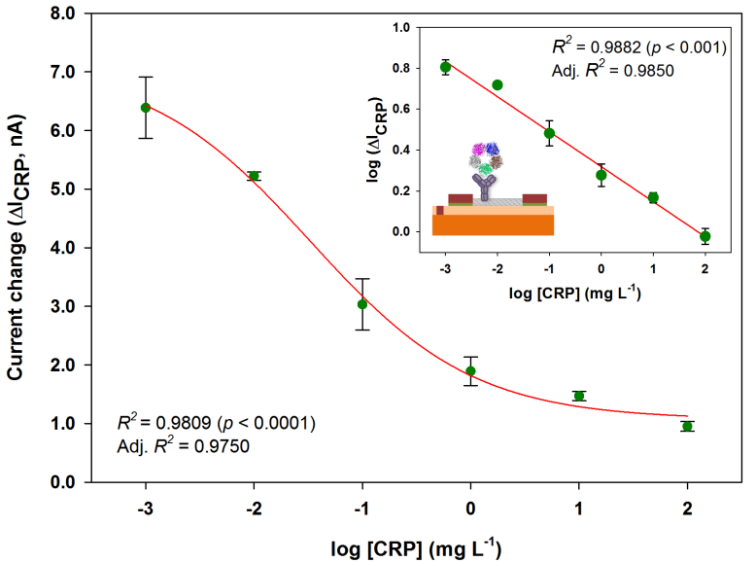

Figure 5.9 Logistic regression based on the 4PL model obtained from three individual NTFET (error bars show the standard deviations of three individual NTFET). The inset graph shows the log-log regression plot for the mean current change of the NTFET to the CRP through immunoreaction; a schematic of the principle of detection in the NTFET is also included in the inset graph.

The 4PL curve is given by the following equation:

$$y = \frac{A-D}{1+10^{(x-\log C)\times(-B)}} + D \qquad [5.1]$$

where *y* is the response, that is, the current change, *A* is the asymptotic maximum of the equation (maximum signal in the absence of analyte), *B* is the slope coefficient at the inflection point given by the parameter *C* which is the CRP concentration (*x*) to produce 50 % of the maximum *y* range, and *D* is the asymptotic minimum of the equation (background signal).

This 4PL calibration model can be applied to experimental results when the recommendations proposed by Findlay and Dillard (2007) are met, that is, a minimum of five concentrations and not more than eight are used, the measurements should be analyzed in duplicate or triplicate, and the concentration progression should be logarithmic. Such recommendations have been considered as important to ensure the adequate estimate of the four parameters of the calibration model, to reduce the standard

error of the response, and to use a fixed dilution ratio for the preparation of analyte concentrations through serial dilutions.

An appropriate adjustment to the experimental data was obtained since acceptable value for the determination coefficient was found as estimate of the goodness of fit (R^2 of 0.9809; $p < 0.001$). An adequate standard error of the estimate ($s_{y/x}$) of 0.3161 was also found as estimate of the variability of the regression model based on the measure of the accuracy of predictions, corresponding to 0.32 % of the R^2. However, such 4PL model shows as the main limitation that only the linear region of the function (with three calibration points from 10^{-2} to 10^{1} mg L^{-1}) can be used for further determination of unknown concentrations, thus restricting the working range. Therefore, if the estimated concentrations are outside such linear range, then the experiments should be repeated by diluting the sample, becoming a major drawback for the application of the method on a routine basis.

In order to attempt using the entire range of concentrations, the analytical response from Figure 5.8 was plotted in a logarithmic scale as a function of the logarithmic concentration of CRP, as shown in the inset of Figure 5.9, and the corresponding analytical parameters are shown in Table 5.3 in order to compare them with those obtained with the 4PL model. Then, a six-point log-log curve fitting was obtained with a better goodness of fitting (R^2 = 0.988, $p < 0.001$, and adjusted R^2 of 0.985) than that obtained by the 4PL model, with the possibility of using it in a much broader range of CRP concentrations (six orders of magnitude).

Table 5.3 Analytical parameters for the two regression plots of Figure 5.9.

Regression equation	4PL model	Log-log regression
	y = D + [(A - D) / (1 + (x/C)^-B]	log*y* = a + b.log*x*
Equation parameters	A = 7.1380 ± 0.5382 B = - 0.5764 ± 0.1112 C = 0.0333 ± 0.0132 D = 1.0694 ± 0.1834	a = 0.319 ± 0.0167 b = - 0.171 ± 0.00937
R^2	0.9809	0.9882
Adjusted R^2	0.9750	0.9850
$s_{y/x}$	0.3161	0.0390

$s_{y/x}$ - Standard error of estimate

In order to improve the dynamic linear range, an additional CRP solution was used with a concentration of 10^{-4} mg L^{-1}, and the log-log curve fitting was improved in comparison

with that of six points. Thus, the regression plot obtained, as shown in Figure 5.10, has a standard error of the estimate ($s_{y/x}$) of 0.036, a value of 0.9924 for the R^2, and a value of 0.9910 for the adjusted R^2, which are better than those observed in Table 5.3 for the six-point log-log curve.

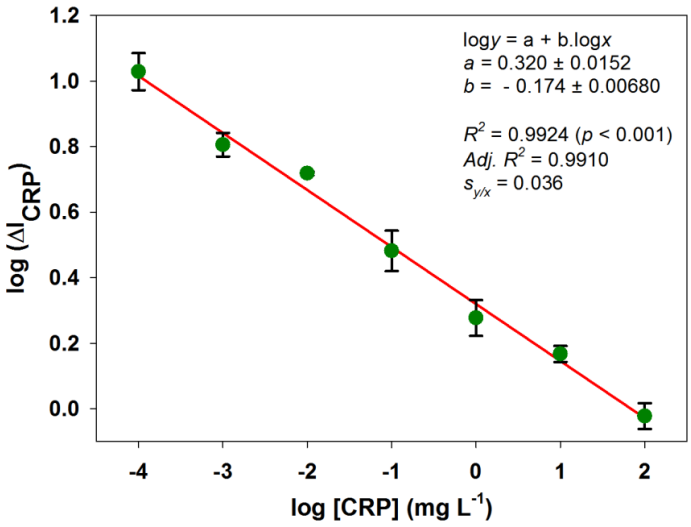

Figure 5.10 Log-log regression plot for the analytical response obtained from three individual NTFET for CRP concentration between 10^{-4} and 10^{-2} mg L^{-1} (error bars show the standard deviation of three individual NTFET).

The practical value of such disposable biosensing devices is here highlighted since it includes the normal concentration range of CRP levels in human blood serum (1 - 3 mg L^{-1}), as well as it includes values well below 1 mg L^{-1}, and well above 3 mg L^{-1} of the CRP. In other words, the residual CRP levels between 10^{-4} and 1 mg L^{-1} can be detected corresponding to the typical values for a healthy subject without any sign of inflammations, as well as it becomes possible to identify pathological cases, that is, levels higher than 10 mg L^{-1}. In addition, the dynamic linear range obtained with the NTFET (10^{-4} - 10^{2} mg L^{-1}) is much broader than in the case of traditional high-sensitivity immunoassays for CRP in serum, which is between 5 to 10 mg L^{-1} (Dominici *et al.*, 2004; FDA, 2005).

Concerning the sensitivity of the NTFET, estimated as the experimental slope of the calibration curve (Figure 5.10), it is shown that a decrease of response (current change) by about 0.2 % is observed for every 1 % increase of the CRP concentration. In turn, the limit of detection (LOD) obtained was about 10^{-4} mg L^{-1}, considering the LOD as the lowest concentration of the CRP, which is far better by 2 to 3 orders of magnitude than the traditional immunochemical assays (LOD from 0.03 to 0.2 mg L^{-1}). Furthermore, the LOD of these NTFET is much lower than the clinical relevant range of concentrations in serum,

and it is better than other measurement systems used for the detection of the CRP, such as optical RNA-based aptasensor (Bini *et al.*, 2008), chemiluminescence-based microfluidic system (Yang *et al.* 2009), and magnetic sensor (Meyer *et al.*, 2007), with LOD values of $5x10^{-3}$, $1.25x10^{-2}$, and $2.5x10^{-2}$ mg L^{-1}, respectively. It is important to highlight that the calculation of the LOD accordingly to the traditional method, that is, considering $y_{LOD}=y_B+3s_B$ (Miller and Miller, 2005) is not possible in a log-log graph, since in a graph with logarithmic axis, it is not possible to calculate the value when *x* approaches zero, because the corresponding *y* value tends to infinite. In the context of this work, the CRP solution without analyte has an electrical signal equal to the anti-CRP, since the relative electrical response of the NTFET is considered as I_{CRP}-$I_{anti\text{-}CRP}$, and thus the value for the NTFET only with the anti-CRP ($x = 0$) is zero, and that is insignificant in the context of the curve fitting shown in Figure 5.10. Then, the LOD is considered as the lowest concentration of CRP, that is, about 10^{-4} mg L^{-1}. Finally, only 1 µL of the CRP solution are required for performing the analytical determinations in the range of 10^{-4} and 10^{2} mg L^{-1} which is an additional advantage and a factor of competitiveness in comparison with the above mentioned biosensing systems. Table 5.4 shows such a favourable comparison of the analytical figures of merit (linear range and LOD) of this work against some recent biosensors forwarded for the CRP detection.

Table 5.4 Comparison of figures of merit from biosensors for the CRP detection.

Biosensor	Linear range (µg/mL)	LOD (µg/mL)	References
NTFET immunosensor	10^{-4} - 10^{2} (R^2 = 0.992)	10^{-4} [a]	This work
SPR-based immunosensor	2.0 - 5.0 (R^2 = 0.987)	1.0 [b]	Meyer *et al.*, 2006
Magnetic immunosensor	$2.5x10^{-2}$ - 2.5 (R^2 = 0.989)	$2.5x10^{-2}$ [c]	Meyer *et al.*, 2007
Electrochemical immunosensor with MWCNT	$5x10^{-4}$ - 0.5	$5x10^{-4}$ [d]	Buch and Rishpon, 2008
Optical RNA-based aptasensor	up to 0.1 (R^2 = 0.982)	$5x10^{-3}$ [e]	Bini *et al.*, 2008
QCM immunosensor	$1.3x10^{-4}$ - $2.5x10^{-2}$ (R^2 = 0.979)	$1.3x10^{-4}$ [f]	Kim *et al.*, 2009
MEMS-based microfluidic chip	NA	$1.25x10^{-2}$ [g]	Yang *et al.*, 2009
Capacitive immunosensor	$2.5x10^{-2}$ - $8.0x10^{-1}$ (R^2 = 0.9255)	NA	Quershi *et al.*, 2009
Potentiometric immunosensor with ZnO nanotubes	10^{-5} - 1 (R^2 = 0.990)	10^{-3} [e]	Ibupoto *et al.*, 2012

SPR - Plasmon surface resonance; MWCNT - Multi-walled carbon nanotubes; QCM - Quartz crystal microbalance; MEMS - Micro-electro-mechanical-systems; NA - Not Available. [a]minimum detectable concentration; [b]LOD is higher than four times the background (0.5 AU, Arbitrary Units); [c]LOD is 10 times the background noise; [d]3 times the standard deviation from the blank; [e]NA; [f]3 times the standard deviation from the baseline drift; [g]signal-to-noise ratio of 3.

The absence of systematic errors was tested by means of recovery functions, as stated by Danzer *et al.* (2004). Thus, the comparison of the CRP concentration estimated by the regression model (Figure 5.10) with respective known concentration was performed, and recoveries of 102, 93, 115, 93, 88, and 98 % were obtained from CRP concentrations of 10^{-4}, 10^{-3}, 10^{-2}, 10^{-1}, 10^{1}, and 10^{2} mg L^{-1}.

5.3. Separation of SWCNT by electronic type

According to the methodologies described in the Section 2.1.4, and taking into consideration the facilities of the available laboratories, some techniques were tested for the separation of the SWCNT by electronic character, that is, the selective reaction of a diazonium salt with the m-SWCNT, and methodologies based on agarose gel, that involves manual squeezing of the frozen and thawed gel, centrifugation, diffusion and permeation, were tested.

The methodology developed by Ghosh and Rao (2009), which employed the selective reaction of a diazonium salt of 4-heptadecafluororooctylaniline with the m-SWCNT of a dispersion, was tested and ended-up in failure by several reasons. Firstly, the experimental details are not entirely described in their work in terms of proportions of reagents, and experimental conditions. Secondly, the need of synthesis of an unstable gas (HNO_2) is very difficult, since its formation is *in situ* after the addition of a cooled aqueous solution of $NaNO_2$ to fluorous aniline in HCl, which should be cooled at 4 ºC, requiring specific laboratory conditions and safety precautions, and not clearly identified in the article of Ghosh and Rao (2009). Thirdly, in any step, a complete degree of dryness must not exist since diazonium salts are unstable at temperatures above 5-10 ºC, and some could explode if allowed to dry, being a dangerous methodology.

Methodologies based on agarose gel, that involves manual squeezing of the frozen and thawed gel, centrifugation, diffusion, and permeation (Tanaka *et al.*, 2009a) were also tested, but with no success at all. The main problem with those methods is the need for heating in order to remove the gel impurities from s-SWCNT: the gel is melted and a brief centrifugation removes the gel from s-SWCNT (Tanaka *et al.*, 2011), but such separation is not easy to perform. The control of temperature when preparing the CNT-containing gel is slightly difficult, since too high temperature of melting agarose gel may diminish the dispersability of the surfactant.

Finally, the separation process to obtain s-SWCNT and m-SWCNT from a SWCNT network was carried out in this thesis, using a column separation method with agarose beads, as reported by Tanaka *et al.* (2009b), since it was found easier and adequate to use besides allowing to obtain reproducible results.

5.3.1. Experimental methods

The column chromatography is used in this work as a method for the separation of the CNT by their electronic nature: agarose beads are used as stationary phase, sodium dodecyl sulphate (SDS) is used to eluting the m-SWCNT, and the sodium deoxycholate (DOC) solution is used to eluting the s-SWCNT. Thus, the methodology developed by Tanaka *et al.* (2009b) is a continuous separation method where the s-SWCNT show more affinity with the stationary phase than the m-SWCNT, being selectively adsorbed on the agarose beads, and then eluted with a DOC solution. The mechanism of retention of the s-SWCNT in agarose is not well understood, and various works aimed at studying this phenomenon: a) Silvera-Batista (2011) stated that the selective interaction of s-SWCNT with agarose is caused by the van der Waals forces between s-SWCNT coated with SDS molecules and agarose beads, or by their electrostatic interactions, and b) Duque *et al.* (2010) explained such interaction on the basis of the differences in surfactant coverage between the m-SWCNT and the s-SWCNT, since the m-SWCNT could be likely surrounded by a larger number of surfactant molecules. Thus, the s-SWCNT in the initial suspension could have a surfactant structure with the molecules lying flat on the sidewall of the SWCNT while the m-SWCNT could have the surfactant orientated away from the nanotube surface. As a consequence, the m-SWCNT and the s-SWCNT have weaker and stronger interaction with the agarose matrix, respectively, as explained by Silver-Batista (2011), and, when the eluent is changed from SDS to DOC, the SDS configuration is disrupted and the DOC molecules might also adsorb strongly to agarose and displace the adsorbed s-SWCNT.

A schematic diagram of the process of the SWCNT separation is shown in Figure 5.11. A 5 mL disposable syringe is filled with 2.5 mL of agarose beads (bead size range: 60 - 200 μm; Sepharose 2B, GE Healthcare). In order to make the agarose gel ready for the experiments, the purchased agarose gel, which was supplied in 20 % ethanol, was previously washed with distilled water using a vacuum pump for the complete removal of the ethanol. After the addition of the agarose gel to the syringe, the gel was washed with

water, and equilibrated with 1 % SDS solution in order to obtain a compactable bed volume. Then, 3.5 mL of SWCNT dispersion, referred as initial SWCNT network, was loaded onto the column, with the successive application of 4 mL of SDS 1 % solution to remove the shorter m-SWCNT. In this way, s-SWCNT are adsorbed in the upper region of agarose beads, while the m-SWCNT are eluted and collected at the bottom of the column into a fraction enriched in m-SWCNT, thus called m-fraction. Then, the s-SWCNT were eluted with the addition of 3 mL of 1 % DOC solution, and collected into a fraction enriched in s-SWCNT, thus called s-portion. This methodology is quick since small agarose gel beads are used, providing a large surface area of contact of the SWCNT with the stationary phase of agarose.

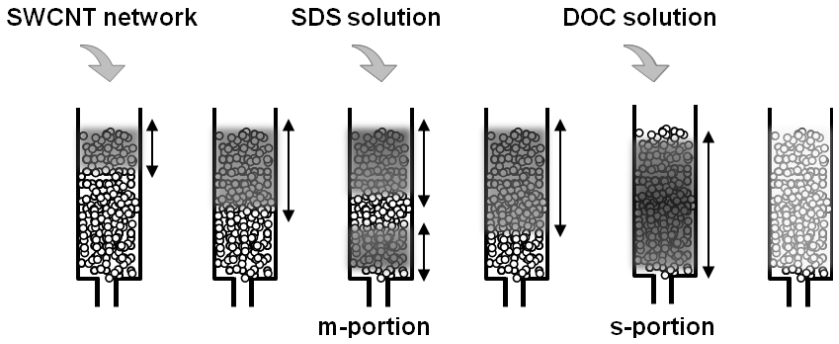

Figure 5.11 Schematic diagram of the chromatographic separation of the m- and the s-SWCNT from an initial SWCNT network.

The assessment of the relative content of the m-SWCNT and the s-SWCNT both in the m-portion and in the s-portion can be obtained by absorption spectroscopy, as suggested by Haddon *et al.* (2004). In this thesis, the UV-Vis spectroscopy and the Raman spectroscopy were used to evaluate the effectiveness of separation of the SWCNT dispersion in the m-portion and s-portion through the calculation of the content of m-SWCNT and s-SWCNT in both portions. According to Haddon *et al.* (2004), the Raman spectroscopy can be more useful when a large distribution of SWCNT diameters is present in the dispersion of the SWCNT network, since in this case the S_{22} and the M_{11} can be overlapped in absorbance spectra. Regarding UV-Vis spectroscopy, the contents of m-SWCNT and s-SWCNT in separated fractions were evaluated through the methodology discussed in Section 3.3.1, where the quantitative determination of m-SWCNT and s-SWCNT in a typical SWCNT dispersion was exemplified (Figure 3.5b), and compared with the initial network SWCNT sample before separation in order to assess whether any change in the s-SWCNT and the m-SWCNT percentages has occurred with

separation. According to An and Lee (2006), the absorbance intensity is proportional to the amount of SWCNT dispersed in the solution and furthermore, it provides information from the peaks produced by the van Hove singularities.

5.3.2. Results and discussion

After the collection of the two portions, the percentages of m-SWCNT and s-SWCNT were determined and they were compared with those of the initial SWCNT network sample by UV-Vis spectroscopy. Figure 5.12 shows the absorbance spectra obtained from the initial SWCNT network together with those obtained from the m- and s-portions after the chromatographic separation.

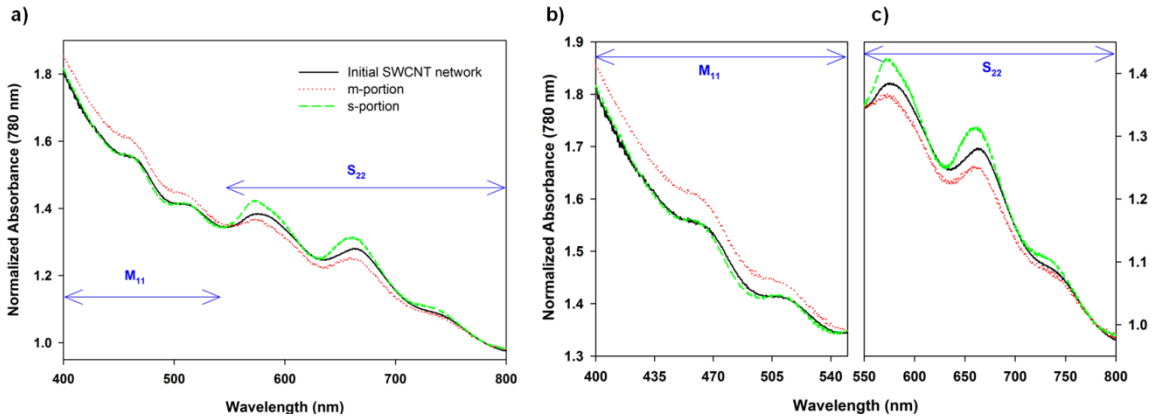

Figure 5.12 a) UV-Vis spectra of the initial SWCNT network and the separated s- and m- portions, b) zoom of the absorbance spectra in the M_{11} region corresponding to the absorbance bands of the m-SWCNT, and c) zoom of the absorbance spectra in the S_{22} region corresponding to the absorbance bands of the s-SWCNT.

According to Figure 5.12a, the absorbance features obtained from the two SWCNT portions are different from that obtained from the initial SWCNT network. Based on the methodology reported in Section 3.3.1 used to determine the content of m- and s-SWCNT from a SWCNT network, the percentages of the m- and s-SWCNT calculated from the initial SWCNT network and the separated m- and s-portions obtained by the chromatographic separation are identified in Table 5.5.

Table 5.5 Percentages and ratio of m- and s-SWCNT in the initial SWCNT network and in the separated m- and s-portions.

Sample	% m-SWCNT ($M_{11}/M_{11}+S_{22}$)x100	% s-SWCNT ($S_{22}/M_{11}+S_{22}$)x100	m- to s-SWCNT ratio
Initial SWCNT network	23.2	76.8	1/3.3
m-portion	33.0	67.0	1/2.0
s-portion	19.4	80.6	1/4.2

In the M_{11} region (Figure 5.12b), the absorbance is higher for the m-portion, which means that higher content of metallic SWCNT (33 %) was collected on the m-portion than in the s-portion (19 %), as expected. On the other hand, the s-portion has fewer m-SWCNT (19 %) than initial SWCNT dispersion (23 %), indicating a higher concentration of s-SWCNT, which was also expected and in agreement with the observations of Fujii *et al.* (2009). In the S_{22} region (Figure 5.12c), where the absorbance bands correspond to the s-SWCNT, an increase of s-SWCNT in the s-portion (81 %) was observed in comparison to the initial SWCNT network (77 %). According to Figure 5.12, in the M_{11} region, the higher absorbance was observed for the collected m-portion and in the S_{22} region, the higher absorbance was observed for s-portion, suggesting an enrichment of s-SWCNT in the last collected portion.

As discussed in section 2.1.3, the exact method for purity assessment of the SWCNT sample is not yet defined, and uncertainties still exist. For that, Raman spectroscopy has also been used to assess the purity of SWCNT, and Figure 5.13 shows the Raman spectra recorded for the initial SWCNT network and the separated m- and s-portions.

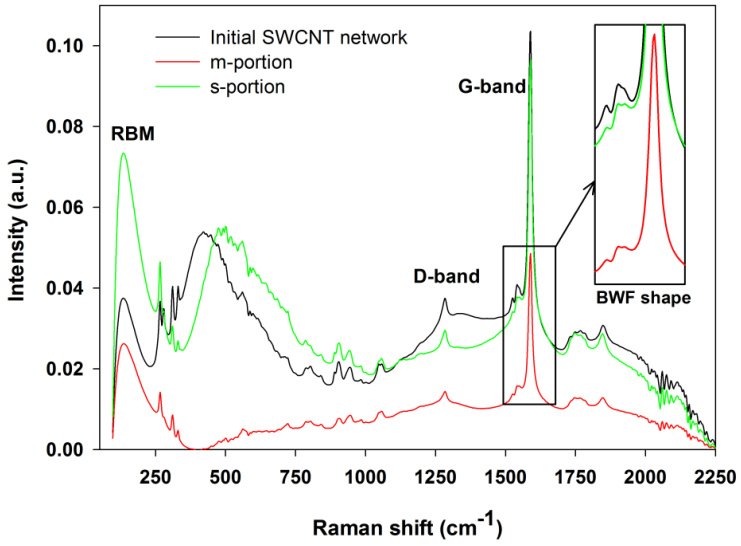

Figure 5.13 Raman spectra of the initial SWCNT network and the separated s- and m-portions.

The increasing of peaks associated with the s-SWCNT and the m-SWCNT in s- and m-portions, respectively, was also observed in Raman spectra and they could be considered as important qualitative results. From Figure 5.13, the radial breathing modes (RBM) at 149 cm^{-1} is observed for the three portions, with different intensities: the highest intensity was observed for the s-portion, being higher than that obtained for the initial SWCNT network and also higher than that obtained for m-portion. Such order of RBM intensities is in agreement with that obtained by Feng *et al.* (2011), where density gradient ultracentrifugation was used to separate the m- from the s-portions in samples of SWCNT. Regarding the intensity height of D-bands at approximately 1250 cm^{-1} which characterizes the structural disorder of the sp^2-hybridized carbons on the SWCNT, they are similar for the s- and the m-portion, as well as for the raw SWCNT, which suggests that defects were not added with the separation.

Raman spectra in the range of 1400 to 1700 cm^{-1} is associated with changes in the metallic content. A large peak was observed at 1590 cm^{-1} corresponding to the G-band, and it is well known that the G-band for the m-SWCNT has an asymmetric and broad band around 1530 - 1560 cm^{-1}, called Breit-Wigner-Fano (BWF) line shape (Brown *et al.*, 2001). In the inset of the Figure 5.13, there is an enlargement of the G-band where such BWF shape is observed for the m-portion, suggesting the metallic contribution. Such BWF shape only appears in the m-portion being absent in the Raman spectra of the initial SWCNT network and in s-portion, which means that a lower content of m-SWCNT is present in the initial SWCNT network and in the s-portion, in comparison to the content of m-SWCNT in the m-portion, which is confirmed with the percentages from the absorbance spectra observed in Table 5.5.

The separated s-portion was tested as conducting channel in the NTFET to evaluate the potential of separated SWCNT for the enhancement of biosensing activity, that is, for the detection of the CRP. The procedures for biosensing assays were the same as those described in Section 5.2, but using the separated s-portion rather than the SWCNT dispersion. The regression plot obtained for the analytical response of the NTFET to the CRP using separated SWCNT is shown in Figure 5.14, together with the same type of plot obtained with the SWCNT network. The corresponding analytical parameters are reported in Table 5.6.

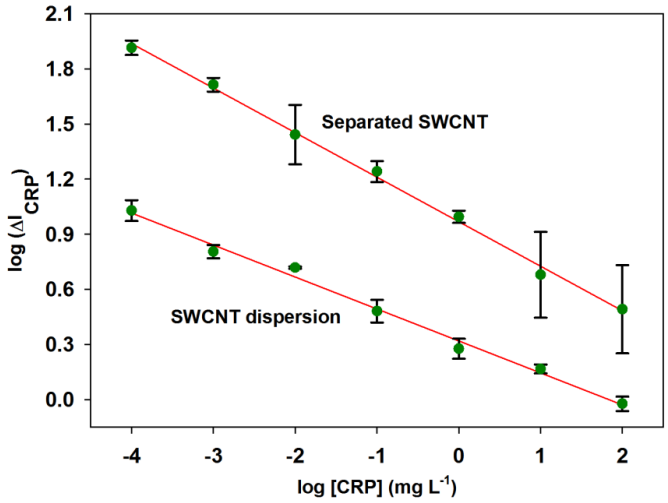

Figure 5.14 Comparison of the responses of NTFET fabricated with the SWCNT dispersion and with the separated s-portion.

Table 5.6 Analytical parameters for the regression plots of Figure 5.14.

	SWCNT dispersion	Separated SWCNT
Regression equation	log*y* = a + b.log*x*	
	a = 0.320 ± 0.0152 b = - 0.174 ± 6.80x10^{-3}	a = 0.969 ± 0.0309 b = - 0.242 ± 1.38x10^{-2}
R^2	0.992	0.942
Adjusted R^2	0.991	0.939
$s_{y/x}$	0.036	0.127

It is shown in Figure 5.14 and demonstrated in Table 5.6, that a higher sensitivity is obtained with NTFET with the separated s-SWCNT than with the SWCNT dispersion. However, the coefficients R^2 and adjusted R^2 are higher for the calibration curve obtained with the SWCNT dispersion, which means that the calibration curve obtained from the SWCNT dispersion displays a better goodness of fit than that obtained with the s-SWCNT. Similarly, a higher standard error of the estimate ($s_{y/x}$) was obtained for the separated s-SWCNT. Although there is a statistically significant difference (p = 0.012) between the data of the two calibration curves, which was estimated from a Holm-Sidak comparison method at p = 0.05, the SWCNT dispersion was considered to be used for all biosensing experiments, due to its better cost-effectiveness, since only one surfactant is needed to disperse the SWCNT, contrarily to the mechanism and the labour-intensive process to obtain the separated s-SWCNT, which needs of a chromatographic assemblage with

expensive agarose beads. On the other hand, it is considered that the increase of s-SWCNT content from the initial SWCNT network (77 %) to the separated s-portion (81 %) does not justify the expensive and time-consuming tasks involved in the separation.

5.4. Application of the NTFET to the determination of the CRP in blood serum and saliva

In this Section, the application of NTFET as immunosensors is reported for the determination of CRP concentrations in samples of undiluted blood serum and saliva collected from volunteer patients. The concentrations of CRP determined by the NTFET were compared with those obtained from a traditional methodology (ELISA technique) for the validation of the sensor. Furthermore, the CRP levels in blood serum and saliva were compared in order to identify a possible correlation between them. The correlation between serum CRP and other risk factors associated with the development of cardiovascular diseases (CVD) has also been evaluated.

5.4.1. Introduction

The CRP is a diagnostic biomarker of systemic inflammation, which is a mechanism in the atherogenesis, that is, in the accumulation of lipids on the innermost layer of arterial walls as well as the presence and accumulation of monocyte-derived macrophages and T lymphocytes in fatty streaks, resulting in cardiovascular events (Ablij and Meinders, 2002; Ridker *et al.*, 2004). The CRP is considered as a positive acute-phase protein since its level increases in response to a wide variety of disease states including CVD and systemic inflammatory conditions. The CVD are classified mainly as coronary heart disease (CHD), and lead to angina, heart attack, and congestive heart failure, thus becoming the world leading cause of morbidity and mortality, even bigger than cancer. According to the latest data by the American Heart Association, 40 % of all worldwide deaths are caused by CVD (Roger *et al.*, 2012). Furthermore, the CRP is a strong indicator of myocardial infarction, stroke, sudden cardiac death, and peripheral vascular disease (Ledue and Rifai, 2003).

The levels of CRP have no significant diurnal variation, and can thus be accurately measured (Macy, 1997). According to Smith *et al.* (2004), the CRP levels could be stable

at very high values even three months after an ischemic stroke. It is well established that the following levels of the CRP in blood serum are considered as low (< 1 mg L^{-1}), moderate (1 - 3 mg L^{-1}), and high (> 3 mg L^{-1}) risks of development of CVD (Pearson *et al.*, 2003; Danesh *et al.*, 2004). According to Adams *et al.* (2008), CVD are associated with smoking, hypertension (blood pressure ≥ 140/90 mmHg), elevated low-density lipoprotein (LDL cholesterol ≥ 160 mg dL^{-1}), low high-density lipoprotein (HDL cholesterol < 35 mg dL^{-1}), *diabetes mellitus* (plasma glucose ≥ 126 mg dL^{-1}), and predisposing factors, such as obesity and physical inactivity. Therefore, it is also of crucial importance, the interpretation of the CRP levels together with other CVD risk factors, in order to provide better prognostic information.

In comparison to the invasiveness of blood sampling, the collection of saliva is advantageous for being cost-effective, non-invasive, pain-free, stress-free, and it can be performed without special laboratory equipment (Pfaffe *et al.*, 2011). Thus, saliva may be a potential biological fluid for the diagnosis and monitoring of systemic conditions including CVD, due to the presence of many analytes derived from serum, for example, CVD biomarkers (Foley *et al.*, 2012).

5.4.2. Experimental

5.4.2.1. Collection of blood and saliva samples from volunteer patients

All serum and saliva samples were collected from volunteers at the S. João Hospital (Oporto, Portugal). All participants in this study were provided with signed and approved consent forms before sample collection, and the procedures were in accordance with Ethics Boards of the S. João Hospital through Institutional Human Ethics Committee. A copy of the consent form and the information provided to the volunteer patients before sample collection are provided in Appendix I.

Serum and saliva samples from 30 volunteer patients were used in this study: 15 samples were from healthy individuals undergoing a physical health examination, and other 15 samples were from patients with various recent inflammation conditions or diseased individuals suffering from coronary heart diseases and ischemic heart disease from the CVD unit at the Hospital. The first group of 15 healthy individuals were taken as the control patients, while the second group of diseased individuals were taken as the CVD risk patients group. The participants completed a questionnaire about their medical

history and daily habits, and a sample copy is provided in Appendix II. In the questionnaire, demographic data (gender and age) and complete lipoprotein profile (total cholesterol, LDL cholesterol, HDL cholesterol, and triglycerides) were reported together with the data on the vascular risk factors, including hypertension, *diabetes mellitus*, dyslipidemia, previous transient ischemic attack, CHD, and lifestyle factors, such as cigarette smoking, and consumption of coffee and alcohol. The complete database of results of medical history and lifestyle factors collected from questionnaires of volunteer patients is provided in Appendix III, together with the classification of risk parameters as low, normal, and high levels. The collection of biological fluids was made to more than 50 volunteer participants, but some serum and saliva samples had to be discarded for several reasons. In some cases, saliva samples were contaminated with blood, the volume of collected saliva was insufficient for further analysis, and some patients, mainly from the CVD unit, were not able to provide saliva, and thus, both the blood and saliva samples of such patients were not used in this study.

A standardized protocol was used for collection and storage of venous blood samples, that is, a volume of 8 mL of peripheral blood was drawn using Venosafe tubes with gel and clot activator, and all serum samples were isolated after centrifugation at 5000 RPM for 15 minutes at 4 ºC. The serum was divided into three aliquots and stored at -20 ºC. Regarding the collection of saliva samples, oral swabs were used, as recommended by Salimetrics Europe Ltd, collecting saliva between cheek and gum. The samples were centrifuged at 5000 RPM for 15 minutes at 4 ºC in order to pellet the mucins, and all supernatant samples were stored immediately after centrifugation at -20 ºC.

5.4.2.2. Determination of the CRP concentration in serum and saliva samples by NTFET and enzyme-linked immunosorbent assay (ELISA)

After their collection, the serum samples were assayed for the CRP, as well as for the parameters characteristic of the lipoprotein profile (that is, total cholesterol, HDL cholesterol, and triglycerides) in a reference laboratory and through diagnostic kits of Beckman Coulter. The methods used for such assays and corresponding figures of merit are grouped in Table 5.7. Only the LDL cholesterol content was not directly determined from samples, but it was estimated through the Friedewald equation, that is, LDL cholesterol is estimated from quantitative measurements of total and HDL cholesterol and

triglycerides using the relationship established by Friedewald *et al.* (1972) as follows (all concentrations are expressed in mg dL^{-1}):

$$[\text{LDL cholesterol}] = [\text{Total cholesterol}] - [\text{HDL cholesterol}] - \left(\frac{[\text{Triglycerides}]}{5}\right) \qquad [5.2]$$

The results of these assays listed in Table 5.7 were used to select the serum samples of control and CVD risk patients: control patients have CRP levels lower than 3 mg L^{-1} (corresponding to low and normal CVD risk) as well as parameters characteristics of the lipoprotein profile at normal levels, and CVD risk patients have CRP levels higher than 3 mg L^{-1} (corresponding to high CVD risk) as well as parameters characteristic of the lipoprotein profile at levels which are borderline high, high, and very high.

Table 5.7 Methods and corresponding figures of merit obtained from the determination of various parameters on blood serum of volunteer patients.

Parameter	Method and assay principle	Limit of detection	Precision (% CV)	Linearity
CRP	Immunoturbidimetric assay (immunoreaction)	0.14 mg L^{-1}	< 3.8	0.2 - 480 mg L^{-1} (R = 0.998)
Total cholesterol	Colorimetric enzymatic assay (reaction with cholesterol esterase, cholesterol oxidase, and peroxidise)	2.71 mg dL^{-1}	< 1.45	20 - 700 mg dL^{-1} (R = 0.996)
HDL cholesterol	Colorimetric enzymatic assay (reaction with cholesterol esterase, cholesterol oxidase, and peroxidase, after immunoreaction)	0.077 mg d^{-1}	< 1.92	2 - 180 mg dL^{-1} (R = 0.993)
Triglycerides	Colorimetric enzymatic assay (reaction with lipase, glycerol kinase, glycerol phosphate oxidase, and peroxidase)	0.885 mg dL^{-1}	< 1.76	10 - 1000 mg dL^{-1} (R = 1)

As above mentioned, the serum and saliva samples of selected 30 patients were used to determine the CRP concentration through the NTFET and by the ELISA traditional technique for comparison and validation of the NTFET, and also to assess whether the NTFET could be used to accurately sense the CRP level. The traditional methodology was performed using the CRP ELISA kits from Sigma-Aldrich (Portugal) for the determination of the CRP in serum and from Salimetrics Europe Ltd for the determination of salivary CRP. The design, fabrication, and assemblage of the NTFET have been described in Chapter 4, in Section 5.1, and also in a published work by Justino *et al.*

(2013a). The results regarding the concentrations of the CRP in standard solutions by NTFET were obtained from a standard calibration curve through the methodology reported in Section 5.2 of this thesis as well as in the published paper found elsewhere (Justino *et al.*, 2013b).

Prior to all assays, the frozen samples were brought to laboratory temperature (approximately 23 ºC), and they were slowly and gently mixed. The ELISA technique was performed using a human CRP ELISA kit for the determination of CRP levels in duplicate, according to the protocol provided by Salimetrics Europe Ltd. based on an enzyme-linked immunoassay with standard 96-well microplates. As the relationship between the response (optical density) and the CRP concentration in each sample may change from one assay to another, two ELISA microplates were used to estimate the inter-assay precision of the ELISA technique. Briefly, the ELISA protocol includes the following basic steps, as depicted in Figure 5.15:

a) transfer of 50 µL of 1:10 diluted saliva samples in phosphate buffered solution, standard solutions, control solutions corresponding to high and low levels of the CRP in a saliva-like matrix, and blanks (phosphate buffered solution) to the microplate wells pre-coated with mouse antibodies to human CRP;
b) addition of 150 µL of 1:250 diluted enzyme conjugate solution (that is, goat anti-human CRP antibodies linked to horseradish peroxidase, in phosphate buffered solution) to each well, and incubation at 25 ºC for 2h with mixing at 250 RPM;
c) washing of wells 4 times by adding 300 µL of phosphate buffered solution and decanting the liquid to remove unbound components;
d) addition of 200 µL of tetramethylbenzidine (TMB) to each well for color development (reaction of peroxidase enzyme with TMB for formation of the CRP peroxidase), and incubation in the dark, at 25 ºC for 30 minutes with mixing at 250 RPM; and,
e) addition of 50 µL of stop solution (2 M aqueous solution of sulphuric acid), and mixing for one minute at 250 RPM.

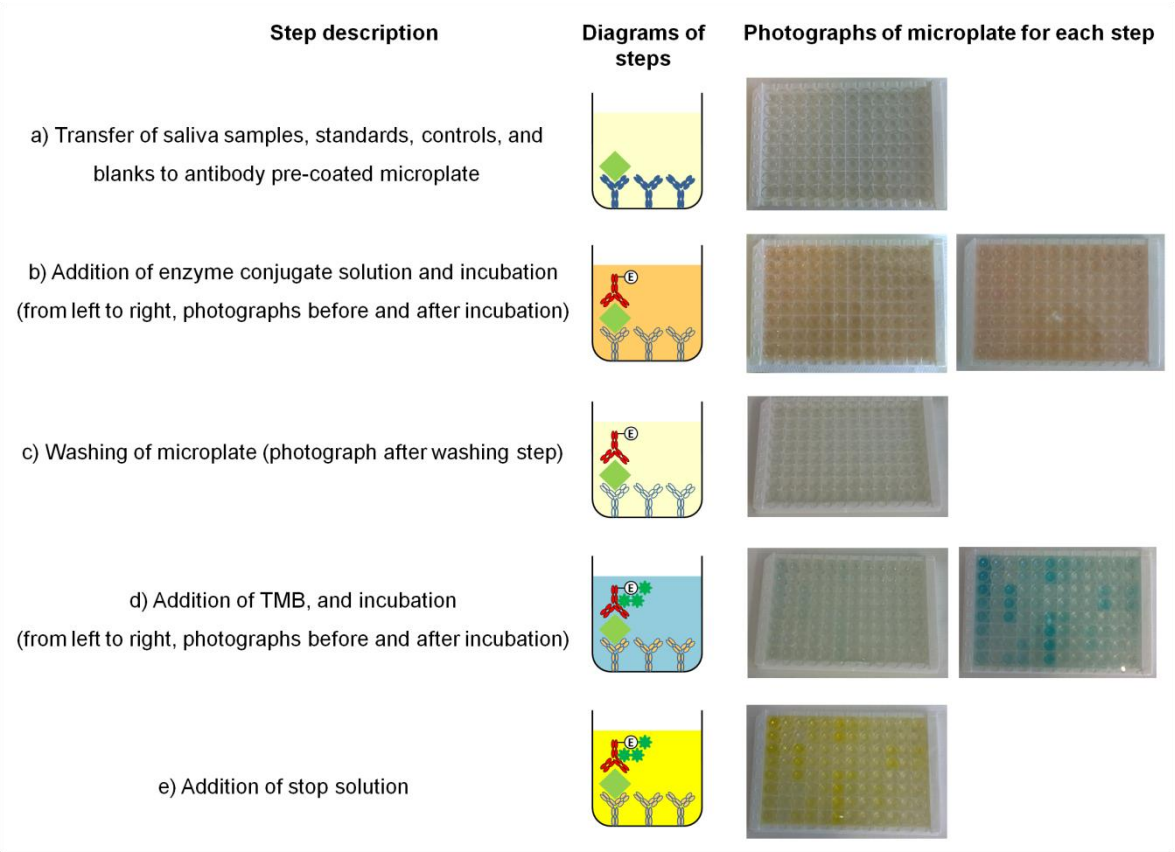

Figure 5.15 Schematic of the basic steps of the ELISA technique and corresponding photographs of microplate.

After addition of the stop solution, the readings of optical density (OD) at 450 nm with correction at 630 nm were performed on a microplate reader (SpectraMax PLUS 384). The mechanism of detection of ELISA technique is based on the proportionality between the amount of the CRP peroxidase and the concentration of the CRP. The OD values obtained from standard solutions were plotted against the CRP standard concentrations in order to obtain the calibration curve, and the OD values of saliva samples were used to determine the corresponding CRP concentrations from the calibration curve. The OD values of high and low salivary controls were used to certify that the obtained CRP concentrations with ELISA technique are similar to those claimed by the manufacturer. The intra-assay precision was determined by averaging the concentrations of CRP in duplicates high and low control samples for each of the two individual ELISA microplates, and the inter-assay precision was determined by averaging the CRP concentration of such samples obtained from the two individual plates.

Regarding the ELISA technique used for the estimation of the CRP concentration in serum samples, the procedures employed were in accordance to the supplier (Sigma-

Aldrich Química, Portugal), and they are a little different than the ELISA technique discussed above for saliva samples. The ELISA assay for serum samples was based on the quantitative sandwich enzyme immunoassay technique on a 96-well microplate pre-coated with an antibody specific for the human CRP. Serum samples were diluted 50000-fold by diluting the original serum sample with the diluent buffer provided in the ELISA kit by adding 2 µL of serum sample in 398 µL of diluent buffer to prepare a 200-fold dilution, and then, adding 2 µL of such diluted sample in 498 µL of diluent buffer. Standard solutions were obtained by diluting 12 µL of a 25 µg L^{-1} stock standard solution on 488 µL of diluent buffer to prepare a 600 ng L^{-1} standard solution (Standard 1). Then, a dilution series was produced by the consecutive addition of 400 µL of diluent buffer to 200 µL of each standard solution to prepare 200, 66.67, 22.22, 7.41, and 2.47 ng L^{-1} standard solutions (Standards 2 to 6, respectively). Control samples were obtained by dilution of standards, that is, the high control with the CRP concentration of 100 ng L^{-1} was obtained by diluting 2-fold the Standard 2, and the low control with the CRP concentration of 11.11 ng L^{-1} was obtained by diluting 2-fold the Standard 4. A volume of 100 µL of each of the CRP standard solutions, serum and control samples, were added to duplicate wells, and the microplate was covered and incubated for 2.5 hours at approximately 25 ºC at 250 RPM. In this way, the CRP present in a sample was bound to the wells through the immobilized antibody. The protocol then includes washing of wells 4 times by adding followed by discarding 300 µL of wash buffer, and addition of 100 µL of 80-fold diluted biotinylated CRP detection antibody (in buffer solution). The microplate was incubated during one hour at 25 ºC and 250 RPM. The unbound biotinylated antibodies were removed by washing the wells 4 times, and by adding followed by discarding 300 µL of wash buffer. Then, 100 µL of 300-fold diluted HRP-conjugated streptavidin solution (in buffer solution) was added to the wells, and the microplate was incubated 45 minutes at 25 ºC and 250 RPM. An additional washing step was performed 4 times by adding followed by discarding 300 µL of wash buffer. A volume of 100 µL of TMB substrate solution (3,3',5,5'-tetra-methylbenzidine in buffered solution) was then added to the wells for colour development. The microplate was incubated 30 minutes at 25 ºC in the dark and 250 RPM. The resulting colour intensity was proportional to the amount of bound CRP in the initial step. The final step included the addition of 50 µL of stop solution (0.2 M sulphuric acid) to each well, which changed the colour from blue to yellow, and the intensity of the yellow colour was measured immediately, at 450 nm in a microplate reader (SpectraMax PLUS 384). The obtained OD values for the standard solutions were plotted against the concentrations of standard solutions, and an equation was fitted in order to

obtain a calibration model, which could be used for estimation of the concentration of the CRP in the serum samples and controls.

According to Pearson *et al.* (2003), the patients with persistently CRP levels higher than 10 mg L^{-1}, should be evaluated for noncardiovascular etiologies, which means that they should be examined for sources of infection or inflammation other than CVD. In this work, 5 of the 30 serum samples from volunteer patients have values of the CRP higher than 10 mg L^{-1}. For validation of the NTFET, all data of the serum CRP were used, but for the study of the correlation of the CRP with other risk factors, the samples with levels of the CRP higher than 10 mg L^{-1} were discarded.

5.4.3. Results and discussion

5.4.3.1. Overview of clinical characteristics of the sample of population under study

The clinical characteristics of the sample of population under study are grouped in Table 5.8, according to the database of Appendix III, where the medical history and lifestyle factors are reported for each of the 30 volunteer patients. A visual inspection of Table 5.8 can lead to some conclusions regarding differences between the two groups of patients, mainly on the parameters of lipoprotein profile and consumption of tobacco, alcohol, and coffee.

In quantitative terms, the application of the *t*-test with a significance level of 5 % to the independent samples of the control (N=15) and the CVD risk (N=15) group, obtained from the SPSS software (SPSS, 2012), shows that there is a statistically significant difference for total cholesterol ($p < 0.001$), LDL cholesterol ($p < 0.001$), ratio of total/HDL cholesterol ($p < 0.001$), triglycerides ($p = 0.006$), CRP ($p < 0.001$), and age ($p = 0.011$). In other words, the two groups have patients with different patterns regarding the mentioned parameters. However, no statistically significant difference between the two groups were found for HDL cholesterol ($p = 0.132$) and body mass index (BMI) ($p = 0.131$). In this way, the *t*-test was used to compare the means of each quantitative parameter between the independent patients.

Table 5.8 Clinical characteristics of the sample of population under study.

Clinical characteristics		Control group	CVD risk group
Total, N		15	15
Men, N (%)		10 (67%)	13 (87%)
Age (years)		49 ± 13	61 ± 12
BMI (kg m^{-2})		26 ± 4	28 ± 4
CRP (reference laboratory) (mg L^{-1})		0.9 ± 0.7	8.3 ± 6.4
Lipoprotein profile	Triglycerides (mg dL^{-1})	104 ± 33	166 ± 73
	Total cholesterol (mg dL^{-1})	166 ± 19	208 ± 35
	HDL cholesterol (mg dL^{-1})	52 ± 14	45 ± 8
	LDL cholesterol (mg dL^{-1})	94 ± 17	130 ± 32
	Total / HDL cholesterol ratio	3.4 ± 0.7	4.8 ± 1.5
Tobacco consumer	Ex-smoker, N (%)	5 (33%)	3 (20%)
	Never, N (%)	10 (67%)	6 (40%)
	Occasionally, N (%)	0	6 (40%)
Alcohol consumer	No, N (%)	5 (33%)	7 (47%)
	Occasionally, N (%)	4 (27%)	2 (13%)
	>2x / week, N (%)	6 (40%)	6 (40%)
Coffee consumer	No, N (%)	3 (20%)	5 (33%)
	Occasionally, N (%)	3 (20%)	9 (60%)
	Daily, N (%)	9 (60%)	1 (7%)
Regular physical activity		8 (54%)	0
Family history of CVD		7 (47%)	6 (40%)
Stress		10 (67%)	10 (67%)
Comorbidities	*Diabetes mellitus*, N (%)	3 (20%)	5 (33%)
	Hypertension (%)	4 (27%)	12 (80%)
	Coronary Heart Disease (CHD), N (%)	3 (20%)	8 (54%)
	Dyslipidemia, N (%)	2 (14%)	9 (60%)
	Cerebral Haemorrhage (CH), N (%)	1 (7%)	3 (20%)
	Transient Ischemic Attack (TIA), N (%)	0	2 (14%)

In order to obtain a comparison between the means of the qualitative parameters, the data for all patients was coded (for example, for gender, 1 = Male and 2 = Female), as displayed in Appendix IV, and from the application of a *t*-test, a statistically significant difference was obtained between the two groups for physical activity ($p < 0.001$), hypertension ($p = 0.002$), dyslipidemia ($p = 0.001$), and Framingham score ($p < 0.001$),

which are parameters associated with the development of CVD, and there is no statistically significant difference between the two groups of patients for *diabetes* mellitus (p = 0.130), gender (p = 0.208), stress (p = 1.000), family history of CVD (p = 0.724), tobacco consumption (p = 0.682), alcohol consumption (p = 0.664), and coffee consumption (p = 0.382). Curiously, in the sample of population under study, both the control and the CVD patients are associated with conditions of stress, also observing that there is not a statistically significant difference for the family history of CVD, being two of the CVD risk factors.

5.4.3.2. Determination of the concentration of the CRP in serum and saliva samples by the NTFET and the ELISA: data comparison

As an initial step of data analysis, box plots were produced as statistics to compare the data of the CRP concentration obtained with NTFET and ELISA from the serum and saliva samples of each patient of the control and the CVD risk groups, and displayed in Appendix Va (total of 30 patients). Figure 5.16 shows the box plots obtained with SigmaPlot software (2008) and it allows comparing the maximum and the minimum values, the percentiles, and medians of such data. The medians have the advantage of being unaffected by the outliers values, and their identification is important for further statistical analysis, as also shown in Figure 5.16: the maximum and minimum observed values correspond to the upper and lower whiskers of the box, respectively; the 75^{th} and 25^{th} percentiles correspond to the upper and lower edge of the box, respectively, and the median, which marks the 50^{th} percentile, correspond to the solid line within box. Concerning the outliers, they are data points which are lower than the lower quartile or higher than the upper quartile, by more than 1.5 times the interquartile range.

Figure 5.16 shows that the levels of the CRP are higher in the CVD risk patients than in the control patients, both for serum and saliva samples, and there is a statistically significant difference between the medians of the two groups of patients for serum CRP obtained by NTFET (p (T = 120.00) < 0.001), and by ELISA (p (T = 120.00) < 0.001), as well as for salivary CRP determined by NTFET (p (T = 127.00) < 0.001), and by ELISA (p (T = 123.00) < 0.001), using a Mann-Whitney rank sum test.

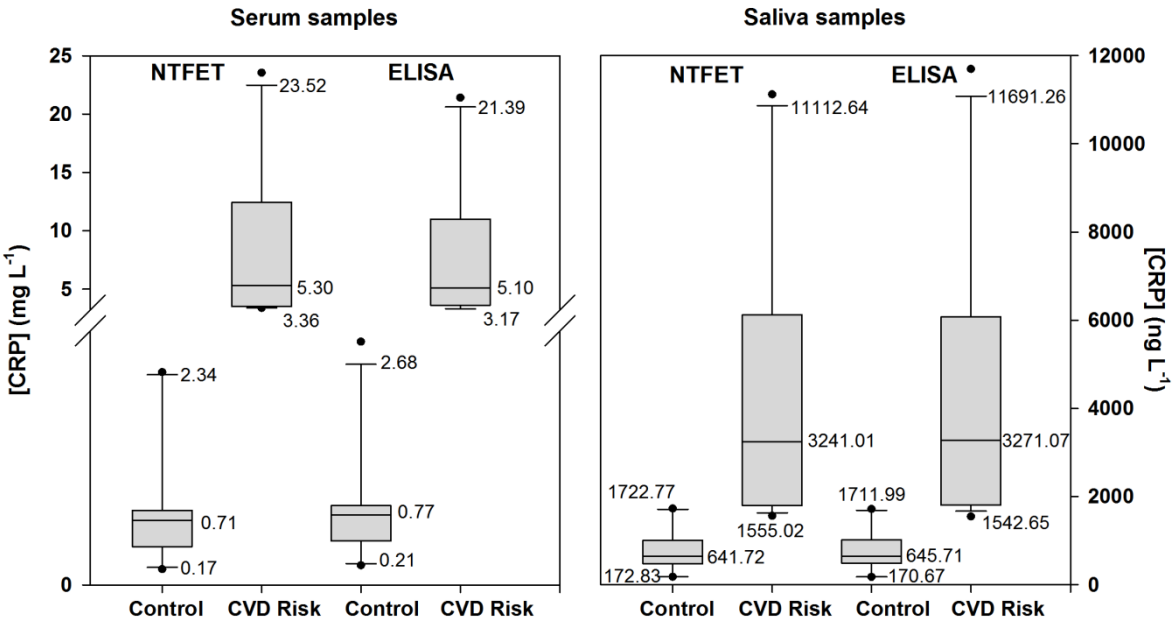

Figure 5.16 Distribution of the CRP concentrations obtained in the serum and the saliva samples of patients from CVD risk and control groups.

Based on the distribution of the CRP concentration observed in the box plots (Figure 5.16), a little overlap can be observed between the groups of patients for CRP of saliva samples determined by both the NTFET and the ELISA, since the minimum value for the box plot of CVD risk patients is slightly lower than the maximum value for the box plot of control patients. That is not observed in the box plots obtained for the CRP levels of serum samples, and the significance tests should be considered in order to compare groups for significant differences. A visual inspection of the box plots of Figure 5.16 allows to conclude that for serum samples: a) the median of the CRP levels of control patients is 0.71 and 0.77 mg L^{-1}, when determined by NTFET and ELISA, respectively, and b) the median of the CRP levels of the CVD risk patients is 5.30 and 5.10 mg L^{-1}, when determined by the NTFET and the ELISA, respectively. From the box plots, it is also observed that for saliva samples: a) the median of the CRP levels of the control patients is 641.72 and 645.71 ng L^{-1}, when determined by the NTFET and the ELISA, respectively, and b) the median of the CRP levels of the CVD risk patients is 3241.01 and 3271.07 ng L^{-1}, when determined by the NTFET and the ELISA, respectively. From the significance tests, it is concluded that there is no statistically significant difference between the median values of the CRP determined by the NTFET and the ELISA for serum samples of the control patients (p (T = 209.50) = 0.350), for serum samples of the CVD risk patients (p (T = 236.00) = 0.901), for saliva samples of the control patients (p (T = 231.00) =0.967),

and for saliva samples of the CVD risk patients (p (T = 229.00) = 0.901), using a Mann-Whitney rank sum test. Thus, the determination of the CRP in saliva and serum samples of the volunteer patients is not affected by the methodology employed, when medians of the CRP obtained from the two methodologies are compared. It can also be highlighted that the LOD obtained for the ELISA technique, calculated as three times the standard error of the estimate (Miller and Miller, 2005) was about 170.9 ± 49.6 ng L^{-1} when applied to the salivary CRP (mean and standard deviation for two ELISA microplates), and when the ELISA technique was applied to the serum CRP, the LOD of 44.3 ± 12.9 ng L^{-1} was obtained (mean and standard deviation for two ELISA microplates). The calibration details for each ELISA microplate are shown in Appendix VI. The LOD obtained for the NTFET developed in this work (Section 5.2.2.3) for serum and salivary CRP (100 ng L^{-1}) is comparable to that obtained with the ELISA technique, being better for the salivary CRP and slightly higher for the serum CRP.

From the box plots of Figure 5.16, some outliers were identified for four patients, and a statistical test for outliers was performed to evaluate whether each outlier could be discarded at a given significance level from the population under study. The Grubbs' test, which is recommended for outliers testing by ISO, was performed for each outlier by calculating the G value through the equation [5.3], thus comparing the deviation of the suspect value from the sample mean ($\bar{x}$) with the standard deviation of the sample population (s):

$$G = \frac{|\text{suspect value} - \bar{x}|}{s} \qquad [5.3]$$

The calculated value of G should be compared to the critical value of G for p = 0.05, which in this case, for 15 patients in each box plot, is about 2.41. As the G values were lower than the critical G value, the suspect values identified in the box plots should not be discarded, since they cannot be considered as outliers.

In order to summarize the descriptive statistics of the sample population (shown in Appendix Va), the mean and standard deviation (SD) were also calculated, as shown in Table 5.9, and variations in the CRP levels of serum and saliva samples collected from the control and the CVD risk patients determined by the NTFET and the ELISA technique could be compared.

Table 5.9 Mean and SD calculated of serum and salivary CRP for the 30 patients, as determined by the NTFET and the ELISA technique.

Serum CRP (mg L^{-1})	**Control patients** (N = 15)	**CVD risk patients** (N = 15)
NTFET devices	0.88 ± 0.67	8.57 ± 6.68
ELISA technique	0.93 ± 0.70	8.17 ± 5.99
Salivary CRP (ng L^{-1})		
NTFET devices	813.20 ± 520.35	4304.89 ± 3149.38
ELISA technique	814.21 ± 512.10	4350.90 ± 3218.47

Table 5.9 shows that the means of the CRP levels are similar between the NTFET and the ELISA, but they are very different between the control and the CVD risk patients, both for serum and saliva samples. In order to estimate the strength of the contribution of each source of variation, that is, type of patients (control *vs.* CVD risk), methodology (NTFET *vs.* ELISA), and clinical sample (serum *vs.* saliva), for the total variance of the results, a statistical test based on three-way ANOVA was performed with the data present in Appendix Va, and the results obtained are shown in Table 5.10. In other words, the three-way ANOVA could allow concluding whether the variation caused by the changing of a factor leads to a significant difference in the CRP levels. As the normality and the equal variance tests have failed ($p < 0.05$), that is, the data do not follow a normally distributed population, and there is variability between the group means, respectively, the Holm-Sidak test was used for all pairwise comparisons, confirming the *p* values obtained.

Table 5.10 shows that there is no statistically significant difference between the NTFET and the ELISA when they are used to determine the CRP levels ($p = 0.912$), which means that the difference in the mean values among the two levels of the factor “methodology” is not great enough to exclude the possibility that the difference is just due to random sampling variability. On the other hand, there is a statistically significant difference between the means of the CRP levels in the serum and the saliva samples ($p < 0.001$), and between the CRP levels of the control and the CVD risk patients ($p < 0.001$). Such results are explained on the basis of the comparison between the mean square of each source of variation (type of patients, methodology, and clinical sample) and the residual mean square. Thus, concerning the interactions, only the interaction between the type of patients and the clinical sample is significant since the respective mean square is higher than the residual mean square, which is understandable because the CRP levels in serum and saliva sample are very different as occurred with the CRP levels between the two groups of patients.

Table 5.10 ANOVA for the results obtained with the determination of the serum and the salivary CRP with the NTFET and the ELISA for the control and the CVD risk patients.

Source of variation	DF	SS	MS	*F*	*p*
Type of patients (control *vs.* CVD risk)	1	418.92	418.92	41.12	< 0.001
Methodology (NTFET *vs.* ELISA)	1	0.13	0.13	0.012	0.912
Clinical sample (Serum *vs.* Saliva)	1	650.70	650.70	63.87	< 0.001
Type of patients *vs.* Methodology	1	0.38	0.38	0.037	0.848
Type of patients *vs.* Clinical sample	1	418.13	418.13	41.04	< 0.001
Methodology *vs.* Clinical sample	1	0.13	0.13	0.012	0.912
Type of patients *vs.* Methodology *vs.* Clinical sample	1	0.38	0.38	0.037	0.848
Residual	112	1140.99	10.19		
Total	119	2629.75	22.10		

DF – degrees of freedom; SS – Sum of squares; MS – Mean square

The results shown in Figure 5.16 and in Tables 5.9 and 5.10 allowed a statistical analysis of the sample of the population under study by comparison of the medians and means obtained for serum and salivary CRP levels from the control and the CVD risk patients determined by NTFET and ELISA. However, the variability of the data which leads to the estimative of the reproducibility of the methodologies should also be addressed, since the CRP levels were obtained by three individual NTFET and two ELISA microplates. The results for all determinations are displayed in Appendix Va, and they show that the variability on the CRP levels assessed as coefficient of variation is between 1.0 % and 18.9 % (median of 3.6 %) when determined in serum samples of the control and the CVD patients with the NTFET, between 0.3 % and 29.9 % (median of 6.5 %) when determined in serum samples of the control and the CVD patients with the ELISA technique, between 0.2 % and 4.4 % (median of 1.4 %) when determined in saliva samples of the control and the CVD patients with the NTFET, and between 4.4 % and 39.7 % (median of 19.5 %) when determined in saliva samples of the control and the CVD patients with ELISA technique. Thus, NTFET have the capability to determine the CRP levels with lower variability than ELISA independently of the clinical sample is serum or saliva. For each of the three NTFET, three successive measurements have been performed, and taking into account the data shown in Appendix Vb, the repeatability of the NTFET, assessed as coefficient of variation, was approximately about 8.5 % for the serum CRP determinations, and about 2.5 % for the salivary CRP determinations, which

suggests a good repeatability, being lower than the reproducibility of the NTFET, as expected.

Among the many sources of variations which can be commonly found in immunoassays there are the timing, the relative humidity, as well as the washing steps of microplate, the dispensing of different volumes of samples due to the manual pipetting, and the differences in the adsorptive properties of different microplates or at different locations on the same microplate. For that, the inter-assay and the intra-assay precisions have been determined in the immunoassays performed in this work through control samples with high and low CRP levels. The inter-assay precision expresses the plate-to-plate consistency, and the intra-assay precision is a measure of variability between duplicates on the same plate. The results of the precision study for the determination of the salivary CRP and the serum CRP by ELISA methodology are depicted in Table 5.11 and Table 5.12, respectively. The intra-assay precision was evaluated from the mean of duplicates control samples in each ELISA microplate. The inter-assay precision was evaluated from the mean of duplicates of control samples for two ELISA microplates.

Table 5.11 Precision data for the determination of the salivary CRP by the ELISA technique.

	Sample	Plate	Mean (ng L^{-1})	N	SD (ng L^{-1})	CV (%)
Intra-assays[1]	High Control[3]	#1	2154	2	114.2	5 %
		#2	2119	2	206.3	10 %
	Low Control[4]	#1	138.7	2	1.083	1 %
		#2	163.2	2	11.38	7 %
Inter-assays[2]	High Control[3]		2136	4	160.3	8 %
	Low Control[4]		150.9	4	6.232	4 %

[1]CV in the ELISA kits is 1.9 % for high control sample, and 5.9 % for low control sample; [2]CV in the ELISA kits is 3.7 % for high control sample, and 11.2 % for low control sample; [3]Expected value for the high control sample as defined in ELISA kit: 2085 ± 320.2 ng L^{-1}; [4]Expected value for the low control sample as defined in ELISA kit: 166.1 ± 87.40 ng L^{-1}.

The experiments for assessing the precision allowed concluding that the CV are less than 15 %, which is quite acceptable for immunoassays. Furthermore, the expected values for the high and low control samples provided by the manufacturer of the ELISA microplates for salivary CRP, are in accordance with the mean CRP obtained in this work, as shown in Table 5.11. Only the CV for the high control samples is higher in this work than the value provided by the manufacturer of ELISA microplates for salivary CRP. This was not observed for the determinations of serum CRP, since the CV provided by the

manufacturer (Table 5.12) is higher than the values obtained in this work, and the values obtained for the high control samples were smaller than expected. Thus, it could be concluded that the ELISA technique could be used to compare the CRP levels of the patients both in saliva and in serum with those obtained with the NTFET since the results obtained were precise and accurate. On the other hand, a lower variability was observed for the determination of salivary and serum CRP levels with NTFET, allowing their use for the non-invasive monitoring of CRP.

Table 5.12 Precision data for the determination of the serum CRP by the ELISA technique.

	Samples	Plate	Mean (ng L^{-1})	N	SD (ng L^{-1})	CV (%)
Intra-assays[1]	High Control[3]	#1	72.28	2	1.125	2 %
		#2	78.89	2	1.864	2 %
	Low Control[4]	#1	15.54	2	2.090	13 %
		#2	9.42	2	0.363	4 %
Inter-assays[2]	High Control[3]		75.58	4	1.495	2 %
	Low Control[4]		13.39	4	1.226	10 %

[1]CV in the ELISA kits is less than 10 %; [2]CV in the ELISA kits is less than 12 %; [3]Expected value for the high control sample: 100 ng L^{-1}; [4]Expected value for the low control sample: 11.11 ng L^{-1}.

5.4.3.3. Determination of the concentration of the CRP in serum and saliva samples by the NTFET and the ELISA: possible correlation of CRP between the two clinical samples

As shown in the previous Section, the values of the concentrations of CRP can vary greatly from sample to sample and the values of CRP in saliva are about six orders of magnitude lower than in serum samples. A ratio between saliva and serum CRP of approximately 1/1138 for control group, and 1/1940 for CVD risk group were recorded in this study, and these ratios are in agreement with those observed by Ouellet-Morin *et al.* (2011), where a CRP ratio of 1/1634 was found. The low content of the CRP in saliva due to the limited transfer of the CRP from blood to saliva is due to the non-lipophilic nature and the high molecular weight of the CRP, thus the usually known mechanisms of transfer of lipophilic serum constituents to saliva (that is, passive diffusion or ultrafiltration) are not likely to occur, as studied by Kaufman and Lamster (2002) and Pfaffe *et al.* (2011). At stated by Ouellet-Morin *et al.* (2011), the transfer mechanism of the CRP molecules from serum to saliva remains unclear, although some studies have provided interesting conclusions. For example, Giannobile *et al.* (2009) concluded that CRP may reach saliva

through the gingival crevicular fluid or the salivary glands, during inflammation promoted by periodontal diseases. The gingival crevicular fluid is a serum exudate produced as a result of inflammation, thus the CRP and other biomarkers of serum can easily be transferred to saliva (Megson *et al*., 2010).

In order to estimate the extent of the correlation between the serum and the salivary CRP determined by the NTFET and the ELISA technique, regression analysis was performed on the data reported in Appendix Va, and the results are shown in Figure 5.17. As mentioned in section 5.4.2.2, the levels of the CRP higher than 10 mg L^{-1} should be checked for sources of infections and inflammations other than CVD, and then they cannot be considered to the study of CRP concentrations as a inflammatory biomarker for assessing the CVD risk. Thus, the five patients from the CVD risk group with the CRP levels higher than 10 mg L^{-1} were discarded. Polynomial functions with different degrees were attempted as fitting equations for the results of the salivary and the serum CRP determined by the NTFET and the ELISA methodologies, in order to determine the best curve fitting, taken into account the values of the determination coefficient (R^2) and adjusted determination coefficient (adj. R^2) as shown in Table 5.13. It should be highlighted that the adj. R^2 takes into account the number of degrees of freedom becoming crucial to conclude about the best curve fitting.

Table 5.13 Results obtained from the study of fitting polynomial functions with increasing degrees.

Degree of polynomial function	NTFET		ELISA technique	
	R^2	Adj. R^2	R^2	Adj. R^2
$y = bx$	0.775	0.765	0.770	0.760
$y = bx + cx^2$	0.882	0.872	0.863	0.853
$y = bx + cx^2 + dx^3$	0.887	0.871	0.871	0.851

As shown in Table 5.13, the evolution of the adj. R^2 allows concluding that the quadratic model is the best to estimate the correlation between the serum and the salivary CRP with the NTFET and the ELISA technique. Thus, the quadratic functions obtained from the serum and salivary CRP determined by the NTFET and the ELISA. As shown in Figure 5.17, the saliva results were plotted as dependent variable (in *y*-axis, with 25 values obtained by the NTFET and 25 values obtained by the ELISA technique) and serum samples were plotted as independent variable (in *x*-axis, also with 50 values) for possible prediction of CRP levels in serum through salivary CRP. The quadratic functions

were plotted with a zero intercept, since it is expected that the CRP is absent in saliva if the CRP in serum is zero, and the analytical parameters obtained are shown in Table 5.14.

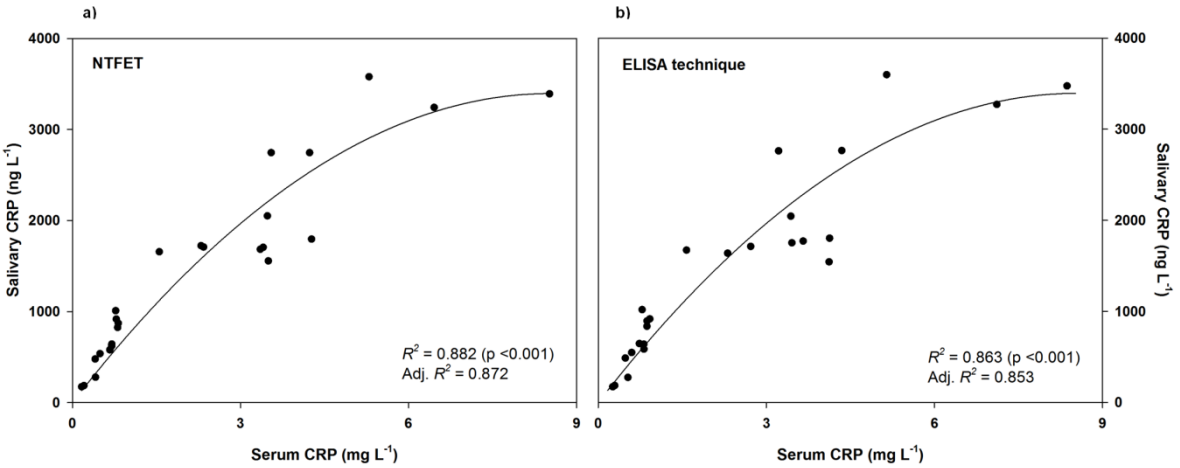

Figure 5.17 Regression plots obtained for the serum and the salivary CRP obtained by a) NTFET and b) ELISA technique.

Table 5.14 Analytical parameters associated with the regression plots of Figure 5.17.

$y = bx + cx^2$				NTFET		
Parameter	**Coefficient**	**SD**	***t* value**	**95% Confidence limits**		***p* value**
b	794.95	60.96	13.04	668.84	921.06	< 0.001
c	- 46.54	10.2	- 4.58	- 67.54	- 25.53	< 0.001
R^2 = 0.882 (p < 0.001)						
Adj. R^2 = 0.872						
$y = bx + cx^2$				ELISA		
Parameter	**Coefficient**	**SD**	***t* value**	**95% Confidence limits**		***p* value**
b	771.14	66.19	11.65	634.22	908.07	< 0.001
c	- 43.42	10.98	- 3.96	- 66.13	- 20.71	< 0.001
R^2 = 0.863 (p < 0.001)						
Adj. R^2 = 0.853						

According to Figure 5.17, the two methodologies have similar responses patterns with similar regression parameters (b and c) and similar determination coefficient (R^2), thus suggesting that the CRP concentrations determined by the NTFET are similar to those determined by the ELISA technique. The NTFET can then be advocated as an alternative to the traditional and expensive immunoassays. Moreover, there is no statistically significant difference between the serum CRP determined by the two methodologies

(p (T = 614.0) = 0.655), and between the salivary CRP determined by the two methodologies (p (T = 629.0) = 0.877). Therefore, a quadratic regression with all values could be used to estimate the correlation between the serum and the salivary CRP, then increasing the degrees of freedom, as shown in Figure 5.18. Table 5.15 shows the corresponding results obtained through the application of an ANOVA to the regression curve.

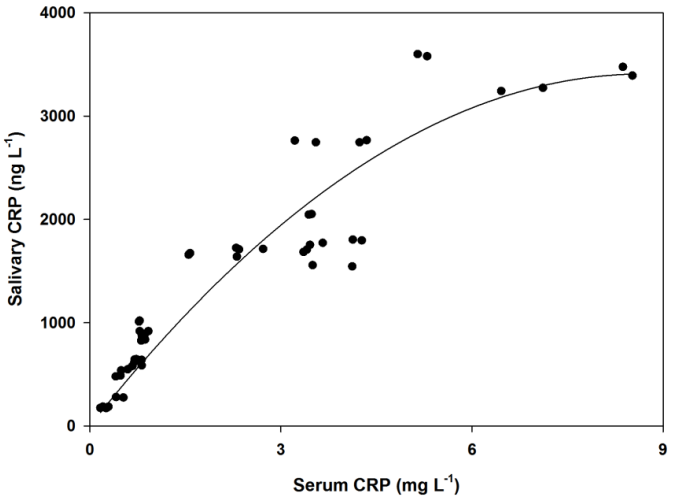

Figure 5.18 Regression plot obtained for the serum and salivary CRP data obtained by the NTFET and the ELISA technique.

Table 5.15 Analytical parameters obtained from the results of the CRP determinations (Figure 5.18), and corresponding ANOVA analysis.

		$y = 783.02x - 44.98x^2$			
Regression equation		**Coefficient**	**Standard error**	***t***	***p***
($y = bx + cx^2$)	b	783.02	44.09	17.76	< 0.001
	c	- 44.98	7.33	- 6.14	< 0.001
R^2			0.872		
Adj. R^2			0.867		
$S_{y/x}$			372.896		

Analysis of Variance	**DF**	**SS**	**MS**	***F***	***p***
Regression	2	$4.5x10^7$	$2.2x10^7$	160.56	< 0.001
Residual	47	$6.5x10^6$	$1.4x10^5$		
Total	49	$5.1x10^7$	$1.0x10^6$		

According to Figure 5.18 where the quadratic model is used to fit the data corresponding to the CRP concentrations obtained by the NTFET and the ELISA technique, correlating the serum CRP and the salivary CRP, it is shown that the central

part of the curve contains the set of data most dispersed in comparison to the sets of data at both extremes of the curve. That is, around the concentration value considered as the separation limit between patients with normal levels of serum CRP (< 3 mg L^{-1}) and patients with high risk of development of CVD (CRP > 3 mg L^{-1}), a large dispersion occurs approximately between 2.5 mg L^{-1} and 4.5 mg L^{-1} for serum CRP which corresponds to the salivary CRP levels approximately between 1700 ng L^{-1} and 2600 ng L^{-1}. On the other hand, in the lower part of the curve, there is a linear relationship between the serum CRP and the salivary CRP, while at the final part of the curve, when the high values of the CRP occur, the levels of salivary CRP tend to reach a plateau. Thus, the CRP concentration of approximately 8 mg L^{-1} was determined as the inflexion point of the curve through the first derivative of the function, which could be mean that above 8 mg L^{-1}, saliva could not contribute to the detection of the risk of a patient to develop a CVD, since the salivary CRP values do not significantly change above that value. However, even taking into consideration the above mentioned argument, the saliva samples do not lose their advantage as a non-invasive sampling method, since the CRP concentrations below and above 3 mg L^{-1} are well-determined, corresponding to patients with normal levels of CRP (with low risk of developing CVD) and patients with high risk to develop a CVD, respectively. Thus, this work is an additional contribution to clarify the correlation between the salivary and the serum CRP, which is not yet well defined in the literature. Some controversies have been found in recent works of Punyadeera *et al.* (2011), Ouellet-Morin *et al.* (2011), and Dillon *et al.* (2010). A significant association was observed by Punyadeera *et al.* (2011) with R^2 = 0.84 (p < 0.001) in cardiac patients, a moderate-to-strong association was reported by Ouellet-Morin *et al.* (2011) with R^2 = 0.52 (p < 0.001) in healthy patients, and a non significant association was found by Dillon *et al.* (2010) with R^2 = 0.001 in healthy patients. However, no information about the clinical characteristics of the participants is provided by Dillon *et al.* (2010), and then, the correlation of the serum and the salivary CRP with other risk factors associated with the CVD risk could not be tested. In this work and according to Table 5.15, a good determination coefficient (R^2 of 0.872) was obtained, which is higher than that obtained on the three works above mentioned, meaning that salivary CRP and serum CRP could be better correlated through the identified quadratic function. This correlation suggests that the saliva samples could constitute a potential advancement for the monitoring of the CRP through a non-invasive sampling, providing valuable information for assessing the risk of CVD, without involving an invasive and sometimes painful sampling procedure. Furthermore, a prediction of serum CRP levels from saliva can also be made from the regression plot of Figure 5.18,

that is, an analytical correspondence can be estimated. As the normal range of the serum CRP levels is currently well-established (Ridker *et al.*, 2003a), it should be estimated that for CRP levels at the reference value or cut-off of 3 mg L^{-1} (maximum limit below high risk levels), a correspondence for the salivary CRP levels of approximately 1900 ng L^{-1} can be established. In the same way, patients with the CRP levels in saliva approximately below 700 ng L^{-1} have low risk to develop a CVD, which corresponds to the serum level of 1 mg L^{-1} in serum. Only Ouellet-Morin et al. (2011) have determined a salivary CRP cut-off of approximately 1600 ng L^{-1}, which is quite similar to that suggested in this work. In order to confirm the cut-off value of 1900 ng L^{-1} suggested in this work for the salivary CRP, Receiver Operator Characteristic (ROC) curves, that is, plots of sensitivity (y-axis) *vs.* (1-specificity) (x-axis), were obtained to provide a statistical comparison of diagnostic accuracy of methodologies (in this case, NTFET and ELISA) in the determination of a specific analyte (in this case, the salivary CRP) through the comparison of the area under the curves, also known as the *c* statistic values (Cook, 2007), as shown in Figure 5.19a. The diagnostic capability for each methodology was determined by calculating the sensitivity (the fraction of patients with CVD risk that the test correctly identifies as positive, and determined by [true positives / (true positives + false negatives)]) and the specificity (the fraction of patients without CVD risk, that is, control patients that the test correctly identifies as negative, and determined by [true negatives / (true negatives + false positives)]), at all possible values for cut-off used to determine whether the results of the methodology are positive, as shown in Figure 5.19b, discriminating diseased *vs.* nondiseased patients, and determining the cut-off value that separate both patients. The closer the ROC curve comes to the upper left corner, the higher the overall accuracy, since sensitivity, and specificity reaches maximum values (100%). The area under the curve represents the effectiveness of the NTFET or the ELISA in discriminating the CVD risk group from the control group, and a value of area under curve of 1 represents the most accurate NTFET or ELISA, while values of the area under curve less than 0.5 indicate no discrimination, that is, poor reliability, corresponding to the diagonal line in the ROC plot (Figure 5.19a). If there are significant differences between the areas under the curves, then the corresponding *p* value is less than 0.05. The statistical parameters obtained for the ROC curves of the NTFET and the ELISA are shown in Table 5.16.

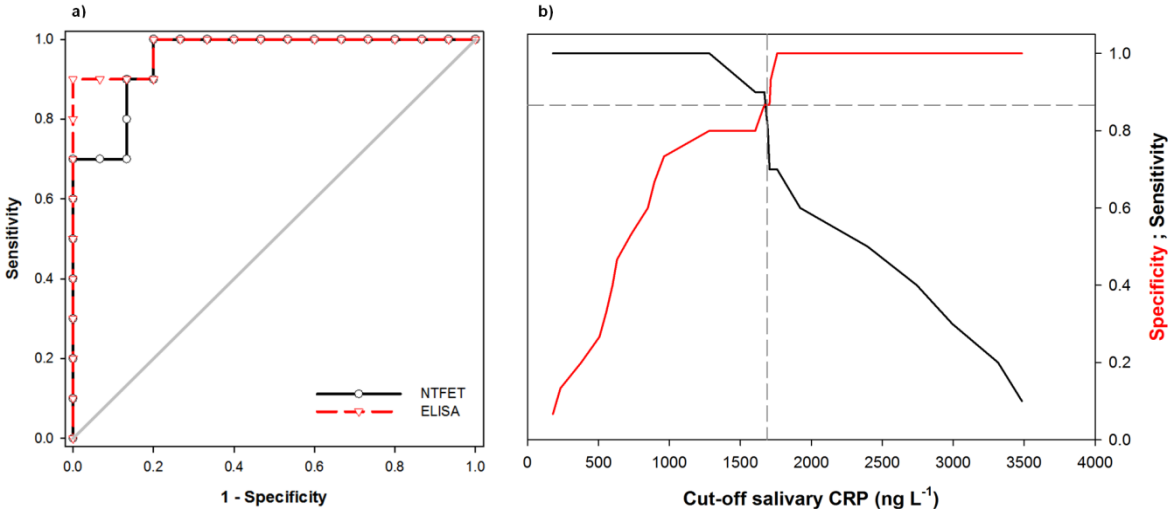

Figure 5.19 a) ROC curves obtained for the salivary CRP determined by the NTFET and the ELISA technique and b) Plot of sensitivity and specificity *vs.* salivary CRP cut-off determined by the NTFET.

From the ROC curves plotted in Figure 5.19a, the area under curve is 0.95 for the NTFET and 0.98 for the ELISA technique, as shown in Table 5.16, which means that both methodologies display similar performances as diagnostic tests for determination of the salivary CRP, with a slight advantage for the ELISA technique. Both methodologies could accurately distinguish the CVD risk patients from the control patients, since a area under curve higher than 0.96 indicates an excellent discriminatory ability, as stated by Fan *et al.* (2006). On the other hand, the ROC curve analysis shows that the NTFET achieved a 70 % sensitivity (percentage of positive samples correctly identified) and 87 % specificity (percentage of negative samples correctly identified), demonstrating that the NTFET could be used as an accurate method for measuring the salivary CRP, as shown in Figure 5.19a.

From Table 5.16, it can be concluded that the two methodologies do not show a statistically significant difference (p = 0.29), obtained from the difference between the area under the ROC curves. From Figure 5.19b, where sensitivity and specificity curves are shown in function of cut-off values, a cut-off of approximately 1700 ng L^{-1} was found for the salivary CRP determined by the NTFET, which is the intersection between the sensitivity and the specificity curves, thus allowing to discriminate the control patients from the CVD risk patients. The cut-off found is similar to that obtained from Figure 5.18 (1900 ng L^{-1}), where the salivary CRP was plotted in function of the serum CRP.

Table 5.16 Statistical parameters obtained through ROC curves for the NTFET and the ELISA technique.

Test variables	Area under curve	Standard error	95% confidence intervals	*p* value	Sample size	
					Control patients	CVD risk patients
NTFET	0.9533	0.03670	0.8814 to 1.025	$1.6x10^{-4}$	15	10
ELISA	0.9800	0.02268	0.9356 to 1.024	$<1.0x10^{-4}$	15	10

Comparison of ROC curve area	
Area difference	- 0.0267
95% confidence intervals	- 0.0765 to 0.0232
***p* value**	0.2942

Punyadeera *et al.* (2011) have established a saliva reference range with a homogeneous bead based assay, showing that the mean level of the CRP in the saliva of health human volunteers was 285 ng L^{-1}, and in cardiac patients was 1680 ng L^{-1}. Such results for healthy patients are approximately three times lower than that obtained in this work, where patients from control group with serum CRP lower than 3 mg L^{-1} (0.92 ± 0.67 mg L^{-1}) have salivary CRP concentrations of 814 ± 511 ng L^{-1}, and patients from CVD risk group with serum CRP between 3 and 10 mg L^{-1} (4.6 ± 1.7 mg L^{-1}) have salivary CRP concentrations of 2460 ± 771 ng L^{-1}. In turn, Ouellet-Morin *et al.* (2011) have obtained salivary CRP values of 1188 ng L^{-1} for healthy patients, which are different than that obtained by Punyadeera *et al.* (2011), but more similar than that obtained in this work. Thus, the determination of the salivary CRP in different works show an expected variability in their estimate of critical values, mostly due to the conditions of saliva sampling, that is, the period during the day, the time of collection, the effectiveness of brushing teeth (which should be made one hour prior the collection), or the rinsing of mouth before collection. For example, Out *et al.* (2012) have found that the salivary CRP is, on average, higher in the morning than in the evening. However, taking into account the various estimative of the salivary CRP, this thesis contributes with the most acceptable values due to the statistical control of the results reported along this work.

5.4.3.4. Correlation of the CRP concentrations in serum samples with other risk factors for the development of cardiovascular diseases (CVD)

In order to find a possible correlation between the serum CRP from the volunteer patients and other risk factors for the development of the CVD, Pearson correlation coefficients were determined with the data reported in Appendix IV. Thus, the age, the total cholesterol, the LDL cholesterol, the HDL cholesterol, the triglycerides, the BMI, and the serum CRP were correlated, together with Framingham risk score, which is an estimation of the percent probability of having a coronary heart disease in 10 years (NCEP, 2001). The calculation of Framingham score includes as risk factors the age, gender, total cholesterol, systolic blood pressure, treatment for hypertension, and cigarette consumption. According to the reference values for each risk factor, and associate Framingham score, the total points are calculated and the total risk score, that is, the 10-year risk is then estimated for myocardial infarction and coronary deaths. This current strategy for global risk assessment may have the potential to increase the accuracy of cardiovascular risk prediction, as studied by Ridker *et al.* (2003b). Furthermore, the Framingham score was also calculated for each patient of the population under study, as shown in Appendix VIIa, where the data to calculate the Framingham score for each patient is present, based on Tables of Appendixes VIIb and VIIc, which identify the reference values to calculate the Framingham score for the estimate of 10-year risk for men, and for women, respectively. It should be highlighted that the systolic blood pressure was considered with the minimum score for each patient, since the patients were not provided their blood pressure in the questionnaires, and thus, the 10-year risk percentages are displayed by default and not by excess.

The application of the *t*-test to quantitative parameters obtained from the control patients (N = 15) and from the CVD risk patients (N = 10) allowed to establish a statistically significant difference for total cholesterol (p = 0.002), LDL cholesterol (p = 0.001), Framingham risk score (p < 0.001), and triglycerides (p = 0.018) between the two groups of patients. For HDL cholesterol (p = 0.266) and body mass index (p = 0.087), there is no statistically significant difference between the two groups of patients. Correlations between all quantitative parameters were also determined by Pearson correlation coefficients to measure the extent to which each pair of variables is linearly related, and Table 5.17 shows the results obtained for the control group and the CVD risk group of patients. According to Table 5.17, and for the control patients, only correlations between total cholesterol and LDL cholesterol (73.4 %, p = 0.002), Framingham score and

triglycerides (67.2 %, p = 0.006), as well as Framingham risk score and age (70.7 %, p = 0.003) are significant. Regarding the group of CVD risk patients, the CRP levels were found to be strongly correlated with total cholesterol (80.5 %, p = 0.005), and LDL cholesterol (74.2 %, p = 0.014). Recently, the CRP and the LDL cholesterol have been identified as equally strong predictors of cardiovascular risk, being both equally important for quality clinical care, as stated by Ridker *et al.* (2013), which can explain the results of Table 5.17.

Table 5.17 Correlation coefficients (R) and respective p values for each pair of parameters obtained from serum samples of the control patients and the CVD risk patients (the bold values are statistically significant at the p = 0.05).

Control patients							
R ***p* values**	**Serum CRP**	**Total chol.**	**HDL chol.**	**LDL chol.**	**Triglycerides**	**Age**	**BMI**
Total chol.	0.183 0.515						
HDL chol.	0.042 0.882	0.470 0.077					
LDL chol.	0.132 0.639	**0.734** 0.002	-0.163 0.561				
Triglycerides	0.092 0.745	-0.035 0.901	-0.344 0.209	-0.147 0.602			
Age	-0.307 0.266	0.025 0.929	-0.063 0.825	-0.077 0.784	0.399 0.141		
BMI	0.371 0.174	0.017 0.953	0.239 0.390	-0.148 0.598	-0.076 0.788	0.151 0.590	
Framingham score	0.000 1.000	0.065 0.818	-0.250 0.369	0.012 0.965	**0.672** 0.006	**0.707** 0.003	-0.271 0.328
CVD risk patients							
R ***p* values**	**Serum CRP**	**Total chol.**	**HDL chol.**	**LDL chol.**	**Triglycer.**	**Age**	**BMI**
Total chol.	**0.805** 0.005						
HDL chol.	-0.054 0.882	0.217 0.547					
LDL chol.	**0.742** 0.014	**0.954** 0.000	0.241 0.503				
Triglycerides	0.342 0.334	0.203 0.573	-0.527 0.118	-0.061 0.868			
Age	-0.178 0.623	-0.049 0.892	**0.661** 0.037	0.111 0.760	**-0.766** 0.010		
BMI	0.130 0.721	-0.061 0.867	-0.459 0.183	-0.050 0.891	0.182 0.614	-0.632 0.050	
Framingham score	0.224 0.534	0.154 0.671	0.202 0.671	0.070 0.847	0.148 0.684	0.377 0.283	-0.544 0.104

According to Ledue and Rifai (2003), the main sources of variability which affect the CRP results are the race and the ethnicity, the age and gender, lifestyle factors such as physical activity, smoking, alcohol, anti-inflammatory drugs, and hormone therapy influence. In this way, it is recommended, for accurate practice, that the interpretation of the CRP concentrations should be made in the context of the medical history of patients, as stated by Suarez (2004). Thus, besides the correlation between quantitative parameters, as shown in Table 5.17, it is important to know how the interaction between quantitative parameters (such as serum CRP, total cholesterol, HDL cholesterol, LDL cholesterol, triglycerides, BMI, age, and Framingham score) and qualitative parameters (such as gender, stress, hypertension, dyslipidemia, *diabetes mellitus*, family history of CVD, physical activity, as well as the consumption of tobacco, alcohol, and coffee) could explain the differences of clinical characteristics between the control and the CVD risk patients. Thus, a categorical principal components analysis (CATPCA) was performed with SPSS software (SPSS, 2012) to study both quantitative and qualitative parameters that is, using both nominal and ordinal parameters. Linting *et al.* (2007) reviewed this specific type of principal components analysis, mostly used in social and behavioural sciences, where each observed value is referred to a category, and a large number of variables can be reduced to a much smaller number of uncorrelated linear combinations of these variables, called components loadings, that reproduce as much variance from the variables as possible. Appendix IV shows the set of results, obtained for each patient of the control and the CVD risk group, and used to perform the CATPCA. For each variable, here called parameter, eigenvalues are calculated as a measure of describing the variance explained by each parameter. Then, the higher variance explained by such parameters occurred when the eigenvalues attained the unit, as shown in Table 5.18, where the eigenvalues obtained from the CATPCA performed with the 18 parameters, and corresponding variance are shown.

Table 5.18 Eigenvalues obtained from the 18 parameters measured and corresponding variance in the data.

Principal components	Eigenvalues	Variance (%)	Cumulative variance (%)
1	4.82	26.8	26.8
2	3.07	17.0	43.8
3	1.93	10.7	54.5
4	1.91	10.6	65.1
5	1.42	7.9	73.0
6	1.11	6.1	79.1
7	0.91	5.1	84.2
8	0.80	4.4	88.6
9	0.59	3.3	91.9
10	0.39	2.1	94.0
11	0.29	1.6	95.6
12	0.23	1.3	96.9
13	0.18	1.0	97.9
14	0.16	0.9	98.8
15	0.10	0.5	99.3
16	0.05	0.3	99.6
17	0.04	0.19	99.8
18	0.02	0.11	99.9
Total	18	100	

Table 5.18 shows that the data can be explained by six components, since their eigenvalues are higher than the unit, accounting for about 79% of the total variance. The two first components were used to produce a biplot, according to the coefficients shown in Table 5.19 for components loadings, which explain 44 % of the total variance of the data (Table 5.18). The component loadings are measures obtained from the parameters and they are equal to the correlation coefficients between the principal component and the parameter. According to Table 5.19, the higher contributions (component loadings > |0.5|) to the first component are observed for the CRP, total cholesterol, LDL cholesterol, BMI, age, hypertension, dyslipidemia, and Framingham score at positive level, as well as by physical activity at negative level. On the other hand, triglycerides, stress, alcohol consumption, and coffee consumption contribute positively, and dyslipidemia contributes negatively to the second component.

Table 5.19 Coefficients obtained for the object points and the components loadings.

Sample	Object points		Parameters	Component loadings	
N. º	Component 1	Component 2		Component 1	Component 2
1	1.298	2.204	CRP	0.788	0.354
2	0.973	0.875	Tot_Chol	0.631	0.310
3	1.176	-1.594	HDL_Chol	-0.170	-0.426
4	0.886	0.291	LDL_Chol	0.536	0.210
5	0.104	-0.159	Triglyc	0.455	0.575
6	1.008	-0.117	BMI	0.510	0.052
7	0.828	0.174	Age	0.623	-0.468
8	1.960	1.158	Gender	-0.419	-0.400
9	1.307	-1.030	Stress	-0.322	0.529
10	0.867	-0.152	Hypertension	0.756	-0.224
11	-0.664	0.500	Dyslipidemia	0.661	-0.589
12	-0.272	0.449	*Diab_mell*	0.482	-0.252
13	-1.316	-0.414	Fam_Hist	-0.235	-0.333
14	-1.252	0.993	Phys_Activ	-0.656	0.367
15	-1.288	0.959	Tobacco	-0.007	0.144
16	-1.032	0.497	Alcohol	-0.091	0.756
17	-0.624	-0.061	Coffee	0.198	0.536
18	-1.104	0.478	Framing_score	0.756	0.203
19	-0.156	1.015			
20	-1.068	-0.777			
21	-1.418	-0.838			
22	-0.839	0.248			
23	0.204	-1.023			
24	0.090	-1.111			
25	0.333	-2.563			

The dispersion of the object points, which correspond to the 15 control patients and to the 10 CVD risk patients, is shown in Figure 5.20a, according to the coefficients calculated for each component, and the biplot with the object points and with the component loadings is displayed in Figure 5.20b.

From Figure 5.20, the two groups of patients are separated, since the patients who have similar clinical characteristics have similar components loadings, that is, they lie close to each other in the space defined by the parameters measured. Thus, the various CVD risk patients are included in the right quadrants of the biplot, where the parameters triglycerides, serum CRP, total cholesterol, LDL cholesterol, BMI, Framingham score, hypertension, dyslipidemia, and *diabetes mellitus* are the most strongly associated with such patients. These results reflect the association of CVD risk patients with the parameters which are considered as risk factors for the development of a CVD, which allows concluding that the determination of the serum CRP also contributes as a predictor of the risk to develop a CVD in association with other risk factors. It should be pointed that

the patient 5 of the CVD group is slightly detached from the other patients of this group (Figure 5.20a), but its characteristics do not justify its exclusion from the group. Thus, as shown in Figure 5.20 containing the results obtained from the CATPCA, the patient 5 is also included in the oval form which groups the CVD risk patients.

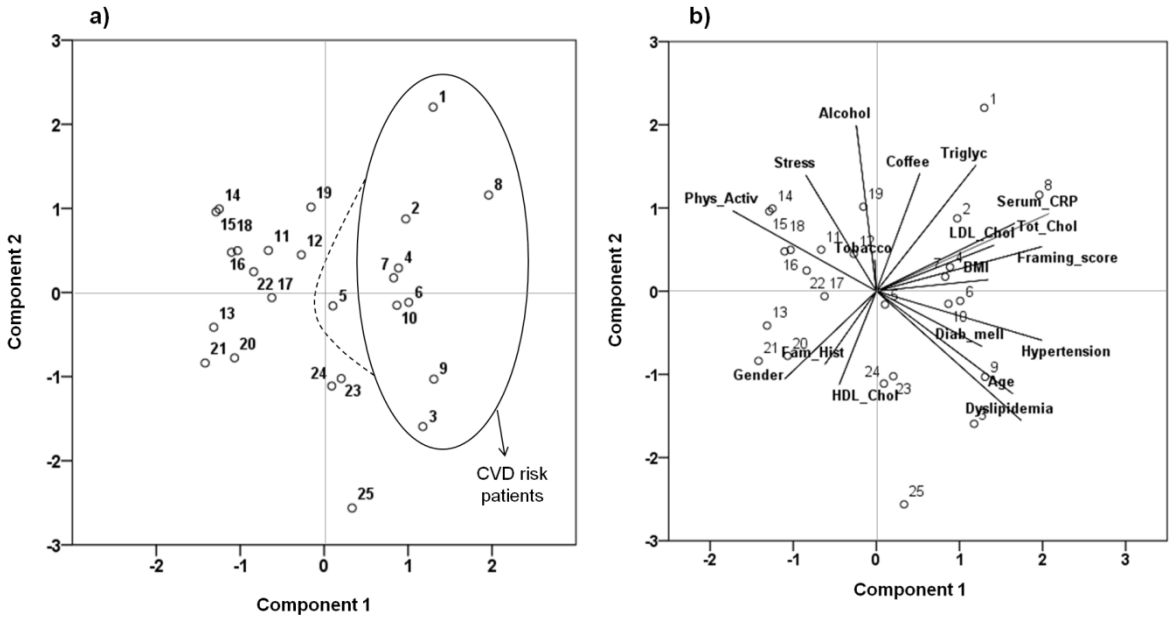

Figure 5.20 Results obtained from CATPCA: a) plot of the object points, which correspond to the CVD risk patients (number from 1 to 10) and the control patients (points from 11 to 25) and b) biplot for the two first components with different patients and measured parameters (component loadings).

According to the National Institutes of Health (NCEP, 2001), *diabetes mellitus* is regarded as a high risk contributor to develop a coronary heart disease, and the major risk factors that are associated with high LDL cholesterol, known as the major cause for coronary heart diseases, are the tobacco consumption, hypertension, family history of CVD, and age, also conferring higher risk to develop CVD in 10 years, determined by the Framingham score. In this way, and also taking into account the conclusions of the American Heart Association (Ridker, 2003a), where the CRP levels are considered to be increased by a positive history of smoking, elevated BMI, elevated triglycerides, and *diabetes mellitus*, it should be highlighted that the results obtained in this work, mainly from the biplot of Figure 5.20b, could contribute to the elucidation of the association of the CRP with the CVD risk factors. Only the family history of CVD does not contribute to the separation between the control and the CVD risk patients. For example, Albert *et al.* (2003) have reported the relation of the plasma concentration of the CRP and the

calculated Framingham score, indicating that individuals in the lowest CVD risk were at least half of those individuals in the highest CVD risk category. When BMI increases, an increase in adipocytes occurs with elevation of interleukin-6 (IL-6), and thus increasing the CRP, since IL-6 is one of the cytokines that cause an increase in acute-phase reactants, such as the CRP, according to the findings of Ford (1999). In turn, Rawson *et al.* (2003) concluded that an elevated CRP is associated with both high BMI and low physical activity in cross sectional studies. In fact, in this work, the physical activity is not expressed as significant parameter for the CVD risk patients, contrarily to the BMI. Although CRP levels are affected by obesity, as referred by Gupta *et al.* (2012), they have been concluded that the association between CRP and atherosclerosis decreases in obese individuals.

5.5. Conclusions

The NTFET were developed for biosensing of the CRP in clinical samples that is, blood serum and saliva, using SWCNT networks as transduction components. The assemblage of the NTFET was performed with a uniform and stable SWCNT dispersion, which was obtained after 60 minutes of sonication, and 5 minutes of centrifugation at 2000 × g, and with the FET fabricated with 100 nm of gold layer, a distance between electrodes of 2.5 µm, and 10 electrodes.

According to the results obtained, the NTFET were capable of quantifying the CRP concentrations over a large linear range between 10^{-4} and 10^{2} mg L^{-1}, using a log-log regression model with a strong determination coefficient (R^2 = 0.992; $p < 0.001$). Thus, the residual levels of the CRP in healthy persons without any sign of inflammation (with the CRP levels below 3 mg L^{-1}), as well as critical levels of the CRP responsible for pathological evidences (that is, higher than 3 mg L^{-1}) could be detected with the NTFET. The cost-effectiveness of analysis as well as the rapid, label-free, and simple use associated with the disposable NTFET makes them much more fit for purpose and advantageous than the currently available analytical systems.

When applied to clinical samples, the NTFET provided analytical results comparable with those obtained by a traditional ELISA methodology, taking into account the similar CRP levels in blood and saliva samples from volunteer patients, since there was no statistically significant difference between the two methodologies (p = 0.912). Furthermore, as a strong correlation was found between the salivary and the serum CRP both determined by the NTFET and the ELISA, it is suggested that the developed NTFET constitute an alternative for the use of point-of-care testing methodology to detect the risk

of developing a CVD, based on a non-invasive sampling, and also leading to the establishment of a new range of CRP levels in saliva samples.

From this work, it was also found that triglycerides, serum CRP, total cholesterol, LDL cholesterol, BMI, Framingham score, hypertension, dyslipidemia, and *diabetes mellitus*, known as risk factors to develop a CVD, are the parameters responsible for the separation of the control and the CVD risk patients used in this study, when an optimized principal components analysis was performed.

References

Ablij H.C., Meinders A.E., 2002. C-reactive protein: history and revival. *Eur. J. Intern. Med.* 13, 412-422.

Adams J.E., Clinical integration of C-reactive protein for primary and secondary risk factor stratification. In: Adams J.E., Apple J., Jaffe A.S. (Eds.) Markers in cardiology: a case-oriented approach, Blackwell Publishing Ltd, Oxford, 2008.

Ah C.S., Park C.W., Yang J.-H., Lee J.S., Kim W.-J., Chung H., Baek I.B., Kim J., Sung G.Y., 2012. Detection of uncharged or feebly charged small molecules by field-effect transistor biosensors. *Biosens. Bioelectron.* 33, 233-240.

Albert M.A., Glynn R.J., Ridker P.M., 2003. Plasma concentration of C-reactive protein and the calculated Framingham coronary heart disease risk score. *Circulation* 108, 161-165.

Allen B.L., Kichambare P.D., Star A., 2007. Carbon nanotube field-effect-transistor-based biosensors. *Adv. Mater.* 19, 1439-1451.

An K.H., Lee Y.H., 2006. Electronic-structure engineering of carbon nanotubes. *NANO: Brief Rep. Rev.* 1, 115-138.

Bini A., Centi S., Tombelli S., Minunni M., Mascini M., 2008. Development of an optical RNA-based aptasensor for C-reactive protein. *Anal. Bioanal. Chem.* 390, 1077-1086.

Balasubramanian K., Burghard M., 2005. Chemically functionalized carbon nanotubes. *Small* 1, 180-192.

Bradley K., Briman M., Star A., Grüner G., 2004. Charge transfer from adsorbed proteins. *Nano Lett.* 4, 253-256.

Brown S.D.M., Jorio A., Corio P., Dresselhaus M.S., Dresselhaus G., Saito R., Kneipp K., 2001. Origin of the Breit-Wigner-Fano lineshape of the tangential *G*-band feature of metallic carbon nanotubes. *Phys. Rev. B* 63, 155414 (1-8).

Buch M., Rishpon J., 2008. An electrochemical immunosensor for C-reactive protein based on multi-walled carbon nanotube-modified electrodes. *Electroanalysis* 20, 2592-2594.

Cao Q., Rogers J.A., 2008. Random networks and aligned arrays of single-walled carbon nanotubes for electronic device applications. *Nano Res.* 1, 259-272.

Chen R.J., Choi H.C., Bangsaruntip S., Yenilmez E., Tang X., Wang Q., Chang Y.-L., Dai H., 2004. An investigation of the mechanisms of electronic sensing of protein adsorption on carbon nanotube devices. *J. Am. Chem. Soc.* 126, 1563-1568.

Cid C.C., Riu J., Maroto A., Rius F.X., 2008a. Detection of human immunoglobulin G at physiological conditions with chemically functionalizated carbon nanotube field effect transistors. *Curr. Nanosci.* 4, 314-317.

Cid C.C., Riu J., Maroto A., Rius F.X., 2008b. Carbon nanotube field effect transistors for the fast and selective detection of human immunoglobulin G. *Analyst* 133, 1005-1008.

Cid C.C., Riu J., Maroto A., Rius F.X., Biosensors based on carbon nanotube-network field-effect transistors. In: Carbon nanotubes: methods and protocols, methods in molecular biology, Balasubramanian K., Burghard M. (Eds.), Humana Press, New York, 2010.

Collins P.G., Avouris P., 2000. Nanotubes for electronics. *Sci. Am.* 2000, 62-69.

Cook N.R., 2007. Use and misuse of the receiver operating characteristic curve in risk prediction. *Circulation* 115, 928-935.

Curutchet A., Théron D., Werquin M., Ducatteau D., Happy H., Dambrine G., Bethoux J. M., Derycke V., Gaquière C., 2008. Nonlinear characterization and modeling of carbon nanotube field-effect transistors. *IEEE Trans. Microwave Theory Techn.* 56, 1505-1510.

Danesh J., Phil D., Wheeler J.G., Hirschfield G.N., Eda S., Eiriksdottir G., Rumley A., Lowe G.D.O., Pepys M.B., Gudnason V., 2004. C-reactive protein and other circulating markers of inflammation in the prediction of coronary heart disease. *N. Engl. J. Med.* 350, 1387-1397.

Danzer K., Otto M., Currie L.A., 2004. Guidelines for calibration in Analytical Chemistry - Part 2. Multispecies calibration. *Pure Appl. Chem.* 76, 1215-1225.

Derycke V., Martel R., Appenzeller J., Avouris P., 2001. Carbon nanotube inter- and intramolecular logic gates. *Nano Lett.* 1, 453-456.

Dillon M.C., Opris D.C., Kopanczyk R., Lickliter J., Cornwell H.N., Bridges E.G., Nazar A.M., Bridges C.G., 2010. Detection of homocysteine and C-reactive protein in the saliva of healthy adults: comparison with blood levels. *Biomark. Insights* 5, 57-61.

Dominici R., Luraschi P., Franzini C., 2004. Measurement of C-reactive protein: two high sensitivity methods compared. *J. Clin. Lab. Anal.* 18, 280-284.

Duque J.G., Densmore C.G., Doorn S.K., 2010. Saturation of surfactant structure at the single-walled carbon nanotube surface. *J. Am. Chem. Soc.* 132, 16165-16175.

Fan J., Upadhye S., Worster A., 2006. Understanding receiver operating characteristic (ROC) curves. *Can. J. Emerg. Med.* 8, 19-20.

FDA, Food and Drug Administration, Guidance for industry - review criteria for assessment of C-reactive protein (CRP), high sensitivity C-reactive protein (hsCRP) and cardiac C-reactive protein (cCRP) assays, 2005. Available at: <http://www.fda.gov/downloads/MedicalDevices/DeviceRegulationandGuidance/GuidanceDocuments/UCM071017.pdf> [Last access: 20 August 2013].

Feng Y., Miyata Y., Matsuishi K., Kataura H., 2011. High-efficiency separation of single-wall carbon nanotubes by self-generated density gradient ultracentrifugation. *J. Phys. Chem. C* 115, 1752-1756.

Findlay J.W.A., Dillard R.F., 2007. Appropriate calibration curve fitting in ligand binding assays. *AAPS J.* 9, 260-267.

Foley J.D., Sneed J.D., Steinhubl S.R., Kolasa J., Ebersole J.L., Lin Y., Kryscio R.J., McDevitt J.R., Campbell C.L., Miller C.S., 2012. Oral fluids that detect cardiovascular disease biomarkers. *Oral Surg. Oral Med. Oral Pathol. Oral Radiol.* 114, 207-214.

Ford E.S., 1999. Body mass index, diabetes, and C-reactive protein among U.S. adults. *Diabetes Care* 22, 1971-1977.

Friedewald W.T., Levy R.T., Frederickson D.S., 1972. Estimation of the concentration of low-density lipoprotein cholesterol in plasma without use of the preparative ultracentrifuge. *Clin. Chem*. 18, 499-502.

Fujii S., Tanaka T., Nishiyama S., Kataura H., 2009. High performance thin-film transistors using moderately aligned semiconducting single-wall carbon nanotubes. *Phys. Stat. Sol. B* 248, 2692-2696.

Ghosh S., Rao C.N.R., 2009. Separation of metallic and semiconducting single-walled carbon nanotubes through fluorous chemistry. *Nano Res.* 2, 183-191.

Giannobile W., Beikler T., Kinney J.S., Ramseier C., Morelli T., Wong D.T., 2009. Saliva as a diagnostic tool for periodontal disease: current state and future directions. *Periodontology 2000* 50, 52-64.

Gruner G., 2006. Carbon nanotube transistors for biosensing applications. *Anal. Bioanal. Chem.* 384, 322-335.

Gupta N.K., de Lemos J.A., Ayers C.R., Abdullah S.M., McGuire D.K., Khera A., 2012. The relationship between C-reactive protein and atherosclerosis differs on the basis of body mass index: the Dallas Heart Study. *J. Am. Coll. Cardiol.* 60, 1148-1155.

Haddon R.C., Sippel J., Rinzler A.G., Papadimitrakopoulos F., 2004. Purificaton and separation of carbon nanotubes. *MRS Bull.* 29, 252-259.

Hecht D., Hu L., Grünera G., 2006. Conductivity scaling with bundle length and diameter in single walled carbon nanotube networks. *Appl. Phys. Lett.* 89, 133112 (1-3).

Hone J., Kim P., Huang X.M.H., Chandra B., Calwell R., Small J., Hong B.H., Someya T., Huang L., O'Brien S., Nuckolls C.P., 2004. Growth of nanotubes and chemical sensor applications. *Proc. SPIE* 5593, 1-12.

Hong S., Myung S., 2007. A flexible approach to mobility. *Nat. Nanotechnol.* 2, 207-208.

Ibupoto Z.H., Jamal N., Khun K., Willander M., 2012. Development of a disposable potentiometric antibody immobilized ZnO nanotubes based sensor for the detection of C-reactive protein. *Sens. Actuators B* 166, 809-814.

Javey A., Wang Q., Ural A., Li Y., Dai H., 2002. Carbon nanotube transistor arrays for multistage complementary logic and ring oscillators. *Nano Lett.* 2, 929-932.

Justino C.I.L., Freitas A.C., Rocha-Santos T.A.P., Duarte A.C., 2012. Screening of single-walled carbon nanotubes by optical fiber sensing. *Talanta* 89, 105-108.

Justino C.I.L., Rocha-Santos T.A.P., Amaral J.P., Cardoso S., Duarte A.C., 2013a. Effects of geometry parameters of NTFET devices on the I-V measurements. *Solid State Electron.* 81, 32-34.

Justino C.I.L., Freitas A.C., Amaral J.P., Rocha-Santos T.A.P., Cardoso S., Duarte A.C., 2013b. Disposable immunosensors for C-reactive protein based on carbon nanotubes field effect transistors. *Talanta* 108, 165-170.

Kamahori M., Ishige Y., Shimoda M., 2007. A novel enzyme immunoassay based on potentiometric measurement of molecular adsorption events by an extended-gate field-effect transistor sensor. *Bios. Bioelectron.* 22, 3080-3085.

Kaufman E., Lamster I.B., 2002. The diagnostic applications of saliva – a review. *CROBM* 13, 197-202.

Karp G., Ya'akobovitz A., David-Pur M., Ioffe Z., Cheshnovsky O., Krylov S., Hanein Y., 2009. Integration of suspended carbon nanotubes into micro-fabricated devices. *J. Micromech. Microeng.* 19, 085021 (1-8).

Kim N., Kim D.K., Cho Y.J., 2009. Development of indirectcompetitive quartz crystal microbalance immunosensors for C-reactive protein. *Sens. Actuat. B* 143, 444-448.

Kim J.-Y., Ahn J.-H., Choi S.-J., Im M., Kim S., Duarte J.P., Kim C.-H., Park T.J., Lee S.Y., Choi Y.-K., 2012. An underlap channel-embedded field-effect transistor for biosensor application in watery and dry Environment. *IEEE Trans. Nanotechnol.* 11, 390-394.

Kreupl F., Carbon nanotubes in microelectronic applications. Hierold C. (Ed.) Advanced micro and nanosystems. Carbon nanotube devices. Wiley-VCH, 2008.

Lay M.D., Novack J.P., Snow E.S., 2004. Simple route to large-scale ordered arrays of liquid-deposited carbon nanotubes. *Nano Lett.* 4, 603-606.

Ledue T.M., Rifai N., 2003. Preanalytic and analytic sources of variations in C-reactive protein measurement: implications for cardiovascular disease risk assessment. *Clin. Chem.* 49, 1258-1271.

Lim J.-A., Phiboolsirichit N., Mubeen S., Rheem Y., Deshusses M.A., Mulchandani A., Myunga N.V., 2010. Electrical and sensing properties of single-walled carbon nanotubes network: effect of alignment and selective breakdown. *Electroanalysis* 22, 99-105.

Linting M., Meulman J.J., Groenen P.J.F., Van der Kooij A.J., 2007. Nonlinear principal components analysis: Introduction and application. *Psychol. Met.* 12, 336-358.

Little J.A., 2004. Comparison of curve fitting models for ligand binding assays. *Chromatographia* 59, 177-181.

Macy E.M., Hayes T.E., Tracy R.P., 1997. Variability in the measurement of C-reactive protein in healthy subjects: implications for reference intervals and epidemiological applications. *Clin. Chem.* 43, 52-58.

Martel R., Derycke V., Lavoie C., Appenzeller J., Chan K.K., Tersoff J., Avouris P., 2001. Ambipolar electrical transport in semiconducting single-wall carbon nanotubes. *Phys. Rev. Lett.* 87, 256805 (1-4).

Megson, E., Fitzsimmons, T., Dharmapatni, K., Barthold, P.M., 2010. C-reactive protein in gingival crevicular fluid may be indicative of systemic inflammation. *J. Clin. Periodontol.* 37, 797-804.

Meyer M.H.F, Hartmann M., Keusgen M., 2006. SPR-based immunosensor for the CRP detection – A new method to detect a well known protein. *Bios. Bioelectron.* 21, 1987-1990.

Meyer M.H.F., Hartmann M., Krause H.J., Blankenstein G., Mueller-Chorus B., Oster J., Miethe P., Keusgen M., 2007. CRP determination based on a novel magnetic biosensor. *Bios. Bioelectron.* 22, 973-979.

Miller J.N., Miller J.C., Statistics and chemometrics for Analytical Chemistry, 5th ed., Pearson Prentice Hall, New York, 2005.

NCEP – National Cholesterol Education Program, Third report of the National Cholesterol Education Program (NCEP) expert panel on detection, evaluation, and treatment of high blood cholesterol in adults (Adult Treatment Panel III) Executive Summary, National Heart, Lung, and Blood Institute, and National Institutes of Health, NIH Publication 01-3670, 2001.

Out D., Hall R.J., Granger D.A., Page G.G., Woods S.J., 2012. Assessing salivary C-reactive protein: longitudinal associations with systemic inflammation and cardiovascular disease risk in women exposed to intimate partner violence. *Brain Behavior Immun.* 26, 543-551.

Ouellet-Morin I., Danese A., Williams B., Arseneault L., 2011. Validation of a high-sensitivity assay for C-reactive protein in human saliva. *Brain Behavior Immun.* 25, 640-646.

Pearson T.A., Mensah G.A., Alexander R.W., Anderson J.L., Cannon III R.O., Criqui M., Fadl Y.Y., Fortmann S.P., Hong Y., Myers G.L., Rifai N., Smith S.C., Taubert K., Tracy, R.P., Vinicor F., 2003. Markers of inflammation and cardiovascular disease: application to clinical and public health practice: a statement for healthcare professionals from the centers for disease control and prevention and the American Heart Association. *Circulation* 107, 499-511.

Peng G., Trock E., Haick H., 2008. Detecting simulated patterns of lung cancer biomarkers by random network of single-walled carbon nanotubes coated with non-polymeric organic materials. *Nano Lett.* 8, 3631-3635.

Pfaffe T., Cooper-White J., Beyerlein P., Kostner K., Punyadeera C., 2011. Diagnostic potential of saliva: current state and future applications. *Clin. Chem.* 57, 675-687.

Punyadeera C., Dimeski G., Kostner K., Beyerlein P., Cooper-White J., 2011. One-step homogeneous C-reactive protein assay for saliva. *J. Immunol. Methods* 373, 19-25.

Quershi A., Gurbuz, Y., Krag W.P., Davidson J.L., 2009. A novel interdigitated capacitor based biosensor for detection of cardiovascular risk marker. *Bios. Bioelectron.* 25, 877-882.

Rawson E.S., Freedson P.S., Osganian S.K., Matthews C.E., Reed G, Ockene I.S., 2003. Body mass index, but not physical activity, is associated with C-reactive protein. *Med. Sci. Sports Exerc.* 35, 1160-1166.

Ridker P.M., 2003a. Clinical application of C-reactive protein for cardiovascular disease detection and prevention. *Circulation* 107, 363-369.

Ridker P.M., Buring, J.E., Cook, N.R., Rifai N., 2003b. C-reactive protein, the metabolic syndrome, and risk incident cardiovascular events. *Circulation* 107, 391-397.

Ridker O., Rifai N., Koenig W., Blumenthal R.S., 2006. C-reactive protein and cardiovascular risk in the Framingham study. *Arch. Intern. Med.* 166, 1327-1328.

Ridker P.M., Wilson P.W.F., Grundy S.M., 2004. Should C-reactive protein be added to metabolic syndrome and to assessment of global cardiovascular risk? *Circulation* 109, 2818-2825.

Ridker P.M., Kastelein J.J.P., Genest J., Koenig W., 2013. C-reactive protein and cholesterol are equally strong predictors of cardiovascular risk and both are important for quality clinical care. *Eur. Heart J.* 34, 1258-1261.

Robison-Cox J.F., 1995. Multiple estimation of concentrations in immunoassay using logistic models. *J. Immun. Methods* 186, 79-88.

Roger V.L., Go A.S., Lloyd-Jones D.M., Benjamin E.J., Berry J.D., Borden W.B., Bravata D.M., Dai S., Ford E.S., Fox C.S., Fullerton H.J., Gillespie C., Hailpern S.M., Heit J.A., Howard V.J., Kissela B.M., Kittner S.J., Lackland D.T., Lichtman J.H., Lisabeth L.D., Makuc D.M., Marcus G.M., Marelli A., Matchar D.B., Moy C.S., Mozaffarian D., Mussolino M.E., Nichol G., Paynter N.P., Soliman E.Z., Sorlie P.D., Sotoodehnia N., Turan T.N., Virani S.S., Wong N.D., Woo D., Turner M.B., 2012. Heart disease and stroke statistics - 2012 update. A report from the American Heart Association. *Circulation* 125, 2-220.

Shim H.C., Song J.-W., Kwak Y.K., Kim S., Han C.-S., 2009. Preferential elimination of metallic single-walled carbon nanotubes using microwave irradiation *Nanotechnol.* 20, 065707 (1-5).

SigmaPlot 11.0 (Statistical Analysis Software), Systat Software Inc., Germany, 2008.

Silvera-Batista C.A., Scott D.C., McLeod S.M., Ziegler K.J., 2010. A mechanistic study of the selective retention of SDS-suspended single-wall carbon nanotubes on agarose gels. *J. Phys. Chem. C* 115, 9361-9369.

Smith C.J., Emsley H.C.A., Gavin C.M, Georgiou R.F., Vail A., Barberan, A.M., del Zoppo G.J., HallenbeckJ.M., Rothwell N.J., Hopkins S.J, Tyrrell P.J., 2004. Peak plasma interleukin-6 and other peripheral markers of inflammation in the first week of ischaemic stroke correlate with brain infarct volume, stroke severity and long-term outcome. *BMC Neurology* 4, 2 (1-8).

Snow E.S., Novak J.P., Campbell P.M., Park D., 2003. Random networks of carbon nanotubes as an electronic material. *Appl. Phys. Lett.* 82, 2145-2147.

SPSS software, version 21.0.0.0, IBM Corporation. New York, 2012.

Star A., Gabriel J., Bradley K., Grüner G., 2003. Electronic detection of specific protein binding using nanotube FET devices. *Nano Lett.* 3, 459-463.

Star A., Han T.-R., Joshi V., Stetter J.R., 2004. Sensing with nafion coated carbon nanotube field-effect transistors. *Electroanalysis* 16, 108-112.

Suarez E.C., 2004. C-reactive protein is associated with psychological risk factors of cardiovascular disease in apparently healthy adults. *Psychosomatic Med.* 66, 684-691.

Tanaka T., Jin H., Miyata Y., Fujii S., Suga H., Naitoh Y., Minari T., Miyadera T., Tsukagoshi K., Kataura H., 2009a. Simple and scalable gel-based separation of metallic and semiconducting carbon nanotubes. *Nano Lett.* 9, 1497-1500.

Tanaka T., Urabe Y., Nishide D., Kataura H., 2009b. Continuous separation of metallic and semiconducting carbon nanotubes using agarose gel. *Appl. Phys. Express* 2, 125002 (1-3).

Tanaka T., Liu H., Fujii S., Kataura H., 2011. From metal/semiconductor separation to single-chirality separation of single-wall carbon nanotubes using gel. *Phys. Status Solidi RRL* 5, 301-306.

Teker K., Wickstrom E., Panchapakesan B., 2006. Biomolecular tuning of electronic transport properties of carbon nanotubes via antibody functionalization. *IEEE Sens. J.* 6, 1422-1428.

Testing protocol, Cat. #1-3302, Salimetrics™. Available at: <http://www.salimetrics.com/documents/CRP_Kit_Insert.pdf> [Last access: 20 August 2013].

Tey J.N., Wijaya P.M., Wang Z., Goh W.H., Palaniappan A., Mhaisalkar S.G., Rodriguez I., Dunham S., Rogers J.A., 2009. Laminated, microfluidic-integrated carbon nanotube based biosensors. *Appl. Phys. Lett.* 94, 013107 (1-3).

Villamizar R.A., Maroto A., Rius F.X., Inza I., Figueras M.J., 2008. Fast detection of Salmonella infantis with carbon nanotube field effect transistors. *Bios. Bioelectron.* 24, 279-283.

Villamizar R.A., Maroto A., Rius F.X., 2009. Improved detection of Candida albicans with carbon nanotube field effect transistors. *Sens. Actuat. B* 136, 451-457.

Villamizar R.A., Maroto A., Rius F.X., 2011. Rapid detection of Aspergillus flavus in rice using biofunctionalized carbon nanotube field effect transistors. *Anal. Bional. Chem.* 399, 119-126.

Wang S., Humphreys E.S., Chung S.-Y., Delduco D.F., Lustig S.R., Wang H., Parker, K.N., Rizzo N.W., Subramoney S., Chiang Y.-M., Jagota A., 2003. Peptides with selective affinity for carbon nanotubes. *Nat. Mater.* 2, 196-200.

Wind S.J., Appenzeller J., Martel R., Derycke V., Avouris P., 2002. Vertical scaling of carbon nanotube field-effect transistors using top gate electrodes. *Appl. Phys. Lett.* 80, 3817-3819.

Yang Y.-N., Lin H.-I., Wang J.-H., Shiesh S.-C., Lee G.-B., 2009. An integrated microfluidic system for C-reactive protein measurement. *Bios. Bioelectron.* 24, 3091-3096.

Chapter 6

Concluding Remarks

In this thesis, disposable NTFET were developed to be used as immunosensors for the biosensing of the CRP in clinical samples that is, blood serum and saliva, using a SWCNT network as transduction components. The assemblage of the NTFET was performed with uniform and stable SWCNT dispersions in SC, which were obtained after 60 minutes of sonication, and 5 minutes of centrifugation at 2000 × g, and with the FET fabricated with a gold layer of 100 nm, a distance between electrodes of 2.5 µm, and 10 electrodes.

The developed NTFET were capable of detecting concentrations of the CRP over a linear range between 10^{-4} and 10^{2} mg L^{-1}, with an analytical error of 3.6 % and an acceptable reproducibility of less than 15 %, when applied to standard solutions of CRP.

The NTFET showed a very low LOD of 100 ng L^{-1}, which is comparable with that obtained with ELISA technique for the determination of salivary and serum CRP. The best calibration model was based on a log-log curve with an acceptable value for the R^2 of 0.9924 and for the adjusted R^2 of 0.9910.

The cost-effectiveness of the analysis, the simple use associated with the disposable and label-free NTFET, and the need for low sample volumes (of about 1 µL) makes this biosensor much more fit for purpose and advantageous for the determination of the CRP than the currently and readily available analytical systems, such as the ELISA technique.

When applied to clinical samples, the NTFET also provided analytical results comparable with those obtained with a traditional ELISA methodology, taking into account the similar CRP levels in blood and saliva samples from volunteer patients. Thus, the residual levels of CRP in healthy persons without any sign of inflammation, that is, with the CRP levels in serum below 3 mg L^{-1}, as well as critical levels of the CRP responsible for pathological evidences, that is, higher than 3 mg L^{-1}, could be detected with the NTFET.

A strong correlation was found between the salivary and the serum CRP, both determined by the NTFET and the ELISA, which suggests that the developed NTFET is appropriate and can be suggested as a real alternative to point-of-care testing for detecting the risk of CVD. The successful application and performance of the NTFET for the determination of the CRP in saliva makes it suitable for non-invasive testing, with the possibility of becoming useful for the self point-of-care testing at home.

The correlation between the salivary and the serum CRP allowed to establish a new range of CRP levels in saliva associated with: a) patients with the salivary CRP below 700 ng L^{-1} and consequently with low risk to develop a CVD (corresponding to the serum CRP below 1 mg L^{-1}), b) patients with the salivary CRP levels between 700 ng L^{-1} and 1900 ng L^{-1}, and consequently with a moderate risk to develop a CVD (corresponding to the serum CRP between 1 and 3 mg L^{-1}), and finally c) patients with the salivary CRP higher than 1900 ng L^{-1}, and consequently with a high risk to develop a CVD (corresponding to the serum CRP higher than 3 mg L^{-1}).

Finally, the triglycerides, serum CRP, total cholesterol, LDL cholesterol, BMI, Framingham risk score, hypertension, dyslipidemia, and *diabetes mellitus*, known as risk factors contributing to the development of CVD, were found to be the parameters responsible for the separation of the data obtained in this study for the control and the CVD risk patients.

Appendix I

Consent form and information provided to volunteer patients before sample collection

DECLARAÇÃO DE CONSENTIMENTO

Considerando a "Declaração de Helsínquia" da Associação Médica Mundial
(Helsínquia 1964; Tóquio 1975; Veneza 1983; Hong Kong 1989; Somerset West 1996 e Edimburgo 2000)

Designação do Estudo (em português):

Desenvolvimento de um Nanosensor para Detecção de Risco de Doenças Cardiovasculares (CARDIOSENSOR)

Eu, abaixo-assinado, (nome completo)

Responsável pelo doente (nome completo)

, declaro que o mesmo não participa em nenhum outro projecto de investigação durante este internamento, tendo compreendido a explicação que me foi fornecida acerca da sua situação clínica e da investigação que se tenciona realizar. Foi-me ainda dada oportunidade de fazer as perguntas que julguei necessárias, e de todas obtive resposta satisfatória.

Tomei conhecimento de que, de acordo com as recomendações da Declaração de Helsínquia, a informação ou explicação que me foi prestada versou os objectivos, os métodos, os benefícios previstos, os riscos potenciais e o eventual desconforto. Além disso, foi-me afirmado que tenho o direito de recusar a todo o tempo a sua participação no estudo, sem que isso possa ter como efeito qualquer prejuízo na assistência que lhe é prestada.
Por isso, consinto que lhe seja aplicado o método, o tratamento ou o inquérito proposto pelo investigador.

Data: ____ / _____ / 2013

Assinatura do Responsável pelo doente: _____

O Investigador responsável:

Nome: Paulo Manuel Barreiros de Castro Chaves

Assinatura:

INFORMAÇÃO AO PARTICIPANTE

Título do estudo: Desenvolvimento de um Nanosensor para Detecção de Risco de Doenças Cardiovasculares (CARDIOSENSOR)

Investigador responsável: Paulo Manuel Barreiros de Castro Chaves
Contacto do Investigador responsável: [redacted]

Objectivo da investigação:
Actualmente, a Proteína C Reactiva (PCR) é medida no sangue usando imunoturbidimetria, ensaios imunoelectroforéticos, ELISA ou ensaios imunofluorescentes. Contudo, estes ensaios são técnicas invasivas de avaliação do risco cardiovascular. O desenvolvimento de um nanosensor para determinação dos níveis da PCR na saliva permitirá efectuar o seu doseamento de uma forma simples e não invasiva.
O presente projecto tem os seguintes objectivos:
- desenvolvimento e validação de um nanosensor para determinação da PCR;
- comparação dos dados obtidos utilizando um ensaio de ELISA no sangue (método invasivo) e um nanosensor no sangue e saliva (invasivo e não invasivo);
- comparação do método de ELISA e do nanosensor em indivíduos em risco de eventos cardiovasculares;
- desenvolvimento de um protótipo para aplicação da metodologia do nanosensor em serviços de saúde.

Metodologia a utilizar:
De forma a atingir os objectivos expostos acima, será feito um inquérito para colheita de dados pessoais e clínicos relativos ao doente em causa. Proceder-se-á em seguida à colheita de uma amostra de sangue por punção em veia periférica e a uma colheita de saliva por emissão. As amostras serão em seguida processadas e analisadas.

Benefícios esperados e riscos possíveis:
Este projecto desenvolverá um novo nanosensor para determinação do risco cardiovascular que será sensível e selectivo à PCR e que aliará o reduzido tempo de análise à não necessidade de pré-tratamento das amostras e fornecerá resultados in-situ, contribuindo para aumentar a qualidade dos diagnósticos médicos.

Incómodos derivados da participação:
O do desconforto associado às colheitas de sangue por venipunctura.

Outras informações a prestar ao participante:

Relativamente à participação neste projecto é importante sublinhar os seguintes aspectos:
- a participação tem carácter voluntário;
- será fornecido tempo para reflectir sobre o pedido de participação, inclusive poder ouvir opinião de familiares e/ou amigos;
- haverá total liberdade para decidir sobre a participação no projecto;
- haverá, em qualquer momento, possibilidade de retirada do estudo sem que se comprometa o relacionamento com o médico nem o respeito pelos direitos à assistência que lhe é devida;
- haverá total garantia de privacidade e confidencialidade;
- a investigação foi submetida e aprovada pela Comissão de Ética para a Saúde do Centro Hospitalar de S. João - EPE.

____ / ___ / ___

O Investigador Responsável,

_____

Appendix II

Questionnaire provided to volunteer patients before sample collection

QUESTIONÁRIO

O presente questionário tem como objectivo identificar indivíduos que apresentem factores de risco associados à ocorrência de doenças cardiovasculares e que possam ser indicadores do possível surgimento de situações agudas, caso os mesmos se mantenham. Os dados obtidos são anónimos, e não terão outra utilização que não o propósito científico a que se destinam. Este estudo está integrado num projecto financiado pela Fundação para a Ciência e Tecnologia, Projecto Cardiosensor (Ref. Ref. PTDC/SAU-BEB/099042/2008) e os dados obtidos no âmbito do mesmo ficarão na posse exclusiva dos investigadores envolvidos.

1. Caracterização do Inquirido

1.1. Idade ___

1.2. Sexo: Feminino ☐ Masculino: ☐

1.3. Peso: _____ **Altura:** _____

1.4. Profissão: _____

1.5. Considera que possui uma profissão de risco ou de elevado nível de stress?

Sim ☐ Não ☐

Em caso afirmativo, indique porquê: _____----

_____

1.6. Possui tensão arterial elevada?

Sim ☐ Não ☐ Valores:_____ (máxima);_____ (mínima)

Em caso de resposta afirmativa, toma algum tipo de medicação para controlar a hipertensão?

Sim ☐ Não ☐ Qual? _____

1.7. Qual o seu nível de colesterol total, a última vez que fez análises ao sangue?

Menor que 200 mg/dL ☐ Não sei, só sei que era elevado ☐

200-239 mg/dL ☐ Não sei, só sei que era baixo ☐

Maior que 240mg/dL ☐ Não sei ☐

Em caso de resposta afirmativa, toma algum tipo de medicação para controlar o colesterol?

Sim ☐ Não ☐ Qual? _____

1.8. Já lhe foi diagnosticada algum tipo de doença crónica/prolongada:

Sim ☐ Não ☐

1.9. Que tipo de doença crónica/prolongada?

Diabetes	☐	Hepatite	☐	Cancro	☐
Obesidade	☐	Asma	☐	Artrites	☐
Intolerância à glucose	☐	Alergias	☐	Bronquites	☐
Arterosclerose	☐	Outra	☐		

Qual? _____

Em caso de resposta afirmativa, toma algum tipo de medicação de forma continuada?

Sim ☐ Não ☐ Qual? _____

2. História Familiar

2.1. Possui algum familiar próximo com doença cardiovascular?

Sim ☐ Não ☐ Qual? _____

Em caso de resposta afirmativa, qual o grau de parentesco? _____

3. Alimentação e Hábitos de Vida

3.1. Pratica desporto?

Sim ☐ Não ☐ Qual? _____

Em caso de resposta afirmativa, com que frequência semanal?

Diariamente	☐	Duas ou mais vezes/semana	☐
Menos de duas vezes/semana	☐	Quando tenho disponibilidade	☐

3.2. Em relação ao sono:

Dorme bem, acorda descansado(a) ☐ Ressona ☐

☐

Dorme agitado(a), acorda cansado(a)

3.3. Hábitos tabágicos:

Não fuma	☐	Convive com fumadores ocasionalmente	☐
Já fumou mas deixou de fumar	☐	Convive com fumadores frequentemente	☐
Fuma ocasionalmente	☐	Não convive com fumadores	☐

Se fumador activo, indique o número médio de cigarros/dia: _____

3.4. Consome uma ou mais doses de bebida com que frequência? (Considere uma dose o equivalente a 1 cerveja ou um copo de vinho)

Nunca	☐
Ocasionalmente, 1 dose	☐
Ocasionalmente, mais de 1 dose	☐
Uma vez por semana, 1 dose	☐
Uma vez por semana, mais de 1 dose	☐
Duas vezes por semana, 1 dose	☐
Duas vezes por semana, mais de 1 dose	☐
Mais de 2 vezes por semana, 1 dose	☐
Mais de 2 vezes por semana, mais de 1 dose	☐

3.5. Além das bebidas acima mencionadas, consome outras, como licores fortes e shots?

Sim ☐ Não ☐ Só consumo destas bebidas ☐

3.6. Seleccione um número de 1 a 5 na escala abaixo descrita, para indicar a frequência com que come cada um dos alimentos abaixo indicados:

1 - Em menos de 2 dias da semana
2 – Em 2 a 3 dias da semana
3 – 1 vez por dia, em todos os dias da semana
4 – 2 vezes ou mais por dia, em alguns dias da semana
5 – 2 ou mais vezes por dia, em todos os dias da semana

Peixe	☐	Croissants, bolos, pastéis	☐
Carnes vermelhas estufadas	☐	Feijões e rebentos de soja	☐
Carnes vermelhas grelhadas	☐	Alimentos fritos	☐
	☐		☐
	☐		☐

Carnes brancas | Cereais

Legumes | Frutos secos

3.7. Como tempera os seus alimentos?

Muito sal ☐ | Especiarias em vez de sal ☐

Com uma quantidade moderada de sal ☐ | Sem sal e sem especiarias ☐

Pouco sal ☐ | Temperos com azeite ☐

Temperos com óleos vegetais ☐ | ☐

3.8. Com que frequência consome uma dose de cafeína? (Considere uma dose, um café uma coca-cola ou chá de 33 Cl)

Nunca ☐

Diariamente, uma dose ☐

Diariamente, mais do que uma dose ☐

Ocasionalmente ☐

3.9. Já consumiu/consome (sublinhar a opção correcta) **algum tipo de drogas?**

Sim ☐ Não ☐ Qual? _____

4. Em caso de internamento na UAVC

4.1. Motivo de internamento

AVC isquémico ☐ AVC hemorrágico ☐ Outro _____

4.2. Pontuação NIHSS na admissão _____

4.3. Etiologia provável para o evento isquémico

Doença de grandes vasos ☐ | Doença de pequenos vasos ☐

Cardioembolismo ☐ | Outro/Indeterminado ☐

Muito obrigado pela sua colaboração

Appendix III

Results obtained from the questionnaires provided from each volunteer patient

Medical history and lifestyle factors of each volunteer patient **(cont.)**

	Sample Number	Age	Gender	Weight (kg)	Height (cm)	Stress	Hypertension	Dyslipidemia	Diabetes mellitus	Family history of CVD	Physical activity	Tobacco Consumption	Alcohol Consumption	Coffee Consumption	CVD type
Control Patients	34	59	M	55	174	N	N	N	N	N	Y	Ex-Smoker	>2x/week	Daily	-
	30	47	M	75	166	N	N	N	N	N	N	Ex-Smoker	>2x/week	Occasional	-
	23	38	F	59	155	Y	N	N	N	Y	Y	N	N	Daily	-
	22	36	M	82	181	Y	N	N	N	N	Y	N	Occasional	Daily	-
	20	34	M	61	164	Y	N	N	N	N	Y	N	Occasional	Daily	-
	19	50	M	72	168	Y	N	N	N	N	Y	N	>2x/week	Daily	-
	16	51	M	62	164	Y	Y	N	N	Y	N	Ex-Smoker	>2x/week	Daily	-
	15	41	F	85	155	Y	N	N	N	N	Y	N	Occasional	N	-
	14	58	M	74	173	Y	N	N	Y	Y	Y	N	Occasional	Occasional	-
	4	48	F	66	164	Y	N	N	N	N	N	N	N	N	-
	5	30	F	58	163	Y	N	N	N	Y	N	N	N	Daily	
	67	50	M	85	178	Y	N	Y	N	Y	Y	Ex-Smoker	>2x/week	Daily	CHD
	55	52	M	82	167	N	Y	Y	Y	N	N	Ex-Smoker	>2x/week	Daily	CH
	45	57	M	62	158	N	Y	Do not know	N	Y	N	N	N	Occasional	CHD
	41	82	F	65	148	N	Y	Do not know	Y	Y	N	N	N	N	CHD
CVD Risk Patients	2	48	M	77	164	Y	Y	N	N	N	N	Y	Occasional	Occasional	-
	8	56	M	78	170	Y	Y	Y	N	N	N	Y	>2x/week	Occasional	-
	62	79	M	72	166	N	Y	Do not know	Y	N	N	N	N	N	CHD
	56	73	M	60	160	Y	Y	Do not know	N	N	N	Ex-Smoker	N	N	CH
	51	49	F	80	156	Y	Y	Do not know	N	Y	N	N	N	Occasional	CHD
	53	52	M	122	186	Y	Y	Y	Y	N	N	N	>2x/week	Daily	TIA
	44	52	F	67	160	Y	N	Y	N	Y	N	Y	N	N	CHD
	S24	49	M	91	173	Y	Y	Do not know	Y	Y	N	Y	>2x/week	N	CHD
	S30	61	M	71	167	Y	Y	Y	Y	Y	N	Ex-Smoker	>2x/week	Occasional	CHD
	S6	62	M	74	155	N	Y	Y	N	N	N	N	Occasional	Occasional	CHD
	S7	54	M	84	184	Y	Y	Y	N	Y	N	Y	N	Occasional	TIA
	S13	53	M	95	165	Y	Y	Y	Y	N	N	N	>2x/week	Occasional	CHD
	S15	75	M	74	160	N	Y	Do not know	N	N	N	N	N	N	CH
	S33	83	M	45	155	N	N	Y	N	N	N	Y	N	Occasional	CHD
	S35	73	M	70	165	N	N	Y	N	Y	N	Ex-Smoker	>2x/week	Occasional	CH

CVD - Cardiovascular Disease; CHD - Coronary Heart Disease; TIA - Transient Ischemic Attack; CH - Cerebral Hemorrhage; N - No; Y - Yes; M - Male; F - Female

Medical history and lifestyle factors of each volunteer patient (cont.)

	Sample Number	Total Cholesterol (mg dL^{-1})	HDL Cholesterol (mg dL^{-1})	LDL Cholesterol (mg dL^{-1})	Triglycerides (mg dL^{-1})	CRP Ref. Lab. (mg L^{-1})	Total / HDL Col.	BMI (kg m^{-2})	Framingham Score (% 10-year CVD risk)
Control Patients	34	173	42	94.8	181	0.48	4.1	18.17	8
	30	190	42	130.6	87	0.82	4.5	27.22	1
	23	189	60	120.2	44	0.74	3.2	24.56	1
	22	145	39	86.8	96	0.81	3.7	25.03	1
	20	163	48	95.2	99	0.89	3.4	22.68	1
	19	169	53	89	135	0.22	3.2	25.51	3
	16	147	42	84	105	0.46	3.5	23.05	3
	15	158	52	79.8	131	2.59	3.0	35.38	1
	14	196	47	122	135	2.16	4.2	24.73	8
	4	161	56	88.4	83	0.50	2.9	24.54	1
	5	166	71	83.2	59	1.55	2.3	21.83	1
	67	150	39	90	104	0.74	3.8	26.83	4
	55	190	88	81	103	0.70	2.2	29.40	3
	45	133	38	73	108	0.8	3.5	24.84	6
	41	163	59	85	95	0.23	2.8	29.67	5
CVD Risk Patients	2	210	37	117.4	278	6.73	5.7	28.63	20
	8	205	51	114	200	3.53	4.0	26.99	16
	62	169	51	103	74	4.04	3.3	26.13	12
	56	169	43	100	131	22.30	3.9	23.44	12
	51	222	52	136	171	12.50	4.3	32.87	1
	53	184	46	101	184	3.50	4.0	35.26	5
	44	217	39	141	186	4.14	5.6	26.17	4
	S24	187	39	109	196	3.80	4.8	30.41	12
	S30	205	41	115	244	11.10	5.0	25.46	10
	S6	191	50	129	61	3.50	3.8	30.80	8
	S7	244	27	158	297	10.40	9.0	24.81	20
	S13	295	46	214	173	8.40	6.4	34.89	10
	S15	189	41	130	88	3.30	4.6	28.91	16
	S33	257	59	174	122	5.70	4.4	18.73	20
	S35	182	57	108	85	21.80	3.2	25.71	10

Classification of risk parameters according to several references a, b, c, and d

Total Cholesterol (mg dL^{-1})[a]	HDL Cholesterol (mg dL^{-1})[a]	LDL Cholesterol (mg dL^{-1})[a]	Triglycerides (mg dL^{-1})[a]	CRP Ref. Lab. (mg L^{-1})[b]	Total / HDL Col.[c]	BMI (kg m^{-2})[d]
Desirable < 200	High (Low Risk) > 60	Optimal < 100	Normal < 150	Low Risk < 1.0	Optimal ratio of 3.5:1	Underweight < 18.50
Borderline High 200-239	Low (High Risk) < 40	Above optimal 100-129	Borderline High 150-199	Moderate 1.0 to 3.0	Normal ratio < 5:1	Normal range 18.50 to 24.99
High > 240		Borderline High 130-159	High 200-499	High Risk 3.0 to 10	High ratio > 5	Overweight > 25.00
		High 160-189		Very High > 10		Obese > 30.00
		Very High > 190				

[a] **based on ATP III from National Cholesterol Education Program guidelines;**

[b] **based on Ridker *et al.,* 2003. *Circulation* 107, 363-369;**

[c] **based on The American Heart Association**

Available at: http://www.heart.org/HEARTORG/Conditions/Cholesterol/AboutCholesterol/What-Your-Cholesterol-Levels-Mean_UCM_305562_Article.jsp

[d] **based on The International Classification of World Health Organization**

Available at: http://apps.who.int/bmi/index.jsp?introPage=intro_3.html

Appendix IV

Data used in the SPSS software, and coded from the data reported in Appendix III

	Sample Number in SPSS software	Sample Number	CRP[a] (mg L^{-1})	Total Cholesterol (mg dL^{-1})	HDL Cholesterol (mg dL^{-1})	LDL Cholesterol (mg dL^{-1})	Triglycerides (mg dL^{-1})	BMI (kg m^{-2})	Age	Framingham Score (%)
CVD Risk Patients	**1**	2	6.76	210	37	117	278	28.63	48	20
	2	8	3.49	205	51	114	200	26.99	56	16
	3	62	4.18	169	51	103	74	26.13	79	12
	NA	56	21.81	169	43	100	131	23.44	73	12
	NA	51	12.54	222	46	101	184	35.26	49	5
	4	53	3.41	184	46	101	184	35.26	52	5
	5	44	4.27	217	39	141	186	26.17	52	4
	6	S24	3.36	187	39	109	196	30.41	49	12
	NA	S30	11.91	205	41	115	244	25.46	61	10
	7	S6	3.79	191	50	129	61	30.80	62	8
	NA	S7	11.42	244	27	158	297	24.81	54	20
	8	S13	8.42	295	46	214	173	34.89	53	10
	9	S15	3.44	189	41	130	88	28.91	75	16
	10	S33	5.20	257	59	174	122	18.73	83	2
	NA	S35	21.58	182	57	108	85	25.71	73	10
Control Patients	**11**	34	0.42	173	42	95	181	18.17	59	8
	12	30	0.82	190	42	131	87	27.22	47	1
	13	23	0.70	189	60	120	44	24.56	38	1
	14	22	0.82	145	39	87	96	25.03	36	1
	15	20	0.76	163	48	95	99	22.68	34	1
	16	19	0.23	169	53	89	135	25.51	50	3
	17	16	0.45	147	42	84	105	23.05	51	3
	18	15	2.51	158	52	80	131	35.38	41	1
	19	14	2.28	196	47	122	135	24.73	58	8
	20	4	0.52	161	56	88	83	24.54	48	1
	21	5	1.54	166	71	83	59	21.83	30	1
	22	67	0.72	150	39	90	104	26.83	50	4
	23	55	0.74	190	88	81	103	29.40	52	3
	24	45	0.83	133	38	73	108	24.84	57	6
	25	41	0.19	163	59	85	95	29.67	82	5

NA - Not Applicable;

The data of these patients were used for the application of the *t* -test, but they were not used for the Categorical Principal Components Analysis;

[a]The CRP values are the means of the CRP values obtained by the NTFET and the ELISA technique for each patient

	Sample Number in SPSS software	Sample Number	Gender	Stress	Hypertension	Dyslipidemia	*Diabetes mellitus*	Family history of CVD	Physical Activity	Tobacco Consumption	Alcohol Consumption	Coffee Consumption
CVD Risk Patients	**1**	2	1	2	2	1	1	1	1	2	3	3
	2	8	1	2	2	2	1	1	1	2	2	3
	3	62	1	1	2	3	2	1	1	1	1	1
	NA	56	1	2	2	3	1	1	1	3	1	1
	NA	51	2	2	2	3	1	2	1	1	1	2
	4	53	1	2	2	2	2	1	1	1	2	2
	5	44	2	2	1	2	1	2	1	2	1	1
	6	S24	1	2	2	3	2	2	1	2	2	1
	NA	S30	1	2	2	2	2	2	1	3	3	3
	7	S6	1	1	2	2	1	1	1	1	3	3
	NA	S7	1	2	2	2	1	2	1	2	1	3
	8	S13	1	2	2	2	2	1	1	1	2	3
	9	S15	1	1	2	3	1	1	1	1	1	1
	10	S33	1	1	1	2	1	1	1	2	1	3
	NA	S35	1	1	1	2	1	2	1	3	3	3
Control Patients	**11**	34	1	1	1	1	1	1	2	3	2	2
	12	30	1	1	1	1	1	1	1	3	2	3
	13	23	2	2	1	1	1	2	2	1	1	2
	14	22	1	2	1	1	1	1	2	1	3	2
	15	20	1	2	1	1	1	1	2	1	3	2
	16	19	1	2	1	1	1	1	2	1	2	2
	17	16	1	2	2	1	1	2	1	3	2	2
	18	15	2	2	1	1	1	1	2	1	3	1
	19	14	1	2	1	1	2	2	2	1	3	3
	20	4	2	2	1	1	1	1	1	1	1	1
	21	5	2	2	1	1	1	2	1	1	1	2
	22	67	1	2	1	2	1	2	2	3	2	2
	23	55	1	1	2	2	2	1	1	3	2	2
	24	45	1	1	2	3	1	2	1	1	1	3
	25	41	2	1	2	3	2	2	1	1	1	1

Codification of qualitative parameters:

Gender: 1 = Male, and 2 = Female

Stress, Hypertension, *Diabetes mellitus* , family history of CVD, and physical activity: 1 = No, and 2 = Yes

Dyslipidemia: 1 = No, 2 = Yes, and 3 = Do not know **Tobacco comsumption:** 1 = No, 2 = Yes, and 3 = Ex-Smoker

Alcohol comsumption: 1 = No, 2 = more than 2x in a week, and 3 = Occasional **Coffee comsumption:** 1= No, 2 = Daily, and 3 = Occasional

Appendix V

Database of the serum and the salivary CRP concentrations determined by NTFET and ELISA

Appendix Va: Mean and standard deviation (SD) of the CRP levels for each patient obtained by the NTFET and by the ELISA technique

		Determination of the serum CRP						Determination of the salivary CRP					
	Sample N.º	NTFET [1]			ELISA technique [2]			NTFET [1]			ELISA technique [2]		
		Mean (mg L^{-1})	SD (mg L^{-1})	CV (%)	Mean (mg L^{-1})	SD (mg L^{-1})	CV (%)	Mean (ng L^{-1})	SD (ng L^{-1})	CV (%)	Mean (ng L^{-1})	SD (ng L^{-1})	CV (%)
Control Patients	34	0.41	0.01	2.1	0.44	0.08	17.7	477.73	8.55	1.8	486.26	21.44	4.4
	30	0.81	0.02	2.8	0.82	0.14	17.2	824.57	8.18	1.0	834.71	199.50	23.9
	23	0.71	0.05	6.9	0.69	0.06	8.8	641.72	5.83	0.9	645.71	124.32	19.3
	22	0.82	0.01	1.6	0.83	0.03	3.2	871.20	11.20	1.3	893.04	155.29	17.4
	20	0.78	0.03	3.8	0.74	0.05	7.2	1008.92	4.94	0.5	1017.49	229.10	22.5
	19	0.21	0.04	17.7	0.25	0.04	16.0	185.30	1.62	0.9	184.92	30.59	16.5
	16	0.42	0.03	7.1	0.48	0.02	3.5	278.69	2.44	0.9	273.66	72.30	26.4
	15	2.34	0.09	3.9	2.68	0.39	14.4	1707.77	16.95	1.0	1711.99	350.90	20.5
	14	2.30	0.16	6.8	2.27	0.21	9.3	1722.77	16.78	1.0	1637.33	361.80	22.1
	4	0.49	0.04	8.4	0.55	0.12	22.5	536.86	9.37	1.7	546.44	37.07	6.8
	5	1.55	0.05	3.0	1.53	0.03	1.9	1655.75	29.68	1.8	1671.87	341.16	20.4
	67	0.67	0.03	4.4	0.77	0.06	7.5	578.07	13.00	2.2	584.06	116.83	20.0
	55	0.70	0.06	9.2	0.77	0.04	4.7	620.14	8.86	1.4	638.37	156.86	24.6
	45	0.79	0.03	3.3	0.87	0.17	19.3	915.72	3.33	0.4	916.68	162.15	17.7
	41	0.17	0.03	18.9	0.21	0.06	29.9	172.83	3.01	1.7	170.67	12.47	7.3
		0.88 ± 0.67			**0.93 ± 0.70**			**813.20 ± 520.35**			**814.21 ± 512.10**		
CVD Risk Patients	2	6.46	0.10	1.6	7.07	0.24	3.4	3241.01	106.46	3.3	3271.07	583.63	17.8
	8	3.36	0.04	1.1	3.61	0.12	3.3	1683.11	44.10	2.6	1770.28	314.80	17.8
	62	4.27	0.06	1.5	4.08	0.13	3.1	1794.39	18.77	1.0	1802.33	360.12	20.0
	56	23.52	0.23	1.0	20.09	0.07	0.3	11112.64	493.59	4.4	11691.26	2316.19	19.8
	51	12.44	0.18	1.5	12.65	0.94	7.4	6121.66	13.99	0.2	6077.71	1225.74	20.2
	53	3.41	0.27	7.8	3.41	0.11	3.2	1703.94	58.92	3.5	1752.12	360.63	20.6
	44	4.24	0.09	2.1	4.30	0.31	7.3	2743.69	41.74	1.5	2764.30	363.55	13.2
	S24	3.55	0.17	4.8	3.17	0.15	4.9	2744.06	70.13	2.6	2760.59	386.92	14.0
	S30	12.82	0.36	2.8	11.00	0.48	4.3	7106.98	18.68	0.3	7003.98	913.01	13.0
	S6	3.50	0.12	3.4	4.08	0.32	7.8	1555.02	8.60	0.6	1542.65	360.73	23.4
	S7	11.93	0.81	6.8	10.92	0.60	5.5	5053.58	15.57	0.3	5036.50	1997.18	39.7
	S13	8.52	0.14	1.7	8.32	0.00	0.0	3390.27	57.02	1.7	3474.78	305.62	8.8
	S15	3.48	0.06	1.7	3.39	0.44	12.9	2050.13	22.01	1.1	2044.09	217.67	10.6
	S33	5.30	0.21	4.0	5.10	0.03	0.6	3577.16	61.35	1.7	3597.63	409.88	11.4
	S35	21.77	0.83	3.8	21.39	0.21	1.0	10695.75	236.17	2.2	10674.22	2706.95	25.4
		8.57 ± 6.68			**8.17 ± 5.99**			**4304.89 ± 3149.38**			**4350.90 ± 3218.47**		

[1]Mean, standard deviation (SD), and coefficients of variation (% CV) for three individual NTFET. For each NTFET, three measurements were performed, and the results are shown in Appendix Vb.
[2]Mean, standard deviation (SD), and coefficients of variation (% CV) for two ELISA microplates. For each microplate, duplicates were performed, and the results are shown in Appendix Vc.

Appendix Vb: Mean and standard deviation (SD) of the three measurements for each NTFET **(cont.)**

Serum samples		NTFET #1			NTFET #2			NTFET #3		
		Mean	SD	CV (%)	Mean	SD	CV (%)	Mean	SD	CV (%)
CVD risk patients	2	6.54	0.37	5.6%	6.35	0.40	6.3%	6.50	0.32	4.9%
	8	3.33	0.43	12.9%	3.40	0.32	9.5%	3.34	0.17	5.1%
	62	4.22	0.10	2.5%	4.34	0.13	3.0%	4.25	0.02	0.5%
	56	23.52	0.18	0.8%	23.76	0.88	3.7%	23.29	0.98	4.2%
	51	12.50	0.86	6.9%	12.59	0.90	7.2%	12.24	1.64	13.4%
	53	3.46	0.44	12.7%	3.12	0.10	3.1%	3.64	0.28	7.6%
	44	4.22	0.19	4.5%	4.33	0.12	2.9%	4.16	0.15	3.5%
	S24	3.74	0.26	7.0%	3.48	0.37	10.6%	3.43	0.33	9.5%
	S30	13.16	1.20	9.1%	12.87	0.98	7.6%	12.45	1.41	11.4%
	S6	3.57	0.31	8.5%	3.36	0.05	1.6%	3.56	0.12	3.2%
	S7	12.86	1.01	7.9%	11.52	0.83	7.2%	11.40	1.35	11.8%
	S13	8.44	0.35	4.2%	8.68	0.25	2.9%	8.44	0.38	4.5%
	S15	3.50	0.23	6.7%	3.53	0.44	12.3%	3.42	0.29	8.6%
	S33	5.18	0.15	2.8%	5.17	0.15	2.9%	5.54	0.33	5.9%
	S35	21.74	1.77	8.2%	20.95	0.76	3.6%	22.62	1.73	7.6%
Control Patients	34	0.41	0.07	16.5%	0.41	0.09	22.5%	0.40	0.08	19.5%
	30	0.78	0.03	3.4%	0.81	0.03	3.6%	0.83	0.01	1.3%
	23	0.71	0.06	8.0%	0.75	0.05	6.9%	0.65	0.05	7.1%
	22	0.84	0.03	3.6%	0.81	0.06	7.8%	0.81	0.05	6.5%
	20	0.78	0.08	9.9%	0.80	0.08	10.3%	0.74	0.04	5.0%
	19	0.21	0.05	21.5%	0.24	0.04	17.0%	0.17	0.04	21.0%
	16	0.39	0.08	19.9%	0.44	0.05	10.5%	0.41	0.05	10.9%
	15	2.24	0.36	15.9%	2.36	0.18	7.6%	2.43	0.26	10.7%
	14	2.23	0.20	9.0%	2.19	0.10	4.4%	2.48	0.21	8.4%
	4	0.52	0.04	7.5%	0.52	0.07	13.0%	0.45	0.01	2.7%
	5	1.54	0.13	8.4%	1.51	0.09	6.2%	1.60	0.05	2.9%
	67	0.67	0.10	14.2%	0.64	0.04	6.4%	0.70	0.08	12.0%
	55	0.71	0.02	2.8%	0.76	0.03	4.4%	0.63	0.03	5.0%
	45	0.76	0.03	3.7%	0.79	0.08	9.6%	0.81	0.03	4.3%
	41	0.19	0.07	37.4%	0.18	0.04	23.6%	0.13	0.04	29.9%

Appendix Vb: Mean and standard deviation (SD) of the three measurements for each NTFET

Saliva samples		NTFET #1			NTFET #2			NTFET #3		
		Mean	SD	CV (%)	Mean	SD	CV (%)	Mean	SD	CV (%)
CVD risk patients	2	3174.72	165.16	5.2%	3184.50	158.60	5.0%	3363.80	73.26	2.2%
	8	1677.53	26.21	1.6%	1729.74	23.60	1.4%	1642.07	26.33	1.6%
	62	1811.19	49.50	2.7%	1774.14	88.24	5.0%	1797.85	55.71	3.1%
	56	11538.99	191.90	1.7%	10571.90	484.23	4.6%	11227.03	550.50	4.9%
	51	6137.19	37.13	0.6%	6110.04	23.73	0.4%	6117.75	58.96	1.0%
	53	1746.71	55.16	3.2%	1636.73	38.48	2.4%	1728.38	50.92	2.9%
	44	2749.02	48.50	1.8%	2699.54	130.75	4.8%	2782.51	72.26	2.6%
	S24	2803.92	61.95	2.2%	2761.36	67.24	2.4%	2666.90	57.70	2.2%
	S30	7087.35	75.61	1.1%	7109.07	62.66	0.9%	7124.52	36.23	0.5%
	S6	1559.01	58.98	3.8%	1545.14	30.87	2.0%	1560.89	77.06	4.9%
	S7	5046.98	31.87	0.6%	5071.36	28.68	0.6%	5042.39	39.75	0.8%
	S13	3358.84	91.96	2.7%	3456.09	7.88	0.2%	3355.87	162.87	4.9%
	S15	2041.36	49.90	2.4%	2075.17	3.75	0.2%	2033.85	35.03	1.7%
	S33	3534.90	176.75	5.0%	3549.04	142.31	4.0%	3647.52	99.79	2.7%
	S35	10564.27	194.36	1.8%	10554.58	891.13	8.4%	10968.39	589.12	5.4%
Control Patients	34	474.46	19.84	4.2%	471.31	14.75	3.1%	487.43	13.04	2.7%
	30	833.93	16.78	2.0%	821.01	1.83	0.2%	818.78	13.45	1.6%
	23	640.39	16.92	2.6%	648.10	2.41	0.4%	636.67	15.58	2.4%
	22	874.76	14.17	1.6%	880.19	27.28	3.1%	858.65	25.20	2.9%
	20	1003.24	4.05	0.4%	1012.13	11.80	1.2%	1011.41	7.89	0.8%
	19	186.38	0.96	0.5%	186.07	1.77	0.9%	183.44	2.90	1.6%
	16	276.74	13.95	5.0%	277.91	6.42	2.3%	281.43	11.55	4.1%
	15	1707.51	61.75	3.6%	1690.95	74.43	4.4%	1724.85	58.74	3.4%
	14	1737.05	57.63	3.3%	1726.97	66.10	3.8%	1704.29	58.59	3.4%
	4	526.04	3.45	0.7%	541.90	17.18	3.2%	542.64	17.40	3.2%
	5	1622.00	13.89	0.9%	1667.51	66.10	4.0%	1677.75	54.94	3.3%
	67	592.56	8.54	1.4%	567.41	20.68	3.6%	574.25	18.11	3.2%
	55	626.61	15.02	2.4%	610.04	3.07	0.5%	623.75	10.00	1.6%
	45	912.21	7.67	0.8%	918.83	13.68	1.5%	916.13	7.37	0.8%
	41	169.38	2.01	1.2%	174.90	6.06	3.5%	174.20	4.80	2.8%

Appendix Vc: Mean and standard deviation (SD) of duplicates for each ELISA microplate (cont.)

Salivary CRP determined by ELISA technique

Regression equation (Plate #1)
x=(y-0.0556)/0.0003

	OD (at 450 nm)	Samples	[CRP] (ng L^{-1})	Mean (ng L^{-1})	SD (ng L^{-1})	CV
	0.829	High Control	2577.33	2484.17	131.76	5.3%
	0.773	High Control	2391.00			
	0.104	Low Control	160.80	159.92	1.25	0.8%
	0.103	Low Control	159.03			
CVD Risk Patients	0.152	2	321.87	329.62	10.95	3.3%
	0.157	2	337.36			
	0.109	8	176.70	178.59	2.68	1.5%
	0.110	8	180.49			
	0.109	62	178.33	178.55	0.31	0.2%
	0.109	62	178.77			
	0.385	56	1097.33	1159.52	87.94	7.6%
	0.422	56	1221.70			
	0.253	51	657.67	600.95	80.21	13.3%
	0.219	51	544.23			
	0.107	53	169.60	172.62	4.27	2.5%
	0.108	53	175.63			
	0.152	44	320.67	289.17	44.55	15.4%
	0.133	44	257.67			
	0.132	S24	253.67	286.83	46.90	16.4%
	0.152	S24	320.00			
	0.267	S30	703.20	733.33	42.61	5.8%
	0.285	S30	763.47			
	0.100	S6	148.63	148.43	0.28	0.2%
	0.100	S6	148.23			
	0.182	S7	421.00	418.02	4.22	1.0%
	0.180	S7	415.03			
	0.175	S13	398.50	375.73	32.20	8.6%
	0.162	S13	352.97			
	0.121	S15	218.00	217.98	0.02	0.0%
	0.121	S15	217.97			
	0.163	S33	357.67	381.50	33.71	8.8%
	0.177	S33	405.33			
	0.378	S35	1075.67	1010.33	92.40	9.1%
	0.339	S35	945.00			
Control Patients	0.070	34	47.67	54.33	9.43	17.4%
	0.074	34	61.00			
	0.079	30	77.67	79.93	3.21	4.0%
	0.080	30	82.20			
	0.074	23	62.47	64.37	2.69	4.2%
	0.076	23	66.27			
	0.083	22	92.07	90.37	2.40	2.7%
	0.082	22	88.67			
	0.088	20	106.30	98.65	10.82	11.0%
	0.083	20	91.00			
	0.061	19	18.60	18.88	0.40	2.1%
	0.061	19	19.16			
	0.064	16	26.67	25.65	1.44	5.6%
	0.063	16	24.63			
	0.105	15	162.67	168.76	8.61	5.1%
	0.108	15	174.84			
	0.103	14	158.43	159.38	1.34	0.8%
	0.104	14	160.33			
	0.073	4	56.33	59.98	5.16	8.6%
	0.075	4	63.63			
	0.105	5	165.63	165.02	0.87	0.5%
	0.105	5	164.40			
	0.073	67	57.77	57.83	0.08	0.1%
	0.073	67	57.89			
	0.073	55	58.33	60.85	3.56	5.8%
	0.075	55	63.37			
	0.083	45	89.33	92.42	4.36	4.7%
	0.084	45	95.50			
	0.061	41	18.67	18.72	0.07	0.4%
	0.061	41	18.77			

Salivary CRP determined by ELISA technique **Regression equation (Plate #2)** **(cont.)**

x=(y-0.0371)/0.0004

	OD (at 450 nm)	Samples	[CRP] (ng L^{-1})	Mean (ng L^{-1})	SD (ng L^{-1})	CV
	0.832	High Control	1987.42	1859.42	181.02	9.7%
	0.730	High Control	1731.42			
	0.092	Low Control	136.17	143.23	9.99	7.0%
	0.097	Low Control	150.29			
CVD Risk Patients	0.141	2	259.92	323.17	89.45	27.7%
	0.192	2	386.42			
	0.109	8	180.67	174.83	8.25	4.7%
	0.105	8	168.99			
	0.109	62	180.09	180.50	0.59	0.3%
	0.109	62	180.92			
	0.486	56	1121.92	1169.54	67.35	5.8%
	0.524	56	1217.17			
	0.271	51	584.92	609.29	34.47	5.7%
	0.291	51	633.67			
	0.107	53	173.89	176.09	3.11	1.8%
	0.108	53	178.29			
	0.152	44	288.42	265.04	33.06	12.5%
	0.134	44	241.67			
	0.132	S24	238.10	266.34	39.94	15.0%
	0.155	S24	294.59			
	0.326	S30	722.92	671.15	73.20	10.9%
	0.285	S30	619.39			
	0.100	S6	157.88	157.72	0.23	0.1%
	0.100	S6	157.56			
	0.247	S7	524.54	565.89	58.48	10.3%
	0.280	S7	607.24			
	0.172	S13	336.47	323.89	17.78	5.5%
	0.162	S13	311.32			
	0.107	S15	175.41	192.82	24.63	12.8%
	0.121	S15	210.24			
	0.170	S33	331.40	341.03	13.62	4.0%
	0.177	S33	350.67			
	0.476	S35	1097.67	1104.53	9.71	0.9%
	0.482	S35	1111.40			
Control Patients	0.055	34	44.44	44.01	0.61	1.4%
	0.055	34	43.59			
	0.071	30	85.42	85.54	0.18	0.2%
	0.071	30	85.67			
	0.064	23	68.33	64.47	5.47	8.5%
	0.061	23	60.60			
	0.071	22	85.60	88.10	3.54	4.0%
	0.073	22	90.60			
	0.079	20	103.59	103.59	0.00	0.0%
	0.079	20	103.59			
	0.044	19	17.42	18.13	1.00	5.5%
	0.045	19	18.84			
	0.049	16	29.09	28.56	0.74	2.6%
	0.048	16	28.04			
	0.104	15	167.08	172.03	7.00	4.1%
	0.108	15	176.98			
	0.103	14	165.39	166.06	0.95	0.6%
	0.104	14	166.73			
	0.060	4	56.24	50.25	8.47	16.9%
	0.055	4	44.26			
	0.104	5	166.40	167.78	1.96	1.2%
	0.105	5	169.17			
	0.060	67	57.84	58.57	1.04	1.8%
	0.061	67	59.31			
	0.063	55	65.60	65.79	0.27	0.4%
	0.063	55	65.98			
	0.073	45	90.42	90.50	0.12	0.1%
	0.073	45	90.59			
	0.043	41	15.75	15.75	0.00	0.0%
	0.043	41	15.75			

Serum CRP determined by ELISA technique **Regression equation (Plate #1)** **(cont.)**

x=(y+0.0086)/0.0022

	OD (at 450 nm)	Samples	[CRP] (ng L^{-1})			Mean (ng L^{-1})	SD (ng L^{-1})	CV
	0.1487	High Control	71.48			72.28	1.12	1.6%
	0.1522	High Control	73.07					
	0.0223	Low Control	14.06			15.54	2.09	13.4%
	0.0288	Low Control	17.02					
				x50000	[CRP] (mg L^{-1})			
CVD Risk Patients	0.3047	2	142.39	7119500.00	7.12	7.24	0.17	2.3%
	0.3152	2	147.16	7358136.36	7.36			
	0.1546	8	74.17	3708636.36	3.71	3.70	0.02	0.4%
	0.1536	8	73.72	3685909.09	3.69			
	0.1966	62	93.26	4663181.82	4.66	4.17	0.69	16.6%
	0.1536	62	73.72	3685909.09	3.69			
	0.8776	56	402.80	20139954.55	20.14	20.14	0.00	0.0%
	0.8775	56	402.75	20137681.82	20.14			
	0.5758	51	265.64	13281818.18	13.28	13.31	0.04	0.3%
	0.5785	51	266.84	13342227.27	13.34			
	0.1366	53	65.99	3299545.45	3.30	3.34	0.05	1.5%
	0.1397	53	67.43	3371268.18	3.37			
	0.1875	44	89.12	4455863.64	4.46	4.52	0.10	2.1%
	0.1934	44	91.83	4591363.64	4.59			
	0.1425	S24	68.70	3435045.45	3.44	3.28	0.22	6.6%
	0.1291	S24	62.61	3130500.00	3.13			
	0.4604	S30	213.16	10658136.36	10.66	10.66	0.00	0.0%
	0.4605	S30	213.21	10660409.09	10.66			
	0.1801	S6	85.75	4287681.82	4.29	4.30	0.02	0.4%
	0.1812	S6	86.25	4312681.82	4.31			
	0.4983	S7	230.39	11519500.00	11.52	11.34	0.25	2.2%
	0.4829	S7	223.39	11169500.00	11.17			
	0.3596	S13	167.35	8367727.27	8.37	8.32	0.06	0.8%
	0.3557	S13	165.57	8278590.91	8.28			
	0.1503	S15	72.21	3610409.09	3.61	3.70	0.13	3.6%
	0.1585	S15	75.94	3796772.73	3.80			
	0.2166	S33	102.35	5117727.27	5.12	5.13	0.01	0.3%
	0.2174	S33	102.73	5136495.45	5.14			
	0.9014	S35	413.62	20680863.64	20.68	21.24	0.79	3.7%
	0.9506	S35	435.98	21799045.45	21.80			
Control Patients	0.0089	34	7.96	397859.09	0.40	0.38	0.02	5.5%
	0.0076	34	7.36	368240.45	0.37			
	0.0367	30	20.61	1030500.00	1.03	0.92	0.15	16.2%
	0.0274	30	16.37	818636.36	0.82			
	0.0271	23	16.25	812318.18	0.81	0.73	0.11	15.4%
	0.0201	23	13.06	653227.27	0.65			
	0.0271	22	16.23	811722.73	0.81	0.84	0.05	5.4%
	0.0299	22	17.52	875954.55	0.88			
	0.0259	20	15.70	785045.45	0.79	0.78	0.01	1.7%
	0.0251	20	15.34	766863.64	0.77			
	0.0033	19	5.42	271231.82	0.27	0.28	0.01	2.2%
	0.0037	19	5.60	279868.18	0.28			
	0.0130	16	9.84	491863.64	0.49	0.50	0.01	1.2%
	0.0134	16	10.01	500454.55	0.50			
	0.1036	15	50.98	2549045.45	2.55	2.40	0.21	8.6%
	0.0908	15	45.16	2258136.36	2.26			
	0.0825	14	41.39	2069500.00	2.07	2.12	0.07	3.1%
	0.0866	14	43.27	2163313.64	2.16			
	0.0191	4	12.61	630500.00	0.63	0.64	0.01	2.0%
	0.0199	4	12.97	648681.82	0.65			
	0.0616	5	31.90	1595000.00	1.60	1.51	0.12	8.1%
	0.0540	5	28.44	1421772.73	1.42			
	0.0274	67	16.38	819136.36	0.82	0.81	0.01	1.2%
	0.0268	67	16.11	805500.00	0.81			
	0.0256	55	15.56	778227.27	0.78	0.80	0.02	3.1%
	0.0272	55	16.25	812681.82	0.81			
	0.0352	45	19.89	994500.00	0.99	0.99	0.00	0.0%
	0.0351	45	19.88	994222.73	0.99			
	0.0030	41	5.28	264186.36	0.26	0.26	0.01	2.9%
	0.0026	41	5.07	253590.91	0.25			

Serum CRP determined by ELISA technique

Regression equation (Plate #2)

x=(y+0.0061)/0.0022

	OD (at 450 nm)	Samples	[CRP] (ng L^{-1})			Mean (ng L^{-1})	SD (ng L^{-1})	CV
	0.170	High Control	80.20			78.89	1.86	2.4%
	0.165	High Control	77.57					
	0.015	Low Control	9.68			9.42	0.36	3.9%
	0.014	Low Control	9.17					
				x50000	[CRP] (mg L^{-1})			
CVD Risk Patients	0.300	2	138.91	6945454.55	6.95	6.90	0.07	0.9%
	0.295	2	137.06	6852840.91	6.85			
	0.149	8	70.38	3518750.00	3.52	3.53	0.02	0.5%
	0.150	8	70.84	3542045.45	3.54			
	0.160	62	75.66	3783068.18	3.78	3.99	0.30	7.5%
	0.179	62	84.11	4205568.18	4.21			
	0.891	56	407.55	20377272.73	20.38	20.04	0.48	2.4%
	0.861	56	394.06	19702840.91	19.70			
	0.550	51	252.73	12636397.73	12.64	11.98	0.92	7.7%
	0.492	51	226.59	11329431.82	11.33			
	0.154	53	72.75	3637500.00	3.64	3.49	0.21	6.0%
	0.141	53	66.84	3342045.45	3.34			
	0.172	44	80.73	4036363.64	4.04	4.08	0.06	1.5%
	0.175	44	82.50	4124886.36	4.12			
	0.128	S24	60.88	3043750.00	3.04	3.06	0.03	1.0%
	0.130	S24	61.70	3085227.27	3.09			
	0.492	S30	226.30	11314772.73	11.31	11.33	0.03	0.2%
	0.494	S30	227.09	11354545.45	11.35			
	0.165	S6	77.77	3888636.36	3.89	3.85	0.05	1.4%
	0.162	S6	76.25	3812500.00	3.81			
	0.422	S7	194.80	9739772.73	9.74	10.50	1.08	10.3%
	0.490	S7	225.27	11263636.36	11.26			
	0.360	S13	166.25	8312500.00	8.31	8.33	0.02	0.2%
	0.361	S13	166.75	8337500.00	8.34			
	0.129	S15	61.48	3073977.27	3.07	3.08	0.01	0.4%
	0.130	S15	61.83	3091715.91	3.09			
	0.225	S33	104.82	5240909.09	5.24	5.08	0.23	4.4%
	0.210	S33	98.43	4921704.55	4.92			
	0.957	S35	437.56	21878181.82	21.88	21.53	0.49	2.3%
	0.926	S35	423.75	21187500.00	21.19			
Control Patients	0.015	34	9.61	480340.91	0.48	0.49	0.02	3.5%
	0.016	34	10.09	504431.82	0.50			
	0.025	30	14.20	709886.36	0.71	0.72	0.02	2.7%
	0.026	30	14.75	737500.00	0.74			
	0.022	23	12.98	648977.27	0.65	0.65	0.00	0.5%
	0.022	23	12.88	644204.55	0.64			
	0.029	22	16.16	807954.55	0.81	0.81	0.00	0.2%
	0.029	22	16.10	805113.64	0.81			
	0.025	20	14.11	705681.82	0.71	0.70	0.01	1.0%
	0.025	20	13.91	695454.55	0.70			
	0.003	19	4.14	207045.45	0.21	0.22	0.02	8.1%
	0.004	19	4.64	232159.09	0.23			
	0.016	16	9.93	496590.91	0.50	0.47	0.03	7.2%
	0.014	16	8.97	448295.45	0.45			
	0.120	15	57.16	2857954.55	2.86	2.95	0.13	4.4%
	0.128	15	60.80	3039772.73	3.04			
	0.100	14	48.25	2412613.64	2.41	2.41	0.00	0.1%
	0.100	14	48.33	2416250.00	2.42			
	0.014	4	9.35	467386.36	0.47	0.46	0.01	1.1%
	0.014	4	9.20	460113.64	0.46			
	0.063	5	31.39	1569318.18	1.57	1.55	0.03	1.7%
	0.061	5	30.63	1531477.27	1.53			
	0.026	67	14.61	730681.82	0.73	0.73	0.00	0.0%
	0.026	67	14.62	730795.45	0.73			
	0.027	55	15.10	754886.36	0.75	0.74	0.02	2.1%
	0.026	55	14.65	732693.18	0.73			
	0.029	45	15.97	798511.36	0.80	0.76	0.06	8.1%
	0.025	45	14.25	712500.00	0.71			
	0.001	41	3.25	162264.77	0.16	0.17	0.01	5.3%
	0.002	41	3.50	174920.45	0.17			

Appendix VI

Database of the serum and the salivary CRP concentrations determined by the ELISA technique: calibration study

Salivary CRP determined by ELISA technique (Plate #1)

Standards ($ng\ L^{-1}$)	OD (at 450 nm)	Calculated CRP	Mean	Recovery (%)
3000	1.111	3048.8	3027.3	101%
3000	1.096	3005.8		
1500	0.539	1396.8	1395.4	93%
1500	0.538	1393.9		
750	0.358	872.3	860.1	115%
750	0.349	848.0		
375	0.182	363.6	400.6	107%
375	0.207	437.6		
187.5	0.105	143.9	145.9	78%
187.5	0.107	148.0		
98.75	0.086	88.2	87.9	89%
98.75	0.086	87.6		
0	0.054			
0	0.056			

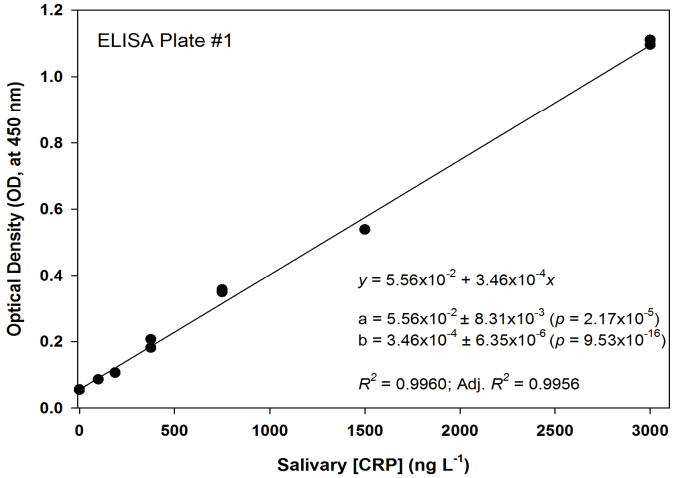

Salivary CRP determined by ELISA technique (Plate #2)

Standards ($ng\ L^{-1}$)	OD (at 450 nm)	Calculated CRP	Mean	Recovery (%)
3000	1.114	3067.7	3046.1	102%
3000	1.099	3024.4		
1500	0.547	1452.9	1442.4	96%
1500	0.540	1431.8		
750	0.282	698.8	703.5	94%
750	0.286	708.1		
375	0.155	336.9	356.2	95%
375	0.169	375.4		
187.5	0.104	189.9	191.6	102%
187.5	0.105	193.3		
98.75	0.086	139.7	139.0	141%
98.75	0.086	138.3		
0	0.046			
0	0.056			

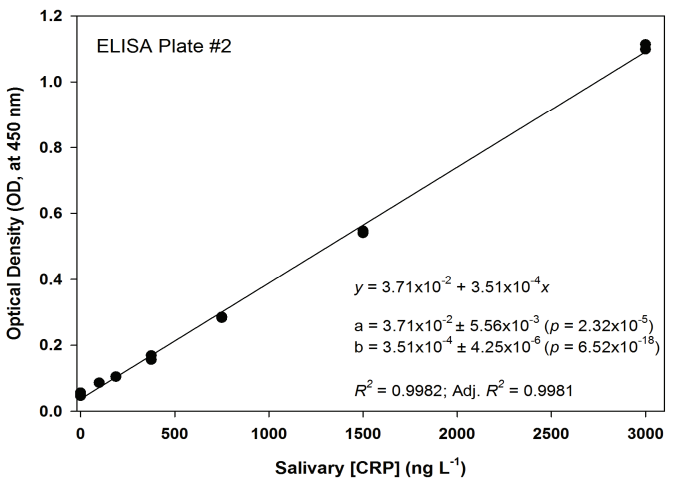

Serum CRP determined by ELISA technique (Plate #1)

Standards (ng L^{-1})	OD (at 450 nm)	Calculated CRP	Mean	Recovery (%)
600	1.3025	595.9	592.5	99%
600	1.2876	589.2		
200	0.3896	181.0	204.4	102%
200	0.4928	227.9		
66.67	0.1094	53.6	53.6	80%
66.67	0.1094	53.6		
22.22	0.0364	20.5	20.3	91%
22.22	0.0357	20.2		
7.407	0.0129	9.8	9.8	132%
7.407	0.0130	9.8		
2.469	0.0004	4.1	4.1	165%
2.469	0.0004	4.1		
0	0.0001			
0	0.0002			

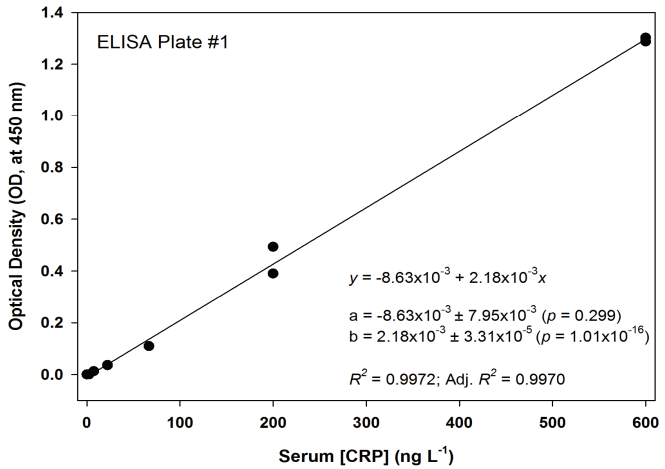

Serum CRP determined by ELISA technique (Plate #2)

Standards (ng L^{-1})	OD (at 450 nm)	Calculated CRP	Mean	Recovery (%)
600	1.2096	552.6	591.9	92%
600	1.3825	631.2		
200	0.4310	198.7	192.5	99%
200	0.4040	186.4		
66.67	0.1628	76.8	63.5	115%
66.67	0.1046	50.3		
22.22	0.0457	23.5	21.3	106%
22.22	0.0359	19.1		
7.407	0.0131	8.7	9.0	118%
7.407	0.0144	9.3		
2.469	0.0005	3.0	3.0	122%
2.469	0.0005	3.0		
0	0.0002			
0	0.0002			

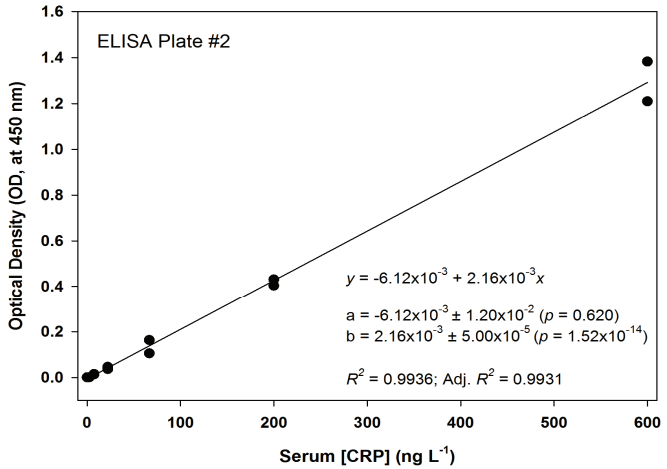

Appendix VII

Calculations of Framingham Risk Score for the serum samples of volunteer patients, and tables with reference values for their calculation

Appendix VIIa: Data to calculate the Framingham score for each patient

	Sample N.º	Age	Genre	Tobacco Consumer	Total Cholesterol (mg dL^{-1})	HDL Cholesterol (mg dL^{-1})	Framingham Point Scores					Estimate of 10-year risk (%)
							Age	Total Ch.	HDL Ch.	Tob. Cons.	Total Points	
Control Patients	34	59	M	Ex-smoker	173	42	8	0	2	1	11	8
	30	47	M	Ex-smoker	190	42	0	0	3	1	4	1
	23	38	F	N	189	60	-3	0	4	-1	0	1
	22	36	M	N	145	39	-4	0	0	2	-2	1
	20	34	M	N	163	48	-9	0	4	1	-4	1
	19	50	M	N	169	53	6	0	2	0	8	3
	16	51	M	Ex-smoker	147	42	6	0	0	1	7	3
	15	41	F	N	158	52	0	0	0	0	0	1
	14	58	M	N	196	47	8	0	2	1	11	8
	4	48	F	N	161	56	3	0	3	0	6	1
	5	30	F	N	166	71	-7	0	4	-1	-4	1
	67	50	M	Ex-smoker	150	39	6	0	0	2	8	4
	55	52	M	Ex-smoker	190	88	6	0	2	-1	7	3
	45	57	M	N	133	38	8	0	0	2	10	6
	41	82	F	N	163	59	16	0	1	0	17	5
CVD Risk Patients	2	48	M	Y	210	37	3	5	5	2	15	20
	8	56	M	Y	205	51	8	3	3	0	14	16
	62	79	M	N	169	51	13	0	0	0	13	12
	56	73	M	Ex-smoker	169	43	12	0	0	1	13	12
	51	49	F	N	222	52	3	0	6	0	9	1
	53	52	M	N	184	46	6	0	2	1	9	5
	44	52	F	Y	217	39	6	4	4	2	16	4
	S24	49	M	Y	187	39	3	5	3	2	13	12
	S30	61	M	Ex-smoker	205	41	10	0	1	1	12	10
	S6	62	M	N	191	50	10	0	1	0	11	8
	S7	54	M	Y	244	27	6	3	4	2	15	20
	S13	53	M	N	295	46	6	0	5	1	12	10
	S15	75	M	N	189	41	13	0	0	1	14	16
	S33	83	M	Y	257	59	13	1	1	0	15	20
	S35	73	M	Ex-smoker	182	57	12	0	0	0	12	10

Appendix VIIb: Framingham Point Scores for Estimate of 10-year risk for men (Source: National Heart, Lung, and Blood Institute; National Institutes of Health; U.S. Department of Health and Human Services).

Age	Points
20-34	-9
35-39	-4
40-44	0
45-49	3
50-54	6
55-59	8
60-64	10
65-69	11
70-74	12
75-79	13

Total Cholesterol	Points				
	Age 20-39	Age 40-49	Age 50-59	Age 60-69	Age 70-79
<160	0	0	0	0	0
160-199	4	3	2	1	0
200-239	7	5	3	1	0
240-279	9	6	4	2	1
≥280	11	8	5	3	1

	Points				
	Age 20-39	Age 40-49	Age 50-59	Age 60-69	Age 70-79
Nonsmoker	0	0	0	0	0
Smoker	8	5	3	1	1

HDL (mg/dL)	Points
≥60	-1
50-59	0
40-49	1
<40	2

Systolic BP (mmHg)	If Untreated	If Treated
<120	0	0
120-129	0	1
130-139	1	2
140-159	1	2
≥160	2	3

Point Total	10-Year Risk %
<0	< 1
0	1
1	1
2	1
3	1
4	1
5	2
6	2
7	3
8	4
9	5
10	6
11	8
12	10
13	12
14	16
15	20
16	25
≥17	≥ 30

Appendix VIIc: Framingham Point Scores for Estimate of 10-year risk for women (Source: National Heart, Lung, and Blood Institute; National Institutes of Health; U.S. Department of Health and Human Services).

Age	Points
20-34	-7
35-39	-3
40-44	0
45-49	3
50-54	6
55-59	8
60-64	10
65-69	12
70-74	14
75-79	16

	Points				
Total Cholesterol	Age 20-39	Age 40-49	Age 50-59	Age 60-69	Age 70-79
<160	0	0	0	0	0
160-199	4	3	2	1	1
200-239	8	6	4	2	1
240-279	11	8	5	3	2
≥280	13	10	7	4	2

	Points				
	Age 20-39	Age 40-49	Age 50-59	Age 60-69	Age 70-79
Nonsmoker	0	0	0	0	0
Smoker	9	7	4	2	1

HDL (mg/dL)	Points
≥60	-1
50-59	0
40-49	1
<40	2

Systolic BP (mmHg)	If Untreated	If Treated
<120	0	0
120-129	1	3
130-139	2	4
140-159	3	5
≥160	4	6

Point Total	10-Year Risk %
<9	< 1
9	1
10	1
11	1
12	1
13	2
14	2
15	3
16	4
17	5
18	6
19	8
20	11
21	14
22	17
23	22
24	27
≥25	≥ 30